THE TURBULENT DYNAMICS OF QUASI-STEADY SPILLING BREAKERS - THEORY AND EXPERIMENTS
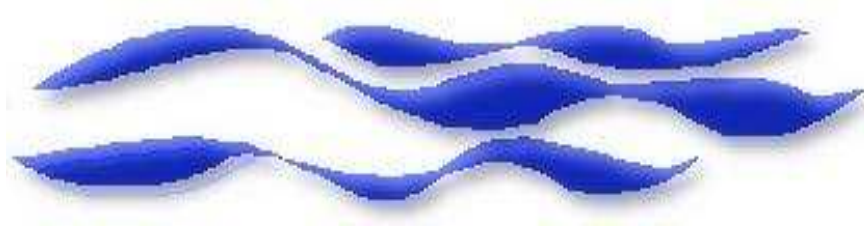
Shubhra K. Misra, James T. Kirby and Maurizio Brocchini

Center for Applied Coastal Research

Ocean Engineering Laboratory

University of Delaware

Newark, DE 19716

ACKNOWLEDGEMENTS

TABLE OF CONTENTS

LIST OF FIGURES

ABSTRACT

This dissertation provides a detailed description of the turbulence structure and its effects on the mean flow of fully-formed quasi-steady spilling breakers. Laboratory experiments are conducted for an air-entraining turbulent hydraulic jump in Froude similitude with saturated surf-zone breakers. Particle image velocimetry measurements are used to investigate the mean and turbulent structure of the flow, with particular attention to the surface intermittency. The streamwise variation of the turbulent length scales and growth rates in the breaker shear layer are in good agreement with values found in mixing layers. The combined effects of flow-deceleration and adverse pressure gradient upstream of the foot of the breaker are responsible for the separation of the shear layer causing breaking. A theoretical model is developed for the evolution of the turbulent dynamics in a spilling breaking wave. The theoretical model provides an accurate mathematical incorporation of the effects of the two-phase surface layer, unsteadiness, curvature, rotation, and non-hydrostatic effects. Evolution equations are derived for the mean flow and turbulent kinetic energy in the breaker shear layer. Several physical mechanisms of the flow in different regimes are studied through geometric and kinematic scaling assumptions and comparisons made with experimental observations. The governing equations are then integrated across the shear layer to develop boundary conditions for the irrotational flow underneath. Coherent turbulent structures are analyzed through kinematic and statistical techniques applied to the experimental data. The sizes and topologies of these structures provide valuable insights into the dominant modes of turbulence in the breaker shear layer.

Chapter 1

INTRODUCTION

The breaking of a wave cannot explain the whole sea

Vladimir Nabokov

Turbulence generation by water-wave breaking is the dominant mechanism governing the mass, momentum, and energy transfer processes that occur in water bodies exposed to atmospheric forcings. In the open ocean, it plays an important role in influencing the Earth's weather and climate through air-sea exchanges of heat and gases, surfactant transport, and marine aerosol production (Melville *et al.*, 2002). Water quality and aquatic life are directly influenced by such interactions as well. In deep water, where wind-generated surface waves are not directly affected by variations in bed topography, breaking typically results in the formation of "whitecaps". The water falling down the face of the wave appears white due to the entrainment and ejection of air-bubbles at the surface. However, micro-breakers, where surface-tension is high enough to prevent air-entrainment, are also believed to be significant in the air-sea exchange processes. In addition to direct wind effects, wave-wave and wave-current interactions can also lead to breaking events that are inherently unsteady. On a much larger and more violent scale, wave breaking poses numerous hazards to navigation at sea. Wave breaking is often induced by ship-wakes. The structural safety of vessels and offshore structures is determined by the wave-breaking environment. A comprehensive review of various aspects of deep-water breaking is provided in Banner and Peregrine (1993).

1

In shallower water, to a large extent, the turbulence generated by depth-limited wave breaking is directly responsible for the sediment suspension and transport through momentum and energy transfer from the waves to the sediment. Further, the breaker turbulence modifies the cross-shore and longshore currents, which in turn affect the accretional and erosional characteristics of the coastline. Some of the earliest classifications of breakers in shallow water were suggested based on experimental observations by Iverson (1952) and Mason (1952). Galvin (1968) popularized the terminology of spilling, plunging, and surging breakers in the surf-zone. As evident from their nomenclature, plunging breakers, typically found on steep beaches, are characterized by a rather spectacular forward overturning of the entire front face of the wave. The moving sheet of water plunges down into the water in front causing significant splashes (sometime reversed in direction) and air-entrainment. Several splash-up cycles can occur before the organized motion due to the wave becomes fully turbulent. This makes them difficult candidates for experimental and theoretical investigations, and knowledge of the resulting turbulent flow remains scarce. Further details can be found in experimental studies of Perlin *et al.* (1996) and Liiv (2001). An inviscid mechanism has also been proposed for the break-up of the jet in a plunging breaker (Longuet-Higgins, 1995).

Compared to plunging breakers, the dynamics of spilling breakers are better understood, and the turbulence generated differs from that in a plunging breaker primarily in the method of energy transfer from the wave motion to turbulent motion (Ting and Kirby, 1995, 1996). Spilling breakers are visually less spectacular, and more subtle processes govern the inception of turbulence. In addition to their ubiquitous presence in deep water, they commonly occur on moderately steep beaches. A spilling breaker is characterized by white water formation on the front face of the wave. A laboratory generated spilling breaking wave is shown in Figure 1.1. The wave propagates from left to right. Numerous theoretical (Longuet-Higgins

Figure 1.1: Laboratory generated spilling breaker. Photograph provided by Dr. B. K. Haus and Dr. M. A. Donelan, Rosenstiel School of Marine and Atmospheric Science, University of Miami.

and Cleaver, 1994; Longuet-Higgins *et al.*, 1994; Longuet-Higgins, 1994; Longuet-Higgins and Dommermuth, 1997; Longuet-Higgins, 1998b) and experimental (Duncan *et al.*, 1994; Lin and Rockwell, 1995; Duncan *et al.*, 1999; Qiao and Duncan, 2001) investigations have contributed to a reasonable understanding of the incipient stages of breaking in a spilling breaker. It is believed that breaking starts from a nonlinear shear instability of the crest flow. The origin and details of the instabilities are strongly dependent on the wave-length, since short wave-length breakers are dominated by surface tension effects. It seems generally true that for longer wave-lengths, the breaking process is started by the development of a coherent jet at the crest when the horizontal component of the fluid velocity reaches the linear group velocity of the dominant wave component. For shorter wave-lengths, the jet is replaced by a rounded bulge, and the fluid velocity remains less than the wave phase speed. Both experimental and theoretical results show capillary waves appearing at the leading edge (toe) of the breaker because of the large curvature. The breaking proceeds with the bulge moving down the front face of the wave. As the curvature

3

at the toe increases, a small-scale separated mixing layer develops, and the capillary pattern is replaced by large-scale distortions of the free surface (Liu and Duncan, 2003).

With the progression of breaking and the development of a fully-formed breaker, the two-phase and fully turbulent region engulfs most of the forward face of the wave. In this region, the turbulent velocities are equal to or exceed the mean velocities, and the effect of turbulence on the mean flow becomes important (Peregrine and Svendsen, 1978; Peregrine, 1983). The motion in a fully-formed breaker is of continuous shearing with a direct and continuous transformation of wave motion into turbulence (Battjes, 1988). The role played by the curvature of the surface and flow streamlines is essential in the evolution of this shearing process. Further, the energy transfer processes occur on varying time scales, and intense coherent events have often been observed under spilling breakers which are ascribed to three-dimensional obliquely descending eddies (ODE) and organized turbulence (Nadaoka, 1986; Ting and Kirby, 1996; Cox and Kobayashi, 2000). In the following, only two-dimensional spilling breakers are discussed. Readers interested in three-dimensional breakers are referred to experimental studies described in She *et al.* (1994), Nepf *et al.* (1998), and Roth *et al.* (1999).

In a recent exhaustive review of spilling breakers, Duncan (2001) notes the visual similarity between the depth-limited unsteady spilling breakers studied by Mason (1952) and laboratory-generated, deep-water spilling breakers (Rapp and Melville, 1990). Spilling breaking waves in the saturated inner surf-zone also have distinct similarities with unsteady bores, and are typically modeled as such (Hibberd and Peregrine, 1976; Svendsen and Madsen, 1984). The distinction between the two is made primarily in the fraction of the wave front covered by turbulence. Depending on whether the turbulent region occupies part of the crest or the whole front face,

the breaker is termed a spilling breaker or a bore (Peregrine, 1983). In the post-breaking regime, the void fraction and turbulence in the aerated region for a spilling breaker can even exceed that for a plunging breaker (Cox and Shin, 2003). In a frame of reference moving with the bore, the unsteady bore reduces to a stationary turbulent hydraulic jump, the classical case of a two-dimensional steady spilling breaker. It is important to note that the analogy between surf-zone spilling breakers and hydraulic jumps can be made only for low Froude number, or weak jumps, and similar upstream to downstream depth ratios (Peregrine and Svendsen, 1978; Battjes and Sakai, 1981). Further, as noted by Duncan (2001), weak hydraulic jumps have a very similar appearance to hydrofoil-generated spilling breakers. Two-dimensional steady breakers, such as those produced by submerged hydrofoils are all classified as spilling breakers (Duncan, 1981; Battjes and Sakai, 1981; Mori, 1986). Strictly speaking, they are quasi-steady, since low-frequency oscillations of the spilling zone have been observed by many investigators (Duncan, 1981; Banner, 1988). Spilling breaking waves in the surf-zone are also referred to as quasi-steady in a frame of reference moving with the wave, since the evolution of the breaker occurs at a time scale larger than that for a particle to cross the layer. However, they are unsteady when compared to the motion of the underlying wave, which has a longer time scale of evolution (Peregrine, 1992).

For quasi-steady, fully-formed spilling breakers, which is the focus of this dissertation, there are few theoretical and experimental studies which provide a detailed description of the turbulence. In the following, only a brief introduction of the key elements of these studies is provided. A detailed discussion is deferred until subsequent chapters when they are referred to in context. One of the major limiting factors towards a direct theoretical or experimental investigation of the turbulent dynamics of spilling breakers has been the associated surface intermittency and air-entrainment. Straightforward Reynolds-averaging techniques fail due

to the two-phase nature of the flow near the interface, and conditional sampling techniques become necessary for an accurate description of the flow (Brocchini and Peregrine, 2001a,b) (hereafter referred to as BP1 and BP2, respectively). Apart from the present study, the author is not aware of their incorporation, even in a mean sense, in any theoretical description of the flow in a breaker. Instead, "bulk" models have been developed, which, while accounting for some of the effects of the turbulence, have made simplified assumptions such as static pressure or neglecting unsteady contributions to the mean flow (Madsen and Svendsen, 1983)(hereafter, MS83). Most of these models have also been physical, guided by the overall breaker characteristics (Tulin and Cointe, 1988; Cointe and Tulin, 1994), and theoretical developments in explicitly including the role of turbulence have been entirely disregarded. Instead, the focus has been on a global representation of the forces on a breaker, with the primary aim of prediction the oscillations of the spilling zone. Further, the role of curvature in modifying the turbulence and, consequently, the mean structure of the breaker shear layer has not been paid any attention. The model for a turbulent bore developed by Svendsen and Madsen (1984), which is essentially an extension of MS83 for unsteady motion, provides a simple framework for the present theoretical approach. A comparison of the physical mechanisms and mathematical details are discussed in Chapter 4.

The theoretical models described above have been motivated and, at times, heavily influenced by experimental observations. Some of the earliest experimental descriptions of spilling breakers were limited to qualitative investigations. Through flow visualization techniques, Peregrine and Svendsen (1978) analyzed the similarity between hydraulic jumps, bores and spilling breakers, and suggested that in all three flow configurations, the turbulence spreads downstream of the toe in the form a mixing layer. The qualitative results of Jansen (1986) indicated that in spilling breakers, high concentrations of entrained air were confined above the still water

level. Most experimental studies of the quantitative turbulence structure under fully-formed spilling breakers have been done with point measurement techniques (Battjes and Sakai, 1981; Nadaoka, 1986; Longo, 2003; Stansby and Feng, 2005). Battjes and Sakai (1981) suggested that the turbulence structure far downstream of the breaker resembled a self-preserving wake. Even though they provide valuable information about the turbulence statistics at various spatial locations, these methods cannot provide a detailed spatial picture of the flow except in an ensemble-averaged sense. Even then, the procedure of manually shifting the probes to the desired location requires pain-staking and tedious manual labor. Instantaneous pictures of the flow cannot be realized. This limitation was overcome with the advent of particle image velocimetry (PIV)(Adrian, 1991; Willert and Gharib, 1991), which has since then developed into an established non-intrusive measurement technique to obtain instantaneous spatial maps of the velocity field. For stationary flows, turbulent fluctuations are obtained by subtracting an ensemble of realizations from each instantaneous realization. Lin and Rockwell (1994) were perhaps the first to provide a detailed instantaneous quantitative structure of a steady spilling breaker. They found that the rapid distortion of the flow along the free surface led to flow separation, in turn giving rise to a mixing layer with concentrated patches of vorticity. Similar conclusions were reached by Lin and Rockwell (1995)(hereafter, LR95). However, the substantial fluctuations of the free surface precluded a meaningful average, and the turbulence fluctuations of either the surface or the velocities could not be estimated. In the study by Chang and Liu (1999), significant aeration at the crest prevented any measurements in that region. They found that under the trough level, turbulence production and dissipation were of the same order of magnitude. With a normal light sheet and digital correlation video-imaging techniques, Govender *et al.* (2002a) and Govender *et al.* (2002b) obtained measurements well into the aerated region of spilling breakers. The highest turbulence intensities were

found in the front part of the wave crest, and because they were significantly higher than earlier measurements restricted to the trough level, it was suggested that existing descriptions of the surf-zone flow field were inadequate. Coherent turbulent structures were not analyzed.

In recent years, with steadily increasing computing resources, numerical modeling of unsteady breaking waves has progressed significantly (Chen *et al.*, 1997; Dimas and Fialkowski, 2000; Iafrati *et al.*, 2001; Song and Sirviente, 2004; Iafrati and Campana, 2005). Typically, mean flow characteristics, and at times, the magnitude and shapes of turbulence statistics are satisfactorily estimated. Qualitative results have also been obtained for large-scale coherent turbulent motions underlying the breaking wave (Christensen and Deigaard, 2001; Rogers and Dalrymple, 2005). However, an accurate resolution of the finer details of the turbulence structure, particularly in the post-breaking phase, still poses computational challenges and conceptual difficulties in a robust formulation for the model. Further, the modeling efforts have been primarily directed at plunging breakers. Spilling breaking waves have received far less attention, and Rhee and Stern (2002) is the only related work that the author is aware of. Quite a few numerical simulations have been performed for turbulent hydraulic jumps (Long *et al.*, 1991; Chippada *et al.*, 1994; Ma *et al.*, 2001; Zhao *et al.*, 2004b), but the agreement of turbulence statistics with measurements, especially near the interface, remains at best qualitative. In addition, the small-scale features of the turbulence are modeled rather than resolved.

Despite their obvious importance, there is still very little understanding of the turbulent dynamics of spilling breakers. This dissertation is aimed at investigating some of those aspects from a theoretical and experimental study of two-dimensional quasi-steady spilling breakers. As eloquently described by Yip (1995), there are two styles of scientific thinking which can be applied to any problem: *Analytical,*

8

following a logical train of thought and symbolic reasoning from premises to conclusions, and *visual*, an analogous representation of the problem so that symbolic and perceptual processes can aid deductive reasoning. For the present problem, whose complexity discourages a direct analytical approach, a certain amount of qualitative and visual imagination is needed to provide the necessary understanding of the physical phenomena. Once the picture is clear, a mathematical approach can take over and lead more efficiently to logical conclusions. These can then be verified by the experimental observations. In Chapter 2, laboratory experiments for an air-entraining weakly turbulent hydraulic jump are described. The jump is set up in Froude similitude with saturated surf-zone breakers. Data-analysis algorithms to estimate the instantaneous air-water interface and velocities are developed. In Chapter 3, the turbulent dynamics of the air-water interface and the mean flow structure are analyzed in detail, with particular attention to the breaker shear layer. Chapter 4 presents a theoretical model for the single-phase turbulent shear layer. Curvilinear coordinates are used to derive governing equations for the flow. Scaling assumptions based on the kinematics and geometry of the layer are then introduced to evaluate the contribution of various physical mechanisms. The equations are then analytically integrated across the layer. The contributions of the two-phase part of the flow are embedded in the boundary conditions applied at the top of the single-phase layer. With this procedure, boundary conditions are derived at the lower edge of this layer which forms the boundary with the irrotational flow below. With the objective of examining the dominant characteristics of the turbulent flow, Chapter 5 investigates the presence of coherent structures in the breaker shear layer through various analytical and statistical techniques. Conclusions from the theoretical results and experimental observations are presented in Chapter 6, followed by a discussion of ongoing and future work at the end of the dissertation.

Chapter 2

EXPERIMENTAL SET-UP AND DATA ANALYSIS ALGORITHMS

An investigator starts research in a new field with faith, a foggy idea, and a few wild experiments. Eventually, the interplay of negative and positive results guides the work. By the time the research is completed, he or she knows how it should have been started and conducted.

Donald Cram

2.1 Introduction

Hydraulic jumps are very common in nature and can be as easily observed in the kitchen sink as in the spillways of dams. They have long been of interest to hydraulic engineers as efficient energy dissipators in the design of control structures. From a different perspective, a hydraulic jump is believed to provide a simplified description of the complicated processes accompanying wave breaking on gently sloping beaches. Spilling breakers in the inner surf-zone are essentially quasi-steady bores. Hornung *et al.* (1995) applied PIV to study the vorticity and angular momentum balance in the unsteady flow induced by a traveling hydraulic jump. Even though the governing equations of unsteady bore motion can be reduced to those of a stationary hydraulic jump, there are physical differences between the two that arise from the boundary conditions, particularly in the bottom boundary layer (Yeh and Mok, 1990). Dabiri and Gharib (1997) (hereafter referred to as DG97) have

10
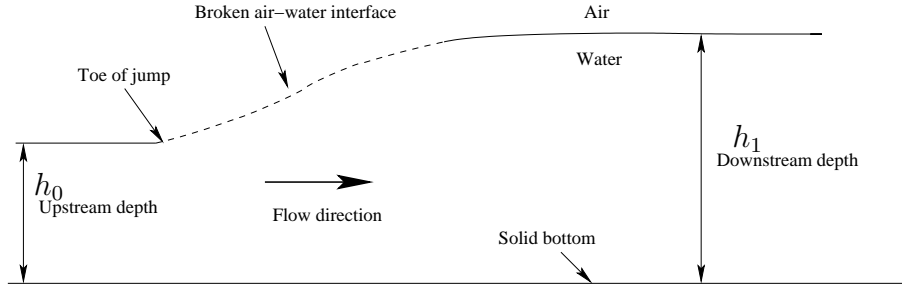
Figure 2.1: Schematic sketch of hydraulic jump.

suggested, based on their PIV experiments, that the turbulent structure of a stationary hydraulic jump can be used to model the local flow of a quasi-steady spilling breaker in the decelerating shear layer below the free surface. They had focussed primarily on the vorticity generation mechanisms.

The similarity of surf-zone spilling breakers with hydraulic jumps is particularly true at low Froude numbers, where the downstream-to-upstream depth ratio ($\xi \equiv \frac{h_1}{h_0}$) is similar to that of typical surf-zone breakers (Battjes and Sakai, 1981). This has important consequences for increasing our knowledge of the underlying flow structure because of the relative ease with which hydraulic jumps can be set up in the laboratory. In the saturated breaking zone for irregular waves, whether narrow or broad banded, both laboratory (Ting, 2002) and field measurements (Thornton and Guza, 1983) have shown that the wave height-to-water depth ratio, known as the breaker index, varies from 0.4 to about 0.7. For a bore, or equivalently, a hydraulic jump, this gives ξ varying from 1.2 to 1.35. Based on Belanger's equation (see equation 3.2), the corresponding upstream Froude number (Fr) varies from 1.15 to 1.26. For such low Froude number jumps, to draw a closer analogy with surf-zone breakers, the energy dissipation in the transition region from supercritical to subcritical flow has to come primarily from sheared turbulence accompanied by free surface air-entrainment. The resulting two-phase flow in this breaker region is

11

highly intermittent in space and time and encompasses a wide range of temporal and spatial scales. This makes it a challenging flow to be investigated experimentally.

In this chapter, the PIV experimental set-up and the data analysis methods to calculate the instantaneous interfaces and velocities are described. Section 2.2 describes the flume geometry, the flow parameters and the PIV set-up. The calibration procedure is discussed in detail. Due to the sensitivity of the flow to external perturbations, intrusive measurement techniques were not considered feasible to measure either the air-water interface or the instantaneous flow velocities. Since detailed streamwise and cross-flow variations of the flow were to be investigated, instantaneous whole field spatial maps, as against point measurements, were desired for both quantities. Therefore, an algorithm based on image processing methods was developed to estimate the air-water interface directly from the raw PIV images. This is described in section 2.3. The parameters in the algorithm are tuned by comparing the interface estimate for a single image with visually interpreted results. The rest of the ensemble is processed in an automated manner without further human intervention. Finally, section 2.4 describes the phase-correlation based algorithm to calculate the instantaneous velocities from the PIV image pairs. The algorithm was developed specifically for these experiments. The accuracy and robustness of the algorithm is evaluated with standardized test images and typical images from the present experimental datasets. The bias errors due to pixel-locking are analyzed in detail, and the relative accuracy of two sub-pixel estimators are compared.

2.2   Experimental set-up

The experiments were performed in a recirculating Armfield S6 tilting flume that is 4.8 m long and 30 cm wide, with glass side walls that are 9 mm thick, and a solid opaque bottom. Figure 2.2 shows a schematic diagram of the flume and the PIV system configuration. Water was pumped into the upstream end of the channel through a number of screens and flow straightening devices, after which it flowed
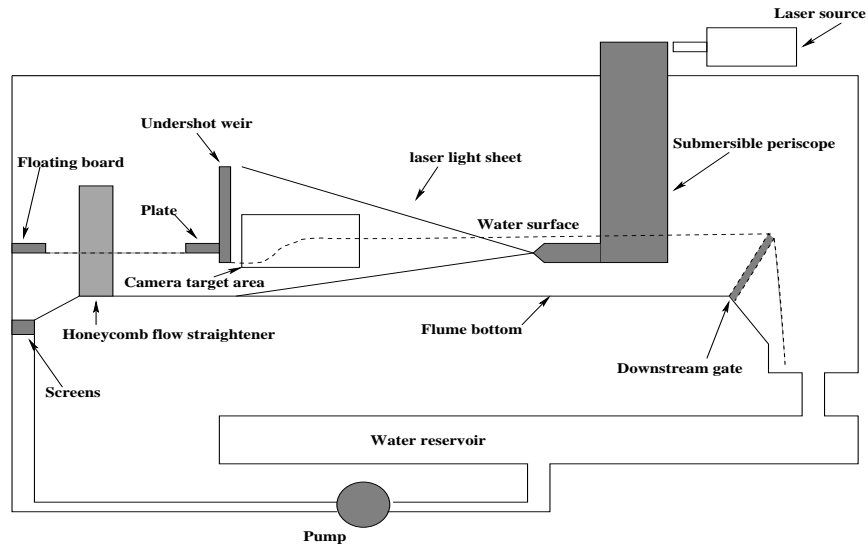
Figure 2.2: Experimental set-up.

past an undershot weir. The undershot weir was constructed from a plexi-glass plate with a thickness of 1 cm, and was wedged in between the flume walls. A metal support fixes the plate to the side rails of the flume. The distance from the bottom of the flume to the bottom edge of the weir can be controlled by a screw attached to the metal support. The lower end of the plate was machined in order to yield a sharp uniform edge on the upstream side to minimize lateral variations of the inflow. The gaps between the weir and the side walls of the flume were made water tight by inserting flexible plastic tubes through grooves cut into the sides of the plate. The flow rate and the height of the weir were used to control the upstream flow velocity and water depth, thereby determining the upstream Froude number. After passing the weir, the supercritical flow transitions to a subcritical flow by dissipating energy through the formation of a hydraulic jump (Henderson, 1970). Further downstream, the water flows over the downstream gate (which was lowered or raised to fix the location of the jump) and into the reservoir. A board floats on the upstream water surface to damp surface fluctuations, and the honeycomb

section prevented large turbulent structures from entering the channel. Just before the weir, the free surface was capped by a foam board to damp out the waves formed on the upstream side (Bakunin, 1995). Even then, concentrated vortical motions sucked down air bubbles into the water passing under the gate. These structures are inherent to such a geometry (see Figure 1.10 in Kobus, 1991) and lead to pre-jump entrainment of air. The toe of the jump, defined here as the point of largest surface curvature, and distinct from the breaking location, was approximately 20 cm downstream of the weir. The flume was kept horizontal throughout the experiments.

The PIV set-up consisted of a 120 mj/pulse Nd-Yag New Wave solo laser source with a pulse duration of 3 to 5 nanoseconds. This was mounted onto a custom-built submersible waterproof periscope which was lowered into the water. The optics were arranged in such a way that the laser beam emerged as a planar light sheet parallel to the flume wall. The laser sheet was aligned with the center plane of the flume, away from the side wall boundary layers. Although the submersible was suitably streamlined, it did change the location of the jump, and had to be adjusted so as to keep the jump stationary within the camera target area. It was kept far enough downstream of the jump to minimize flow interference, and did not cause any visible changes to the flow. The flume bottom and the undershot weir were painted with water resistant black marine paint to minimize reflections from the laser sheet. The water was seeded with 14 μm diameter silver coated hollow glass spheres with a specific gravity of 1.8, obtained from Potters Industries. For particles with densities larger than the density of the surrounding fluid, and diameters small compared to the length scales of the flow, the equation of motion can be described using a simplified form of the equation in Maxey (1987),

$$\frac{dv_p}{dt} = -\frac{v_p - u_f}{T_p},$$ (2.1)

where v_p is the velocity of the particle, u_f is the velocity of the fluid at the particle position, and T_p is the response time of the particle. The particle Reynolds number

14

Table 2.1: Parameters for experimental datasets

Dataset	Target area x(cm) $\times$ y(cm)	CR (cm/pix)	F (cm)	Δ t (μsec)	D (cm)
I	23.1 $\times$ 23.3	0.023	2.5	300	70.20
II	11.09 $\times$ 11.18	0.011	6	300	83.45

in this case is much smaller than unity, and a linear Stokes Drag law can, therefore, be used (Wang *et al.*, 1998). This gives

$$T_p = \frac{2\rho_a a^2}{9\rho_f \nu},$$ (2.2)

where ρ_a and ρ_f are, respectively, the particle and fluid densities, a is the particle radius, and ν the kinematic viscosity. The response time T_p of the particle is calculated to be $T_p = 1.96 \times 10^{-5}$s. Flow time scales comparable to T_p or larger should be faithfully represented by the particles. A Kodak Megaplus 1.0 camera, with a 1016 (vertical) $\times$ 1008 (horizontal) pixel charged coupled device (CCD) array, with its image plane parallel to the flume wall, was used to visualize the flow. The active area was 9.2 mm (vertical) by 9.1 mm (horizontal). The fill factor was 55%. A 532 nm filter was put on the lens to reduce noise due to any ambient light. A Dantec acquisition system was used to acquire the 8-bit gray scale images and store them onto a hard drive. The laser pulses were synchronized with the 30 Hz camera frame rate, which ultimately led to a 15 Hz sampling rate for the instantaneous velocity fields. The time interval between two pulses in each image pair was 300 μ seconds. Each experimental run consisted of an ensemble of 1020 image pairs, equivalent to 1020 instantaneous velocity maps.

There were two conflicting requirements faced when fixing the camera target area. With a given CCD array size, its resolution, and lens set-up, increasing the distance between the object and image plane leads to a larger target area with a resulting decrease in resolution, and vice-versa. Since the aim was to capture the details of the flow not just in the breaker shear layer, but also the upstream (of

15

the foot) and downstream (the wake) regions, several lenses were utilitized with varying focal lengths and the distance between the object and the image plane was adjusted simultanesously. The parameters for the two datasets I and II, which will be presented in this dissertation, are shown in Table 2.1. x and y are the horizontal and vertical coordinates. F is the focal length, Δt is the time interval between two images in each pair, CR is the calibration ratio, and D is the distance from the CCD array to the laser sheet. For each set-up, the camera had to be calibrated with a calibration grid which should ideally have been placed in the plane of the laser sheet. However, it was observed that such an intrusion changed, often irreversibly, the flow characteristics, and would have precluded a meaningful comparison of the different datasets. Therefore, a calibration grid was placed flush with the front side wall of the flume. A section of the *Canny* (a commonly used edge-detection algorithm developed by Canny, 1986) edges detected for the calibration grid from dataset I is shown in Figure 2.3. Each square has a physical edge length of 2.54 cm. The cm/pixel ratio was calculated from an average of 12 squares and was equal to 0.0188 cm/pixel in both vertical and horizontal directions (2.54 cm corresponded to 135.64 pixels). The scale factor due to the refraction of light through the glass and the water was calculated in the following way. In Figure 2.4, the dashed line denotes the light ray and the dash-dot lines are perpendicular to the flume wall and the laser sheet. The refractive indices for toughened glass and water are n_g=1.52 and n_w=1.34 respectively. **PQ** is the image of a single square-edge of the calibration grid on the CCD array, and, in physical distance units, is equal to $y_0 = 135.64$ pixels $\times$ 9 μ m/pixel = 0.1221cm. **RS**=y_1=2.54 cm is the actual physical measure of the square edge on the calibration grid. X_f=2.5 cm is the focal length, X_g=0.9 cm is the thickness of the glass wall and X_w=14.8 cm is the distance of the laser light sheet from the inner side wall. X_a is, as yet, unknown. From simple trigonometric

16
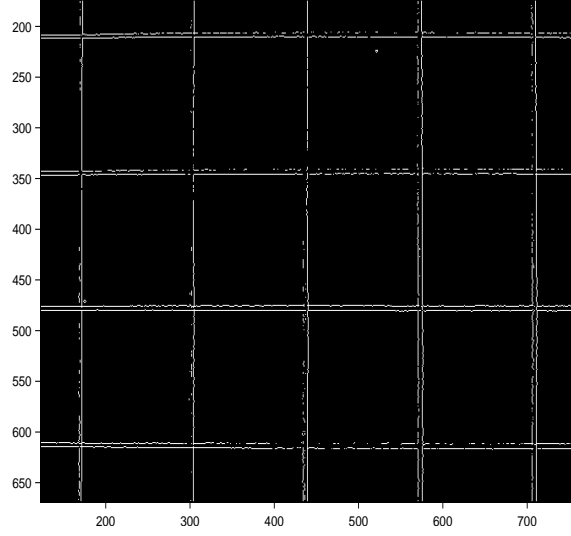
Figure 2.3: *Canny* detected edges for the calibration grid from dataset I.

arguments for similar triangles,

$$X_a = X_f \left(\frac{y_1}{y_0} - 1 \right), \tag{2.3}$$

$X_a =$ 49.51 cm.

$$\theta = \tan^{-1} \left(\frac{y_0}{X_f} \right) = 0.049 \text{ rad} \tag{2.4}$$

From Snell's law,

$$\phi = \sin^{-1} \left[\frac{\sin(\theta)}{n_g} \right], \tag{2.5}$$

which gives $\phi =$ 0.032 rad. So, $\mathbf{JK} = X_g \tan(\phi) = 0.3$ mm. Applying Snell's law again to the glass-water interface, $\alpha = 0.0364$ rad, which gives $\mathbf{LN} = X_w \tan(\alpha) = 0.54$ cm. $\mathbf{LW}$ is the actual physical projection of the calibration grid on the laser light sheet and is thus given by $\mathbf{LW} = \mathbf{LN} + \mathbf{JK} + y_1 = 3.11$ cm. Therefore, the scale factor which accounts for refraction through the glass and the water is $S = \frac{\mathbf{LW}}{y_1} = 1.2244$. The final calibration ratio is given by $S \times 0.0188 = 0.023$ cm/pixel. In a similar manner, for dataset II, the calibration ratio is found to be 0.011 cm/pixel, or in other words, yielding approximately twice the resolution of dataset I.

17
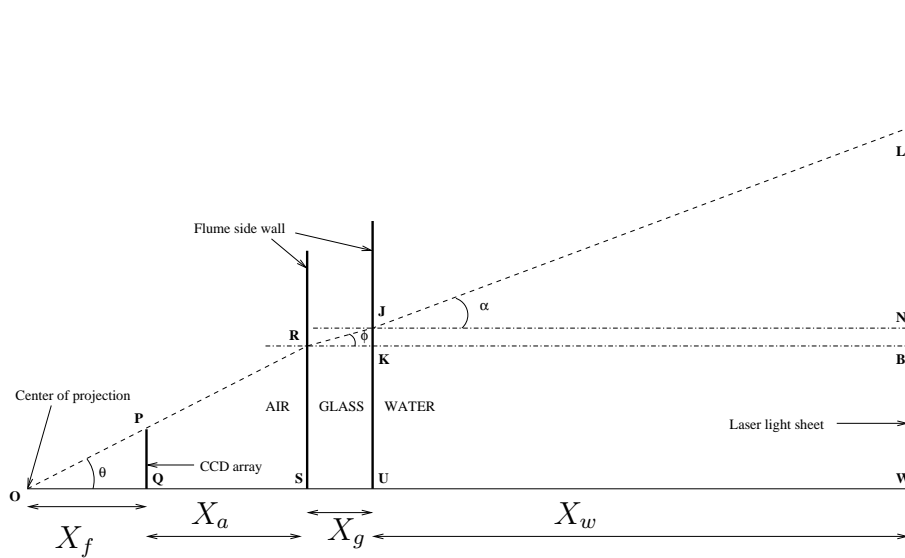
Figure 2.4: Geometry for calculating the refraction scale factor.

2.3 Estimating the instantaneous air-water interface

Before describing the algorithm to estimate the air-water interface, it is instructive to underline its importance in the context of PIV experiments with interfacial flows. Frequently, PIV studies focus on flows where the air-water interface is free (Qiao and Duncan, 2001, dealing with gravity wave breaking) or forced (Donelan *et al.*, 2004, investigating wind shear over gravity waves). It is often desirable to obtain detailed instantaneous flow velocities in either or both phases near the interface. This necessitates an accurate (to, at least, the measurement resolution of the velocities) estimation of the interface. At times, the spatio-temporal characteristics of the interface itself are of interest. Typically, the scalar interface is concurrently visualized by a technique called laser induced fluorescence (LIF), in which fluorescent dye is added to one phase and excited to a particular wavelength by the laser. LIF, in addition to its use as a technique to visualize the flow, is also used to measure the scalar concentrations (Dewey, 1976). In the context of determining the

scalar interface, the LIF images are transformed into binary images by a threshold-detection method and the sharp gradient in the binary image yields the interface (Westerweel *et al.*, 2002). However, there are various associated complications with evaluating scalar interfaces of turbulent flows from LIF images. For example, the treatment of false interfaces, resulting from moderate to high intensity turbulence fluctuations, needs specific thresholding methods applied to the squared gradient and the Laplacian of pixel intensities (Prasad and Sreenivasan, 1989).

Therefore, a simultaneous PIV and LIF experiment requires two separate imaging systems: one camera, with a suitable filter, which records only the particular wavelength of light scattered by the seeding particles to measure the flow velocities, and the other, recording the light emitted by the dye used to vizualize the interface. Recently, in addition to obtaining flow velocities, there have been attempts to estimate the interfaces in fluid-fluid flows directly from the PIV images. Due to the voluminous amount of images generated in a typical PIV experiment, the manual calculation of the interface remains a daunting and, owing to the subjectivity of human perception, an ambiguous task. Hassan *et al.* (1996) identified the interface by tracking illuminated floating particles which, due to their own degrees of freedom, cause frequent interruptions in the calculated surface and might even interfere with the flow. Peirson (1997) used a multiple pulsed single frame PIV technique to study the viscous sub-layer at a wavy air-water interface. Two separate cameras were used to simultaneously measure the wave phase and the particle velocities. This method cannot be used to track the evolution of a time-dependent surface. The author also points out that reliable measurements were not possible in regions of small surface undulations. Law *et al.* (1999) used a fluorescent dye and a gradient based edge detection routine along with optimally adjusted viewing mirrors to estimate the shear-free surface for a confined submerged jet in a tank. The

calculated surface compared reasonably well with single point wave gage measurements. Intensity or luminance based edge detection methods fail when "spurious particle reflections" (described later) are present in the PIV image. This problem is exacerbated in the presence of surface irregularities and cross-plane variations. To overcome similar difficulties, Lin and Perlin (1998) developed a customized water channel and optics configuration set-up based on the Brewster angle for the air-water interface. They point out that their set-up could lead to image distortion which requires further corrections. The method is labor intensive as it involves extensive trial and error arrangements. Some researchers have also used *a posteriori* methods to determine the interface after the velocities have been calculated. Tsuei and Savaş (2000) have proposed a first order accurate method to calculate interfaces in fluid-fluid flows. Their method utilizes the velocity information embedded in a pair of PIV images to extend the image data fields across the interface. This is done by locally translating and reflecting across the interface and reversing the order of images. When dealing with moving or compliant interfaces, the velocities at material points on the interfaces have to be supplied as an input to the algorithm. Dabiri and Gharib (1997) used a no-shear boundary condition on the calculated velocity to determine the free surface in their experiments with spilling breaking waves. It is obvious that such methods imposing kinematic or dynamic constraints on the interface cannot be applied universally.

There is a clear need for a robust, objective, and automated method which would be able to calculate the interface solely based on the information available in a typical PIV image. It is understood, as will become clear further, that the level of accuracy achievable by the proposed method will not be comparable to that offered by LIF. The current methodology is therefore not implied as a replacement for LIF in determining the scalar interface. Instead, given a typical ensemble of PIV images, the aim is to calculate the instantaneous interface efficiently and with a reasonable
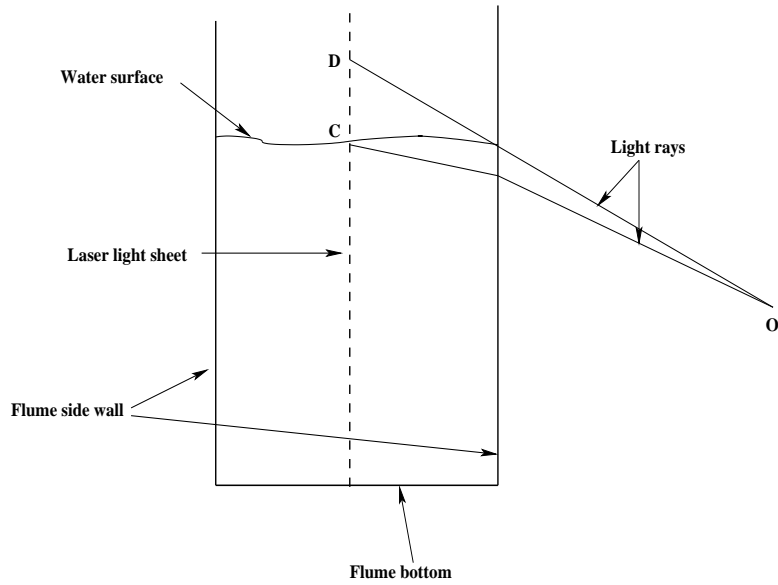
Figure 2.5: Schematic side-view of the flume showing the real and spurious air-water interfaces. See text for description

degree of accuracy. A consequential benefit is the exclusion of possible "spurious particle reflections" arising from a standard optical set-up (see Figure 2.5), which contribute a finite but false correlation in the velocity estimation process. Further, this would obviate the extensive preliminary adjustments required for the imaging equipment, as also the need to impose physical constraints on the flow kinematics when estimating the interface.

The instantaneous air-water interface in the present case is inherently unsteady, with multiple time scales of fluctuations. It is also free, in the sense that the interface does not support any shear. Hereafter, the interface is thus referred to as the "free surface" or simply as the "surface". It was essential to calculate the air-water interface prior to calculating the velocities, since there were "spurious particle reflections" near the interface arising from the perspective viewing angle of the camera. This is shown schematically in a two-dimensional side-view of the flume

21
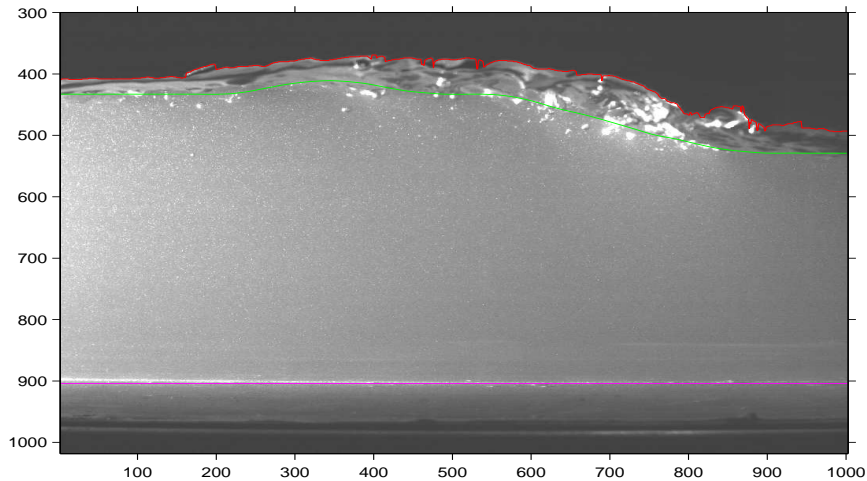
Figure 2.6: Typical raw PIV image showing spurious particle images and the interface estimates. Magenta line : flume bottom, red line : boundary between surface reflection region and air, and green line : calculated actual free surface

in Figure 2.5. **O** is the center of projection of the camera. The actual interface is defined as the intersection of the laser light sheet with the water surface, and is given by the point **C**. **CD** is the spuriously imaged water surface. In addition to the water velocities near the surface, the instantaneous surface itself was of interest for analyzing the intermittency of the turbulent surface fluctuations, and tracking the toe of the jump in time. The detailed corrugations and break-up of the surface were not of primary interest, and in the breaker region, the surface transition from supercritical to subcritical flow is assumed to be smooth and unbroken.

A typical cropped raw image is shown in Figure 2.6. The flow is from right to left. The specularity seen in the raw image near the toe of the jump is from air-bubble entrainment due to turbulent shear and breaking. The physical dimensions of the cropped raw image shown in Figure 2.6 are approximately 23 cm (horizontal) by 16.4 cm (vertical). Due to the rather large size of the target area, the laser light sheet attenuates from left to right, and can be clearly seen visually. A quantitative analysis

22

of the effect of this attenuation on the image properties of interest is discussed later. Four distinct regions can be seen in the image. The intersection of the laser light sheet with the bottom divides the lower region in the image into the fluid region and the solid flume bottom. This boundary is easily detected by standard edge detection techniques such as *Canny* or *Sobel* edge methods, and the result is shown as the magenta line. The black region at the top of the image is air and forms a sharp boundary from the rest of the image. This boundary is the intersection of the water surface with the glass flume wall. This interface is also calculated by a *Canny* edge algorithm, and is shown in the figure as the red line. The "diffuse" region between this boundary and the real surface is the image of the water surface between the laser light sheet and the flume wall. This is the region which gives a finite non-zero correlation when calculating the PIV velocities near the interface, and leads, ultimately, to an artificial shear layer above the real surface. However, the illuminated seeding particles in the fluid region have a distinctive footprint. In the following, the structure of the particle footprint is used to calculate the actual air-water interface, which is the upper limit of the seeding particles dispersed in the fluid phase. Computer vision texture segmentation methods are particularly suited to this task of quantifying and classifying such image information.

Texture classification and segmentation methods such as those based on gray level co-occurrence matrices, abbreviated as GLCM (Haralick *et al.*, 1973), cross-diagonal texture matrix methods (Al-Janobi, 2001), texture spectrum (He and Wang, 1991), Gabor filters (Grigorescu *et al.*, 2002) and wavelets (Chang and Kuo, 1993), to name a few, are powerful and continually advancing, in robustness and accuracy, tools which can be adapted to estimate deformable interfaces undergoing non-rigid motion (Kambhamettu *et al.*, 1994). In conjunction, parametric and

geometric active contours, commonly known as "snakes", are used extensively to locate object boundaries through edge-detection techniques in segmentation and motion tracking (Leymarie and Levine, 1993; Xu and Prince, 1998; Akgul and Kambhamettu, 2003). In the following, an algorithm based on GLCM and "snakes" is developed to calculate the complex turbulent air-water interface directly from the PIV images.

2.3.1 Image segmentation

GLCM (also known as Gray Tone Spatial Dependence matrices) are proven image processing tools to classify and separate the information content of an image (Tuceryan and Jain, 1998). Information measures of image properties such as correlation, variance, contrast, and entropy are used to calculate the inter-pixel dependence of tone and texture (Haralick *et al.*, 1973). The GLCM, a subset of second order structural methods, makes use of the gray level probability density function, which is computed as the conditional joint probability of pairs of pixel gray levels in a local area of the image. A selection of the appropriate quantization level is therefore essential to the level of precision of the texture classifier. However, the computational burden increases with the level of quantization. Marceau *et al.* (1990) have shown that, for purposes of image classification accuracy, there is very little difference between 4-bit and 5-bit quantization. In addition, the statistical validity of GLCM is greatly improved for a 4-bit quantization as compared to an 8-bit quantization since there are more non-zero occurrences for any given intensity value, leading to more robust probability measures. A detailed discussion of quantization effects on co-occurrence texture statistics can be found in Clausi (2002). In the following, the 4-bit values obtained from a down-quantization of the original 8-bit grayscale data are used.

The main assumption behind the GLCM is that the texture-content information is represented by the average inter-pixel gray level spatial relationships. The

co-occurrence of gray levels is represented mathematically by the probability, or relative frequencies of occurrence, conditional on the inter-pixel distance δ (pixels), and the relative orientation θ (degrees). In the following, a brief description of the GLCM is given. The relative frequency of occurrence is given by

$$C_{ij} = \frac{P_{ij}}{\sum_{i,j=1}^{N} P_{ij}}, \tag{2.6}$$

where P_{ij} is the frequency of occurrence of gray levels pair i and j, which are the horizontal and vertical pixel indices respectively. The summation is over the total number of distinct gray levels in the quantized image. N is therefore dependent upon the level of quantization ($m = 4$ in the present case), and $N = 2^m = 16$. Once C_{ij} has been calculated, the texture classes can be defined. Three examples are given here, which are the texture classes used in the present algorithm, and which, because of their physical significance, are easier to interpret intuitively than the others. For a definition of other classes, see Haralick *et al.* (1973). The *contrast* texture is given by

$$\sum_{i=1}^{N} \sum_{j=1}^{N} C_{ij}(i-j)^2. \tag{2.7}$$

The *horizontal mean* is defined in terms of the weighted GLCM itself as

$$\sum_{i,j=1}^{N} iC_{ij}. \tag{2.8}$$

The texture class called *difference entropy* is calculated as

$$-\sum_{k=1}^{N} p_{i-j}(k)\log\{p_{i-j}(k)\}, \tag{2.9}$$

where $p_{i-j}(k) = \sum_{i=1}^{N} \sum_{j=1}^{N} C_{ij}$, $|i - j| = k$, and $k = 1, 2, ..., N$. The primary reason that these are chosen over other classes is because of their low degree of correlation with each other. For classification purposes, it is often advisable to choose one of the contrast measures (*contrast, homogeneity,* and *dissimilarity*), one

of the orderliness measures (*entropy, difference entropy,* and *energy*) and one or more of the descriptive statistical measures (*standard deviation* and *mean*). Typically, either a linear discriminant analysis or maximum-likelihood estimation method is used to assess the contribution of several variables to the classification accuracy (Barber and LeDrew, 1991). Here, a simple trial-and-error method has been used to select the best possible candidates which gave the closest fit to the visually calculated interface for a single image used for tuning the set of parameters in the algorithm. For the images considered here, a different choice of other texture classes, one from each category, gave very similar results. For more information on feature selection and pattern classification, see Weszka *et al.* (1976) and Duda *et al.* (2000).

2.3.2   Pre-processing

Before the GLCM is calculated, the image is pre-processed to make it a more robust candidate for the texture segmentation algorithm. To save computation time, only a section of the raw image spanning the diffuse region is analyzed. The section (hereafter referred to as "image") size is 300 pixels (vertical) $\times$ 1008 pixels (horizontal), spanning the interface. The magnitude of the gradient of this image is calculated as

$$I_m = \sqrt{\left(\frac{\partial I}{\partial x}\right)^2 + \left(\frac{\partial I}{\partial y}\right)^2}, \tag{2.10}$$

where $I(x, y)$ is the grayscale intensity, x, and y are pixel coordinates in the horizontal and vertical directions. The seeding particles show up as cross-shaped features in the gradient image, and can be clearly seen in a zoomed-in region shown in Figure 2.7. The structure of these features shows that the particle image footprint is approximately equal to 1 pixel, which can be verified using the formula for particle image diameter (Prasad, 2000),

$$d_\tau = \sqrt{M^2 d_p^2 + [2.444(1 + M)f^\# \lambda]^2}. \tag{2.11}$$

26
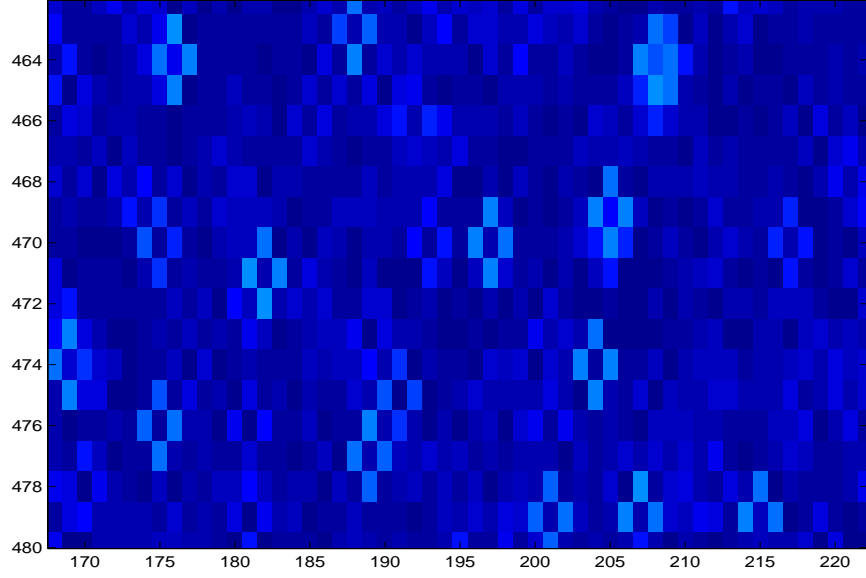
Figure 2.7: Seeding particle footprint in gradient image. Axes numbers are pixel coordinates.

d_τ is the particle image diameter, M is the magnification (=0.04), d_p is the particle diameter (=14 μm), $f^\#$ is the $f-$number of the lens (=6), and λ is the wavelength of the laser (=532 nm). Since the pixel spacing on the CCD is $d_{pix} = 9\mu$m, $\frac{d_\tau}{d_{pix}} = 0.9$.

Based on the particle footprint, a template for a particle is chosen in the form

$$\mathbf{T} = \begin{bmatrix} 0 & 1 & 0 \\ 1 & 0 & 1 \\ 0 & 1 & 0 \end{bmatrix}.$$

To enhance the contribution of the real seeding particles in the image, the template is cross-correlated with the gradient magnitude image and then multiplied with the raw image to yield a "weighted" image shown in Figure 2.8. The fluid region with the particles can be seen separated from the diffuse reflection region and the air above.
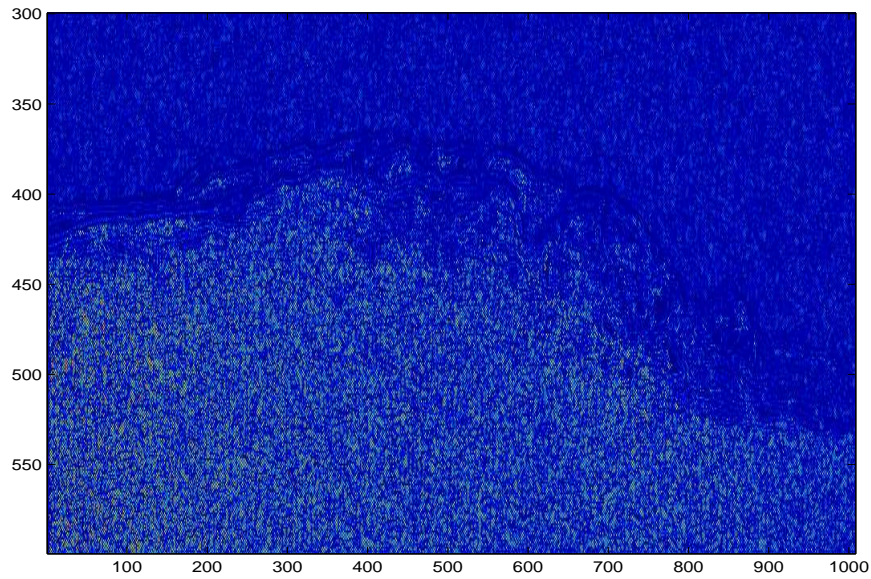
Figure 2.8: Weighted image. Axes numbers are pixel coordinates.

2.3.3 Gray level co-occurrence matrix

The next step is to choose a window size for calculating the GLCM, since the texture statistic is computed as a single measure of the total information content. The size of the window is a trade-off between the robustness of the estimate (directly proportional to the window size) and the resolution (inversely proportional to window size). A window of 24×24 pixels with no overlap was found to work reasonably well. The displacement between the reference and neighbor pixels was chosen as 3 pixels, i.e., $|\delta| = 3$. All four possible relative orientations were taken into account by western ($\theta = 0$), southern ($\theta = 90$), northwestern ($\theta = 135$), and southwestern ($\theta = -135$) offsets. The opposite orientations were accounted for when constructing the symmetric GLCM. The raw GLCM was first formed by summing the frequencies of co-occurrence of gray level values over all possible pixel pairs given by the range of δ and θ values in the window. The symmetric GLCM was calculated by adding the transpose of the raw GLCM to itself. Therefore, it was assumed that

28

the pixel pair gray scale values had no preferred orientation. This is intuitively justified, since the seeding particles are distributed randomly in the fluid phase. The symmetric GLCM was then normalized by its sum, thereby yielding the relative frequencies of occurrence. The normalized texture classes (horizontal mean, contrast and difference entropy) were then calculated, and are shown in Figure 2.9. There is, surprisingly, a remarkable qualitative similarity between them. Considering that these particular texture classes are not well-correlated by definition, the similarity is therefore an indication of the comparable degree of representation of the image content in each of the texture classes. The effect of the light sheet attenuation is evident in the decreasing magnitudes of all the texture classes from left to right and this is more clearly seen in Figure 2.10. The values at each horizontal location have been obtained after averaging vertically.

2.3.4 Singular value decomposition

It has been shown that the information contained within the GLCM is not fully represented by any single texture class (Conners and Harlow, 1980). With that in mind, the texture classes were combined into a single matrix by performing principal component analysis on the texture class covariance matrix (Turk and Pentland, 1991). Each texture class was thus collected together to form $\mathbf{A} = [T_1, T_2, \cdots, T_M]$, where T_i are the individual texture classes, and each row of $\mathbf{A}$ corresponds to a collocated position from each of the classes. The texture covariance matrix can be computed as $\mathbf{C} = \Phi\Phi^T$, where $\Phi = \mathbf{A} - \bar{\mathbf{A}}$, with $\bar{\mathbf{A}}$ being the average texture. A single matrix can be calculated by projecting the texture class data points along K $(K \leq M)$ orthonormal principal vectors obtained by eigenvalue decomposition of the texture covariance matrix. In the computations, it was observed that the first eigenvalue-eigenvector pair provided sufficient robustness to the subsequent stages of the process.
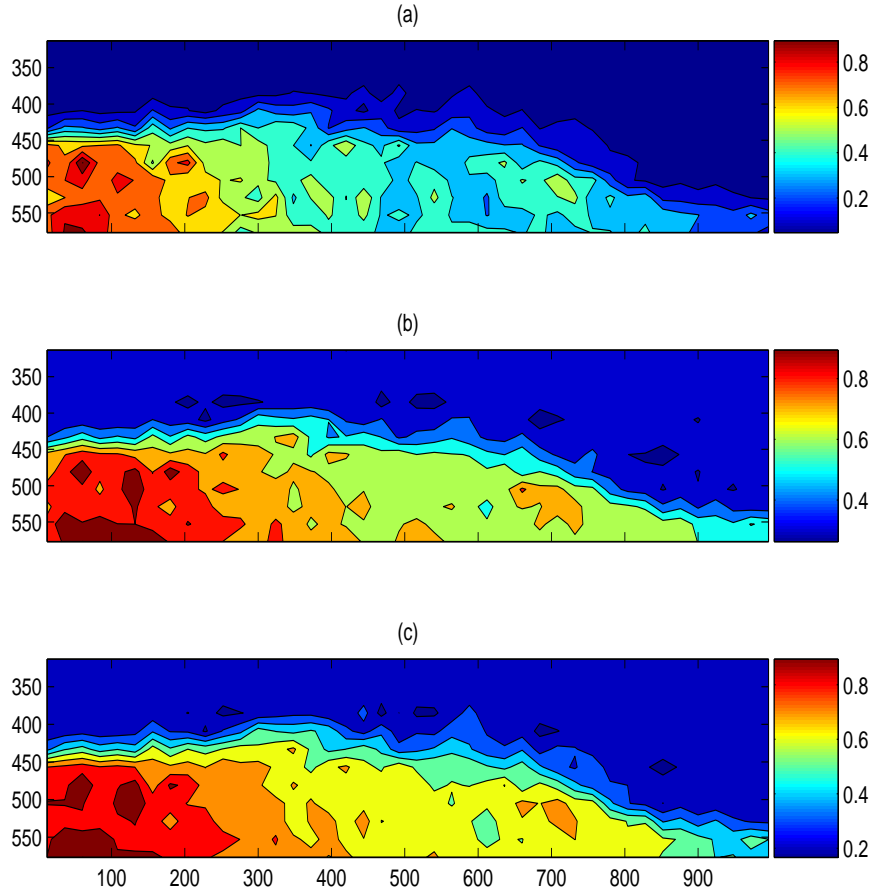
Figure 2.9: Normalized texture classes: (a) *Contrast*, (b) *Horizontal mean*, and (c) *Difference entropy.* Axes numbers are pixel coordinates.

The edge map of the singular value decomposition matrix was calculated using a *Canny* edge detection method. The edge map was then blurred using a Gaussian convolution. It may be less clear why there is any interest in blurring the edge map. However, it does perform a useful intermediate step, and is commonly used in edge-detection routines in image processing (Gonzales and Woods, 2002). A Gaussian Blur is a general purpose low-pass blur filter. This removes fine image detail and noise inherent to an edge detection method (such as *Canny*) leaving only larger scale changes. Therefore, Gaussian Blurs produce smoothing without side
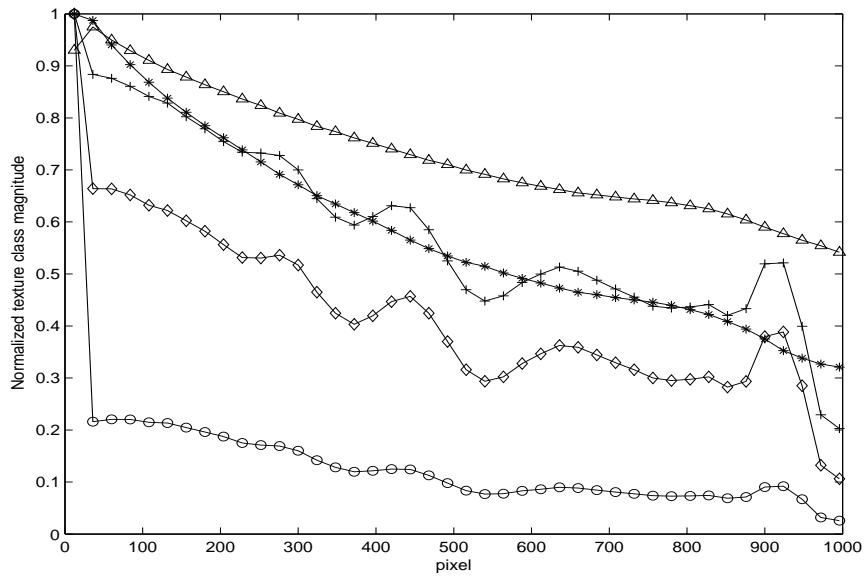
Figure 2.10: Normalized texture classes: *Correlation*(∗), *Difference entropy*(+), *Dissimilarity*(◇), *Contrast*(◦), and *Intensity*(△)

effects. Obviously, the level of detail retained depends on the size of the filter, which is given by the standard deviation. In the present, the Gaussian kernel selected was 3×3 pixels with a standard deviation of 1 pixel. The "Laplacian of the Gaussian" operator can also be used to do both operations (smoothing and edge detection) at once (Marr and Hildreth, 1980).

2.3.5   Active contours

The next step was to determine how to represent the set of first approximation discrete points, obtained from the gradient of the Gaussian blurred image, that have been assumed to lie on an edge, which in the present case is the turbulent interface. Kass *et al.* (1987) were the first to propose a model called active contours or "snakes", in which the final form of the contour is influenced by a feedback from a higher level process essentially minimizing the "energy". "Snakes" were previously used by Duncan *et al.* (1999) to calculate the crest profile evolution for gentle spilling

31

breakers. Hermite cubic polynomials were used to represent the "snakes". The experimental and camera set-up were, however, tuned to solely measure the scalar interface from the dye visualization, and the images analyzed are therefore closer to typical LIF images than PIV images. According to the classical definition, the "snake" is a deformable contour $\mathbf{x}(s) = [x(s), y(s)]$ parameterized by the arc-length $s \in [0, 1]$. The contour is controlled by balancing the internal energy terms (E_{int}) emanating from the shape of the contour, with the external energy (E_{ext}) extracted from the image and/or obtained from a higher level image understanding processes (such as the texture information provided by the GLCM). The energy functional to be minimized takes the form

$$E^* = \int_0^1 [\alpha |\mathbf{x}'(s)|^2 + \beta |\mathbf{x}''(s)| + \gamma E_{ext}] ds. \tag{2.12}$$

Primes denote differentiation with respect to s, and the vertical bars represent the absolute value. The first two terms form the internal energy, while the last term denotes the external energy. The internal energy is responsible for the smoothness of the contour, while the external energy attracts the contour towards the object boundary. The parameters α, β and γ control the importance of each term towards the net energy functional. There are many external energy functionals possible, with the image gradient $E_{ext} = -|\nabla I(\mathbf{x}(s))|$ being the most common choice. This is the functional used in the present algorithm.

The discrete approximation of the active contour renders the minimization of the energy functionals over N discrete samples of $\mathbf{x}(s)$, also known as snaxels ($\mathbf{x}_i = [x_i, y_i]$, $i = 1 \cdots N$). The discrete form of the energy functional is given by

$$E^* = \sum_{i=1}^{N} [\alpha E_{cont}(\mathbf{x}_i) + \beta E_{curv}(\mathbf{x}_i) + \gamma E_{ext}(\mathbf{x}_i)]. \tag{2.13}$$

The derivatives present in the internal energy terms can be replaced by the discrete counterparts as $E_{cont}(\mathbf{x}_i) = (d_{avg} - \|\mathbf{x}_i - \mathbf{x}_{i-1}\|)^2$, which is a first-order continuity constraint similar to the first-derivative term in Kass *et al.* (1987), and seeks to keep

32

points spaced equally along the curve. $E_{curv}(\mathbf{x}_i) = \|\mathbf{x}_{i+1} - 2\mathbf{x}_i + \mathbf{x}_{i-1}\|^2$ is analogous to a second derivative term which seeks to minimize the curvature. d_{avg} is defined as the average distance between the contour points, and is required so that the contour does not shrink towards itself. Note that each term has to be normalized by dividing by the largest value of that term within the neighborhood of the search. In the algorithm, the external energy that is used to control the active contour is based on the data obtained from the texture classes. Thus, the magnitude of the gradient of the texture classes between the seeding particle zone and the non-particle zone is minimized under the constraint that the contour so obtained satisfies first and second order continuity. The contour estimation is repeated with the estimate at one stage forming the initialization to the subsequent stages until the contour stabilizes over the texture classes. In the implementation, the "greedy" algorithm described by Williams and Shah (1992) is used instead of the classical formulation. Here, a local search is performed at the position of each discrete point, and the position that minimizes the energy functional is selected as the new updated position. The local search neighborhood is maintained at 15 vertical pixels (7 on either side) at each iteration. Finally, a cubic spline is used to interpolate the discrete snaxels, and to obtain a continuous contour giving the free surface estimate.

A single randomly selected image is used to tune the parameters discussed above by comparison with the visually-interpreted (hereafter, VI) surface (see 2.3.6) for that image. The rest of the images in the ensemble are batch processed without any further intervention. Nonetheless, to test the algorithm, several images were randomly selected, and on comparing the GLCM surface with the VI surfaces, good agreement was found between the two for the fixed set of parameters ($\alpha = 0.52$, $\beta = 0.7$, $\gamma = 0.12$).
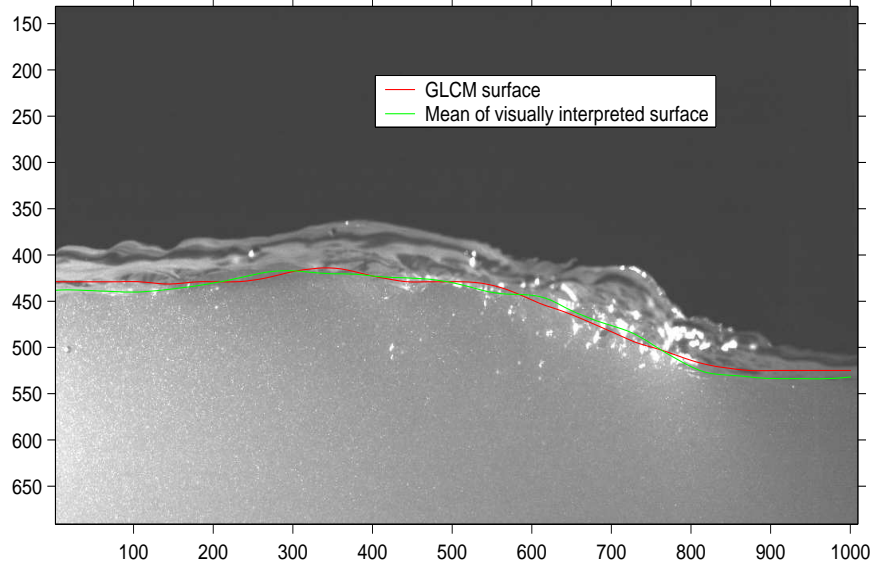
Figure 2.11: Comparison of GLCM and visually calculated interfaces for a typical image (*A*) in dataset I. Axes numbers are pixel coordinates.

2.3.6 Results

Since the flow is very susceptible to external perturbations, no intrusive probes were used to measure the instantaneous surface. Therefore, in-situ measurements were not available as ground truth. However, there are several ways to test the accuracy of the instantaneous as well as ensemble averaged calculated interfaces. In this section, the instantaneous results are assessed with respect to human perception. In Chapter 3, the accuracy of the estimated interface is further demonstrated by comparing the interface fluctuations with theoretical profiles of the intermittency factor. In the same chapter, an indirect check for the location of the interface is provided by integrating the computed velocities over the depth and comparing the volume flux at each vertical section.

The results from the algorithm were assessed first with respect to human perception. Ten randomly selected (from the ensemble) PIV images were distributed
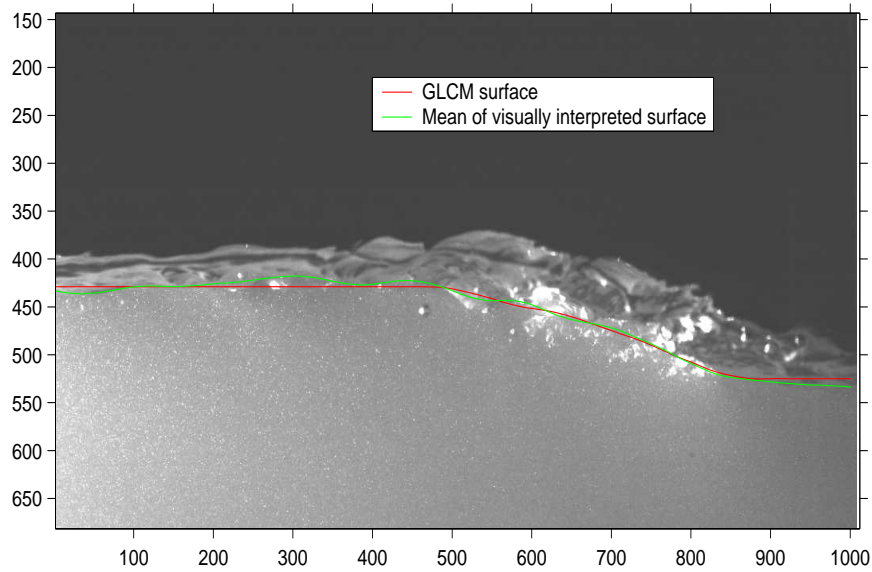
Figure 2.12: Comparison of GLCM and visually calculated interfaces for a typical image (B) in dataset I. Axes numbers are pixel coordinates.

to each of a group of ten participants. A short problem description was provided and the subjects were asked to click on the image where they perceived the position of the true interface. Since the inputs from the subjects could be sparse and not coincident with the GLCM calculated positions, a cubic spline was used to interpolate the VI surface at the GLCM locations. The mean position of the contour was then computed as the average of the contours obtained from the ten participants. Figure 2.11 and Figure 2.12 show the GLCM and VI surfaces for two randomly selected images (A and B) in the ensemble. The overall qualitative agreement is good, even in the breaker region, where the surface is broken up and there is two-phase flow resulting from ejection of water particles into the air and entrainment of air bubbles in the water. As noted earlier, an unbroken smooth contour is assumed through the breaker region. The quantitative disagreement between the GLCM and VI surfaces

35

is shown in Figure 2.13 by plotting the error

$$\epsilon(x) = h(x)_{GLCM} - h(x)_{VI}. \tag{2.14}$$

$h(x)$ is the local water depth. Negative values of ϵ therefore imply that the GLCM surface is below the VI surface and positive values indicate that it is above. A first qualitative, and reassuring, conclusion which can be drawn is that there is no consistent bias towards under- or over-prediction by the GLCM method. The mean, averaged in the horizontal direction, absolute errors for the two images are $\bar{\epsilon}_A = 5.77$ pixels (=1.3 mm) and $\bar{\epsilon}_B = 3.85$ pixels (=0.9 mm), which were within the measurement location resolution for the calculation of the PIV velocities (=8 pixels). The mean non-dimensionalized (by the horizontally averaged GLCM depth) absolute error percentages are $\bar{\epsilon}_A{'} = 1.31\%$ and $\bar{\epsilon}_A{'} = 0.87\%$. As to computational efficiency, in a MATLAB (version 7.0, R14) implementation of the algorithm on a personal computer, with a 3 GHz Intel processor and 1.5 Gb of physical memory, the GLCM surface is calculated for a single image in approximately 15 secs.

Dataset II was collected from an optically zoomed-in target area in the breaker region to study the detailed turbulence structure of the roller region and the breaker shear layer. The physical dimensions were 11.09 cm × 11.18 cm. The surfaces were estimated with the same GLCM and snake parameters, and the VI surface is compared to the GLCM surface in Figure 2.14. The error bars denote one standard deviation of the VI surface. The horizontally averaged absolute error $\bar{\epsilon}$ in this case is 7.9 pixels (=0.8 mm). In dataset II, the specularity in the breaking region occupies a larger (approximately twice) portion of the image. In this region, as noted before, the definition of a smooth unbroken interface is highly subjective and this can be seen in the increasingly wide error bars in that region. However, it is noted that the GLCM does a reasonable job of estimating most of the small scale perturbations of the surface even in this two-phase breaker region.
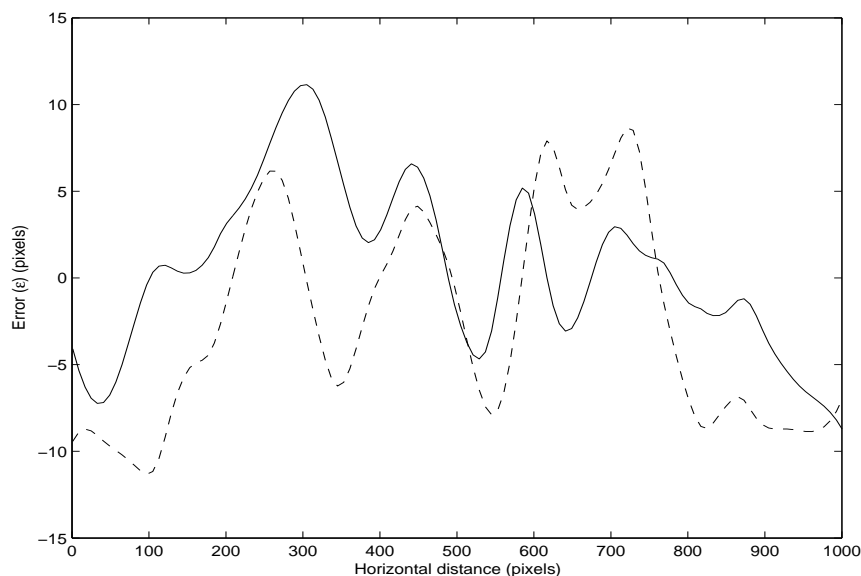
Figure 2.13: Error (ϵ) between GLCM and VI interfaces for image A (solid line) and image B (dashed line) for dataset I.

2.4   The PIV motion estimation algorithm

Typically, algorithms that have been developed for computing velocities from PIV images are region based methods that compute the cross correlation between the interrogation regions obtained from the two images (Adrian, 1991; Willert and Gharib, 1991). Region based techniques estimate the average motion of small groups of particles, thereby making the method noise tolerant and robust (Prasad, 2000). Among the various modifications to the region based methods, Scarano and Riethmuller (1999) proposed an algorithm where the displacement is predicted and corrected by means of an iterative procedure. As reported by the authors, the window displacement iterative multigrid (WiDIM) method is extremely robust. The method proposed in this section is similar to the WiDIM method, but has an additional advantage wherein the total motion is decomposed into a global motion field and a local motion field. This increases the robustness in the estimation of the

37
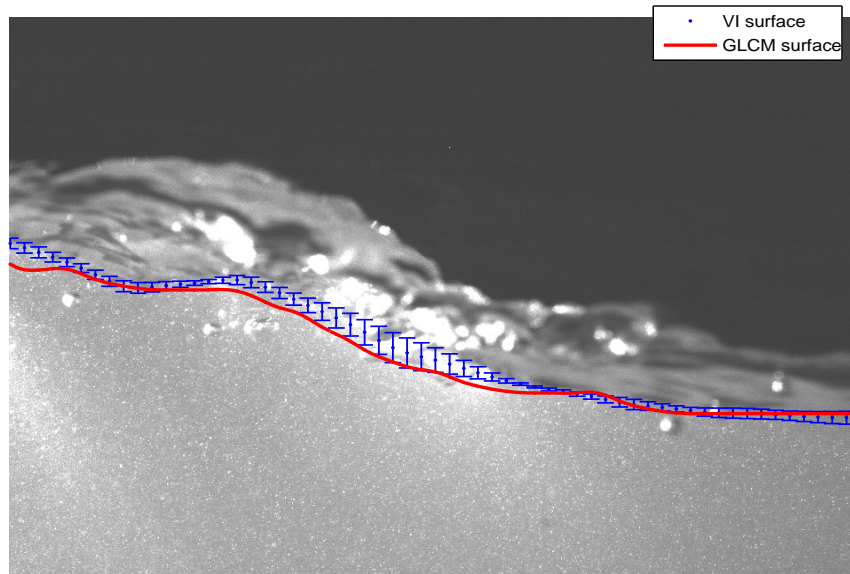
Figure 2.14: Comparison of GLCM and VI interfaces for a typical image in dataset II.

motion of the seeding particles.

Unlike the region based methods, where the intra-region motion is assumed to be accurately modeled as a translation of coherent groups of particles, intensity based differential methods (Quenot *et al.*, 1998) estimate the motion via the optic flow equation (Horn and Schunck, 1981). The biggest disadvantage with the differential methods is the requirement of strong gradient information in the images for the displacement estimates to be accurate. In synthetic images, this condition can be easily fulfilled, but in real images, particularly in the present data, this requirement is frequently violated, leading to inaccurate results.

A consequent and frequently necessary post-processing step involves the detection and replacement of spurious displacements that arise from image "noise" or deficiencies in the evaluation method (Westerweel, 1994; Raffel *et al.*, 1998). For example, the occurrence of spurious vectors can result from a locally low particle image

density or background noise from reflections (Bolinger, 1999). Nogueira *et al.* (1997) describe various post-processing steps for validating the estimated displacements in a PIV experiment, and also provide algorithms for the correction of spurious vectors using interpolating filters. In the PIV validation technique presented by Green *et al.* (2000), forward and reverse projected vectors are computed at chosen analysis points, and the projected vectors are used to test the validity of the vector estimated at the analysis point. This coherence-based validation scheme provides accurate results. However, the estimation of the forward and reverse projected vectors cause a three-fold increase in the computational complexity.

In this section, an algorithm is presented that estimates the motion by first computing a global motion field and then uses the global motion field as an initialization in estimating the local motion. This decomposition into a two level hierarchy of flow estimation helps accurately achieve very high spatial resolution. The global motion field is estimated using phase correlation (Thomas, 1987), while the local motion is obtained using a robust voting scheme composed of both the phase correlation and cross correlation estimates in order to accurately identify possible spurious vectors.

The organization of this section is as follows. First the motion estimation technique is described. This is followed by the details of the implementation, where the global and local motion estimation modules are implemented. Finally, the results of the experiments with the standardized images from JPIV (Okamoto *et al.*, 2000) and the PIV Challenge 2001 (Stanislas *et al.*, 2003) are presented to test the validity of the scheme. Peak-locking errors are analyzed with the standardized images as well as with images from dataset I. Most of the material that follows has appeared in Thomas *et al.* (2005a), and is reproduced here by permission of the authors.

2.4.1 Motion estimation techniques

When a time-lagged pair of images is viewed under the constraint of a small spatio-temporal difference, the "correspondence problem" can be cast as the problem of estimating the apparent motion of the image brightness pattern (Truco and Verri, 1998). Estimating this apparent motion or the optic flow leads to the fundamental equation of motion analysis, the image brightness constancy assumption, $\frac{dE(x,y,t)}{dt} = 0$, where $E(x, y, t)$ is the image intensity, (x, y) are the spatial coordinates, and t is time.

Among the various techniques developed, differential techniques derive directly from optic flow. Due to inherent difficulties in performing numerical differentiation, region-based matching techniques provide a possible alternative in estimating the displacement vector field (Barron *et al.*, 1994). This is done by either minimizing an error criterion such as "Sum of Squared Difference" (ε), or maximizing a similarity measure such as "Normalized Cross Correlation" (ρ) between the current image block and potential candidates within a predefined search window in the previous frame.

$$\varepsilon = \sum_{\mathbf{x},\mathbf{x}'}[E(\mathbf{x},t) - E(\mathbf{x}',t + \Delta t)]^2. \tag{2.15}$$

$$\rho = \frac{\sum[E(\mathbf{x},t) - \overline{E(\mathbf{x},t)}][E(\mathbf{x}',t + \Delta t) - \overline{E(\mathbf{x}',t + \Delta t)}]}{\sqrt{\sum[E(\mathbf{x},t) - \overline{E(\mathbf{x},t)}]^2 \sum[E(\mathbf{x}',t + \Delta t) - \overline{E(\mathbf{x}',t + \Delta t)}]^2}}, \tag{2.16}$$

where $\mathbf{x}$ and $\mathbf{x}'$ are the spatial positions in the time lagged (Δt) images, $\overline{E(\cdot)}$ is the mean of the region under consideration and $\sum$ is defined over all $\mathbf{x}'$ ($\mathbf{x}' = \mathbf{x} + \mathbf{d}$) within a predefined search window, with $\mathbf{d}$ being the displacement to be estimated. The phase correlation algorithm presented in the section below falls under the general class of region based motion estimation.

2.4.2   Phase correlation

Phase correlation, like cross correlation, is derived from the Fourier Shift Theorem, which states that the time lag of a one dimensional signal is equivalent to a phase change in the frequency domain. Thus, for two continuous functions $f(\mathbf{x})$ and $g(\mathbf{x})$ related by $g(\mathbf{x}) = f(\mathbf{x} + \mathbf{d})$ in the two dimensional Euclidean space, the cross correlation between the two can be obtained as the Inverse Fourier transform of the product of the individual Fourier transforms.

$$\Re_{fg}(\mathbf{d}) = \Im^{-1}(\Im(f(\mathbf{x})) \times \Im(g(\mathbf{x}))^{\star}) = \Im^{-1}(F(\mathbf{u})F^{\star}(\mathbf{u})e^{-j2\pi\mathbf{u}^T\mathbf{d}}), \qquad (2.17)$$

where $F(\mathbf{u})$ and $G(\mathbf{u})$ are the corresponding Fourier transforms of f and g with $(*)$ being the complex conjugate and $\mathbf{u}$ being the frequency components in the Fourier space. From the shift theorem, $G(\mathbf{u}) = e^{j2\pi\mathbf{u}^T\mathbf{d}}F(\mathbf{u})$.

Given the correlation surface, motion is estimated by finding the position of the maximum. But due to the aperture problem (Horn and Schunck, 1981), there are situations where the correlation surface contains multiple peaks. Selecting the maximum from the correlation surface in those cases does not necessarily provide the best estimate. A solution to this problem is to sharpen the true cross correlation peak by using "whitening" zero-phase FIR filters, $H_1 = |F(\mathbf{u})|$ and $H_2 = |G^*(\mathbf{u})|$ (Manduchi and Mian, 1993). Thus, prior to computing the inverse transform, the magnitude components from $F(\mathbf{u})$ and $G^*(\mathbf{u})$ are eliminated using the FIR filters. This modified correlation equation provides a Dirac delta function centered at the translation parameters, which can be estimated easily and more accurately.

$$\begin{aligned}
\wp_{fg}(\mathbf{d}) &= \Im^{-1}(\frac{F(\mathbf{u})}{H_1}\frac{G^*(\mathbf{u})}{H_2}) = \Im^{-1}(\frac{F(\mathbf{u})}{|F(\mathbf{u})|}\frac{F^{\star}(\mathbf{u})e^{-j2\pi\mathbf{u}^T\mathbf{d}}}{|F^{\star}(\mathbf{u})|}) \\
&= \Im^{-1}(e^{-j2\pi\mathbf{u}^T\mathbf{d}}) \\
&= \delta(\mathbf{x} - \mathbf{d}). \qquad\qquad\qquad\qquad\qquad\qquad (2.18)
\end{aligned}$$

Extensive studies on the use of phase correlation for motion estimation have been provided in Thomas (1987) and Vernon (2001), and in general, the technique

41

is extremely robust when estimating large displacements. An important advantage of motion estimation methods based on phase correlation is their insensitivity to illumination variation, since the magnitude terms are removed by the whitening filters (Manduchi and Mian, 1993). This was particularly relevant to the analysis of the present datasets because of the effects of laser attenuation and specularity due to breaking. On the other hand, algorithms based on the cross correlation metric perform a selection which is biased towards points having higher intensities and thus could provide incorrect displacements represented by local maxima. The phase-based techniques are also characterized by their insensitivity to correlated and frequency-dependent noise, which render them robust in the estimation space (Foroosh *et al.*, 2002).

The other notable advantage of phase correlation is that the affine parameters, such as rotation, shear and scale, which are coupled in the spatial domain, are separated from the translation components into the magnitude and the phase spectrum respectively in the Fourier domain. This is evident from the affine Fourier theorem as proposed by Bracewell (1993), which provides the generalization to the Fourier Shift theorem under an affine transformation. The affine Fourier theorem describes the separation of the affine terms and the linear terms in the frequency space. The estimation of the displacement parameters can thus be performed in the phase spectrum, while the parameters of the motion governed by the affine parameters can be estimated from the magnitude spectrum (Reddy and Chatterji, 1996; Kruger and Calway, 1996).

In the case where the local motion can be approximated as linear, both cross correlation and phase correlation would have a peak at the correct location. If the underlying motion contains strong affine components, most region based techniques would provide the average motion of the region that is analyzed by the interrogation block. Being a sharpened version of the cross correlation peak, phase correlation is

more sensitive to the presence of affine components in the motion field. It therefore provides a stronger metric in determining the presence of non-linear motion within the interrogation block. This idea forms the basis of the reliability measure used here, i.e., given the phase correlation peak and the cross correlation peak, the estimate is considered extremely reliable in the cases where the peaks of the two estimated metrics coincide. If the peaks of the two surfaces do not coincide, the region under consideration does not have a unique linear velocity, and any linear model would only provide an approximation of the motion. The important advantage of this robust voting scheme is that both the similarity metrics are derived from the Fourier components of the same regions under consideration. Thus, performing the 2-D Fast Fourier transform once does not significantly add to the computational complexity over other cross correlation based techniques.

2.4.3   Algorithm implementation

In computing the optic flow, all techniques face two interdependent problems which arise due to the choice of the analysis window. The smaller the analysis window, the greater the number of potential candidates which have a high correlation with the interrogation block. On the other hand, there is a higher probability of having a combination of various motions when the windows size is large. This problem is called the "generalized aperture problem" and defines the upper bound on the availability of accurate motion estimates at high spatial resolutions (Horn and Schunck, 1981). One approach used in dealing with this problem is to handle the motion estimation at multiple resolutions (Black, 1992). This enables percolation of information from a coarser resolution to a finer resolution in a computationally efficient fashion. The disadvantage with this hierarchical process is that any motion smaller than the degree of decimation is lost during the process of creation of the resolution hierarchy. The method implemented here has three processing components. The first component estimates the global motion that is taking place between

the image pairs using a multi-resolution image hierarchy (Burt and Adelson, 1983). The second component estimates the sub-pixel level local rectilinear motion, and the third component performs the outlier removal and data validation.

2.4.4 Global motion estimation

The global motion field is estimated by performing phase correlation at each level of the image pyramid hierarchy. The image pyramid is computed for each image of the image pair using a Gaussian filter followed by a 1:2 signal down-sampling. This helps reduce the aliasing artifacts that otherwise arise due to the down-sampling (Proakis and Manolakis, 1995). At each level of the pyramid, the down-sampled image pair is divided into a tessellation of blocks and the motion field is computed by performing phase correlation over the entire tessellation of blocks. The global displacement field is median filtered to remove spurious vectors before percolating the estimate from the coarser levels of the pyramid towards the finer resolutions. At the finest resolution of the image hierarchy, the global motion field is obtained. Due to the periodic nature of the discrete Fourier transform, the maximum measurable displacement using the Fourier transform of a signal within a window of size W is $W/2$. Thus, to capture translations of magnitude $\mathbf{d}$, the window size should be at least $2 * \max(d_x, d_y)$, where d_x and d_y are the components of the displacement along the two coordinate directions.

2.4.5 Local motion estimation

The global motion field obtained from the previous stage provides the initial estimate for the local motion estimation. The local motion field is obtained in a similar manner as the global motion estimation, in that phase correlation is performed on a tessellation of blocks over the entire image. To improve the accuracy
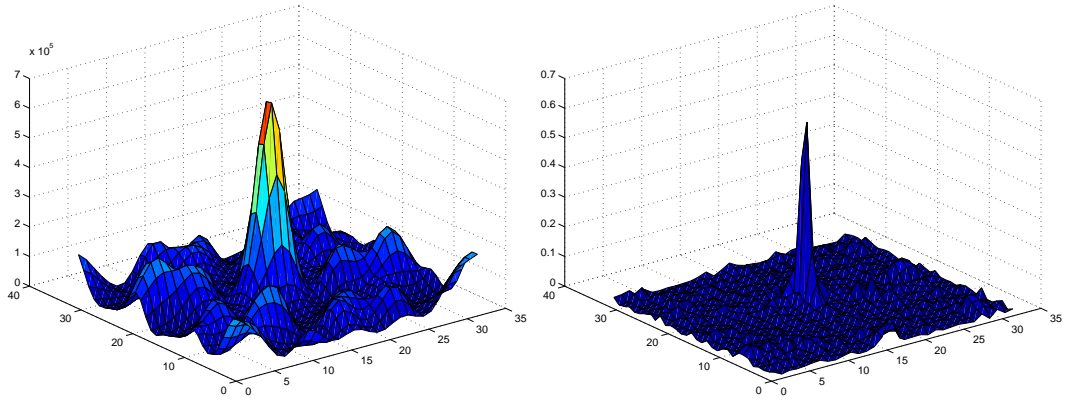
Figure 2.15: Reliability verification using cross correlation (left figure) and phase correlation (right figure).

of the estimate, the position of the peaks obtained by phase correlation is verified by comparing with the position of the peak from the cross correlation surface.

$$\Psi(\mathbf{d}) = [E(\mathbf{x}, t) - \overline{E(\mathbf{x}, t)}][E(\mathbf{x}', t + \Delta t) - \overline{E(\mathbf{x}', t + \Delta t)} \qquad (2.19)$$

Both Ψ and $\wp$ can be computed from the Fourier transform of the image block, and each is used to cross verify the accuracy of the other. If the positions of the two peaks are unchanged, the estimate can be considered a very reliable estimate within the region of comparison as shown in Figure 2.15. Thus, it provides a strong verification metric on the reliability of the estimate. The presence of a mismatch between the peaks indicates the possibility that the region under consideration has significant non-linear motion. This can be seen in Figure 2.16, where two interrogation blocks from a region undergoing non-linear motion are shown. Regions shown in the ellipses have been picked manually to give an indication of the non-linear motion taking place within the region.

Given the two image blocks, the peaks of the cross correlation and phase correlation have a positional mismatch, and as can be seen in Figure 2.17, the maximum of the phase correlation has another strong component in the vicinity.
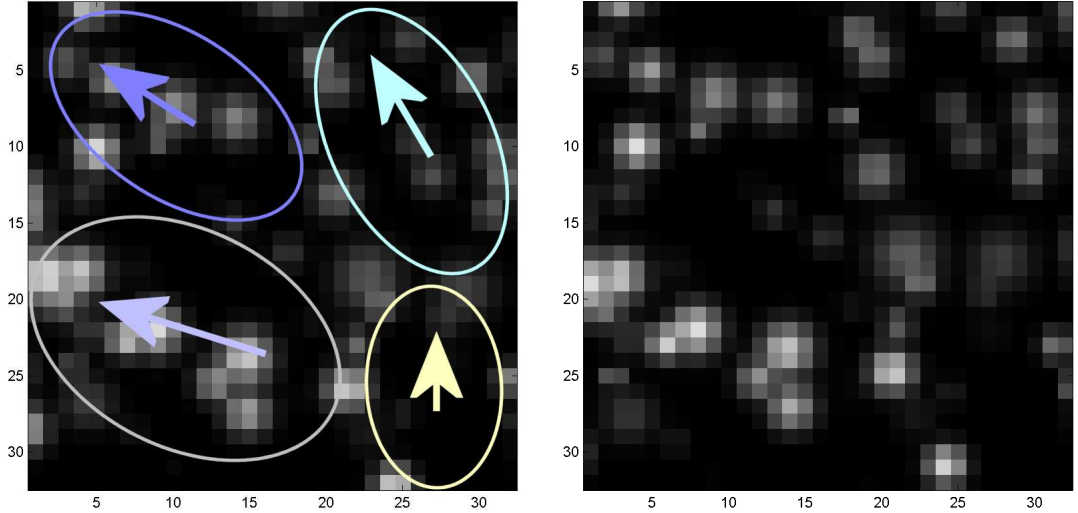
Figure 2.16: Image blocks undergoing non-linear motion. Left figure: block from image 1, right figure: block from image 2.

This positional mismatch indicates the possibility of multiple motions being present in the interrogation blocks. Any linear region based scheme would provide an average estimate of the motion within the window, which would be inaccurate. To rectify this, a set of potential candidates (C) are computed from the phase correlation and cross correlation surface if there is a mismatch between the peaks.

$$C = \{phase_i\} \bigcup \{\max(\Psi(\mathbf{d}))\}, \tag{2.20}$$

where $\bigcup$ denotes the union set, $phase_i = \kappa * \max(\wp(\mathbf{d}))$ are the positional candidates from the phase correlation surface and $\max(\Psi(\mathbf{d}))$ is the position of the maximum from the cross correlation surface. $\kappa = 0.75$ was seen to provide reasonable candidates. The reason that the candidates are selected from the phase correlation surface as against the cross correlation is because of the reduced surface spread around each peak in the phase correlation surface. The best candidate is then obtained by computing "normalized cross correlation" (ρ) at these candidate estimates (C) and selecting the candidate having the highest value of ρ. This technique does
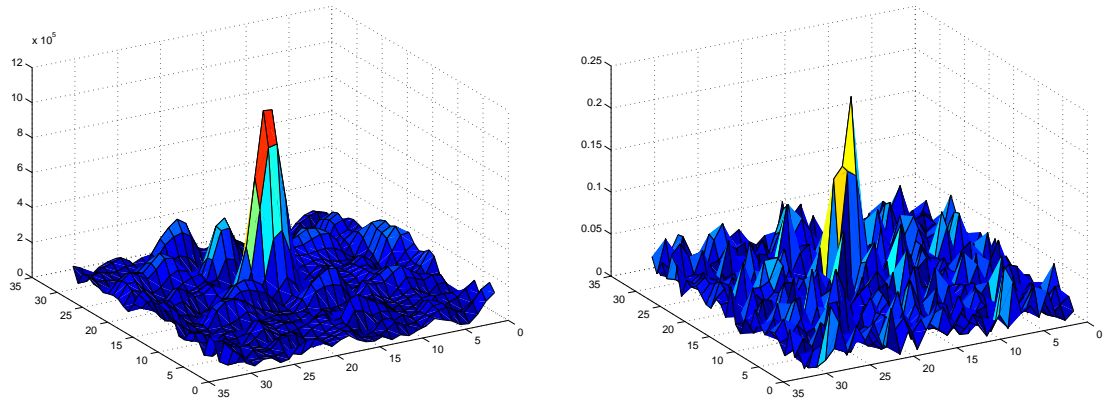
Figure 2.17: Peak mismatch indicating strong non-linear motion using cross correlation (left figure) and phase correlation (right figure).

not provide the parametrization of the higher order motion model, but within the constraint of a piecewise linear motion model, the method provides the most robust solution possible.

Having obtained the integer resolution motion field, sub-pixel level motion interpolation is done by fitting a 3-point gaussian fit over the normalized cross correlation (ρ) values in the neighborhood of the best estimate. Since the logarithm of a Gaussian yields a second order polynomial, the sub-pixel estimate (δ) is estimated by

$$\delta = \frac{\ln \rho_{-1} - \ln \rho_{+1}}{2(\ln \rho_{-1} + \ln \rho_{+1} - 2\ln \rho_0)} \tag{2.21}$$

where ρ_{-1}, ρ_0 and ρ_{+1} are the locations of the normalized cross correlation in the neighborhood under consideration.

2.4.6 Outlier removal and de-noising

Though the voting scheme reduces the possibility of incorrect estimates, image regions containing low gradient information due to insufficient seeding could still provide incorrect estimates. Removal of these spurious vectors is done by using a

modified median filter as proposed by Westerweel (1994), where the velocity vector $U_{2D}(i, j)$ is considered valid if

$$|U_{2D}(median) - U_{2D}(i, j)| < \epsilon_{threshold}, \quad (2.22)$$

where $U_{2D}(median)$ is the median of the vectors in the neighborhood of $U_{2D}(i, j)$ and $\epsilon_{threshold}$ determines the reliability of $U_{2D}(i, j)$. $\epsilon_{threshold}$ was determined in a manner similar to the "dynamic mean value filter" (Raffel *et al.*, 1998). The standard deviation of the vectors in the neighborhood, $\sigma_U(i, j)$, was used to weight two constants, C_1 and C_2 as $C_1 + C_2\sigma_U(i, j)$. For the dynamic median filter in the local motion estimation, the constants, $C_1 = 0.6$ and $C_2 = 0.6$ were found sufficient for performing the outlier detection. From computations done with the standardized images, the "dynamic median value filter" provided a better local neighborhood filtering than the "dynamic mean value filter".

2.4.7 Results

The algorithm has been implemented using a prototype written in Matlab 6.5 R13 by Mani Thomas (Department of Computer and Information Sciences, University of Delaware, Newark, DE 19716, USA). For the global motion estimation, interrogation block sizes were maintained at a constant 32×32 pixels throughout the image hierarchy so as to obtain an amplified and accurate translation at the finer scales. For the local estimation, the interrogation block size was 16×16 pixels. Both global and local estimations were performed with a 50% overlap between adjacent blocks. At each level of the image pyramid, the global motion field was median filtered using a 3×3 motion field neighborhood.

The images used for the validation of the algorithm were obtained from the JPIV (PIV-STD Project) (Okamoto *et al.*, 2000). In applying the algorithm for standard images from JPIV, both the non-transient and transient case have been evaluated to determine the utility of this method. An important part of a PIV
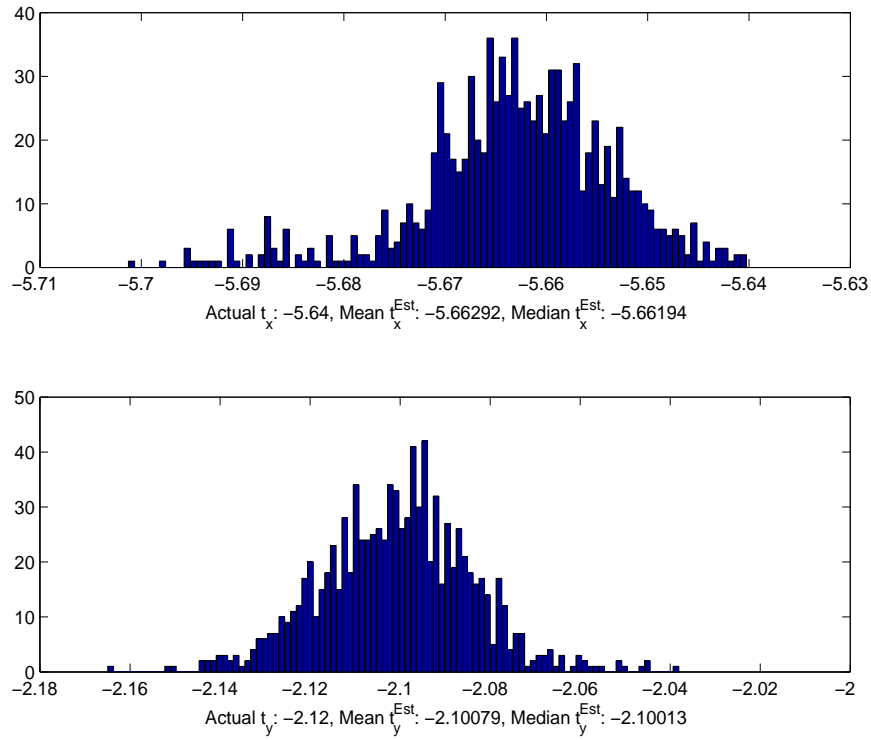
Figure 2.18: Histogram plots of the estimated displacements for two sample actual displacements. t_x and t_y are horizontal and vertical displacements.

algorithm is its ability to minimize the bias errors, specifically peak locking, robustly. In investigating the robustness of the method described in handling the bias errors, the standard images were first warped using known translations, and the motion was estimated. Four specific JPIV test cases (#004, #005, #006, #007) were warped, using bilinear interpolations, with translations in the range $[2.0, 2.1, \cdots, 8.0]$. The four test cases account for a typical displacement/seeding density scenario in a standard PIV experiment.

Histogram plots for a few of the translations are shown in Figure 2.18. For results of other cases, see Thomas *et al.* (2005a). As can be seen from the plot, the sub-pixel estimator is considerably robust. Though the existence of peak locking
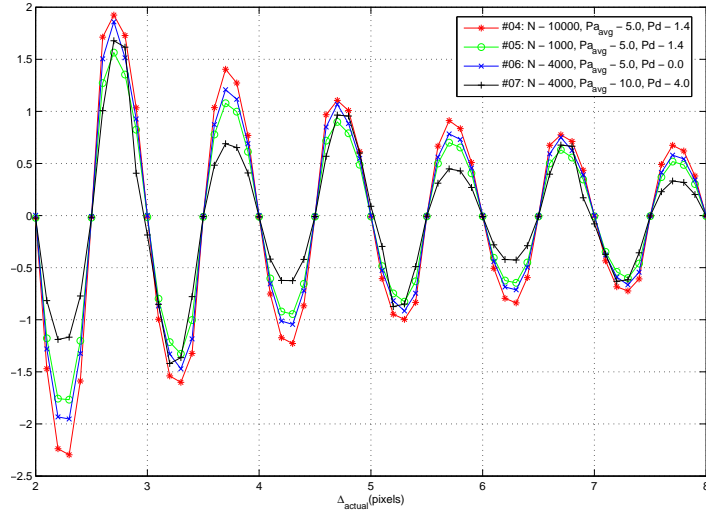
Figure 2.19: Variation of error under synthetic translation. μ is the mean estimated displacement. Δ: actual displacement, Pa_{avg} and P_d: average and standard deviation of the particle diameter.

cannot be ruled out completely when using the standard Gaussian interpolation function (Roesgen, 2003), the most important point to be considered in analyzing sub-pixel estimators is the error significance, which can be obtained as the ratio between the deviation to the actual translation. This is shown in Figure 2.19, where the percentage deviation has been plotted for the four test cases. The presence of the error oscillations indicates the presence of peak locking, but as can be seen, the amplitudes of the oscillations are within 2% of the actual displacement range. The bias error variations, with increasing/decreasing seeding density and/or the pixel diameter, agree with trends observed by Collicott (1993) and Prasad (2000). With an increased seeding density, the errors seem larger than with lower seeding density. With increasing particle size, the bias error deviations decrease, with bias error being zero at full pixel and half pixel resolution. The above results were obtained by running the simulations using an interrogations window size of 16×16 pixels
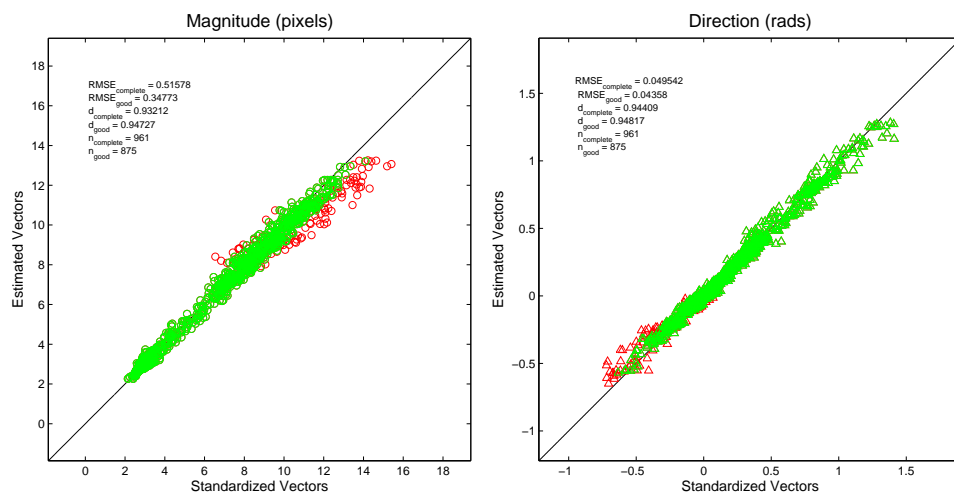
Figure 2.20: Scatter plot for estimated vectors versus standardized vectors for JPIV test case #001 (non-transient). See text for legend explanations.

with 50% overlap.

Next, the non-transient case is considered. Figure 2.20 is a sample scatter plot obtained from the magnitude and phase variation between the estimated and the ground truth displacement vectors for spatially collocated positions. The green markers in the scatter plots are the vectors whose magnitude are within 1 pixel difference from the standardized vectors while the red markers indicate those estimates that deviate from the standardized vector by more than 1 pixel in magnitude. $n_{complete}$ are the total number of estimates which have been compared and n_{good} are the estimated vectors which are within 1 pixel difference of the ground truth. RMSE denotes the root mean square error. The algorithm provides accurate estimates when compared to the ground truth vectors for all image pairs, except Image No. 2 (Thomas *et al.*, 2005a). The main reason for this was due to the large non-rigid motion present in the image pair. Most region based techniques fail for this pair of images because of the extreme changes in the position of the particles

51

and the gradient of the velocity vectors. For results with the transient case and the PIV challenge (Stanislas *et al.*, 2003) (both of which show very good agreement between ground-truth and estimated vectors), see Thomas *et al.* (2005a).

2.4.8 Pixel-locking analysis

As mentioned in the introduction, one of the major causes of errors in velocity estimation from PIV is peak-locking or pixel-locking; a bias error that in the presence of actual sub-pixel displacements, biases the displacements calculated from a sub-pixel estimator towards integer and half-integer values. Prasad *et al.* (1992) were perhaps the first to systematically analyze the sources of this error. From tests carried out with real PIV images of turbulent channel flow, they concluded that the bias error results from an inaccurate resolution of the correlation peak. There was a periodic behaviour of the error, with zero crossings at full- and half-pixel values, as has already been seen from the test cases with the standardized images. They also point out the bias errors resulting from inadequate pixel resolution for the position of individual particles (quantified by the ratio of particle image diameter and pixel spacing, $\frac{d_\tau}{d_{pix}}$) are not critical in PIV (unlike Particle Tracking Velocimetry), since a displacement estimate from a finite window incorporates several particle images, and the bias error should cancel out. However, Keane and Adrian (1990) had shown earlier that the location of the correlation peak is proportional to this ratio, and therefore, larger values should reduce bias errors. The RMS errors on the other hand, increase with d_τ. Westerweel (2000) showed that peak-locking effects are supposed to occur when the particle-image diameter is less than two pixel units. Several other sources of pixel-locking errors have been identified, such as in-plane loss of correlation (Westerweel *et al.*, 1997), image noise and correlation processing (Huang *et al.*, 1997), the size of the interrogation window (Nogueira *et al.*, 2001) and the choice of sub-pixel estimator itself (Forliti *et al.*, 2000). Since peak-locking errors influence not just the mean flow, but the turbulence statistics as well (Christensen, 2004),

several precautions and remedies have been suggested to prevent and overcome many of these problems. One such is the recent sinc-kernel based sub-pixel algorithm suggested by Roesgen (2003), which was found to increase the accuracy compared to the commonly used method of fitting a three-point Gaussian around the peak. Even though the estimated vectors from the motion estimation algorithm have been shown to be in good agreement with the ground-truth vectors for the standard JPIV images, a 5-point (both in the horizontal and vertical directions) least squares Gaussian sub-pixel estimator was implemented, which was seen to further increase the accuracy of the estimated sub-pixel displacement for the real images. Reducing the bias error was essential in reliably estimating the turbulent quantities, since pseudo-turbulence can be generated in PIV datasets from bias errors due to pixel-locking (Chang and Liu, 2000). The lower accuracy for a standard 3-point Gaussian fit arises due to its inability to take into account background "noise", which is amplified in the real images as compared to the synthetic images. The non-linear least squares algorithm uses the Levenberg-Marquardt method (Moré, 1977).

In the present study, the raw images, compared to typical PIV images, were sub-optimal (due to the rather large field of view, low optical resolution, and visually observed laser sheet attenuation, among other random noise inherent to PIV). A further source of concern was the relatively low average pixel displacement, which was approximately 1 pixel. For such low displacements, bias errors, such as those caused by pixel-locking, become large and are known to dominate over random errors (Prasad, 2000). However, these trends are only confirmed for quadratic and three-point Gaussian estimators. As will be seen, even in cases of low particle displacements as in the present case, the least squares sub-pixel estimator reduces this bias error to less than 1%. A high accuracy in the velocity field was essential toward making sensible analyses of the mean and turbulent flow structure. Therefore, it was imperative to test the algorithm's accuracy with the present images.
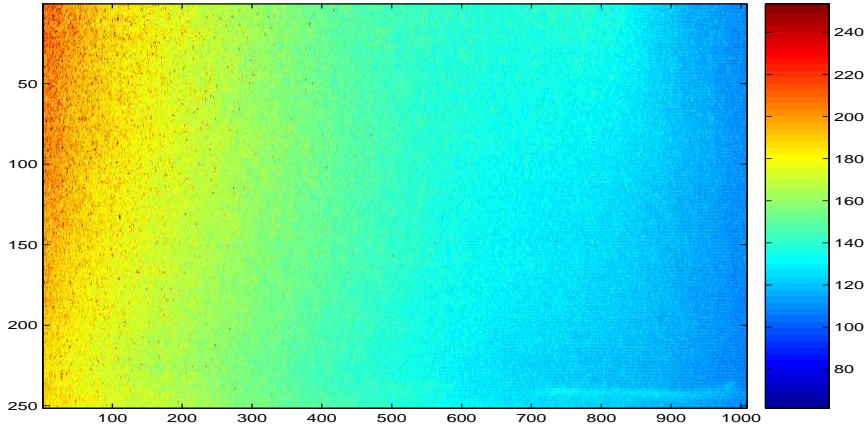
Figure 2.21: Section of scaled raw image from dataset I used for pixel-locking analysis. Coordinates are in pixels and the colorbar shows intensity levels.

A 256×960 section of a randomly selected image from the ensemble was chosen as the first image for the tests, and is shown in Figure 2.21. It is stressed that this is a real raw image from the dataset and not synthetically constructed. The second image pair was constructed by warping (using a bilinear interpolation) the first image with a prescribed known (integer $\pm$ sub-pixel) translational displacement Δ_{actual}. A range of displacements, typically found in the experiment, were used. The window size was kept fixed at 16×16. The mean of the estimated displacement ($\mu_{\Delta_{estimated}}$) was then calculated by averaging over the entire flow field. Histogram plots of the estimated displacements are shown in Figure 2.22. The non-dimensionalized error is shown as a function of the actual displacement in Figure 2.23. Several features are immediately obvious. The overall accuracy is very good, and the maximum non-dimensionalized error is only 3%, at an actual total displacement of 0.6 pixel. The modulus of the error decreases as the displacement increases. The error is very close to zero at integer and half-integer displacements. There still is clear evidence of the effect of pixel-locking, since, for actual displacements greater

54
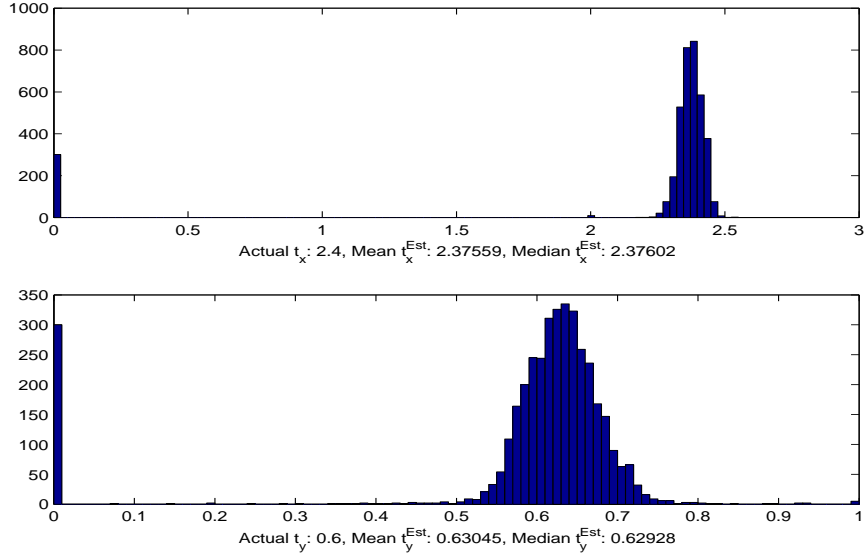
Figure 2.22: Histograms of actual and estimated mean and median displacements for two sample actual displacements. t_x and t_y are horizontal and vertical displacements.

than integer and half-integer displacements, the error is negative and vice-versa. The large errors always occur at roughly 0.1 pixels away from integer and half-integer value. The cause of this is not known. Since the estimated mean (averaged over the entire domain) instantaneous pixel displacement in the experimental data, was found to be around 1 pixel, the errors in the estimated displacement are therefore within 1%. There was also no bias in the variation of the estimated displacements in the horizontal direction, confirming that laser attenuation did not lead to any degradation in the estimated vector fields.

Once the real surface and bottom have been calculated, the raw image was cropped off at the location of the flume bottom, and above the envelope of the highest surface fluctuations, to save computation time. All pixel values outside the fluid domain of interest were replaced with zeroes. The cropped image was then subdivided by finite windows of size 16×16 pixels with a 50% (8 pixels) overlap in
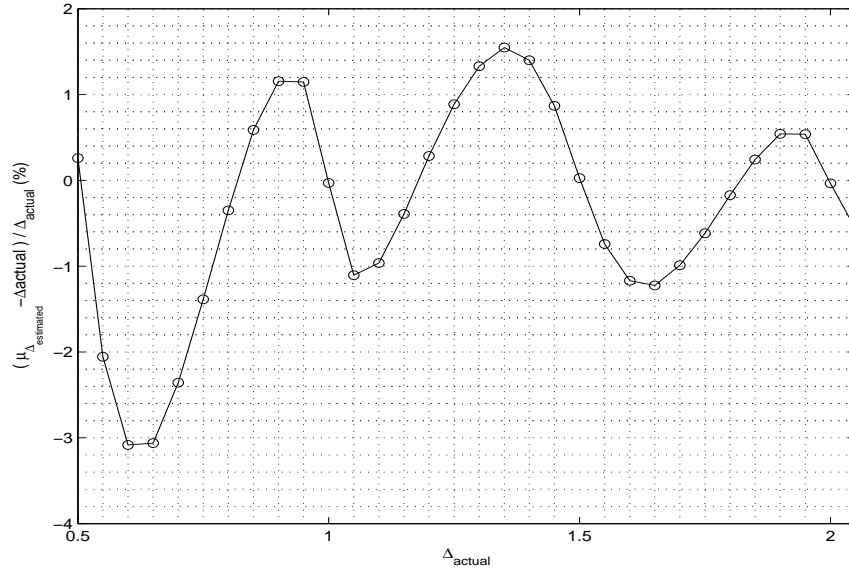
Figure 2.23: Non-dimensionalized error in estimated displacements. Δ_{actual} (pixels) : actual displacement, $\mu_{\Delta_{estimated}}$ (pixels) : mean of estimated displacements.

the horizontal and vertical directions. The horizontal and vertical resolutions were, respectively, $\Delta x = \Delta y = 0.184$ cm. The global window size is 32×32 pixels. In the vertical direction, the first calculation point was 8 pixels below the instantaneous surface, whereas the last calculation point was 16 pixels ($y_1 = 3.66$mm) above the calculated bottom. These limitations were imposed by the size of the window used for computing the global motion. It was observed that typical vector fields after the local flow estimation had less than 1% spurious vectors, which indicated the robustness of the algorithm. Most of these were concentrated along the edges of the image. The spurious vectors were then removed and substituted by the dynamic median filter. For the range of displacements in the present experiment, the mean error was approximately $\pm 1\%$.

2.5 Conclusions

The raw PIV images are analyzed to estimate the instantaneous complex air-water interfaces using image processing methods. The algorithm presented in section 2.3, a second order statistical method based on GLCM, is simple to implement and gives a first approximation to the location of the interface. Several pre-processing steps are introduced to increase the robustness of the candidate for the GLCM. A singular value decomposition is performed on the combined selected texture classes to initialize the edge map for the subsequent contour mapping process. Active contours, or "snakes", minimizing energy functionals based on the internal (controlling the shape of the contour) and external (characterizing image information) energies of the contour are used to increase the accuracy of the predicted interface. A disadvantage with the algorithm is that the texture measures employed, and the parameter values chosen for the contour extraction, are obtained from an empirical evaluation. However, this is a small price to pay in light of the size of the ensemble, since a single image is used to tune the algorithm and the rest of the ensemble is analyzed in an accurate and computationally efficient manner. This process is completely automated. The estimated interface is compared to the visually interpreted interface and the deviation is found to be within the measurement resolution for the fluid velocities. For the two images shown, the horizontally averaged absolute errors were 5.77 pixels and 3.85 pixels. An accurate estimation of the surface enabled the exclusion of spurious inter-facial reflections in the images and ensured volume flux conservation throughout the domain, which will be discussed in the next chapter.

A robust and accurate motion estimation algorithm based on phase-correlation has been developed to estimate the instantaneous fluid velocities. This algorithm is composed of a two stage technique, the global motion field estimation followed by local differential motion estimation. This provides the best possible estimate that

can be obtained using region-based schemes. A significant component of the algorithm is the voting scheme, which is used to improve the reliability of the estimated vectors. Cross correlation in itself is not illumination invariant, but in combination with an illumination invariant metric such as phase correlation, it provides a more accurate estimation of the flow velocities. One of the advantages of using the hierarchical two stage estimation technique is the possibility of obtaining a smooth and accurate motion field at high resolution (using interrogation windows up to 8×8 pixels with a 50% overlap). This accurate motion estimation is due to the initialization of the local motion field estimation using the global motion. Standardized PIV images are used to test the algorithm, and the comparative results between the estimated vectors and the ground truth vectors indicate that the hierarchical phase correlation is quite accurate for the estimation of the motion. This is mainly due to the inherent robustness of phase correlation to illumination variation. The effect of peak-locking is discussed in detail, both with respect to the standardized images and images collected during the experiment. Increased sub-pixel accuracy is obtained by fitting a least squares Gaussian to the displacement peak. The average errors for the range of displacements obtained during the experiment are approximately one to three percent.

Chapter 3

ENSEMBLE-AVERAGED INTERFACE PROPERTIES AND FLOW STRUCTURE

When Einstein stopped creating, it was because he stopped thinking in concrete physical images and became a manipulator of equations

Richard P. Feynman

3.1 Introduction

In the attempt of clarifying the details of the flow structure for turbulent hydraulic jumps, many laboratory experiments have been performed with various techniques like hot-wire anemometry (Rouse *et al.*, 1959; Resch and Leutheusser, 1972) and laser Doppler anemometry (Long *et al.*, 1990). Cheaper and easier to use point measurement probes such as micro acoustic Doppler velocimeters have also been used by Liu *et al.* (2004) to investigate low Froude number ($Fr \sim 2.0, 2.5, 3.2$) jumps. The authors, however, found that the signal quality deteriorated with increased noise levels near the free surface due to air-bubble entrainment. Consequently, they were unable to obtain any information about the flow near the free surface or in the roller region. It is also doubtful whether such an intrusive method is appropriate to measure the kinematics of a flow which is very sensitive to perturbations. Several experimental studies have also focussed on the aeration characteristics of the two-phase region. A qualitative video study undertaken by Mossa and Tolve

59

(1998) showed a correlation between the vortex pairing process and air concentration in the roller region. However, flow velocities were not measured. Chanson and Brattberg (2000) used dual-tip conductivity probes to measure the void fraction and bubble frequency distributions in the air-water flow region of jumps with partially developed inflow. The turbulent velocities in the water were measured by a Pitot tube. Resch and Leutheusser (1972), using hot-film anemometry, showed that the air entrainment process, the momentum and energy transfer, and the energy dissipation are strongly dependent on inflow conditions. Minor changes in the flow and channel characteristics, such as bottom roughness (Henderson, 1970), inflow velocity profile, and pre-jump air entrainment (Chanson, 1996) cause drastic qualitative and quantitative changes in the nature of the jump. These are discussed further. Being single point measurement techniques, these at best provide a sparse picture of the flow field. Reconstructing a spatial map can only be done in an ensemble-averaged sense.

Recently, Lennon and Hill (2004) did PIV experiments analyzing undular jumps in the Froude number range $1.5 \sim 3$. They were unable to generate fully turbulent breaking jumps at these low Froude numbers. The complete flow field could not be investigated even using a mosaic of ensemble-averaged spatial maps because the laser sheet access was blocked by optically-opaque metal supports on the channel bottom. The free surface for the lower Froude number cases could not be measured by a wave gage since it disturbed the flow and caused the jump to move. Standard point gage and image processing techniques were used, but with limited success. The flow field near the crest of the undular jump could not be measured because of significant cross-channel deviations in the water surface slope which obscured the optical path of the camera. They also focused primarily on a detailed estimation of the bottom shear stress. All the above studies, and numerous others that the author is aware of, have either focused on undular jumps, where

the energy is swept downstream by propagating waves, or turbulent jumps with $Fr > 1.5$. As pointed out by Battjes and Sakai (1981), the flow in these jumps are not directly relevant to breakers on a beach. Moreover, there is very little detail about the flow structure in the intermittent region.

The most comprehensive study to date of low Froude number, weakly turbulent jumps with breaking and air entrainment is that of Svendsen *et al.* (2000) (hereafter referred to as IS00), based on the LDV data obtained by Bakunin (1995). The Froude numbers analyzed were 1.37, 1.48 and 1.62. They found that, contrary to the traditionally simplified formulations of a hydraulic jump, the effects of non-uniform velocities and non-hydrostatic pressure are important for mass and momentum conservation. Although a significant amount of the turbulent structure was mapped by vertical profiles of LDV data at several streamwise locations, simplified analytical approximations and assumptions had to be made to calculate streamwise gradients of flow properties, or to neglect the gradients altogether. Little attention was focused on the intermittency of the surface and its influence on the flow structure. A single roller was found to reside in the region bounded from below by, what the authors referred to as, a dividing streamline (above which the net volume flux was zero), and from above by the mean surface. The peak values of the turbulence intensities and Reynolds shear stress were found at the bottom of the roller.

Peregrine and Svendsen (1978), who had provided a qualitative mixing-layer model describing the similarities between breakers, bores, and hydraulic jumps based on photographic visualizations of bubble tracers in breaking waves, had suggested that "the surface roller does not play a dominant role in the dynamics of the wave". The analogy with mixing layers is further supported by the photographic evidence in Hoyt and Sellin (1989), which was based only on the structure of large scale eddies since the high polymer solution used to visualize the flow suppressed the smaller scale motions. An analogy between hydraulic jumps and plane turbulent
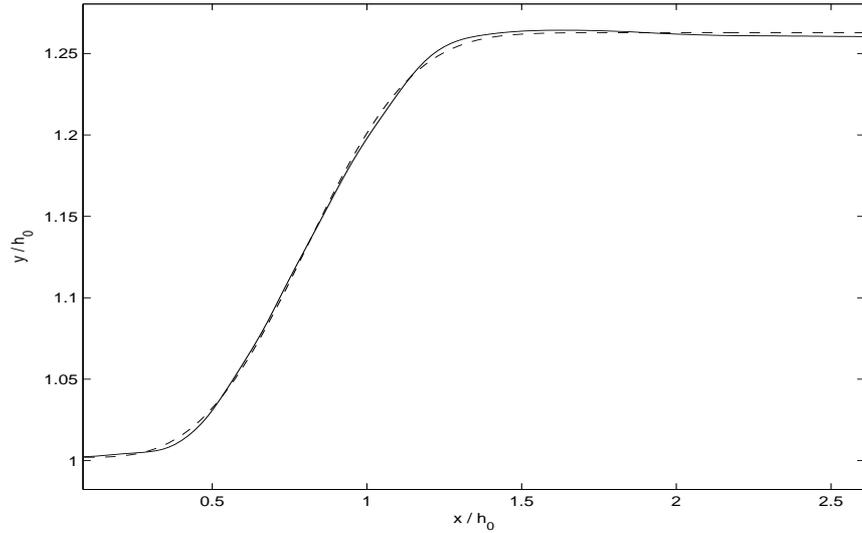
Figure 3.1: Ensemble-averaged free surface (solid line) and Weibull function fit (dashed line).

wall jets has also been suggested by several authors (Rajaratnam, 1965; Narayanan, 1975). Recently, Chanson and Brattberg (2000) have shown that a quantitative comparison between the parameters of the two flows is significantly affected by the air entrainment. This short summary reveals that many questions are still open regarding both the detailed turbulence structure and dissipative mechanisms of a quasi-steady fully-formed spilling breaker (Is the roller an appropriate topological description? Can the breaker shear layer be classified as a mixing layer?) and the extent to which it can be described in terms of a hydraulic jump.

3.2 Interface properties

Once the instantaneous interfaces have been calculated, the ensemble averaged interface is easily obtained and is shown in Figure 3.1. The origin of the coordinate system is defined in the supercritical region at the flume bottom. Therefore, the flow appears from left to right in all the subsequent figures. x increases from

supercritical to subcritical region, and y increases away from the bottom. The super-critical and sub-critical depths (taken here as the distances from the flume bottom to the end points of the ensemble-averaged free surface, where the horizontal gradient of the surface was nearly zero) are found to be $h_0 = 8.62$ cm and $h_1 = 10.85$ cm respectively, giving an upstream-to-downstream depth ratio, $\xi = 1.26$. The calculated values agree well with visually-observed upstream and downstream instantaneous depths of 8.5 cm and 10.9 cm respectively. It is interesting to note that a Weibull function given by

$$\tilde{y} = \tilde{y}_0 + a\left[1 - exp\left\{-\left(\frac{|\tilde{x} - \tilde{x}_0 + bln(2)^{1/c}|}{b}\right)^c\right\}\right] \tag{3.1}$$

shown as the dashed line in Figure 3.1, fits the mean surface data well. $\tilde{x} \equiv \frac{x}{h_0}$, $\tilde{y} = \frac{y}{h_0}$, $a = 0.2609$, $b = 0.8222$, $c = 3.152$, $\tilde{x}_0 = 0.8085$, $\tilde{y}_0 = 1.002$. From Belanger's equation,

$$Fr = \sqrt{\frac{1}{2}\frac{h_1}{h_0}\left(\frac{h_1}{h_0} + 1\right)}, \tag{3.2}$$

the upstream Froude number is calculated to be $Fr = 1.1932$. Due to the error in the surface estimation, the upstream depth is over-predicted, and this leads to an under-prediction of the Froude number of about 3 %. The Froude number can also be determined based on a depth-averaged flow velocity (or volume flux), and is explored further in this chapter. It is perhaps surprising that a breaking jump (which showed no visible undular characteristics) could be set up at such a low Froude number. As mentioned in the introduction, the nature of the jump is very sensitive to the flow conditions and channel characteristics, and it would require carefully designed control experiments to determine the specific cause(s) of breaking. The possible reasons for breaking occurrence in the present case are discussed later.

For laboratory-generated spilling breaking waves, dominant coherent motions of the surface fluctuations and the breaker toe, with peak frequencies in the range 0.47-96 Hz, have been reported by various authors (Duncan, 2001). In the present
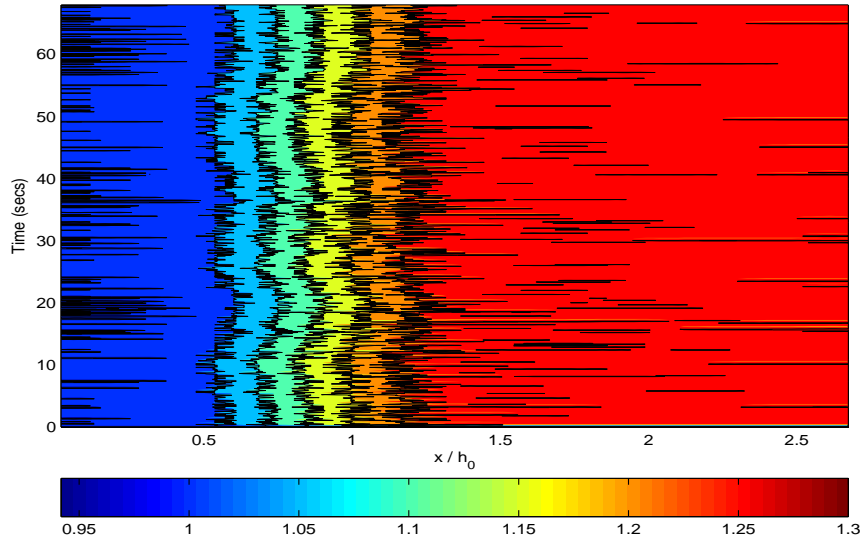
Figure 3.2: Time stack of dimensionless surface fluctuations.

study, even though the sampling rate (15 Hz) is not high enough for capturing the smaller turbulent time scales, it is instructive to look at the unsteady nature of the fluctuations. Figure 3.2 shows a time stack of the dimensionless (with respect to h_0) surface fluctuations over the entire jump. The ensemble spans a total time of 67.93 secs. The downstream region shows the random turbulent fluctuations with surface values clustered around the corresponding ensemble-averaged values. The transitional breaking region however shows coherent oscillations, with a time scale of about 20 s, or a frequency of 0.05 Hz. The intervals of relatively large turbulent fluctuations in the upstream region coincide with the troughs of the low frequency oscillation in the breaking region, around 20, 40 and 60 s respectively.

Low frequency motions in quasi-steady spilling breakers and turbulent hydraulic jumps have also been attributed to toe oscillations. The toe itself is often loosely defined in the literature, as noted by Duncan (2001). The ambiguity is compounded by a toe defined not just with respect to the topology of the free surface, but also with respect to the roller. For incipient breaking of surface tension-dominated

64

waves, the toe is defined as the leading edge of the bulge at the crest where the slope of the surface undergoes an abrupt change (Qiao and Duncan, 2001). There is a sharp curvature at this point, and on large scale, is marked by flow separation (Longuet-Higgins, 1994; Duncan *et al.*, 1999). For a fully evolved quasi-steady breaker with a roller on the front face of the wave, the underlying turbulence and the significant corrugations of the surface make it difficult to precisely locate the toe. Banner (1988) and Qiao and Duncan (2001) have referred to the leading edge of the roller as the toe. In saturated breakers or bores, where the entire front face of the breaker is turbulent, BP2 have recently proposed a descriptive terminology of a "foot" as the base of the breaker. When looking down from above, the fluctuations of the boundary between smooth and turbulent flow were defined as "toes". In the present case, the air-water interface is approximated by a smooth unbroken curve. The toe is defined as the location of the maximum positive curvature of the free surface. The curvature (κ) of the instantaneous free surface (η) is calculated as

$$\kappa = \frac{\frac{d^2\eta}{dx^2}}{\left[1 + \frac{d\eta}{dx}^2\right]^{3/2}}. \tag{3.3}$$

An ensemble average of the locations of the maximum curvature calculated from the instantaneous surfaces is found to coincide with the location of the maximum curvature of the ensemble averaged surface at $\tilde{x} \sim 0.47$. The ensemble-averaged curvature is shown in Figure 3.3. The negative peak for the curvature is located at $\tilde{x} \sim 1.18$. The oscillatory nature of the curvature in the breaker region is linked to the surface estimation process. In this region, the high specularity in the images due to breaking and air bubbles leads to small bumps, which are amplified by the second derivative in the curvature. It is interesting to note that in the present case, the slope of the mean surface shown in Figure 3.3(b) at the location of the maximum curvature is found to be around 11 degrees. This is close to the stable equilibrium value ($\sim$ 10 degrees) typically used in the inner surf-zone for Boussinesq modeling
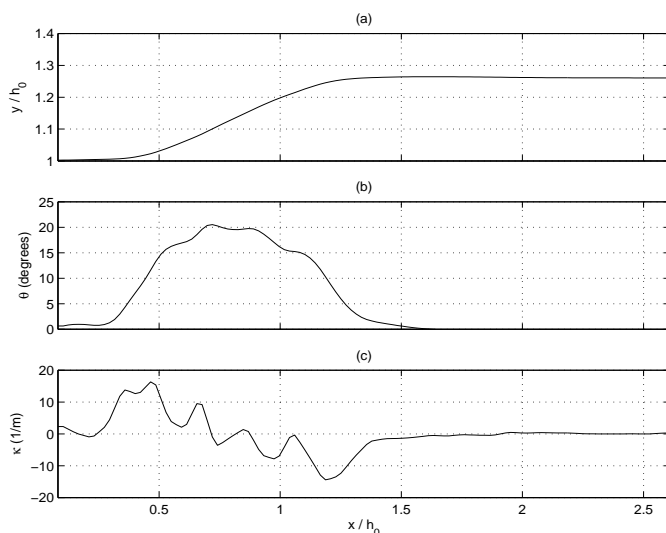
Figure 3.3: (a) Ensemble-averaged free surface, (b) slope of mean surface (degrees), and (c) Gaussian curvature of mean surface.

of broken waves (Schaffer *et al.*, 1993). The slope is also in good agreement with Longuet-Higgins (1973), who, in a theoretical model of flow separation at a free surface, showed that immediately upstream of the toe, the free surface should be inclined to the horizontal at angle lying between 10 and 20 degrees.

The toe motion in time can be tracked by computing the time series of the location of the peak curvature. Since the length of the time series is small for a reliable Fourier spectral analysis, and there are possible nonlinear effects in the signal, wavelet and Hilbert-Huang transforms were also used to compute the power spectrum of the time series. A wavelet spectrum of the "Morlet family" has been used as computed from the toolbox developed by Torrence and Compo (1998). The Hilbert-Huang transform was computed with 6 intrinsic mode functions and a residual of 0.1. A 1024 FFT length with 50 % overlap and a Hamming window were used to compute the Fourier spectrum. It is reassuring to see that all three peaks coincide at a frequency of 0.05 Hz, which is the observed fluctuation frequency in
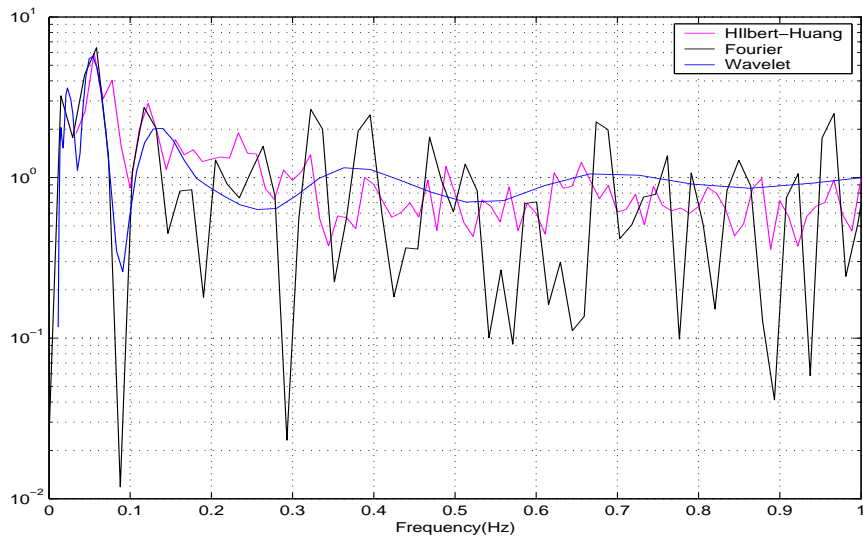
Figure 3.4: Fourier, Hilbert-Huang, and wavelet power spectra for time series of toe location.

the surface elevations. The puzzling origin of this very low frequency oscillation was due to pump instabilities. Two Sontek acoustic Doppler velocimeters were placed near the inflow and outflow sections of the channel, 200 cm upstream of the weir and 160 cm downstream of the toe. Time series of streamwise velocities were collected at 25 Hz, and the spectral analyses showed a dominant peak at 0.05 Hz at both locations (Figure 3.4). Therefore, the observed surface fluctuations in the breaker region and the toe oscillations cannot be directly related to the breaker instability since the 20 sec oscillation masks any faster-scale toe oscillations.

Next, the turbulent dynamics of the interface fluctuations are analyzed. Free surface turbulent flows are known to be inherently intermittent in the outer regions of the flow, with high frequency bursts of characteristic turbulent fluctuations followed by intervals of weaker and slower fluctuations (Townsend, 1976). Therefore, it was essential to implement a conditional averaging technique for defining ensemble averages of the turbulent flow field, especially for the intermittent region. Note
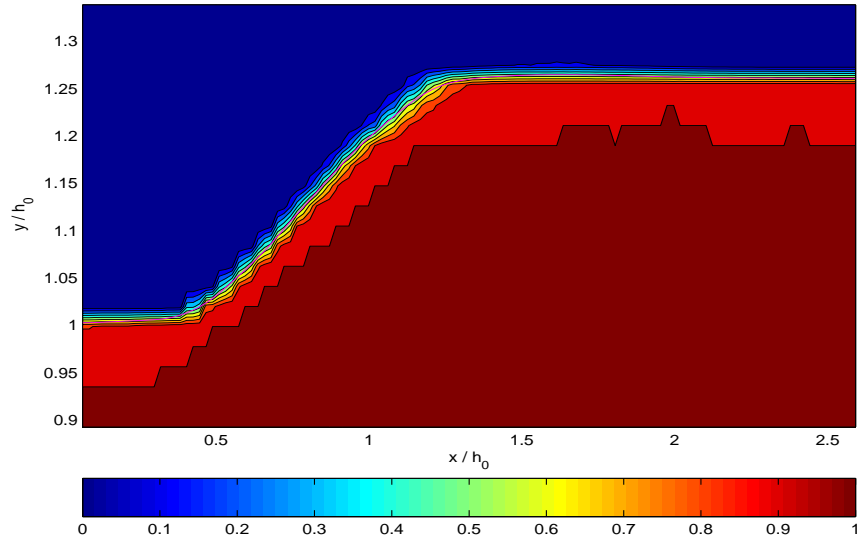
Figure 3.5: Intermittency factor γ. The solid magenta line is the ensemble-averaged surface.

that the intermittency arises from both the fluctuation of the instantaneous surface and the two-phase bubbly region due to the air entrainment and the break-up of the surface due to turbulence. Here, the interface is assumed to be continuous and unbroken, separating the air and water phases, and no attempt was made to resolve the entrained bubbles in the flow. For a detailed description of the interaction between free surface aeration and turbulence, see Chanson and Toombes (2003) and BP1. To deal with the interface intermittency, a zone-averaging technique (Antonia, 1981) is used. The zone-average is obtained as the ensemble of values during times when a given point is either in water or air. An intermittency function $I(x, y, i)$ is defined at a spatial location (x, y) for the ith realization as

$$
I(x, y, i) = \begin{cases} 1, & \text{if } \eta(x, i) > y, \text{ i.e if the point is in water} \\ 0, & \text{otherwise, i.e if the point is in air,} \end{cases}
$$

where $\eta(x, i)$ is the instantaneous water surface.

68

The zone-averaged intermittency factor $\gamma(x,y)$ is given by

$$\gamma = \frac{\sum_{i=1}^{N} I}{N},$$ (3.4)

where N is the total number of realizations ($N = 1020$), and is shown in Figure 3.5. Water is indicated by the red region with $\gamma = 1$, and air is indicated by the blue region, with $\gamma = 0$. As expected, there is a smooth transition throughout the breaking region. For fluctuating interfaces with multiple time scales of oscillations, a definition of the mean is not always without ambiguity. An analogous problem with reference to the shoreline oscillations on a beach has been analyzed by Brocchini and Peregrine (1996). In the present case, the ensemble-averaged free surface is found to coincide with the contour of $\gamma = 0.5$.

Corrsin and Kistler (1955) have shown that the inferred distributions of surface displacement closely follow Gaussian error law distributions,

$$p(\eta) = \frac{1}{\sqrt{2\pi\sigma^2}} \exp\left[-\frac{1}{2} \left(\frac{y - <\eta>}{\sigma} \right)^2 \right]$$ (3.5)

where $< . >$ denotes an ensemble average. $p(\eta)$ and σ are respectively, the probability density function and the standard deviation for the displacement η. The intermittency factor is related to $p(\eta)$ as

$$\gamma(x,y) = \int_{y}^{\infty} p(\eta,x)d\eta,$$ (3.6)

and leads to an Error Function profile (BP2),

$$\gamma(x,y) = \frac{1}{2} \left[1 - \mathrm{erf}\left(\frac{\eta - <\eta>}{\sqrt{2}\sigma} \right) \right].$$ (3.7)

Figure 3.6 shows the calculated intermittency factor compared to the Error Function profile at various locations inside the breaker region. The calculated values fit the profiles well, with accuracy increasing in the downstream direction. This shows that the instantaneous surface is calculated accurately, and its unsteady fluctuations are captured well by an automated calculation of the GLCM interface.
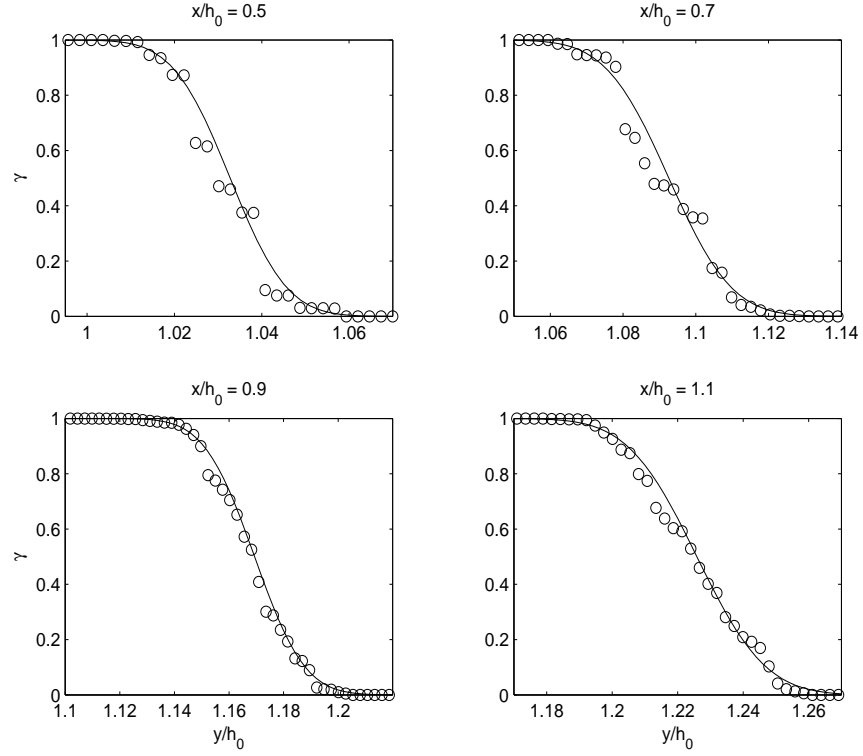
Figure 3.6: Intermittency factor γ in the breaker region: measured data (o), Error Function profile from equation 3.7 ($-$).

3.3 The flow structure

In this section, the ensemble-averaged flow structure is analyzed. The conditionally-averaged mean velocities are calculated as

$$< \mathbf{v} > = \frac{\sum_{i=1}^{N} I\mathbf{v}}{\sum_{i=1}^{N} I}, \tag{3.8}$$

and are represented hereafter as U and V in the x and y directions. $\mathbf{v} = (u, v)$, where u and v are the instantaneous horizontal and vertical velocities respectively. The horizontal root mean square (RMS) "turbulent velocity" is computed as

$$u' = \sqrt{\frac{\Sigma_{i=1}^{N}[I(u - U)]^2}{N\gamma}} \tag{3.9}$$

and similarly for v'. γ has been defined in equation 3.4. The turbulent kinetic energy (k) and Reynolds shear stress (τ') are computed as

$$k = \frac{\Sigma_{i=1}^{N} I \frac{1}{2}[(u-U)^2 + (v-V)^2]}{\gamma N}, \qquad (3.10)$$

$$\tau' = -\frac{\Sigma_{i=1}^{N} I (u-U)(v-V)}{\gamma N}. \qquad (3.11)$$

3.3.1 Mass flux conservation

Although there were no in-situ measurements of the flow velocities, the accuracy of the computed flow field can be checked by examining an integral constraint based on mass flux conservation. Note that this can be used indirectly as a check on the accuracy of the estimated surface as well. The mean volume flux across a vertical section can be computed as

$$Q(x) = b \int_{y_1}^{\tilde{h}(x)} U(x,y)dy. \qquad (3.12)$$

where b is the width of the channel, and the integration is done numerically. The upper limit of integration, $\tilde{h}(x)$, is the vertical location where $\gamma = 0$. Note that the lower limit of integration is the upper boundary, y_1, of the bottom boundary layer, and not the flume bottom. The contribution to the flux near the bottom, including the boundary layer, cannot be estimated because of lack of data. No attempts were made to extrapolate the velocity to the bottom by fitting analytic profiles. The standard deviation (Q_σ) and mean ($\overline{Q}$) are 0.5682 l/s and 21.6646 l/s respectively, which gives $\frac{Q_\sigma}{\overline{Q}} = 0.0262$. Similar estimates were found by Bakunin (1995) from his LDV data. In addition to the bottom boundary layer, there are cross-channel variations in the flow and side-wall boundary layers, the effects of which are not taken into account. The artificial shear layer near the surface in the upstream region also reduces the volume flux there. By fitting analytic velocity profiles to the data of Bakunin (1995), and incorporating the non-negligible reductions in the total volume flux due to side-wall and bottom boundary layers, IS00 found that the volume flux

71
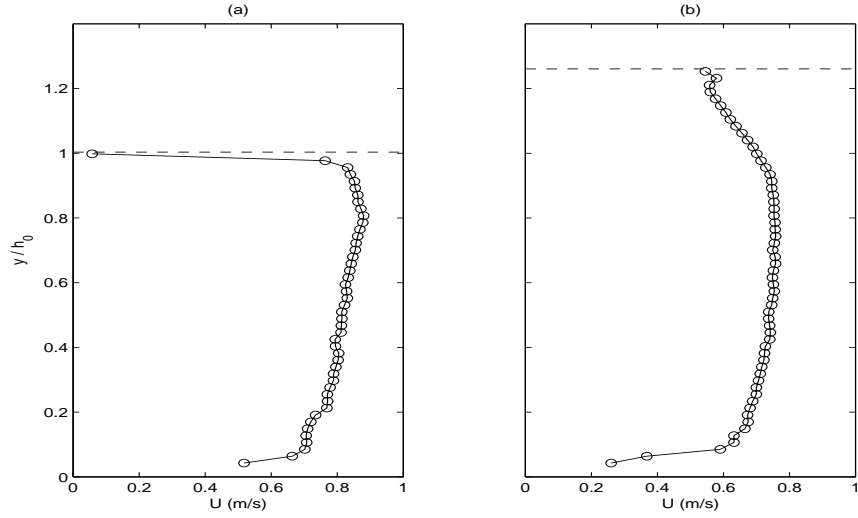
Figure 3.7: Vertical profiles of the ensemble-averaged horizontal velocity (U) (m/s). (a) $\tilde{x} = 0.15$, and (b) $\tilde{x} = 2.50$. The dashed lines show the location of the mean free surface.

error could be reduced further. The mass conservation in the present study was also checked locally by numerically calculating the divergence of the mean velocity field to second-order accuracy, and was found to be satisfied within measurement and discretization errors.

The Froude number can be calculated from the volume flux as

$$Fr' = \frac{Q}{(bh')\sqrt{gh'}}, \tag{3.13}$$

where b is the width of the channel and $h_0' = h_0 - y_1$. The upstream Froude number is thus calculated to be $Fr' = 1.023$, which is smaller than Fr calculated from equation (3.2). This is in agreement with Bakunin (1995) and IS00, who found that the Froude number calculated from Belanger's equation consistently over-predicted a depth-averaged velocity or volume flux based estimate.

72

3.3.2 Mean flow structure

Figure 3.7 shows the vertical profiles of the mean horizontal velocity at $\tilde{x} = 0.15$ and $\tilde{x} = 2.50$. The dashed line is the elevation of the mean free surface at this location. At the upstream location, artificial shear near the mean surface at the top two measurement locations can be seen. Chanson (1996) has indicated (based on the experimental data of Thandaveswara, 1974) that the turbulence level near the free surface for fully developed inflow conditions is much higher than with partially-developed inflow without pre-jump aeration. For fully-developed inflow conditions, Leutheusser and Kartha (1972) found from their experiments ($Fr > 10$) that the measured upstream Froude number was over-predicted by the Belanger equation, as in the present study. Therefore, the upstream condition in the present case is a combination of pre-jump entrainment of air resulting from the vortical structures upstream of the weir (Chanson, 1996, Figure 7-3), and possibly a partially developed boundary layer, since the toe of the jump was approximately 20 cm downstream of the weir. These could be the reasons for breaking at such a low Froude number. At the downstream location shown in the right panel, the thickness of the shear layer is approximately 3 cm, showing that the flow has not relaxed to its depth-uniform open channel configuration.

Since the spatially dense velocity measurements afford a whole map of the flow, it is instructive to look at filled contour plots which present the whole spatial map of the flow field. Note that the flow field is shown only up to the mean surface. The flow structure in the intermittent region is analyzed later. In Figure 3.8, the solid red line is the ensemble-averaged free surface. The mean horizontal velocity is shown in the top panel. As the mean surface curves upward sharply at the toe, the adverse pressure gradient induces a rapid axial deceleration of the upstream horizontal flow velocity. Although the velocities are nearly uniform around mid-depth,
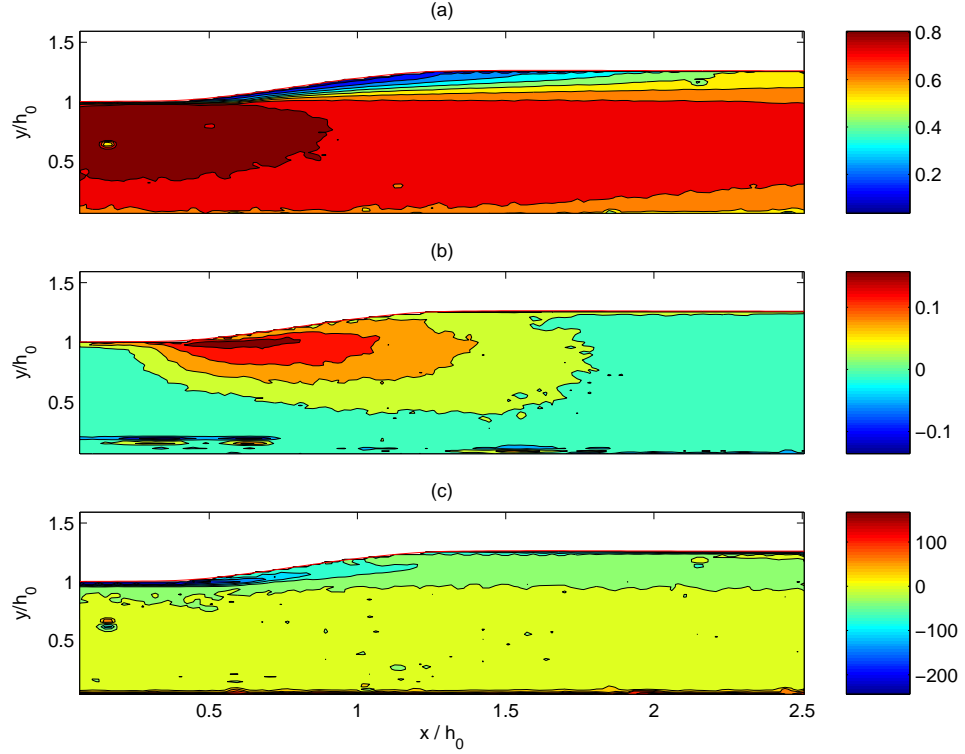
Figure 3.8: Mean flow structure. (a) Ensemble-averaged horizontal velocity (U) (m/s), (b) ensemble-averaged vertical velocity (V) (m/s), and (c) ensemble-averaged vorticity (ω) (1/sec). The red solid line is the ensemble-averaged free surface.

there are significant deviations from the assumption of depth-uniform flow, particularly in the "breaker shear layer". This is the shear layer which spreads downstream from the foot of the breaker, and whose dynamics differ from that of a typical shear layer in several aspects which are clarified in the following. The momentum and pressure correction factors are analyzed in detail by IS00. The bottom boundary layer, with positive vorticity, also grows in the downstream direction. The vertical velocity is almost an order of magnitude smaller than the horizontal velocity. It reaches its peak value downstream of the foot at $\tilde{x} \sim 0.68$, $\tilde{y} \sim 0.99$. The large negative values in V near $\tilde{y} \sim 0.2$, and near the bottom in the downstream region,

are due to artifacts in the data caused by image noise arising from imperfections on the flume wall. This was confirmed by looking at the raw PIV images.

There is a thin, concentrated region of negative vorticity in the breaker shear layer. Near the toe, the negative vorticity decays rapidly away from the mean surface, reaching 1% of its peak value at a distance of approximately 2.2 cm. Therefore, the bulk of the flow can be modeled as irrotational. IS00 calculated the vorticity based on an analytic fit to the horizontal velocity data. Since the measurements were made only along a few vertical transects, they had to neglect the contribution from the streamwise gradient of the mean vertical velocity. Even when this is justified in the calculation of the mean vorticity, small values of $\frac{\partial V}{\partial x}$ can cause significant changes in the turbulence structure of thin, curved shear layers due to streamline curvature effects (Bradshaw, 1973). Curvature effects on the anisotropy of the turbulent structure is discussed in detail in Chapter 4 and Chapter 5. The vanishing vorticity at the mean surface in IS00 was a consequence of the zero mean shear stress condition for the analytic fit to the horizontal velocity. In the present study, there is non-zero vorticity at the mean surface. As shown in Figure 3.9(b), the mean vorticity has its peak negative value at $\tilde{x} \sim 0.41$, $\tilde{y} \sim 0.99$, upstream of the toe, and decreases in the downstream direction, parallel to the mean surface.

DG97, analyzing the thin (~ 0.3 cm) layer of positive vorticity below the surface and above the negative vorticity layer, have shown that the location of the peak positive vorticity flux in their steady breaker coincided with the peak of the deceleration of the fluid layer. The positive vorticity was due to the shear generated by the high-speed surface layer (originating from the specific nature of breaker generation) overlaying a slower layer of fluid. The coincident location of the peaks in positive vorticity and curvature was attributed to the oscillation of the vorticity layer. It was concluded that the source of vorticity was not due to curvature or entrainment of bubbles due to breaking, as observed by Hornung *et al.*

75
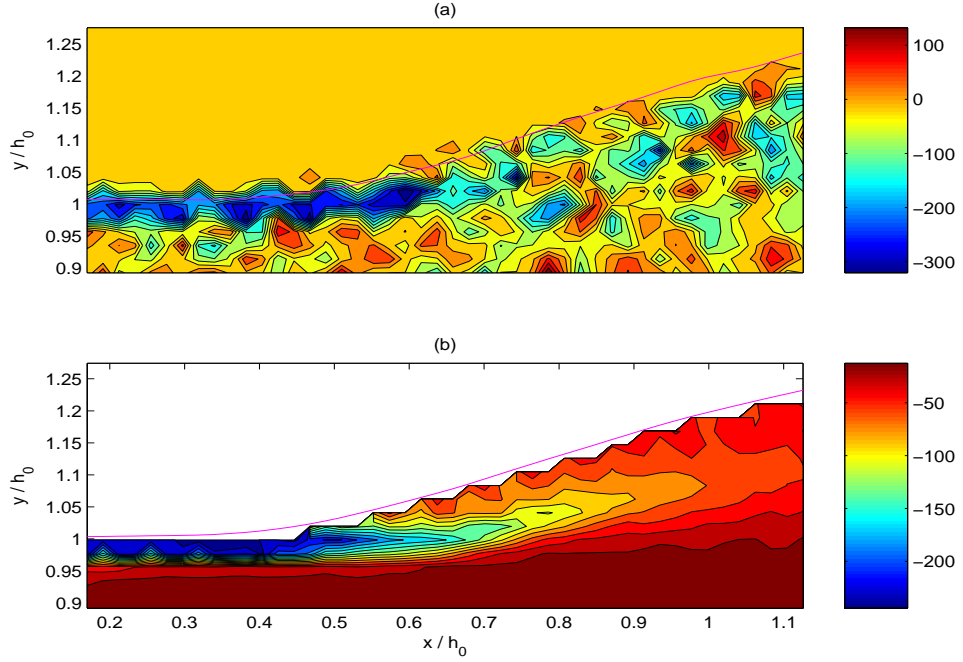
Figure 3.9: (a) Instantaneous vorticity (1/s), and (b) ensemble-averaged vorticity (1/s).

(1995), but solely due to the deceleration effect.

However, LR95 observed from experiments done with spilling breaking waves generated by a towed submerged hydrofoil, that the surface curvature serves as a source of vorticity, thereby giving rise to a separated mixing layer. From instantaneous realizations of incipient and fully-evolved breakers, they observed that "detailed distortion of the flow adjacent to the free surface during the onset and development of flow separation, in conjunction with the change in slope of the free surface, plays a central role in determining the maximum vorticity". They found a very low-velocity separated region beneath the free surface. Longuet-Higgins (1998a) has shown that for purely two-dimensional flow with a steady surface, the vorticity (ω) is directly related to the curvature (κ) and the tangential velocity (q) of the

surface

$$\omega = -2\kappa q \qquad (3.14)$$

In the present study, the mechanism for breaking is different from both DG97 and LR95. Further, as opposed to resolving the small-scale structure of the instantaneous flow field, the focus of the present study is to analyze the ensemble-averaged quasi-steady flow. No attempt has therefore been made to resolve the detailed corrugations of the instantaneous surface. The resolution in the present study (0.0229 cm) is also much coarser than DG97 (~ 0.003 cm) and LR95 (~ 0.0008 cm). Nevertheless, no evidence of a high-speed surface layer was found in the instantaneous velocity fields. For the instantaneous flow field, a negative vorticity layer is found below the surface, shown in Figure 3.9(a).

To analyze the mean flow effects close to the mean surface, the mean surface is treated as a streamline, and the coordinate system chosen is a mobile, locally orthogonal, curvilinear system (s, n) fixed on the mean surface (Misra *et al.*, 2004, BP2). s and n are measured along the surface parallel and normal directions, respectively. The deceleration is of interest close to the mean surface near the toe, where the flow is highly curved. Since the gradients of scalar quantities are not coordinate invariant, it is essential to perform a coordinate transformation to attach a direct and more accurate physical significance to the calculated gradients. The mean surface-parallel and surface-normal velocities are, respectively, calculated as

$$\hat{U}_s = U\cos\theta + V\sin\theta, \quad \text{and} \qquad (3.15)$$

$$\hat{V}_n = -U\sin\theta + V\cos\theta. \qquad (3.16)$$

$\theta(x) = \tan^{-1}\left[\frac{\partial <\eta(x)>}{\partial x}\right]$ is the angle that the tangent to the mean surface makes with the $x-$axis, shown in Figure 3.3(b). Since θ is determined from the local slope of the mean surface, the transformation is accurate only near the mean surface, where the streamlines closely follow the surface. The surface-normal and surface-parallel gradients are therefore only shown until 5 measurement points below the
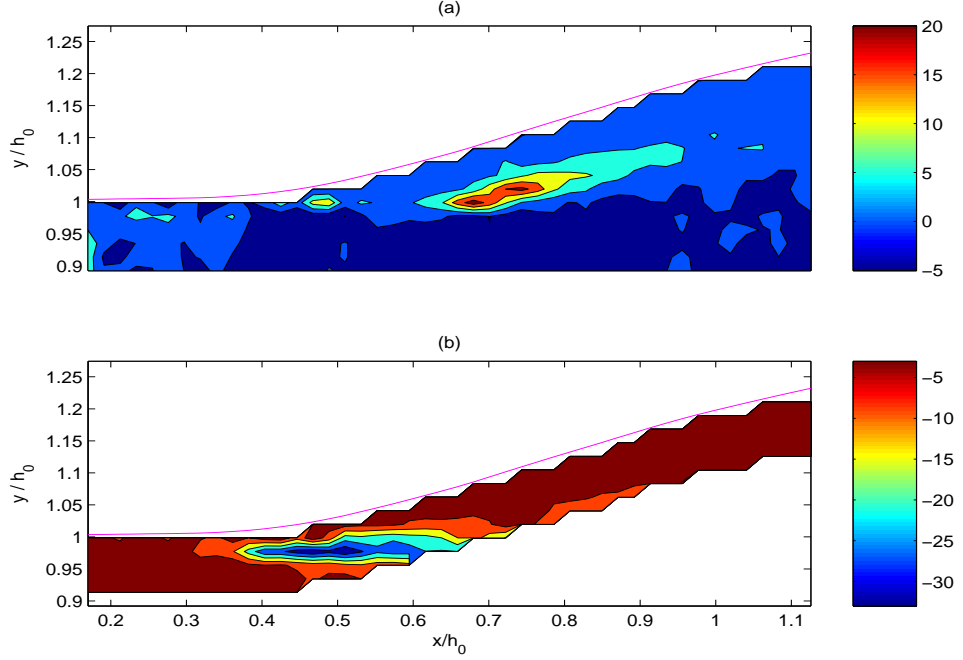
Figure 3.10: (a) Ensemble-averaged horizontal Cartesian convective acceleration $\left(U\frac{\partial U}{\partial x}\right)$ (m/s²), (b) ensemble-averaged surface-parallel convective acceleration $\left(\hat{U}_s\frac{\partial \hat{U}_s}{\partial s}\right)$ (m/s²).

mean surface. The deceleration effect due to $\hat{U}_s\frac{\partial \hat{U}_s}{\partial s}$ is shown in Figure 3.10(b). The Cartesian component $(U\frac{\partial U}{\partial x})$ is shown in the top subplot to illustrate the importance of the coordinate transformation in aiding a correct physical interpretation of the flow. As can be seen in the top subplot, in the region $\tilde{y} < 1$, where the streamlines are straight and nearly parallel to the x-axis, $U\frac{\partial U}{\partial x} < 0$ gives a correct physical insight into the deceleration of the flow related with the adverse pressure gradient. Near $\tilde{x} \sim 0.75$, the positive values indicate an unphysical convective acceleration. This results from the improper representation of a curved flow in the Cartesian coordinate system. Although the peak negative value occurs at $\tilde{x} \sim 0.46$, $\tilde{y} \sim 0.98$ (see figure 3.10 (b)), which is coincident within the measurement resolution with the toe location, intense flow deceleration is seen to occur upstream of the peak vorticity
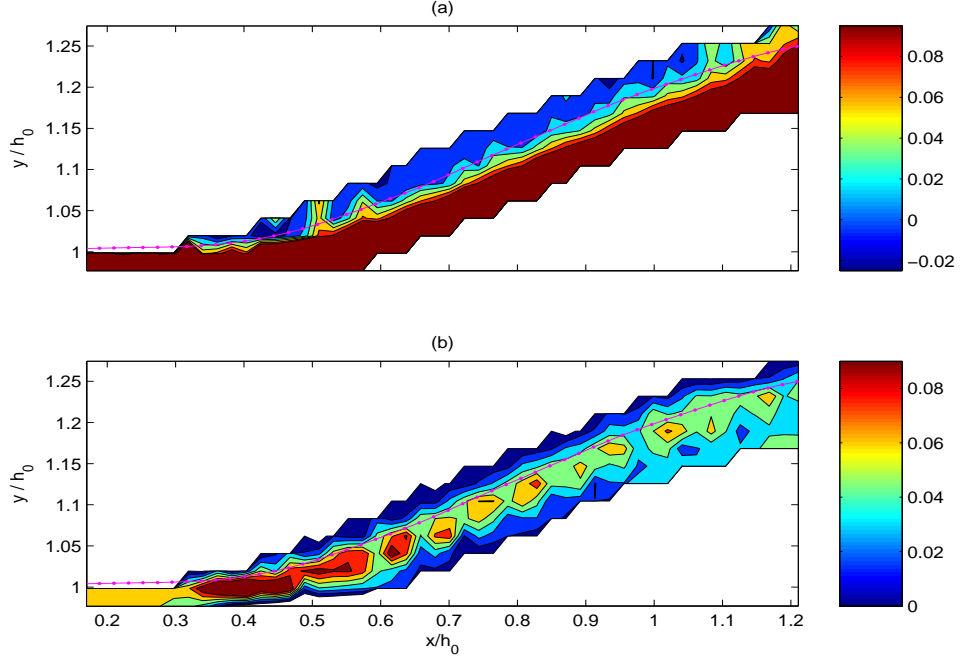
Figure 3.11: (a) Mean surface-parallel velocity $(\hat{U}_s)$ (m/s). (b) mean surface-normal velocity $(\hat{V}_n)$ (m/s). Dotted magenta line is the ensemble-averaged free surface.

location. The localization of the deceleration, indicative of the strong reduction in velocity over a small streamwise direction along the surface, is in good agreement with LR95. Hornung *et al.* (1995) suggest that the vorticity seen downstream of a hydraulic jump is due to air entrainment from breaking. In the present study, the peak vorticity is upstream of the breaking location (approximated by the peak value of air entrainment at $\tilde{x} \approx 0.64$) in agreement with the observations of DG97.

It seems intuitive that there should be a reverse flow near the surface due to breaking as observed during the experiments, and its structure should be influenced, if not wholly determined, by the topology of the mean surface. As discussed in section 3.1, several researchers have confirmed, theoretically and from experimental observations, that there is a weak eddy residing above the dividing streamline.

Before analyzing the flow in the roller region, it is noted that even though the mean quantities are obtained by an ensemble conditional averaging and yield stable estimates, the values for the vertical velocities are close to uncertainty limits in the estimated instantaneous velocities, and any quantitative analyses should be made with caution. Figure 3.11 shows the mean surface-parallel ($\hat{U}_s$) and surface-normal ($\hat{V}_n$) velocities in that region. The dotted magenta line is the mean surface. A weak reverse flow (the largest negative velocity is found to be 2.38 cm/s) is clearly seen, and is localized entirely above the mean surface. IS00 determine the location of the dividing streamline by calculating the elevation at which the depth-integrated volume flux (obtained from an analytic fit to the measured velocities) goes to zero. This is in no way a trivial calculation. In the present case, there is not enough vertical resolution in the very thin roller region to accurately estimate the flux. However, if the roller is visualized as a recirculating region, intuitively, the bottom boundary of the roller can be estimated by assuming that the positive velocities at the bottom boundary should be approximately equal to the maximum negative velocity in the reverse flow region. The bottom boundary is therefore just below the mean surface. This is a different scenario than IS00, where the entire roller was interpreted to be confined below the mean surface. The difference arises because of the treatment of intermittency in the present case. Banner and Phillips (1974) had hypothesized that "the definite location of the free surface in the breaking eddy must be replaced by an intermittent zone". This is certainly implemented in the present study, since γ shows a smooth transition in this region, with the mean surface closely coincident with $\gamma = 0.5$.

The surface-normal velocity is nearly zero in the reverse flow region. There are large, positive values of $\hat{V}_n$ near the bottom of the roller and are an indication of the entrainment of water from below. This is in agreement with the 'starting plume' model of Longuet-Higgins and Turner (1974) (see their Figure 7), where the

spilling region is regarded as a turbulent gravity current riding down the front face of a wave, with entrainment of water from below. The data of Bakunin (1995) also shows positive values of $\hat{V}_n$ along the lower boundary of the roller, even though this was not explicitly investigated by IS00. It is also clear from the present data that, though most of the entrainment occurs near the toe, inflow from below occurs all over the roller length with approximately equidistant peaks of upwelling. This seems in conflict with the perspective of the roller as a mass of fluid in global rotation with no mass exchange with the fluid below. It also implies that the lower boundary is not a dividing mean streamline. It should be pointed out that, even though a large amount of confidence cannot be placed in the physical significance of the small scale structure seen in the vertical velocity, it is nevertheless resolved by the measurement location grid ($\Delta \tilde{x} = \Delta \tilde{y} = 0.0213$), and is not merely an artifact of the contour plotting routine. As opposed to the assumption made by IS00, the mean shear is finite at the mean surface. Lastly, regarding the geometry of the roller, the mean inclination is calculated to be 18.5 degrees. The length of the roller is L_r =6.36 cm. For their lowest Froude number case ($Fr = 1.38$) IS00 found a non-dimensionalized roller length of $\frac{L_r}{h_0} \sim 1$. In the present case $\frac{L_r}{h_0} = 0.74$.

3.3.3 Turbulence structure

Before looking at the turbulence structure, the convergence of the quantities of interest were examined at a number of spatial locations. This was performed by calculating running averages of the turbulence statistics over the entire ensemble. A location in the breaker shear layer near the toe of the breaker, at $\tilde{x} = 0.51$, $\tilde{y} = 1.02$ was chosen. The convergence rates for the turbulent statistics are shown in Figure 3.12. Stable estimates are obtained near the end of the ensemble after about 900 realizations. It is expected that convergence rates would be similar for other locations in the breaker region, and faster as we progress away (downward) from the surface and further downstream. This is seen in Figure 3.13 which shows

81
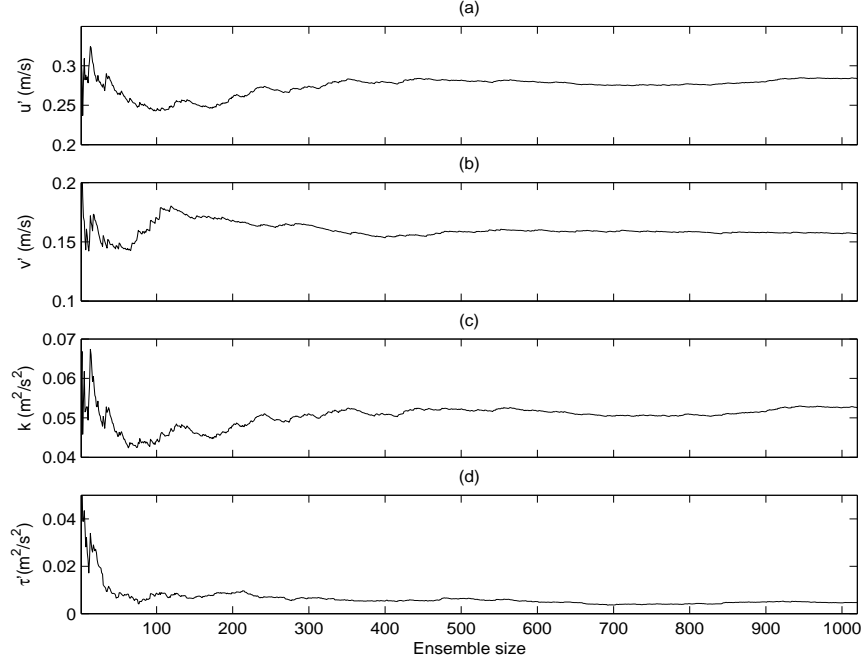
Figure 3.12: Convergence of turbulence statistics in the breaker region at $\tilde{x} \sim 0.51$, $\tilde{y} \sim 1.02$. (a) RMS horizontal turbulent velocity (u') (m/s), (b) RMS vertical turbulent velocity (v') (m/s), (c) turbulent kinetic energy (k) (m^2/s^2), and (d) Reynolds shear stress (τ') (m^2/s^2).

convergence rates at $\tilde{x} \sim 1.97$, $\tilde{y} \sim 0.42$. The convergence of the mean quantities are, everywhere, much faster than that of the turbulent quantities.

Figure 3.14 shows the spatial structure of the turbulence in the breaker shear layer. Note that only a sub-section of the entire domain is shown here for more detail and clarity. The spatial distribution shows that the turbulence is strongly anisotropic, in agreement with experimental observations of turbulence in laboratory generated spilling breaking waves (Govender *et al.*, 2002b; Stansby and Feng, 2005). As expected, the turbulence intensity decays rapidly over depth, only to increase near the bottom due to the turbulence generated in the boundary layer. The horizontal and vertical root mean square turbulent velocities in the shear layer are
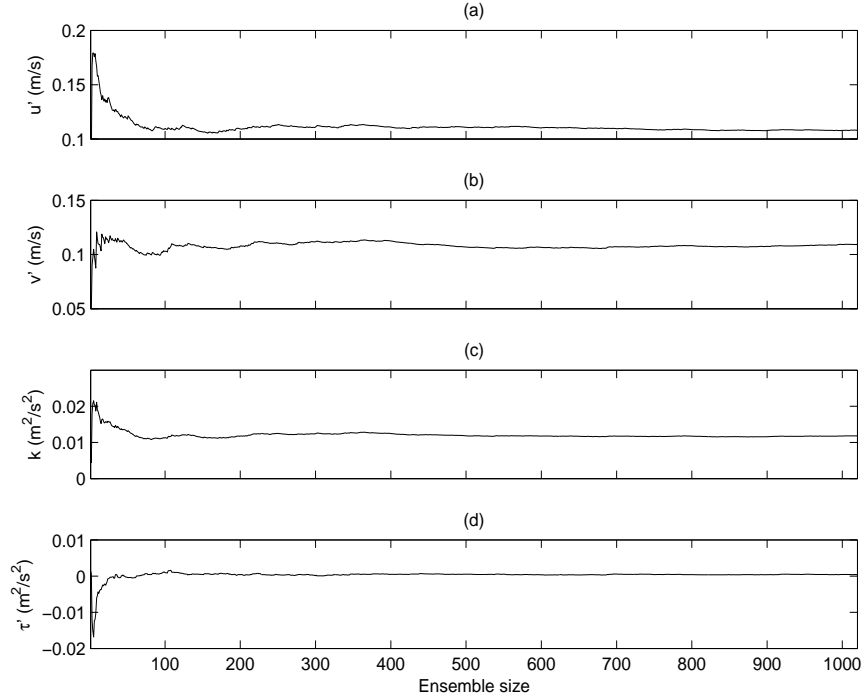
Figure 3.13: Convergence of turbulence statistics at mid-depth, $\tilde{x} \sim 1.97$, $\tilde{y} \sim$ 0.42. (a) RMS horizontal turbulent velocity (u') (m/s), (b) RMS vertical turbulent velocity (v') (m/s), (c) turbulent kinetic energy (k) (m²/s²), and (d) Reynolds shear stress (τ') (m²/s²).

of the same order as the mean velocities, with u' being slightly larger than v'. This shows that the flow field near the mean surface is dominated by turbulent fluctuations. The peak value for the horizontal turbulence intensity is found near the toe, at $\tilde{x} \sim 0.47$, $\tilde{y} \sim 1.0$. For the vertical turbulence velocity, the largest values occur at $\tilde{x} \sim 0.80$, $\tilde{y} \sim 1.06$. The turbulent kinetic energy has its peak value at $\tilde{x} \sim 0.47$, $\tilde{y} \sim 0.99$, at the toe. The reason for this is that the dominant contribution to k comes from the horizontal turbulence intensity, which originates from the intense shear at the toe of the breaker. The Reynolds shear stress is negative throughout the shear layer, implying an upward diffusion of momentum. The Reynolds shear stress has its largest value at $\tilde{x} \sim 0.59$, $\tilde{y} \sim 1$, downstream of the toe. The location

83
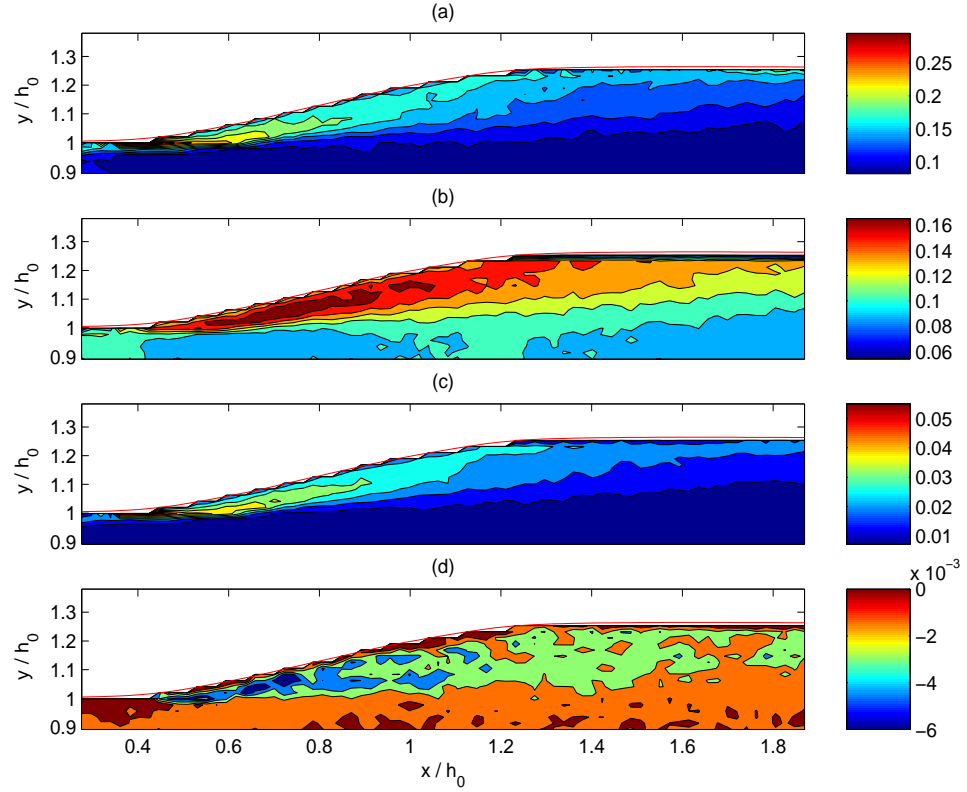
Figure 3.14: Turbulence structure. (a) RMS horizontal turbulent velocity (u') (m/s), (b) RMS vertical turbulent velocity (v') (m/s), (c) turbulent kinetic energy (k) (m²/s²), and (d) Reynolds shear stress (τ') (m²/s²). The solid red line is the ensemble-averaged free surface.

of the maximum negative mean simple shear $\left(\frac{\partial U}{\partial y}\right)$ occurs at $\tilde{x} \sim 0.41$, $\tilde{y} \sim 0.98$, indicating that in addition to the simple shear, there are extra strain rates such as streamline curvature which affect the Reynolds stress structure. This is discussed further in Chapter 4. In the following section, the Reynolds shear stresses in the roller and mixing layer regions are analyzed in more detail.
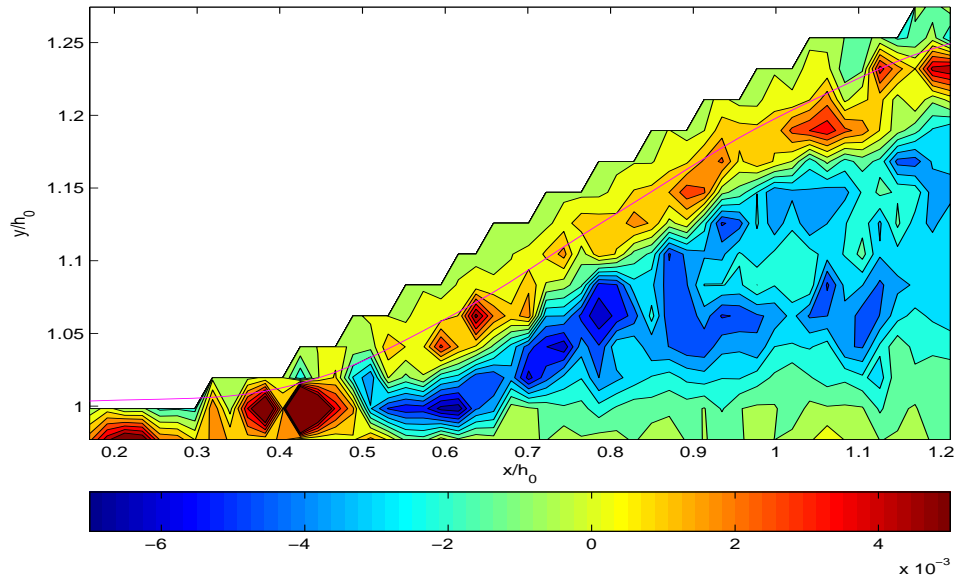
Figure 3.15: Reynolds shear stress in the roller region, τ' (m^2/s^2).

3.3.4 The roller region

Figure 3.15 shows that there is a region of positive Reynolds shear stress just below the mean surface, indicating a downward flux of momentum from the roller region into the mixing layer. The magnitudes of the Reynolds stress are, on average, smaller than the mixing layer values. The turbulent kinetic energy in the roller region is an order of magnitude smaller than in the shear layer. The horizontal and vertical turbulence intensities are qualitatively very similar to the turbulent kinetic energy distribution, and decay monotonically away from the mean surface toward $\gamma = 0$. They are also an order of magnitude smaller than their values in the mixing layer region. These results indicate that the roller is essentially a stagnant and weak eddy, in agreement with the findings of Cointe and Tulin (1994), who found that the area integrated circulation in the roller was almost negligible.

3.3.5 The mixing layer region

It is fairly well-established that there is an intense shear layer formed below a fully-formed, quasi-steady spilling breaker, which spreads downstream from the foot of the breaker. The dynamics of the breaker shear layer are different from those of a typical shear layer in several aspects. The outer boundary of the shear layer is marked by a turbulent interface with a strong density difference between air on one side, and water on the other. The localized effects of an adverse pressure gradient and streamline curvature, along with the entrained air and unsteadiness of the external flow, also modify the flow structure. There is still so little knowledge of the detailed turbulence structure of a breaking wave, that it is indeed a tempting and meaningful pursuit to search for similarities with well known turbulent flows, since established results can then be used as a starting point for a more detailed understanding and modeling of the complicated processes accompanying wave breaking. It should be kept in mind, that "for all we know, the turbulence below breakers does represent a special type of turbulent flow, which in spite of similarities with other known turbulent flows, has its own characteristics"(Svendsen, 1987). In the much simpler context of stationary hydraulic jumps, as already discussed, Rajaratnam (1965) has provided evidence that the hydraulic jump can be modeled as a wall jet. Banner and Phillips (1974) were the first to suggest that the turbulent flow downstream of the breaking region resembled a wake, which was confirmed by the results of Battjes and Sakai (1981). This was based on the observed downstream variations of the mean velocity defect, turbulence intensity and shear-layer thickness. The far field was analyzed sufficiently downstream from the physical origin of the shear layer, so that the flow had settled down to self-preservation. Peregrine and Svendsen (1978) were perhaps the first to suggest that the breaker region should be modeled as a mixing-layer. This was based on qualitative observations of bubble clouds which acted as tracer particles in experiments conducted with propagating

86
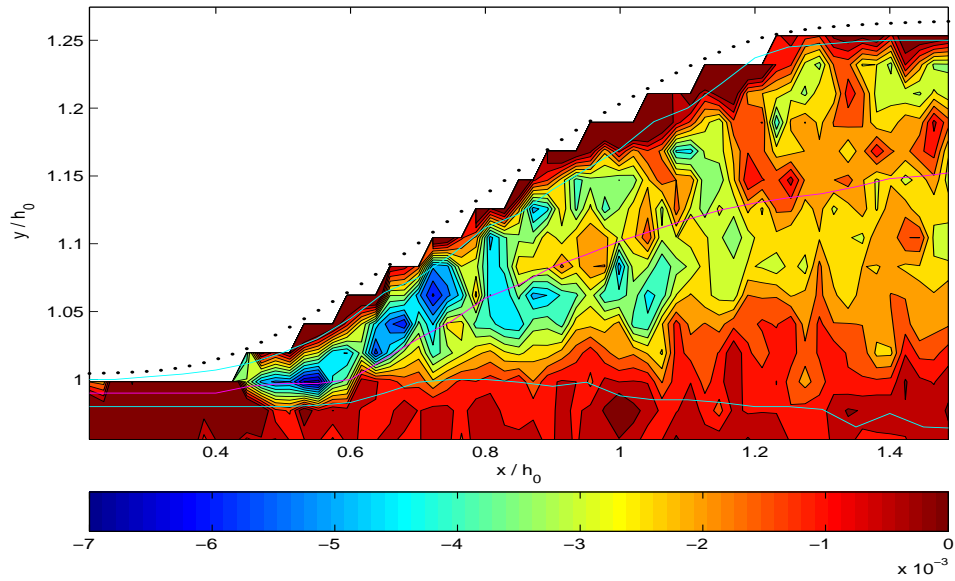
Figure 3.16: Reynolds shear stress, τ' (m^2/s^2) in the mixing layer. Black dotted line is the mean surface. The magenta line is the contour of maximum shear, and the top and bottom light blue lines are contours of $U_0 = 0.12$ m/s and $U_s = 0.74$ m/s, respectively.

breaking waves, hydraulic jumps and bores. They mention that other authors had earlier suggested the presence of a "mixing zone" in hydraulic jumps. Lin and Rockwell (1994) had found coherent vortical motions, and concentrated vorticity along a "mixing layer" originating from the toe. However, this was visualized in a frame of reference moving at half the free-stream velocity and the suggestion of a vortical motion in the mixing layer was, as noted by them, an artifact of the particular reference frame of observation. However, there has been no detailed experimental evidence for the suggested classification of the shear layer in a fully-formed breaker as a mixing layer.

In Figure 3.16, the detailed structure of the Reynolds shear stress in the shear layer below the mean surface (the black dotted line) is shown. The structural similarity of the main turbulent motion was compared with other plane shear flows, as

indicated by the parameters listed in Townsend (1976), but without any conclusive results. This is not unexpected, since the percentage difference in the listed parameters, from one type of flow to the other, is very small, and the scatter is attributed not just to contributions from large eddies, but also to errors of measurement. A more robust classification of the comparative structure of two-dimensional plane wakes, jets and mixing layers has been suggested by Tennekes and Lumley (1972) by describing the typical downstream variation of U_s, l and R_l. U_s is defined as the scale for the cross-stream variation of the streamwise mean velocity component, and for shear layers, is equal to the maximum free-stream velocity. l is the cross-stream length scale, defined as the distance from the center line to the location at which $(U - U_0)$ is equal to $\frac{1}{2}U_s$, where U_0 is the scale for the velocity of the mean flow in the streamwise direction. R_l is the local Reynolds number defined as $R_l \equiv \frac{\tilde{u}'l}{\nu}$, where $\tilde{u}'$ is the turbulence velocity scale, and ν is the kinematic viscosity. It is expected that for mixing layers, U_s is constant, and l and R_l increase linearly with downstream distance. In turbulent mixing layers, the turbulent region is separated from the irrotational region by irregularly distorted bounding curves as a consequence of entrainment. In a practical sense, a finite percentage value of the maximum magnitude of the Reynolds shear stress in the region of interest has to be chosen to define the boundaries of the mixing layer. At low values of τ' used to define the boundaries, the results were too noisy to allow any robust and conclusive arguments. This is evident from the complicated turbulent structure seen in Figure 3.16. The boundaries are chosen at the location where the Reynolds shear stress decayed to 10% of its maximum value ($\tau'_{max} \sim -0.0067$ m^2/s^2). The contours are shown as the light blue lines in Figure 3.16. It was found that the mean streamwise velocity contours of 0.12 m/s and 0.74 m/s fit the τ' contours reasonably well, as shown in Figure 3.16 and Figure 3.17. These values were approximately 10% of the maximum mean streamwise velocity in this region, and were chosen as U_0 and U_s respectively.
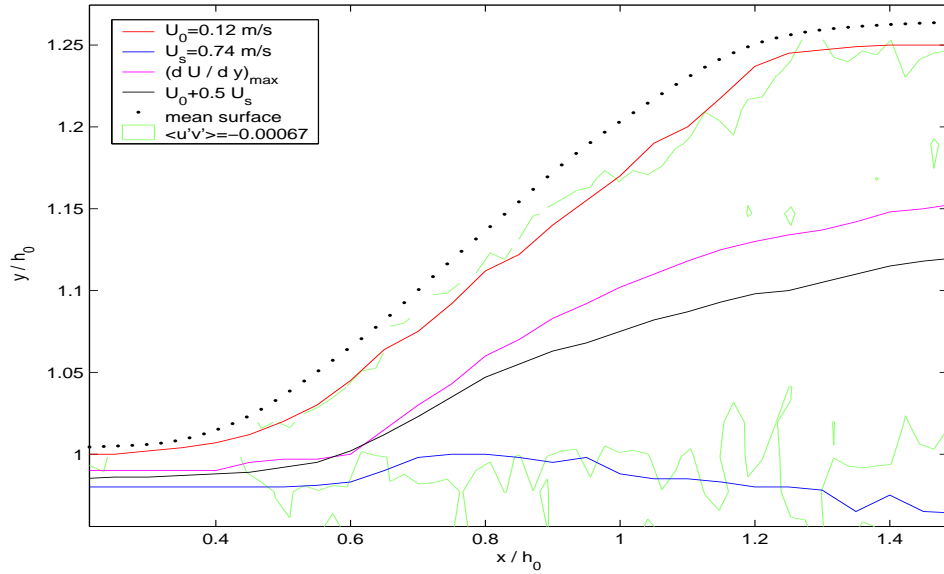
Figure 3.17: Contours defined in the mixing layer region. See text for description.

The constancy of U_s with downstream distance is thus automatically satisfied. The centerline of the layer was defined as the location of maximum shear, and is shown as the magenta line in Figure 3.17. The velocity contour for $U_l \equiv U_0 + \frac{U_s}{2} = 0.49$ m/s is shown as the black line. The length scale is thus calculated as the distance from this line to the centerline.

In the visualization studies with mixing layers done by Brown and Roshko (1974), the virtual origin for the downstream coordinate was defined based on characteristic thicknesses calculated from their density and velocity profiles. The intersection of a linear fit to these thicknesses with the x-axis yielded the virtual origin. A similar approach was used by Battjes and Sakai (1981) based on a linear fit to the calculated velocity defects. In the present case, a simpler visual approach is taken. By drawing tangents to the 10 % contours of the Reynolds stress, the location of their intersection is found at $\tilde{x}_0 \sim 0.4$, upstream of the toe. This seems a
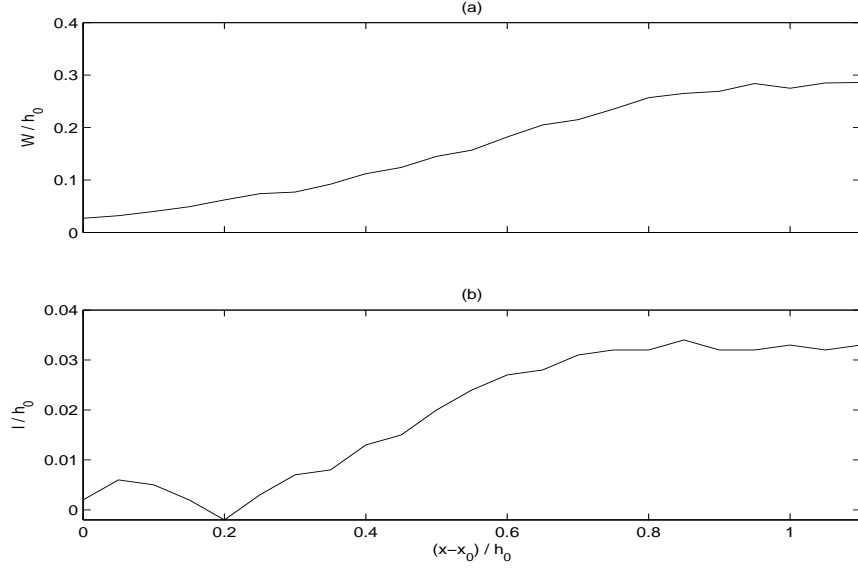
Figure 3.18: (a) Dimensionless width of the mixing layer , $\frac{W}{h_0}$, and (b) dimensionless length scale, $\frac{l}{h_0}$.

physically reasonable choice for the virtual origin, since the Reynolds shear stress reaches its characteristic value further downstream of this location. The width of the mixing layer, W, is calculated and made dimensionless with h_0. From Figure 3.18, in terms of the absolute coordinate $\tilde{x} = \left[0.4 + \left(\frac{x-x_0}{h_0}\right)\right]$, it is seen that there is a linear increase in the width until about $\tilde{x} \sim 1.2$, after which it becomes approximately constant. This is in good qualitative agreement with the spreading rate of mixing layers, where the "wedge" is known to spread in a linear fashion. The dimensionless length scale is shown in the bottom subplot. This shows a linear increase from $\tilde{x} \sim 0.6$ till $\tilde{x} \sim 1.2$ after which it attains a constant value. This indicates that the breaker shear layer can be classified as a mixing layer, with its origin downstream of the toe and extending downstream till it changes to a wake type flow. This transition occurs at approximately the location of the peak negative curvature.

90

Another parameter of interest is the ratio $\frac{W}{x-x_0}$, referred to as the growth rate by Brown and Roshko (1974). In Brown and Roshko (1974), the linear fit to the data for a density ratio of unity is

$$\frac{W}{x - x_0} = 0.38 \left[\frac{U_s - U_0}{U_s + U_0} \right]. \tag{3.17}$$

For $\frac{U_s - U_0}{U_s + U_0} = 0.72$ (U_s and U_0, here, are taken equivalent to U_1 and U_2 in their case), this gives $\frac{W}{x-x_0} = 0.27$. This is in good agreement with the mean value (averaged over the values from $\tilde{x} \sim 0.6$ to $\tilde{x} \sim 1.2$) for the growth rate in the present case, equal to 0.29. Even as the above results indicate, qualitatively and quantitatively, that the flow structure upstream of the toe bears resemblances to a mixing layer followed by a wake further downstream, a more robust quantification of the length scales can be obtained by an analysis of the coherent turbulent structures, and this is discussed in Chapter 5.

3.3.6   Entrainment

For free turbulent flows, the ratio of standard deviation to the mean value of the interface fluctuations ($R = \frac{\sigma(\eta)}{\eta_0}$) is a measure of the corrugations of the bounding surface, and in conjunction with the intensity of the interface vortices, gives a measure of the turbulent entrainment at the interface (Townsend, 1976). R is known to vary considerably depending on the turbulent flow regime, and since the definition of η_0 is dependent on the choice of the datum, it is first necessary to choose an appropriate length scale characterizing the surface fluctuations. The width of the intermittent region (where γ varies from 0 to 1) is chosen as η_0. The calculated entrainment ratio is shown in Figure 3.19 (b). It is noted that the turbulence entrainment for a free air-water interface (with a density ratio ~ 1000), approximately ranging between 0.05 and 0.25, is smaller than across a turbulent interface (between the irrotational and turbulent regions of the same fluid or comparable density fluids) for typical jets ($R \approx 0.22$) and wakes ($R \approx 0.38$). The order
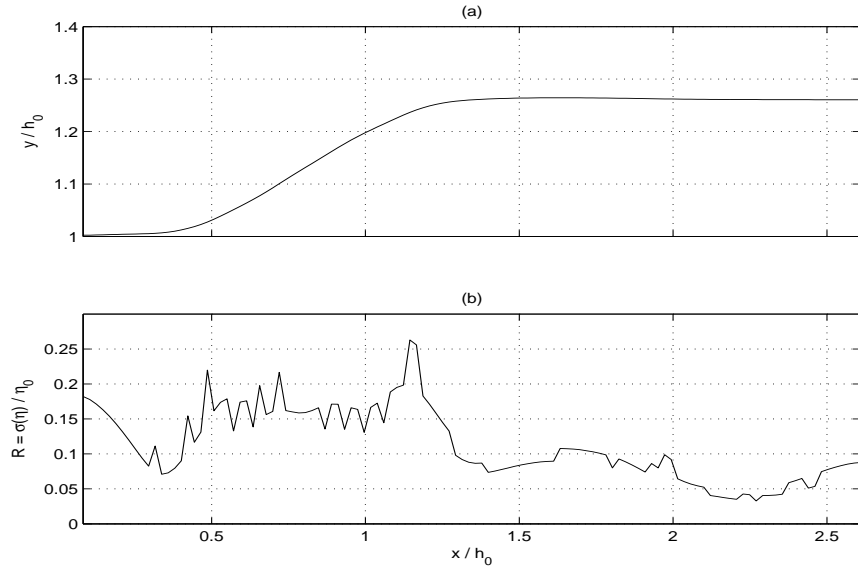
Figure 3.19: (a) Ensemble-averaged free surface, and (b) ratio of standard deviation to ensemble mean of the free surface, $R = \frac{\sigma(\eta)}{\eta_0}$.

of magnitude agreement between the present values for R and the values reported by Townsend (1976) (Table 6.2) is obviously dependent on the choice of η_0, which seems adequate for the present flow. The entrainment ratio is seen to increase into the breaker region, where it stays approximately constant, and then decreases further downstream. This gives a good qualitative insight into the variation of the intensity of the surface turbulence of the flow.

There are several factors which influence the entrainment. A qualitative, and admittedly simplified, argument can be made for the trends observed in R by looking at the curvature of the ensemble-averaged surface shown in Figure 3.3(c). A positive curvature implies concavity of the surface. Therefore, the normal pressure gradient (with the positive normal being directed away from the surface) is negative. This in turn implies an increase in entrainment downstream, since a parcel of entrained fluid encounters a favorable pressure gradient. The situation is reversed

for convexity, when the curvature is negative, leading to a positive pressure gradient which opposes entrainment. In the presence of an adverse pressure gradient, as in the present case, the influence of the curvature on the entrainment is reduced, compared to a zero-pressure-gradient case, since the outer region streamlines are less curved than the surface (Simpson, 1989). This might be a reason for the increase in entrainment taking place further upstream compared to the location of the peak positive curvature. Although the pressure was not directly measured, the mean pressure gradients can be calculated from the Cartesian momentum equations, where it is assumed that the flow is steady, i.e., $\frac{\partial U}{\partial t} \approx 0$, $\frac{\partial V}{\partial t} \approx 0$. Note that this neglects the quasi-steady dynamics associated with the toe oscillations. The horizontal and vertical pressure gradients are thus calculated as

$$\frac{1}{\rho}\frac{\partial P}{\partial x} \approx -U\frac{\partial U}{\partial x} - V\frac{\partial U}{\partial y} - \frac{\partial}{\partial x}\Big(<u'^2>\Big) - \frac{\partial}{\partial y}\Big(<u'v'>\Big), \qquad (3.18)$$

$$\frac{1}{\rho}\frac{\partial P}{\partial y} \approx -U\frac{\partial V}{\partial x} - V\frac{\partial V}{\partial y} - \frac{\partial}{\partial x}\Big(<v'^2>\Big) - \frac{\partial}{\partial x}\Big(<u'v'>\Big). \qquad (3.19)$$

P is the ensemble-averaged pressure. The streamwise and surface-normal gradients are given by

$$\frac{\partial P}{\partial n} = -\sin(\theta)\frac{\partial P}{\partial x} + \cos(\theta)\frac{\partial P}{\partial y}, \qquad (3.20)$$

$$\frac{\partial P}{\partial s} = \cos(\theta)\frac{\partial P}{\partial x} + \sin(\theta)\frac{\partial P}{\partial y}. \qquad (3.21)$$

As can be seen from Figure 3.20 (b), there is a strong adverse (positive) streamwise gradient of the specific pressure (per unit density), with its peak value located at $\tilde{x} \sim 0.42$, $\tilde{y} \sim 0.98$, which is slightly upstream of the toe. The sharp curvature of the surface is thus induced by the flow separation, which in turn is caused by the adverse pressure gradient. A short distance upstream of the peak value, the magnitude of the streamwise pressure gradient decreases drastically. This is typical of flows approaching separation, and is attributed to the rapid thickening of the layer as a separation point is approached (Townsend, 1976). The normal
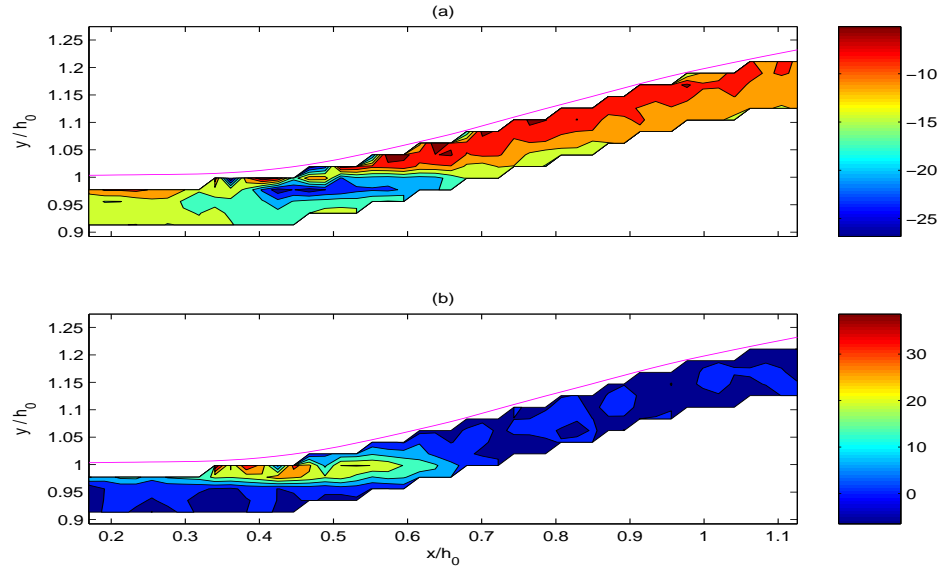
Figure 3.20: (a) Surface-normal gradient of the specific pressure, $\frac{\partial P}{\partial n}$ (m/s^2), and (b)surface-parallel gradient of the specific pressure, $\frac{\partial P}{\partial s}$ (m/s^2).

gradient has a negative peak at $\tilde{x} \sim 0.42$, $\tilde{y} \sim 0.98$. The overall rate of entrainment is also known to be typically enhanced by the presence of shearing of the mean flow which aligns the boundary vortices with the mean interface, hence, making them more efficient in engulfing the ambient fluid (Mobbs, 1968). A highly anisotropic turbulence also contributes to a larger entrainment.

It is known that the local air entrainment in the surface roller of a hydraulic jump occurs in a manner similar to that in a plunging jet (Kobus, 1991). The entrainment is followed by transport and detrainment. The detrainment rate is directly proportional to the transport capacity of the flow, among other parameters such as bubble size distribution. Even though the detrainment rate variation in the downstream direction depends on inflow conditions, the decay is rapid, with most of the air bubbles escaping back into the atmosphere. An estimate of the location of the maximum air entrainment at the surface can be obtained by considering an
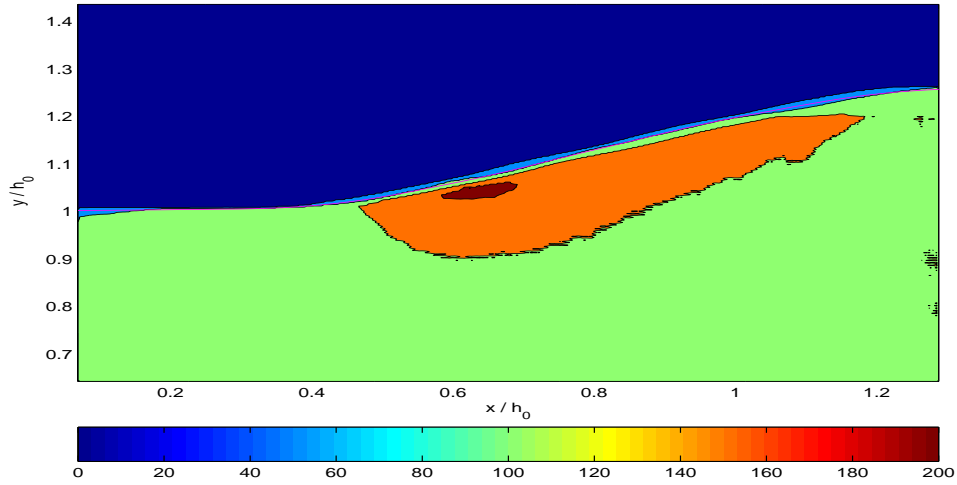
Figure 3.21: The ensemble-averaged filtered image showing the region of maximum air entrainment. Values are in grayscale pixel intensity (0-255). The solid magenta line is the ensemble-averaged free surface.

ensemble average of the processed raw images. Since the air bubbles show up as bright spots in any instantaneous image, the mean intensity map should give the location of the highest concentration of bubbles. It was observed that the scattering of the laser light from the bubbles and the clumping of seeding particles (which are silver coated to maximize laser light scattering), also show up as high-intensity regions. This should, however, decrease on ensemble averaging, because of their random spatial distribution. Even then, the footprints of the randomly distributed seeding particles are first removed by doing a morphological opening (Horebeek and Tapia-Rodriguez, 2001) on the instantaneous grayscale images. A disk-shaped structural element (which acts like a convolution kernel) with a radius of 2 pixels is used. A median filtering yields nearly identical results. The filtered image is then averaged over the entire ensemble, and the resulting intensity map is shown in Figure 3.21. The location of the peak intensity is seen to occur at $\tilde{x} = 0.64$ and $\tilde{y} = 1.03$.

This is in good agreement with visual observation of the location of the reverse-flow impingement at the surface, which was downstream of the toe. It is seen that the slightly lower intensity patch, characterized by the fluctuation of the breaking location, and the downstream bubble transport, extends, while decaying (due to bubble collapse and detrainment) downstream, to $\tilde{x} \sim 1.2$, where the curvature attains its maximum negative value.

3.4 Conclusions

The hydraulic jump set-up is in Froude similitude with saturated surf-zone breakers with an upstream Froude number of 1.2 and depth ratio $\xi=1.3$. The interface properties and PIV velocities are analyzed. An accurate estimation of the surface enabled the exclusion of spurious interfacial reflections in the images and ensured volume flux conservation in the domain. The intermittency factor representing the turbulent fluctuations of the interface was seen to fit theoretical profiles well, with accuracy increasing in the downstream direction. The geometric slope of the ensemble-averaged surface near the foot of the breaker agreed with the value used in numerical simulations of saturated spilling breakers, and a theoretical model of flow separation at a free surface.

An intense and thin shear layer originates near the toe of the breaker. The deceleration of the surface-parallel velocity has its largest (negative) value at the toe, but large values are found at the peak vorticity location, which is slightly upstream of the toe location. The surface-parallel pressure gradient is highly localized and has its peak, positive value, upstream of the toe, approximately coincident with the peak vorticity location. Breaking for gravity-dominated steady breakers is, thus, driven by a surface-parallel adverse pressure gradient and a streamwise flow deceleration, both occurring upstream of the toe location. Both effects force the shear layer to thicken rapidly, inducing a sharp free surface curvature change at the toe. The mean shear is finite at the mean surface. A weak reverse flow is found in the roller, above the mean

surface. The lower limit of the roller was estimated to be just below the mean surface. In this region, the mean surface-normal velocity was positive, indicating entrainment of water from below. This is in good agreement with the "entraining plume" model of Longuet-Higgins and Turner (1974). Consequently, the lower boundary of the roller cannot be a mean streamline. Therefore, the roller topology in the present case is different from the concept of an isolated recirculating eddy bounded on the top by the mean surface and on the bottom by a dividing streamline. As noted by Banner and Phillips (1974), and implemented in the present study, it is essential to replace the idea of a mean surface in the roller by an intermittency zone.

The convergence of turbulence statistics was examined, and the ensemble size was found large enough to yield stable estimates. The turbulent kinetic energy is maximum at the toe, coincident with the peak mean shear location. The Reynolds shear stress is positive just below the mean surface, signifying the downward transfer of momentum from the roller region, into the shear layer. In the shear layer, the Reynolds shear stress is negative, indicative of an upward diffusion of momentum from the nearly irrotational flow below. The structural similarity of the turbulence structure in the shear layer was compared to those of well-known plane shear flows. The breaker shear layer is seen to resemble a plane mixing layer; the width of the layer and the length scale grow linearly with distance from the toe, until they become constant around the location of the maximum negative curvature, where-after, the flow resembles a wake. The mean value of the non-dimensional growth rate in the mixing layer is found to be in good agreement with values found earlier by Brown and Roshko (1974).

Chapter 4

THE THEORETICAL MODEL

Mathematics is not a deductive science – that is a cliche. When you try to prove a theorum, you do not just list the hypotheses, and then start to reason. What you do is trial and error, experimentation, and guesswork.

Paul R. Halmos

4.1 Introduction

In a recent review of spilling breakers, Duncan (2001) states that "theoretical models of spilling breakers are rare". As he mentions, they are rarer still for fully formed unsteady breakers, and as will be seen below, virtually non-existent in providing a description for the turbulent flow in the breaker region itself. The complicated physical processes involved in a two-dimensional form of a quasi-steady spilling breaker have already been observed in Chapter 3. In addition to the fully turbulent and two-phase nature of the breaker region, the surface intermittency precludes the straight-forward application of Reynolds averaging techniques. The significance of intermittency dynamics toward a meaningful interpretation of the turbulent and mean flow structure will be discussed further within the theoretical framework in this chapter. In this section, a chronological summary, by no means complete, is given of the theoretical developments that have focussed not just on the incipient stages of breaking but also on an analytic description of the breaker region
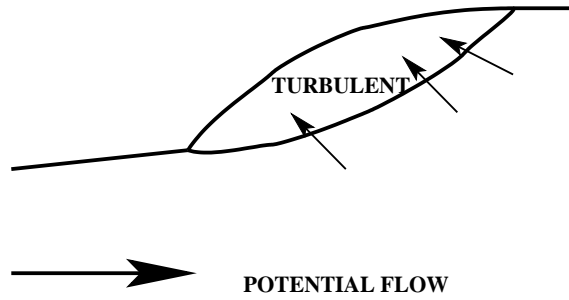
Figure 4.1: Schematic representation of the entraining plume model of Longuet-Higgins and Turner (1974). Adapted from MS83.

in fully formed spilling breakers. The major features of each model are discussed leading up to the motivation behind the development of the present model.

It was Longuet-Higgins (1973) who first proposed a simple model for the local turbulent flow near the forward edge of a steady spilling breaker or a hydraulic jump, which, within the context of his model, are comparative flows marked by flow separation at the discontinuity in the slope of the free surface. The significant point in the model was its approach in treating certain regions of the flow as laminar and others as turbulent, the dynamics of the latter being represented by an eddy viscosity. A balance was assumed between the Reynolds stresses and gravity in the equations of motion for the mean flow. The effect of air entrainment was included in the solution for the surface profile in the turbulent wedge originating from the point of discontinuity. Non-hydrostatic pressure was suggested to be important near the toe. Banner and Phillips (1974) examined the incipient spilling breaking conditions in the presence of a wind drift, and based on laboratory observations, suggested simple properties of the post-breaking flow. By integrating the vorticity equation in a small surface-drift dominated viscous layer near the surface, they found that the wind drift substantially reduced the incipient breaking wave-height compared to Stokes' limiting irrotational wave. From their experimental observations, they

suggested that the breaking region had no stagnation point as proposed by Longuet-Higgins (1973). Instead, there was an intermittent zone in the breaking eddy marked by a low velocity tumbling region immediately in front of the crest. Remarkably, perhaps unknown to Banner and Phillips (1974), in that same year, and in the same journal, Longuet-Higgins and Turner (1974) proposed the 'entraining plume' model which treated the spilling breaker as a turbulent gravity current riding down the forward slope of a wave while entraining laminar flow from below. A schematic representation of the flow is shown in Figure 4.1. The entrainment was modeled by a finite tangential stress at the boundary between the turbulent and laminar flows. This was also the first attempt at describing the unsteady motion of the toe front based on the 'starting plume' model of Turner (1962). The surface slope and the magnitude of the downslope velocity were found to be in agreement with laboratory observations of spilling breakers.

In a deviation from the model of Longuet-Higgins and Turner (1974), and motivated by the observations of Peregrine and Svendsen (1978), MS83 developed a theoretical model for the mean velocity field and surface profiles for steady bores and hydraulic jumps. The turbulence was not assumed to be concentrated on the front face of the wave, but to spread downstream in a wedge originating at the toe of the breaker front (Figure 4.2). The turbulence was modeled by a simplified $k - \epsilon$ model allowing for non-equilibrium in the turbulent kinetic energy. This was important in including the effects of surface-generated turbulence. A cubic polynomial profile was assumed for the mean horizontal velocity in the turbulent wedge with depth-uniform flow in the irrotational flow underneath. The coefficient of the cubic term was obtained by fitting the velocity profiles to available data. Static pressure was assumed and the equations of motion were satisfied "at large" by integrating them over the turbulent region and the total depth. The accuracy of the velocities and shear stresses near the surface could not be evaluated because

100
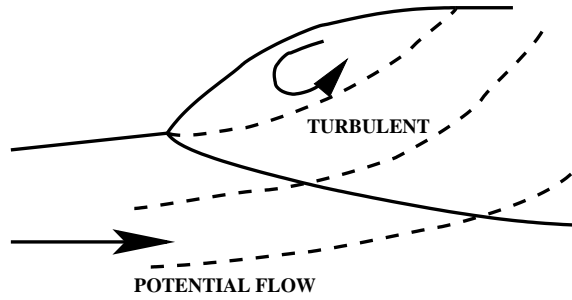
Figure 4.2: Schematic representation of the hydraulic jump/bore model of MS83. Adapted from MS83.

of lack of data. Svendsen and Madsen (1984) extended this model to unsteady bore motion over varying water depth even though the turbulence modeling and the cubic velocity profile remained the same. The governing partial differential equations were found to be of hyperbolic type. The characteristics at the toe were found analytically. In a major difference with the model of Longuet-Higgins (1973), where the toe was considered a stagnation point, the difference between the surface velocity in the turbulent region and the irrotational velocity in the upstream flow was found to be finite at the toe and much smaller than the phase speed.

Motivated by the experimental results of Duncan (1981), Cointe (1987), Tulin and Cointe (1988) and Cointe and Tulin (1994) provided a theoretical framework for steady breakers by implementing the concept of an essentially stagnant, aerated eddy riding on the front face of the wave, sustained by the turbulent shear stresses between the eddy and the underlying flow. A mixing layer model for the turbulent wedge was explicitly included, with a turbulent wake extending behind the breaker region. It was shown, again based on the measurements of Duncan (1981), that the dynamic pressure as a proxy for the motions within the eddy was an order of magnitude smaller than the hydrostatic pressure; hence the "stagnant" nature of the eddy. A global balance of the forces on a breaker was derived to analyze the

stability of the breaker with respect to the toe oscillations. Strong breakers were shown to be stable. Explicit representations of the turbulence were not included.

To explain the striking preliminary results from the detailed experimental work done by Duncan *et al.* (1994) in investigating incipient breaking of surface-tension dominated breakers, Longuet-Higgins (1994), Longuet-Higgins and Cleaver (1994), and Longuet-Higgins *et al.* (1994) showed that the capillary waves seen on the front face of the wave were due to shear flow instabilities. The role of flow separation due to the sharp curvature of the toe was significant in describing the source of the capillary instabilities, which in turn, were a strong source of vorticity capable of producing recirculating zones ("rollers") in the crest. Alluding to the later stages of evolution into a fully-formed breaker, Longuet-Higgins (1994) suggested the development of turbulence in spilling breakers in the form of a layer of vortices which, by merging, would finally form a mixing layer. This was conceptually addressed later by Longuet-Higgins (1998b). A model for a horizontal shear flow with a free surface was developed and the instabilities were analyzed using linear stability analysis. The analytically predicted wavelengths were found to be comparable to the fluctuations of surface elevation in the experimental data of Coakley and Duncan (1997).

The first set of Reynolds averaged equations for turbulent free-surface flows with appreciable surface fluctuations was developed recently by Hong and Walker (2000) as an extension of the low Froude number model developed by Walker (1997). The model was specifically aimed at investigating the origin of the surface current, which is the large outward velocity that exists in a thin layer adjacent to the surface. A significant aspect of the model was its treatment of the free-surface turbulent flow as a two-fluid flow separated by an interface. The departure from the conventional Reynolds averaged equations appeared in the additional terms incorporating the intermittency factor and representing the average effect of the forces acting instantaneously on the free surface. No turbulence model was included, and an order

102

of magnitude analysis was performed to show the importance of Reynolds stress anisotropy and interface fluctuations in determining the magnitude of surface current. The model was not applied to free surface turbulence generated by breakers.

From the summary outlined above, several things become clear. There are no existing theoretical models for modeling the dynamics of the highly unsteady two-phase turbulent flow generated in spilling breakers. The recurring underlying concepts in the simplified "bulk" models are those of a "roller" or "stagnant eddy" near the crest, the turbulent wedge in the form of a breaker shear layer/mixing layer originating from the toe due to flow separation, and a wake further downstream. As discussed in Chapter 3, the roller model, in which the turbulent region is modeled as a separate flow region passively riding the wave crest, is seen to be only a partial solution as it is evident that the fluid content of the roller itself is continually mixing with the rest of the turbulent flow. It is also clear that the intermittency due to the surface fluctuations and the inherent unsteadiness of the breaking process have to be taken into account. M. Brocchini and D. H. Peregrine have recently initiated a very detailed theoretical investigation into the dynamics of free-surface turbulence, with a final goal of providing a theoretical description of spilling breaking waves (BP1,BP2). A three-layer system for the breaking wave is adopted, where the top surface-layer represents the two-phase flow in the intermittent region near the fluctuating broken interface. The middle layer is the single phase turbulent layer, which is the focus of this chapter. The flow underneath the middle layer is assumed to be irrotational. Part 2 focusses on the integral formulations of the governing equations of motion in the liquid phase. After suitable conditional averaging techniques are applied accounting for the intermittency, the equations are integrated across the surface layer to yield boundary conditions at the upper boundary of the single phase layer. Simplified versions of the boundary conditions are derived in Brocchini (2002) (hereafter MB02) for weakly-splashing flows assuming a thin surface layer. Results

from both BP2 and MB02 will be discussed and implemented in this chapter. It is stressed that the model is built for unsteady breaking waves, and the hydraulic jump as a steady breaker provides the simplest case for testing the model. Wherever possible, the theoretical developments will be tested with present data.

In the following sections, a detailed theoretical description is provided for the dynamics of the turbulent thin layer which is generated at the crest of spilling breaking waves. A large part of the material in the derivation of the governing equations in section 4.2 and the scaling of the equations in section 4.4 is borrowed, while appropriately modified in context, from Brocchini (1996) by permission of the author, and is provided here for continuity purposes and increased clarity in understanding the subsequent developments. The main new features of the present model include a correct representation of two-phase flow near the surface, curvature, unsteadiness, and local rotation which are all inherent to the dynamics of the layer of turbulent flow. The motivation behind the emphasis on streamline curvature will be discussed later. In the next section, the equations of mass and linear momentum are introduced in covariant form. In the same section, the geometry used to analyze the thin layer of turbulence is given together with suitable curvilinear coordinates. The equations are derived in terms of physical variables for the specific coordinate system. Further, turbulent averaging is introduced and Reynolds-type equations are obtained for the flow. Based on Boussinesq's eddy viscosity concept, a simple $k - \varepsilon$ closure for the Reynolds' stresses is used. A first-order closure is adopted which allows for local non-equilibrium of turbulent kinetic energy. In section 4.4, scaling arguments are introduced in terms of geometric and kinematic parameters to simplify the equations. Three different flow regimes are analyzed in dependence of the kinematic parameter, which decrease from the leading edge ('breaker regime'), where the turbulence intensities are assumed comparable to the mean flow velocity, towards the trailing end ('wake regime'). The final equations together with

104

the boundary conditions discussed in BP2 and MB02 provide the basis for different types of modeling of the spilling breaker dynamics. In principle, the equations can be directly integrated provided that suitable closures are defined. However, resolution of the flow in both streamwise and crossflow directions would require a great computational effort. Therefore, in section 4.5, a profile for the mean velocity is assumed based on experimental observations, and the model solution is provided through matching conditions at the boundaries of the layer. In section 4.7, the equations are integrated in the cross-flow direction, which provide boundary conditions for the irrotational flow underneath.

4.2 The equations of motion

The tools of curvilinear tensor analysis are used because they provide the most direct method by which equations valid for curvilinear coordinate systems may be derived (Aris, 1962; Richmond *et al.*, 1986). The material derivative of a general function A, be it either a scalar or a tensor function of both space and time, is given by

$$\frac{DA}{Dt} = \frac{\partial A}{\partial t} + A_{,j}\frac{d\xi^j}{dt}, \tag{4.1}$$

where ξ^j are general curvilinear coordinates, and the comma refers to partial covariant differentiation. Defining $u^j = d\xi^j/dt$ as the components of the velocity vector, the expression for the material derivative becomes,

$$\frac{DA}{Dt} = \frac{\partial A}{\partial t} + A_{,j}u^j. \tag{4.2}$$

If the general tensor A represents a velocity, then equation (4.2) may be written in terms of contravariant velocity components as:

$$a^i = \frac{Du^i}{Dt} = \frac{\partial u^i}{\partial t} + u^j u^i_{,j} + u^j\left[\frac{\partial u^i}{\partial \xi^j} + \Gamma^i_{jk}u^k\right], \tag{4.3}$$

where Γ^i_{jk} is the Christoffel symbol of the second kind, which essentially represents partial derivatives of basis vectors of the chosen curvilinear coordinate system

105

with respect to coordinate variables. The above equation, which gives the fluid acceleration in general tensor form, assumes a much simpler form when considering orthogonal coordinates and physical variables denoted by $u(i)$:

$$a(i) = \frac{\partial u(i)}{\partial t} + \sum_{j=1}^{3} \frac{u(j)}{h_j} \left[\frac{\partial u(i)}{\partial \xi^j} + \frac{u(i)}{h_i} \frac{\partial h_i}{\partial \xi^j} - \frac{u(j)}{h_i} \frac{\partial h_j}{\partial \xi^i} \right], \quad (4.4)$$

in which the scale factors h_i are linked with the metric tensor g_{ij} by $g_{ii} = h_i^2$.

Mass conservation for an incompressible fluid of constant density ρ takes the following form when considering orthogonal coordinates and physical variables $u(i)$:

$$\frac{\partial}{\partial \xi^i} [h_j h_k u(i)] + \frac{\partial}{\partial \xi^j} [h_i h_k u(j)] + \frac{\partial}{\partial \xi^k} [h_i h_j u(k)] = 0, \quad (4.5)$$

where i, j, k are taken in cyclic order. Similarly, Euler's equation (conservation of linear momentum) reads:

$$\frac{\partial u(i)}{\partial t} + \sum_{j=1}^{3} \frac{u(j)}{h_j} \left[\frac{\partial u(i)}{\partial \xi^j} + \frac{u(i)}{h_i} \frac{\partial h_i}{\partial \xi^j} - \frac{u(j)}{h_i} \frac{\partial h_j}{\partial \xi^i} \right] = F(i) - \frac{1}{\rho h_i} \frac{\partial p}{\partial \xi^i}, \quad (4.6)$$

in which $F(i)$ and p are respectively the components of eventual body forces and the pressure. These equations can be made specific for the model under investigation once the particular set of orthogonal coordinates is chosen.

A model following the description of a spilling breaker given in the introduction is set up for representing the dynamics of the turbulent flow. Turbulence is thus considered to be generated and to develop as for a free shear layer or a mixing layer, except that on one side of the mixing layer, fluid has an initial adverse velocity due to the reverse flow from breaking. The shear layer departs from the wave irrotational flow at the foot of the breaker. In this model, three different time scales are of relevance. They are the time scale for the water particles to cross the layer, the time scale for the evolution of the layer shape and the time scale for the evolution of the shape of the underlying wave (Peregrine, 1992). Even if the spilling breaker is said to be quasi-steady because its evolution occurs at a larger time scale
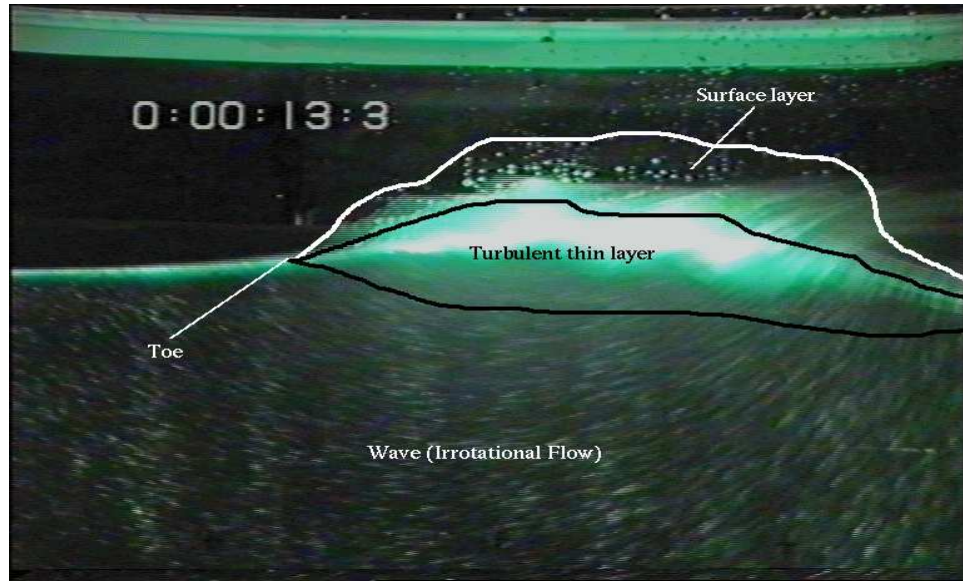
Figure 4.3: Global geometry adopted in the model for the system wave - turbulent thin layer - surface layer. Photograph taken at the Fluid Dynamics unit of the University of Edinburgh. (Courtesy of T.C.D. Barnes.)

than that for a particle to cross the layer, it can be considered unsteady when referring to the motion of the wave because the evolution of the wave shape occurs at a larger time scale than the evolution of the thin layer. The geometry used in the present model for the wave-turbulent thin layer system is shown in Figure 4.3. The surface layer region represents that portion of the turbulent thin layer where the instantaneous free surface fluctuates. Note that in the presence of intense free surface turbulence leading to a break-up of the surface, air-entrainment and the ejection of water particles often lead to a two-phase surface layer.

The proposed model is valid for a two dimensional unsteady spilling breaker, and the assumption of quasi-two-dimensional flow, already introduced in BP2, means that the flow is analyzed in a vertical plane by means of a set of two dimensional orthogonal coordinates which is built based on Moore (1978). Consider a smooth, time-dependent, two-dimensional curve $\Upsilon(t)$ (see Figure 4.4) given parametrically

107
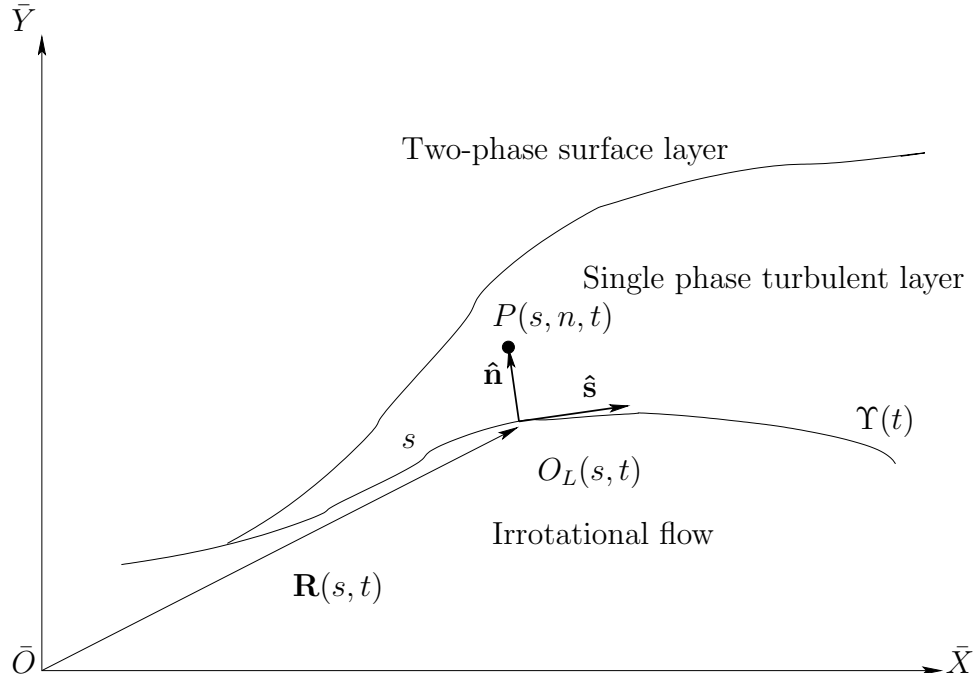
Figure 4.4:   Geometry and coordinates used for the turbulent thin layer.

by the equation

$$\mathbf{r} = \mathbf{R}(\alpha, t), \tag{4.7}$$

where t is time and α is an arbitrary parameter. The curve $\Upsilon(t)$ represents either the wave free surface when no breaking occurs, or an interface between the irrotational flow region below and the region containing turbulent flow above. Due to the typical entrainment of irrotational flow into the region of turbulence, the curve $\Upsilon(t)$ is not a material surface when turbulence is present, i.e., water particles which at time $t = t_0$ are on the surface at a later time $t = t_1$ will not be on the surface any more.

If a parameter s describing the arc length along $\Upsilon(t)$ is introduced, the curve is parametrically given by:

$$\mathbf{r} = \mathbf{R}(\alpha(s), t). \tag{4.8}$$

The dynamics/kinematics for $\Upsilon(t)$ are given in terms of $\mathbf{R}(\alpha(s), t)$, and depend on the dynamics of the turbulent flow above and of the irrotational flow below.

108

While the equations for the dynamics of the turbulent layer are given in the next sections, modeling of the dynamics of the irrotational wave is not considered here. However, it is anticipated that the turbulence/wave interaction occurring at the lower boundary of the turbulent layer is to be represented by mass entrainment across the boundary and by extra pressure at the boundary. These extra terms are to be incorporated respectively in the kinematic and in the dynamic boundary condition for the irrotational wave.

With each "convected point" $O_L(\alpha(s), t)$ of the curve, a unit tangent vector $\hat{\mathbf{s}}(\alpha(s), t)$ to the curve can be defined by

$$\hat{\mathbf{s}} \equiv \frac{\partial \mathbf{R}}{\partial s} \quad \text{so} \quad \frac{\partial \mathbf{R}}{\partial \alpha} = \frac{\partial s}{\partial \alpha} \frac{\partial \mathbf{R}}{\partial s} = \frac{\partial s}{\partial \alpha} \hat{\mathbf{s}}. \tag{4.9}$$

A unit normal vector is given by $\hat{\mathbf{n}}(\alpha(s), t)$. For the sake of simplicity, much of the following analysis is carried out by referring differential quantities to the arc length s rather than to the convected coordinate α. The position of each convected point $O_L(s, t)$ in the fixed frame of reference $\bar{O}\bar{X}\bar{Y}$ is given by

$$\mathbf{r} = \mathbf{R}(s, t). \tag{4.10}$$

Any general point, P, in the turbulent layer is assumed to be close enough to Υ such that there is only one normal to the curve passing through O_L towards P, and the distance $O_L P = n$ is also defined. This is positive if P is on the left hand side of Υ, i.e., above Υ. Moreover, the position of the point P within the thin layer is determined by two coordinates, $\xi^1 = s$, and $\xi^2 = n$, which form a mobile curvilinear coordinate system. This sort of coordinate system is widely used in the analysis of boundary layers (see Goldstein, 1938).

The curve Υ, together with the two vectors $\hat{\mathbf{s}}$ and $\hat{\mathbf{n}}$, is analogous to a Cosserat curve in three dimensions (Aris, 1962). With this convention, the position of P in $\bar{O}\bar{X}\bar{Y}$ is

$$\mathbf{r}_P(s, n, t) = \mathbf{R}(s, t) + \hat{\mathbf{n}}(s, t)n. \tag{4.11}$$

109

Differentiation of (4.11) with respect to the local coordinates s and n gives

$$d\mathbf{r}_P = \frac{\partial \mathbf{R}}{\partial s}ds + n\frac{\partial \hat{\mathbf{n}}}{\partial s}ds + \hat{\mathbf{n}}dn. \qquad (4.12)$$

The Serret-Frenet formulae for a plane curve are

$$\frac{\partial \hat{\mathbf{s}}}{\partial s} = \kappa\hat{\mathbf{n}} , \qquad \frac{\partial \hat{\mathbf{n}}}{\partial s} = -\kappa\hat{\mathbf{s}}. \qquad (4.13)$$

Note that the unit normal vector is defined by the local curvature. Since $\hat{\mathbf{s}} \cdot \hat{\mathbf{s}} = 1$, $\hat{\mathbf{s}} \cdot \frac{d\hat{\mathbf{s}}}{ds} = 0$, so that $\frac{d\hat{\mathbf{s}}}{ds}$ is orthogonal to $\hat{\mathbf{s}}$, and is called the "curvature vector". $\kappa = \left|\frac{d\hat{\mathbf{s}}}{ds}\right|$ is the local curvature. Theerefore, the unit normal is defined as $\hat{\mathbf{n}} \equiv \frac{d\hat{\mathbf{s}}}{ds}/\left|\frac{d\hat{\mathbf{s}}}{ds}\right|$. (4.12) can be written as

$$d\mathbf{r}_P = \hat{\mathbf{s}}(1 - \kappa n)ds + \hat{\mathbf{n}}dn. \qquad (4.14)$$

From equation (4.14), the infinitesimal distance between two points P and Q can be obtained as

$$ds^2 = d\mathbf{r} \cdot d\mathbf{r} = g_{ij}d\xi^i d\xi^j. \qquad (4.15)$$

It is evident that the coordinate system is orthogonal since $g_{ij} = 0$ for $i \neq j$. Note that orthogonality is implicitly assumed in equation (4.13) since torsion is zero for plane curves (Aris, 1962).

The scale factor h_i are the ratios of distance to coordinate difference if an infinitesimal displacement is made in only the ξ^i coordinate. Since

$$\frac{d\mathbf{r}_P}{ds} = (1 - \kappa n)\hat{\mathbf{s}}, \quad \text{and} \qquad (4.16)$$

$$\frac{d\mathbf{r}_P}{dn} = \hat{\mathbf{n}}, \qquad (4.17)$$

$h_1 = (1 - \kappa n)$ and $h_2 = 1$. It has been assumed that the scale parameter $(1 - \kappa n) \neq 0$ within the fluid. The mobile curvilinear coordinate system defines unit contravariant basis vectors $\mathbf{e}^j$ such that

$$\mathbf{e}^1 = \frac{\hat{\mathbf{s}}}{(1 - \kappa n)} \quad \text{and} \quad \mathbf{e}^2 = \hat{\mathbf{n}}. \qquad (4.18)$$

110

The gradient vector is given by

$$\nabla = \left(\frac{1}{(1-\kappa n)} \frac{\partial}{\partial s}, \frac{\partial}{\partial n} \right), \tag{4.19}$$

and the angular velocity $\Omega(s,t)$ of the local frame of reference $(\hat{\mathbf{s}}, \hat{\mathbf{n}})$ at a point with fixed s coordinate is given through one of the following equivalent relations:

$$\frac{\partial \hat{\mathbf{n}}}{\partial t} = -\Omega \hat{\mathbf{s}}, \qquad \hat{\mathbf{s}} \cdot \frac{\partial \hat{\mathbf{n}}}{\partial t} = -\Omega = -\hat{\mathbf{n}} \cdot \frac{\partial \hat{\mathbf{s}}}{\partial t}, \qquad \frac{\partial \hat{\mathbf{s}}}{\partial t} = \Omega \hat{\mathbf{n}}. \tag{4.20}$$

The only non-vanishing Christoffel symbols for this coordinate system are

$$\Gamma_{21}^1 = \Gamma_{12}^1 = \frac{1}{h_1} \frac{\partial h_1}{\partial \xi^2} = -\frac{\kappa}{(1-\kappa n)}, \quad \text{and} \quad \Gamma_{11}^2 = -\frac{h_1}{h_2^2} \frac{\partial h_1}{\partial \xi^2} = \kappa(1-\kappa n). \tag{4.21}$$

The velocity vector of any point P in the layer with given coordinates (s,n) is given by

$$\mathbf{u}_P = \frac{\partial \mathbf{r}_P}{\partial t} = \frac{\partial \mathbf{R}}{\partial t} + n \frac{\partial \hat{\mathbf{n}}}{\partial t} = \frac{\partial \mathbf{R}}{\partial t} - n\Omega \hat{\mathbf{s}}, \tag{4.22}$$

and the flow velocity inside the layer and relative to the generic point P is given by $\mathbf{u}_L = (\mathcal{U}(s,n,t), \mathcal{V}(s,n,t))$.

Therefore, the flow velocity at a point P with respect to the fixed frame of reference $\bar{O}\bar{X}\bar{Y}$ is

$$\mathbf{u}(s,n,t) = \frac{\partial \mathbf{R}}{\partial t} + n \frac{\partial \hat{\mathbf{n}}}{\partial t} + \hat{\mathbf{s}}\mathcal{U} + \hat{\mathbf{n}}\mathcal{V} = \hat{\mathbf{s}}\left(\hat{\mathbf{s}} \cdot \frac{\partial \mathbf{R}}{\partial t} + \mathcal{U} - n\Omega \right) + \hat{\mathbf{n}}\left(\hat{\mathbf{n}} \cdot \frac{\partial \mathbf{R}}{\partial t} + \mathcal{V} \right) = \hat{\mathbf{s}}u(1) + \hat{\mathbf{n}}u(2), \tag{4.23}$$

and can be written in the form

$$\mathbf{u} = \mathbf{u}_L + \frac{\partial \mathbf{R}}{\partial t} - \mathbf{u}_\Omega. \tag{4.24}$$

$\mathbf{u}_L = (\mathcal{U}, \mathcal{V})$ is the local flow velocity relative to P. The symbols $(\mathcal{U}, \mathcal{V})$ are written in calligraphic style to distinguish them from the physical variables and to signify that the flow velocity is made out of two contributions (mean and turbulent fluctuations) as shown in the next section. Finally, $\mathbf{u}_\Omega = (n\Omega, 0)$ is the velocity associated with the rotation of the local frame of reference. This shows that rotation is implicit

111

in the definition of the velocity in this coordinate system, whereas the effects of curvature are felt through the scale factor. The effects of this will be discussed further.

The continuity equation in physical components can be specified for the two-dimensional case from equation (4.5),

$$\frac{\partial[h_2 u(1)]}{\partial \xi^1} + \frac{\partial[h_1 u(2)]}{\partial \xi^2} = 0. \tag{4.25}$$

Substituting for the physical components $u(i)$ of the velocity vector given by equation (4.23), and using the Serret-Frenet formulae (4.13) gives

$$\frac{\partial \mathcal{U}}{\partial s} + \frac{\partial \left[(1 - \kappa n)\mathcal{V}\right]}{\partial n} = n \frac{\partial \Omega}{\partial s}. \tag{4.26}$$

In a similar fashion, the two equations for the conservation of linear momentum are found with a little more effort. In equation (4.6), the left hand side for the component $i = 1$ is simplified using equations (4.16) which define the scaling parameters h_1 and h_2:

$$
\begin{aligned}
a(1) &= \frac{\partial u(1)}{\partial t} + \frac{u(1)}{h_1}\frac{\partial u(1)}{\partial \xi^1} + \frac{u(2)}{h_2}\left[\frac{\partial u(1)}{\partial \xi^2} + \frac{u(1)}{h_1}\frac{\partial h_1}{\partial \xi^2}\right] \\
&= \frac{\partial u(1)}{\partial t} + u(2)\frac{\partial u(1)}{\partial \xi^2} + \frac{u(1)}{h_1}\left[\frac{\partial u(1)}{\partial \xi^1} + u(2)\frac{\partial h_1}{\partial \xi^2}\right].
\end{aligned}
\tag{4.27}
$$

Equations (4.13), (4.16), (4.20), and (4.23), with the introduction of the 'augmented' gravity factor, (which includes the acceleration of the coordinate system)

$$\mathbf{g}' = \mathbf{g} - \frac{\partial^2 \mathbf{R}}{\partial t^2}, \tag{4.28}$$

gives the streamwise component of the momentum equation,

$$\frac{\partial \mathcal{U}}{\partial t} + \left(\mathcal{V} + \hat{\mathbf{n}}\cdot\frac{\partial \mathbf{R}}{\partial t}\right)\frac{\partial \mathcal{U}}{\partial n} + \frac{1}{(1 - \kappa n)}\left(\mathcal{U} + \hat{\mathbf{s}}\cdot\frac{\partial \mathbf{R}}{\partial t} - n\Omega\right)\left(\frac{\partial \mathcal{U}}{\partial s} - n\frac{\partial \Omega}{\partial s} - \kappa\mathcal{V}\right) =$$

$$= \mathcal{V}\Omega + \frac{\partial(n\Omega)}{\partial t} + \hat{\mathbf{s}}\cdot\mathbf{g}' - \frac{1}{\rho(1 - \kappa n)}\frac{\partial \mathcal{P}}{\partial s}. \tag{4.29}$$

$\mathcal{P}$ and ρ are the pressure and the constant density respectively. On the left hand side of the above equation is the total derivative of $\mathcal{U}$ including the rate of change

and convective terms, while on the right hand side, besides the 'gravitational' acceleration and the pressure gradient force, there are two terms which are fictitious body forces. They are the Coriolis acceleration and that due to the acceleration of the local rotation of the frame of reference.

A similar procedure for the component $i = 2$ of equation (4.6) gives the normal component of the momentum equation:

$$\frac{\partial \mathcal{V}}{\partial t} + \hat{\mathbf{n}}{\cdot}\frac{\partial \mathbf{R}}{\partial t}\frac{\partial \mathcal{V}}{\partial n} + \tfrac{1}{2}\frac{\partial \mathcal{V}^2}{\partial n} + \frac{1}{(1-\kappa n)}\hat{\mathbf{s}}{\cdot}\frac{\partial \mathbf{R}}{\partial t}\left(\frac{\partial \mathcal{V}}{\partial s} + \kappa \mathcal{U}\right)$$

$$+\frac{(\mathcal{U} - n\Omega)}{(1-\kappa n)}\left(\frac{\partial \mathcal{V}}{\partial s} + \kappa \mathcal{U}\right) = n\Omega^2 - \mathcal{U}\Omega + \hat{\mathbf{n}}{\cdot}\mathbf{g}' - \frac{1}{\rho}\frac{\partial \mathcal{P}}{\partial n}. \tag{4.30}$$

Again, a simple classification of the terms is given in order to recognize their contribution and meaning. On the left hand side is the total derivative of $\mathcal{V}$ (rate of change and convective terms), while on the right hand side, the fictitious body forces are the Coriolis acceleration and the centrifugal acceleration, $n\Omega^2$. Equation (4.30) can be rearranged into a simpler form. From the continuity equation, the following substitution,

$$\mathcal{U}\frac{\partial \mathcal{V}}{\partial s} = \frac{\partial (\mathcal{U}\mathcal{V})}{\partial s} - n\mathcal{V}\frac{\partial \Omega}{\partial s} + (1-\kappa n)\mathcal{V}\frac{\partial \mathcal{V}}{\partial n} - \kappa \mathcal{V}^2, \tag{4.31}$$

transforms the crossflow momentum equation as

$$\frac{\partial \mathcal{V}}{\partial t} + \hat{\mathbf{n}}{\cdot}\frac{\partial \mathbf{R}}{\partial t}\frac{\partial \mathcal{V}}{\partial n} + \frac{\partial \mathcal{V}^2}{\partial n} + \frac{1}{(1-\kappa n)}\hat{\mathbf{s}}{\cdot}\frac{\partial \mathbf{R}}{\partial t}\left(\frac{\partial \mathcal{V}}{\partial s} + \kappa \mathcal{U}\right)$$

$$+\frac{1}{(1-\kappa n)}\left[\frac{\partial (\mathcal{U}\mathcal{V})}{\partial s} + \kappa \left(\mathcal{U}^2 - \mathcal{V}^2 - n\Omega\mathcal{U}\right) - n\frac{\partial (\mathcal{V}\Omega)}{\partial s}\right] = n\Omega^2 - \mathcal{U}\Omega + \hat{\mathbf{n}}{\cdot}\mathbf{g}' - \frac{1}{\rho}\frac{\partial \mathcal{P}}{\partial n}. \tag{4.32}$$

A simple check on equations (4.30) and (4.32) can be done by considering a non-rotating local frame of reference ($\Omega = 0$) and collapsing the curve Υ on to a circle of fixed radius ($\partial \mathbf{R}/\partial t = 0$). It is easy to show that the above equations reduce to the equations of motion of a flow described by tangential and radial velocities $(\mathcal{U}, \mathcal{V}) \rightarrow (u_r, v_\theta)$, i.e., where plane polar coordinates are used.

4.3 The turbulence model

The next step is to introduce Reynolds averaging for turbulence. By following BP2, and introducing a suitable averaging technique $\langle . \rangle$, the following decomposition holds:

$$\mathcal{U} = U + u \ , \qquad \mathcal{V} = V + v \ , \qquad \mathcal{P} = P + p,$$

$$\langle u \rangle = 0 \ , \qquad \langle v \rangle = 0 \ , \qquad \langle p \rangle = 0, \tag{4.33}$$

for points lying entirely in the liquid. Averaging in the region of the surface layer is discussed in more detail in BP2, and the resulting boundary conditions are valid for ordinary Reynolds' decomposition.

In the continuity equation, substituting for velocity components from equation (4.33) and turbulent averaging gives two different equations valid for the mean velocities and the fluctuations:

$$\frac{\partial U}{\partial s} + \frac{\partial}{\partial n}\left[(1 - \kappa n)V\right] = n\frac{\partial \Omega}{\partial s} \ , \qquad \frac{\partial u}{\partial s} + \frac{\partial}{\partial n}\left[(1 - \kappa n)v\right] = 0. \tag{4.34}$$

It is evident that the term due to the angular velocity only influences the mean motion while curvature effects influence both the mean flow and the turbulent velocities. The streamwise momentum equation for the mean flow variables is obtained by multiplying equation (4.29) times $(1 - \kappa n)$, substituting for $\mathcal{U}$, $\mathcal{V}$ and $\mathcal{P}$, and finally taking the turbulent average:

$$(1 - \kappa n)\frac{\partial U}{\partial t} + (1 - \kappa n)\left[\left(V + \hat{\mathbf{n}}\cdot\frac{\partial \mathbf{R}}{\partial t}\right)\frac{\partial U}{\partial n} + \left\langle v\frac{\partial u}{\partial n}\right\rangle\right] + \frac{1}{2}\left\langle\frac{\partial u^2}{\partial s}\right\rangle - \kappa\langle uv \rangle$$

$$+ \left(U + \hat{\mathbf{s}}\cdot\frac{\partial \mathbf{R}}{\partial t} - n\Omega\right)\left(\frac{\partial U}{\partial s} - n\frac{\partial \Omega}{\partial s} - \kappa V\right) = (1 - \kappa n)\left(V\Omega + \frac{\partial(n\Omega)}{\partial t} + \hat{\mathbf{s}}\cdot\mathbf{g}'\right) - \frac{1}{\rho}\frac{\partial P}{\partial s}. \tag{4.35}$$

It is more useful to express products of turbulent fluctuations in the conservative correlation form $\langle u_i u_j \rangle$, and from the continuity equation for the turbulent fluctuations, the substitution

$$(1 - \kappa n)\left\langle v\frac{\partial u}{\partial n}\right\rangle = (1 - \kappa n)\frac{\partial\langle uv \rangle}{\partial n} - \kappa\langle uv \rangle + \frac{1}{2}\frac{\partial\langle u^2 \rangle}{\partial s} \tag{4.36}$$

114

yields

$$(1 - \kappa n)\frac{\partial U}{\partial t} + (1 - \kappa n)\left[\left(V + \hat{\mathbf{n}}\cdot\frac{\partial \mathbf{R}}{\partial t}\right)\frac{\partial U}{\partial n} + \frac{\partial \langle uv\rangle}{\partial n}\right] + \frac{\partial \langle u^2\rangle}{\partial s} - 2\kappa\langle uv\rangle$$

$$+\left(U + \hat{\mathbf{s}}\cdot\frac{\partial \mathbf{R}}{\partial t} - n\Omega\right)\left(\frac{\partial U}{\partial s} - n\frac{\partial \Omega}{\partial s} - \kappa V\right) = (1 - \kappa n)\left(V\Omega + \frac{\partial(n\Omega)}{\partial t} + \hat{\mathbf{s}}\cdot\mathbf{g}'\right) - \frac{1}{\rho}\frac{\partial P}{\partial s}.$$

$$(4.37)$$

Applying a similar procedure to equation (4.30),

$$\frac{\partial V}{\partial t} + \hat{\mathbf{n}}\cdot\frac{\partial \mathbf{R}}{\partial t}\frac{\partial V}{\partial n} + \frac{1}{2}\frac{\partial V^2}{\partial n} + \frac{\partial \langle v^2\rangle}{\partial n} + \frac{1}{(1 - \kappa n)}\hat{\mathbf{s}}\cdot\frac{\partial \mathbf{R}}{\partial t}\left(\frac{\partial V}{\partial s} + \kappa U\right) + \frac{(U - n\Omega)}{(1 - \kappa n)}\left(\frac{\partial V}{\partial s} + \kappa U\right)$$

$$+ \frac{1}{(1 - \kappa n)}\frac{\partial \langle uv\rangle}{\partial s} + \frac{\kappa(\langle u^2\rangle - \langle v^2\rangle)}{(1 - \kappa n)} = n\Omega^2 - U\Omega + \hat{\mathbf{n}}\cdot\mathbf{g}' - \frac{1}{\rho}\frac{\partial P}{\partial n}. \qquad (4.38)$$

These are the Reynolds' equations for the two-dimensional mean flow in which Reynolds' stress terms $\langle u_i u_j\rangle$ are responsible for momentum exchanges between turbulence and the mean flow. In the case under investigation, Reynolds' equations also contain terms coming from the wave motion, namely its curvature and local rotation. These contributions give a complete account of the motion of the unsteady spilling breaker. They also make these equations very complex and the solution of the complete equations a very difficult task. Assumptions on the dynamics of the turbulence, the wave-layer system, and scaling means are introduced in the next section to obtain analytically feasible solutions.

A suitable turbulence model has to be chosen to close the problem. The level of closure, i.e. the chosen number of transport equations, depends upon the level of detail desired in the description of the turbulent flow. In principle, a more accurate representation of a quantity is given by using its transport equation. However, in practice, the level of closure should not be too high because the difficulties in getting a physical understanding of the algebraic closure increase with the number of equations. Thus, the turbulent closure mechanism is chosen here to be very simple in order to easily identify the physical behavior involved in the phenomenon, and transport equations are used when non-equilibrium conditions are to be reproduced.

It is well known that for a quasi-steady spilling breaker there is an excess of turbulence production relative to the dissipation at the leading edge of the turbulent layer. This is also true for steady breakers, e.g. for a hydraulic jump (See Figure 3 in MS83). Proper modelling of this non-equilibrium for the turbulent kinetic energy density per unit volume, k, requires the use of a transport equation for at least the turbulent kinetic energy,

$$k = \tfrac{1}{2}\langle u^i u_i \rangle = \tfrac{1}{2} g_{ij} \langle u^i u^j \rangle, \tag{4.39}$$

where $\rho = 1$.

Unfortunately, no data is available at the moment for the rate of production, dissipation, and transport of the shear stress terms (e.g. $\langle uv \rangle$) in steady or quasi-steady breakers. However, it is known that shear Reynolds' stresses relax faster from a given non-equilibrium condition towards local equilibrium than either the normal stresses or turbulent kinetic energy. It is thus reasonable to assume local equilibrium for the turbulent shear stresses. The assumption is supported by the measurements of production, dissipation and transport of $\langle uv \rangle$ in straight and curved mixing layers (Castro and Bradshaw, 1976). In the absence of data directly measured in steady or quasi-steady breakers, the above results, valid for a mixing layer, are extended to the turbulent thin layer. Hence, it is assumed that nearly equilibrium conditions are reached for $\langle uv \rangle$, and consequently, Boussinesq's eddy viscosity formulation is used for the algebraic closure of the turbulent shear stresses.

The classical Boussinesq eddy viscosity model assumes that the Reynolds' stresses are linearly related to the mean rate of strain. The relationship is similar to that derived for the viscous stresses in a Newtonian stress tensor,

$$-\langle u^i u^j \rangle = 2\nu_t e^{ij} - \tfrac{2}{3} g^{ij} k, \tag{4.40}$$

where ν_t denotes the isotropic eddy viscosity, which depends upon the local flow conditions and e^{ij} is the rate of deformation tensor. The turbulent kinetic energy

term has been added to make the equation valid when contracted. So,

$$-g_{ij}\langle u^i u^j\rangle = 2\nu_t e^i_i - 2k = -2k, \qquad (4.41)$$

since $e^i_i = 0$ for an incompressible fluid. By replacing the contravariant strain rate with its expression

$$e^{ij} = g^{li}g^{kj}e_{kl} = g^{li}g^{kj}\tfrac{1}{2}\left(\langle u_k\rangle_{,l} + \langle u_l\rangle_{,k}\right), \qquad (4.42)$$

further simplifications yields

$$-\langle u^i u^j\rangle = \nu_t\left(g^{li}\langle u^j\rangle_{,l} + g^{kj}\langle u^i\rangle_{,k}\right) - \tfrac{2}{3}g^{ij}k. \qquad (4.43)$$

Since an algebraically-specified eddy viscosity model is used, substitution of the above equation into the momentum equations (4.37) and (4.38) completes the closure problem. In the present one-equation $k - \varepsilon$ model, the eddy viscosity is related to the turbulent kinetic energy and its rate of dissipation ε by

$$\nu_t = C_\mu \frac{k^2}{\varepsilon}, \qquad (4.44)$$

where C_μ is a constant of order $C_\mu \approx 0.09$ (Launder and Spalding, 1972). In summary, a one-equation closure approach is considered in which only one differential equation for the transport of turbulent energy is required, and an algebraic equation relates the turbulent kinetic energy and its rate of dissipation (ε) through a mixing length which, in the specific case, is chosen to be the total thickness, b, of the turbulent layer. There are various possible definitions of the mixing length for the flow at hand. In wave breaking literature, this is taken as the thickness of the turbulent layer (e.g. MS83, Govender *et al.*, 2002b). Govender *et al.* (2002b) point out that in a breaking wave, most of the dissipation occurs over a thickness comparable to the crest height. For the present measurements, Figure 3.17 and Figure 3.18 suggest that the integral length scale (l) is of the order of the width of the mixing layer.

In light of this, and to facilitate a simpler analysis, b is chosen as a typical mixing length, giving

$$\varepsilon \approx \frac{k^{3/2}}{b} \quad \text{or} \quad \varepsilon = C_\varepsilon \frac{k^{3/2}}{b}, \tag{4.45}$$

where, following Launder and Spalding (1972), $C_\varepsilon \approx 0.08$. Substitution into (4.44) gives

$$\nu_t = \frac{C_\mu}{C_\varepsilon} k^{1/2} b \approx k^{1/2} b. \tag{4.46}$$

A similar approach to the closure problem has been adopted by MS83 in their analysis of a turbulent bore. Comparison of their model results with measurements shows fairly good agreement. This is encouraging and shows that, for the flow under investigation, it is not necessary to adopt a very complicated model to represent the turbulence in order to reproduce experimental data and the main flow characteristics.

The transport equation for the turbulent kinetic energy in covariant form is (see equations (5-7) to (5-9) of Richmond *et al.*, 1986)

$$\frac{\partial k}{\partial t} + \langle u^m \rangle k_{,m} = (\alpha g^{mn} k_{,n})_{,m} - g_{ij} \langle u^j u^m \rangle \langle u^i \rangle_{,m} - \varepsilon, \tag{4.47}$$

where $\alpha \approx \nu_t$ for high Reynolds' number motions. The physical interpretation of the terms in the above equation is readily seen. The two terms at the left hand side make up the material derivative of k following the mean flow, the first term at the right hand side involving the eddy viscosity represents the diffusion of turbulent kinetic energy by the action of turbulence itself, and the second and third terms at the right hand side are respectively the production of turbulent kinetic energy by the rate of strain of the mean flow and the rate of dissipation of turbulent kinetic energy.

Covariant differentiation of a scalar function is a simple partial derivative. Also, only a few of the Christoffel symbols are non zero. Thus, equation (4.47) is readily expanded under the assumption of quasi-two-dimensional flow

$$\frac{\partial k}{\partial t}+\langle u^1\rangle\frac{\partial k}{\partial \xi^1}+\langle u^2\rangle\frac{\partial k}{\partial \xi^2}=\frac{\partial}{\partial \xi^1}\left(\frac{\nu_t}{h_1{}^2}\frac{\partial k}{\partial \xi^1}\right)+\frac{\partial}{\partial \xi^2}\left(\nu_t\frac{\partial k}{\partial \xi^2}\right)-h_1{}^2\langle u^1u^1\rangle\left(\frac{\partial\langle u^1\rangle}{\partial \xi^1}+\Gamma^1_{12}\langle u^2\rangle\right)$$

$$-\langle u^1u^2\rangle\left[h_1{}^2\left(\frac{\partial\langle u^1\rangle}{\partial \xi^2}+\Gamma^1_{12}\langle u^1\rangle\right)+\left(\frac{\partial\langle u^2\rangle}{\partial \xi^1}+\Gamma^2_{11}\langle u^1\rangle\right)\right]-\langle u^2u^2\rangle\left(\frac{\partial\langle u^2\rangle}{\partial \xi^2}+\Gamma^2_{2i}\langle u^i\rangle\right)-\varepsilon. \quad (4.48)$$

Recalling the expressions for the non-zero Christoffel symbols (equation 4.21) and passing to physical variables gives

$$\frac{\partial k}{\partial t}+\frac{\langle u(1)\rangle}{h_1}\frac{\partial k}{\partial \xi^1}+\langle u(2)\rangle\frac{\partial k}{\partial \xi^2}=$$

$$\frac{1}{h_1{}^2}\frac{\partial}{\partial \xi^1}\left(\nu_t\frac{\partial k}{\partial \xi^1}\right)+\frac{\partial}{\partial \xi^2}\left(\nu_t\frac{\partial k}{\partial \xi^2}\right)-\frac{\langle u(1)u(1)\rangle}{h_1}\left(\frac{\partial\langle u(1)\rangle}{\partial \xi^1}+\frac{\partial h_1}{\partial \xi^2}\langle u(2)\rangle\right)$$

$$-\frac{\langle u(1)u(2)\rangle}{h_1}\left(h_1\frac{\partial\langle u(1)\rangle}{\partial \xi^2}+\frac{\partial\langle u(2)\rangle}{\partial \xi^1}-\frac{\partial h_1}{\partial \xi^2}\langle u(1)\rangle\right)-\langle u(2)u(2)\rangle\frac{\partial\langle u(2)\rangle}{\partial \xi^2}-\varepsilon. \quad (4.49)$$

Finally, considering the specific expression of the physical components of the flow velocity vector (4.23) gives

$$\frac{\partial k}{\partial t}+\frac{1}{(1-\kappa n)}\left(U+\hat{\mathbf{s}}\cdot\frac{\partial\mathbf{R}}{\partial t}-n\Omega\right)\frac{\partial k}{\partial s}+\left(V+\hat{\mathbf{n}}\cdot\frac{\partial\mathbf{R}}{\partial t}\right)\frac{\partial k}{\partial n}=\frac{1}{(1-\kappa n)^2}\frac{\partial}{\partial s}\left(\nu_t\frac{\partial k}{\partial s}\right)$$

$$+\frac{\partial}{\partial n}\left(\nu_t\frac{\partial k}{\partial n}\right)-\frac{\langle u^2\rangle}{(1-\kappa n)}\left[\frac{\partial}{\partial s}\left(U+\hat{\mathbf{s}}\cdot\frac{\partial\mathbf{R}}{\partial t}-n\Omega\right)-\kappa\left(V+\hat{\mathbf{n}}\cdot\frac{\partial\mathbf{R}}{\partial t}\right)\right] \quad (4.50)$$

$$-\frac{\langle uv\rangle}{(1-\kappa n)}\left[(1-\kappa n)\left(\frac{\partial U}{\partial n}-\Omega\right)+\frac{\partial}{\partial s}\left(V+\hat{\mathbf{n}}\cdot\frac{\partial\mathbf{R}}{\partial t}\right)+\kappa\left(U+\hat{\mathbf{s}}\cdot\frac{\partial\mathbf{R}}{\partial t}-n\Omega\right)\right]$$

$$-\langle v^2\rangle\frac{\partial V}{\partial n}-\varepsilon.$$

This is simplified by means of equations (4.13) and(4.20), and by using the continuity equation for the mean flow (4.34)

$$\frac{\partial k}{\partial t}+\frac{1}{(1-\kappa n)}\left(U+\hat{\mathbf{s}}\cdot\frac{\partial\mathbf{R}}{\partial t}-n\Omega\right)\frac{\partial k}{\partial s}+\left(V+\hat{\mathbf{n}}\cdot\frac{\partial\mathbf{R}}{\partial t}\right)\frac{\partial k}{\partial n}=\frac{1}{(1-\kappa n)^2}\frac{\partial}{\partial s}\left(\nu_t\frac{\partial k}{\partial s}\right)$$

$$+\frac{\partial}{\partial n}\left(\nu_t\frac{\partial k}{\partial n}\right)+(\langle u^2\rangle-\langle v^2\rangle)\frac{\partial V}{\partial n}-\frac{\langle uv\rangle}{(1-\kappa n)}\left[(1-\kappa n)\frac{\partial U}{\partial n}+\frac{\partial V}{\partial s}+\kappa U\right]-\varepsilon. \quad (4.51)$$

Equation (4.40) is now examined for the three possible combinations of the indices i, j, and using orthogonal coordinates and physical variables. For $i = 1$ and $j = 2$, the shear Reynolds' stress term is

$$-(1-\kappa n)\langle uv\rangle =$$

$$\nu_t\left[\frac{\partial}{\partial s}\left(V+\hat{\mathbf{n}}\cdot\frac{\partial\mathbf{R}}{\partial t}\right)+\kappa\left(U+\hat{\mathbf{s}}\cdot\frac{\partial\mathbf{R}}{\partial t}-n\Omega\right)+(1-\kappa n)\frac{\partial}{\partial n}\left(U+\hat{\mathbf{s}}\cdot\frac{\partial\mathbf{R}}{\partial t}-n\Omega\right)\right].$$
$$(4.52)$$

Using the Serret-Frenel formulae (4.13) and the relations for the angular velocity (4.20), a much simpler expression is found:

$$-(1-\kappa n)\langle uv\rangle = \nu_t\left[\frac{\partial V}{\partial s}+\kappa U+(1-\kappa n)\frac{\partial U}{\partial n}\right]. \quad (4.53)$$

This expression for the Reynolds' shear stress component $\langle uv\rangle$ is similar to that obtained by Gibson and Rodi (1981). The three terms on the right hand side are due to the streamline curvature, the explicit effect of geometric curvature, and the simple shear strain rate. As will be shown later, each term affects the turbulent shear stress at a different order in the geometric parameter (the ratio of the width of the layer to the streamwise length scale).

A similar analysis for the component $i = j = 1$ leads to

$$-(1-\kappa n)\langle u^2\rangle = 2\nu_t\left(\frac{\partial U}{\partial s}-n\frac{\partial\Omega}{\partial s}-\kappa V\right)-\frac{2(1-\kappa n)k}{3}, \quad (4.54)$$

which can be rewritten in a much simpler form by means of the continuity equation for the mean flow (4.34) as

$$\langle u^2\rangle = 2\nu_t\frac{\partial V}{\partial n}+\frac{2k}{3}, \quad (4.55)$$

and, similarly, for the component $i = j = 2$,

$$\langle v^2\rangle = -2\nu_t\frac{\partial V}{\partial n}+\frac{2k}{3}. \quad (4.56)$$

The above expressions for $\langle u^2 \rangle$ and $\langle v^2 \rangle$ are correct for a homogeneous isotropic turbulent flow. However, in general these terms have different strengths according to the particular turbulent flow structure under investigation, as already seen in BP2. Consequently, a different expression from (4.40) is used where the addition of the turbulent kinetic energy is made via a tensor $a^{ij} \neq g^{ij}$:

$$-\langle u^i u^j \rangle = 2\nu_t e^{ij} - 2a^{ij}k. \tag{4.57}$$

The tensor is defined as

$$a^{ij} = 0 \qquad \text{for} \qquad i \neq j, \quad \text{and} \tag{4.58}$$

$$a_1^1 = C_1 \ , \quad a_2^2 = C_2 \ , \quad a_3^3 = C_3, \tag{4.59}$$

so that its trace is $a_i^i = C_1 + C_2 + C_3 = 1$, and equation (4.57) is valid when contracted. This new expression only affects the diagonal terms of the Reynolds' stress components which now read:

$$\langle u^2 \rangle = 2\nu_t \frac{\partial V}{\partial n} + 2C_1 k \ , \qquad \langle v^2 \rangle = -2\nu_t \frac{\partial V}{\partial n} + 2C_3 k. \tag{4.60}$$

Allowing for anisotropy is particularly important in the analysis of breaking wave turbulence in the roller region and the wave crest, whereas below the wave crest and in the wake region, the turbulence approaches isotropy (Govender *et al.*, 2002b). This is true for a steady breaker as well, as has been seen in Chapter 3 (see Figure 3.14)

4.4   The scaling of the equations.

The final equations (4.34), (4.37), (4.38), (4.51), (4.53), (4.55), and (4.60) involve many terms but not all of them have the same weight on the final solution. Scaling arguments are adopted to retain only the most important terms in the basic equations and to help compare relative weights of terms appearing in different

equations. Some of the scaling arguments are derived from Bradshaw (1973) and Tennekes and Lumley (1972).

As is well known, mixing layers (or shear layers) are characterized by a scale velocity $\tilde{U}$ for the cross-stream (n) variation of the mean velocity component in the streamwise direction ($\hat{s}$). A first useful relationship which characterizes the flow in the turbulent layer expresses the observation that the layer is thin, i.e., the thickness, b, is much smaller than the streamwise length scale, L:

$$b \ll L \quad \text{or} \quad \frac{b}{L} = \epsilon \ll 1. \tag{4.61}$$

L represents the size of the region of the wave with the highest curvature. For the present measurements, the radius of curvature at the toe (where the positive curvature is maximum) of the breaker is approximately equal to the streamwise distance between the peak positive and negative curvature (found at the downstream end of the roller region), and either of these can therefore be chosen as L. Further, considering the variation of the calculated length scale of the mixing layer, values of ϵ averaged over the breaker shear layer are of the order of 0.03, which is slightly smaller than typically observed values of order 0.06 for jets and mixing layers (Tennekes and Lumley, 1972). These values are reasonable enough to satisfy the 'thin layer' approximation.

The streamwise rate of change of the mean velocity component scales as

$$\frac{\partial U}{\partial s} = \mathcal{O}\left(\frac{\tilde{U}}{L}\right), \tag{4.62}$$

where $\mathcal{O}$ stands for 'order of magnitude'. A velocity scale, $\tilde{u}$, for the turbulence is introduced such that

$$k = \mathcal{O}(\tilde{u}^2), \quad \langle uv \rangle = \mathcal{O}(\tilde{u}^2), \quad \langle u^2 \rangle = \mathcal{O}(\tilde{u}^2), \quad \text{and} \quad \langle v^2 \rangle = \mathcal{O}(\tilde{u}^2). \tag{4.63}$$

As a consequence, an order of magnitude for the eddy viscosity, ν_t, and the turbulent energy dissipation, ε, is also found. From equation (4.46), which relates ν_t to the

turbulent kinetic energy (and its scale, $\tilde{u}$) and the layer thickness, b, and from equation (4.45),

$$\nu_t = \mathcal{O}\left[\left(\tilde{u}^2\right)^{1/2} b\right] = \mathcal{O}\left(\tilde{u}b\right), \quad \text{and} \quad \varepsilon = \mathcal{O}\left(\tilde{u}^3/b\right). \tag{4.64}$$

By using the above velocity and length scales, the time scale is given by

$$t = \mathcal{O}\left(\frac{L}{\tilde{U}}\right) \tag{4.65}$$

for the mean flow. This is such that the assumption of quasi-steady breaker is satisfied: the evolution of the breaker is comparable with the time scales for fluid particles to pass through the breaker itself. The scale for the cross-stream component, V, of the mean velocity is determined from the continuity equation for the mean flow (4.34), where limiting arguments are used. For a steady breaker, $\Omega = 0$ and, therefore,

$$V = \mathcal{O}\left(\frac{\tilde{U}b}{L}\right) = \mathcal{O}\left(\tilde{U}\epsilon\right). \tag{4.66}$$

The scaling for the curvature κ must be carefully addressed because of the presence of either gentle curvature ($\kappa = \mathcal{O}\left(1/L\right)$) or strong curvature ($1/L < \kappa < 1/b$) for the layer. As discussed previously, the assumption of gentle curvature is satisfied in the breaker region. In the following, gentle curvature is assumed and the final result of the scaling procedure reduces to that of Tennekes and Lumley (1972) for a straight, steady shear layer. The final equations for a curved shear layer in the mixing layer regime contain the same terms as those by Gibson and Rodi (1981), as well as the extra terms due to the motion of the underlying convected points and terms proportional to the angular velocity, Ω, which represents the solid rotation of the local frame of reference $(\hat{\mathbf{s}}, \hat{\mathbf{n}})$.

It is important to properly assess the relationship between the scale for fluctuations ($\tilde{u}$) and that for the mean flow velocity ($\tilde{U}$). This relationship strongly depends on the sort of flow under investigation, or as in the present case where the

flow type is not uniquely defined, on the local flow regime. The region of the spilling breaker which is furthest from the leading edge is analyzed first. In this region, the flow regime is such that its characteristics are similar to those of far wakes (Battjes and Sakai, 1981). In far wakes, turbulence intensities are much smaller than the mean velocities; more precisely the following relationship holds:

$$\frac{\tilde{u}}{\tilde{U}} = \mathcal{O}\left(\frac{b}{L}\right) = \mathcal{O}(\epsilon). \tag{4.67}$$

A completely different situation is found at the leading edge of the breaker. In this region, turbulent flow is due to a local shearing which is similar to that generating a mixing layer (Peregrine and Svendsen, 1978). Observation shows that turbulent velocity fluctuations are so energetic at the leading edge of the breaker that water droplets can be projected vertically upwards to distances comparable to the local variations of surface height. Therefore, it is assumed that close to the leading edge of the breaker, the following relationship holds:

$$\frac{\tilde{u}}{\tilde{U}} = \mathcal{O}(1) \quad \text{or} \quad \tilde{u} = \mathcal{O}(\tilde{U}). \tag{4.68}$$

Such an assumption is well supported by present experimental evidence. For example, in the roller region, the velocity fluctuations are at least of the same order of magnitude as the mean velocities. In the crests of spilling breakers, Govender *et al.* (2002b) found peak horizontal turbulence intensities of more than 50% of the wave phase speed.

It is convenient to introduce a dimensionless parameter μ which represents the ratio of the scales for turbulent velocities and mean velocities, and use it to implicitly estimate the size of the different contributions in the following analysis:

$$\mu = \frac{\tilde{u}}{\tilde{U}} \,, \quad \mathcal{O}(\epsilon) < \mu < \mathcal{O}(1). \tag{4.69}$$

From the present measurements, the streamwise variation of μ is calculated by averaging over the width of the mixing layer. This is shown in figure 4.5. μ

124
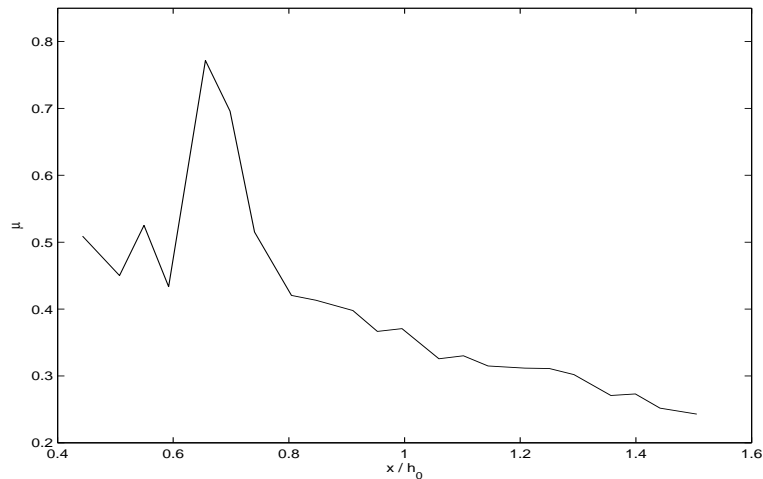
Figure 4.5: Variation of μ in the breaker shear layer. The foot of the breaker is at $x/h_0 \sim 0.47$.

is $\mathcal{O}(1)$ near the leading edge of the breaker and decays downstream towards the wake. The wake for the breaker region in the case of a wave is further downstream of the rear of the crest, and it is expected that in that region the turbulence intensity decays further and $\mu \sim \mathcal{O}(\epsilon)$. Note that, as found by Rapp and Melville (1990) for unsteady deep-water breaking, the region directly affected by the breaking wave is of finite extent in the direction of propagation, whereas for steady breaking, there is an infinite wake which extends downstream.

The 'breaker shear layer' regime can be described both in terms of the nomenclature typical of internal turbulent flows, i.e., a mixing layer of enhanced turbulent strength, and in terms of the nomenclature used for the surface manifestations of turbulence at a free surface (see BP1), i.e., a flow in the splashing regime. In between the two extreme flow regimes, i.e., 'breaker shear flow' and wake flow, the typical mixing layer regime may be found. In this transition region, by applying scaling arguments for mixing layers, the ratio of the turbulent fluctuations to the

mean flow velocity is given according to

$$\frac{\tilde{u}}{\tilde{U}} = \mathcal{O}\left[\left(\frac{b}{L}\right)^{1/2}\right] = \mathcal{O}(\epsilon^{1/2}). \tag{4.70}$$

Applying the scaling procedure to the terms due to the motion of the convected point, the order of magnitude of those terms can be estimated from their definitions (4.12) and (4.20) as follows:

$$\Omega = \mathcal{O}\left(\frac{\tilde{U}}{L}\right) , \qquad \frac{\partial \mathbf{R}}{\partial t} = \mathcal{O}\left(\tilde{U}\right). \tag{4.71}$$

This allows for further simplification of the basic equations.

Dimensionless variables are now introduced to assess the scaling of the equations for mass, momentum, and turbulent kinetic energy. As is common practice in the analysis of boundary layers, the dimensionless variables are denoted by primes which are dropped soon after the simplification to dimensionless equations is complete:

$$s' = \frac{s}{L} , \quad n' = \frac{n}{b} , \quad z' = \frac{z}{L} , \quad t' = \frac{\tilde{U}t}{L} , \quad \kappa' = \kappa L , \tag{4.72}$$

$$U' = \frac{U}{\tilde{U}} , \quad V' = \frac{V}{\tilde{U}\epsilon} , \quad \Omega' = \frac{\Omega L}{\tilde{U}} , \quad \left(\frac{\partial \mathbf{R}}{\partial t}\right)' = \frac{1}{\tilde{U}}\frac{\partial \mathbf{R}}{\partial t} , (\mathbf{g}')' = \frac{\mathbf{g}'L}{\tilde{U}^2}, \tag{4.73}$$

$$P' = \frac{P}{\rho\tilde{U}^2} , \langle u_i' u_j' \rangle = \frac{\langle u_i u_j \rangle}{\tilde{u}^2} , \quad k' = \frac{k}{\tilde{u}^2} , \quad \nu_t' = \frac{\nu_t}{\tilde{u}b} , \quad \varepsilon' = \frac{\varepsilon b}{\tilde{u}^3} , \tag{4.74}$$

$$\frac{b}{L} = \epsilon \ll 1 , \quad \mathcal{O}(\epsilon) < \mu = \tilde{u}/\tilde{U} < \mathcal{O}(1). \tag{4.75}$$

The dimensionless continuity equation for the mean flow is obtained after collecting the dimensional scale factor, $\tilde{U}/L$:

$$\frac{\partial U}{\partial s} + \frac{\partial V}{\partial n} = \epsilon \left[\kappa \frac{\partial(nV)}{\partial n} + n \frac{\partial \Omega}{\partial s}\right]. \tag{4.76}$$

The two components of the equation of motion are obtained by collecting the dimensional scale factor, $\tilde{U}^2/L$. The streamwise component reads

$$\left[\mu^2 \frac{\partial \langle uv \rangle}{\partial n} + \hat{\mathbf{n}} \cdot \frac{\partial \mathbf{R}}{\partial t}\frac{\partial U}{\partial n}\right] + \epsilon \left[\frac{\partial U}{\partial t} + V\frac{\partial U}{\partial n} + \left(U + \hat{\mathbf{s}} \cdot \frac{\partial \mathbf{R}}{\partial t}\right)\frac{\partial U}{\partial s} - \kappa n\hat{\mathbf{n}} \cdot \frac{\partial \mathbf{R}}{\partial t}\frac{\partial U}{\partial n}\right.$$

126

$$-\mu^2 \left(\kappa n \frac{\partial \langle uv \rangle}{\partial n} - \frac{\partial \langle u^2 \rangle}{\partial s} + 2\kappa \langle uv \rangle \right) \Bigg] - \epsilon^2 \left[\kappa n \left(\frac{\partial U}{\partial t} + V \frac{\partial U}{\partial n} \right) + \frac{\partial U}{\partial s} n\Omega + \right.$$

$$\left(U + \hat{\mathbf{s}} \cdot \frac{\partial \mathbf{R}}{\partial t} \right) \left(n \frac{\partial \Omega}{\partial s} + \kappa V \right) \Bigg] + \epsilon^3 \left[n\Omega \left(n \frac{\partial \Omega}{\partial s} + \kappa V \right) \right] = \epsilon \left[\hat{\mathbf{s}} \cdot \mathbf{g}' - \frac{\partial P}{\partial s} \right] +$$

$$\epsilon^2 \left[V\Omega + \frac{\partial (n\Omega)}{\partial t} - \kappa n \hat{\mathbf{s}} \cdot \mathbf{g}' \right] - \epsilon^3 \kappa n \left[V\Omega + \frac{\partial (n\Omega)}{\partial t} \right], \qquad (4.77)$$

while the crossflow component is

$$\mu^2 \frac{\partial \langle v^2 \rangle}{\partial n} + \epsilon \left[\hat{\mathbf{n}} \cdot \frac{\partial \mathbf{R}}{\partial t} \frac{\partial V}{\partial n} - \mu^2 \kappa n \frac{\partial \langle v^2 \rangle}{\partial n} + \kappa U \hat{\mathbf{s}} \cdot \frac{\partial \mathbf{R}}{\partial t} + \kappa U^2 + \right.$$

$$\mu^2 \left(\frac{\partial \langle uv \rangle}{\partial s} + \kappa \left(\langle u^2 \rangle - \langle v^2 \rangle \right) \right) \Bigg] + \epsilon^2 \left[\frac{\partial V}{\partial t} - \kappa n \hat{\mathbf{n}} \cdot \frac{\partial R}{\partial t} \frac{\partial V}{\partial n} + \frac{1}{2} \frac{\partial V^2}{\partial n} \right.$$

$$+ \left(\hat{\mathbf{s}} \cdot \frac{\partial \mathbf{R}}{\partial t} + U \right) \frac{\partial V}{\partial s} - n\Omega \kappa U \Bigg] - \epsilon^3 n \left[\kappa \frac{\partial V}{\partial t} + \kappa \frac{1}{2} \frac{\partial V^2}{\partial n} + \Omega \frac{\partial V}{\partial s} \right]$$

$$= -\frac{\partial P}{\partial n} - \epsilon \left[U\Omega - \hat{\mathbf{n}} \cdot \mathbf{g}' - \kappa n \frac{\partial P}{\partial n} \right] + \epsilon^2 n \left[\Omega^2 + \kappa U\Omega - \kappa \hat{\mathbf{n}} \cdot \mathbf{g}' \right]$$

$$-\epsilon^3 \kappa n^2 \Omega^2. \qquad (4.78)$$

Note that the effects of curvature appear explicitly at $O(\epsilon)$. In a similar fashion, the dimensionless version of the evolution equation for the turbulent kinetic energy is obtained. After collecting the dimensional scale factor, $\tilde{U}^3/L$ and dividing through by μ^2, the final result is given by

$$\hat{\mathbf{n}} \cdot \frac{\partial \mathbf{R}}{\partial t} \frac{\partial k}{\partial n} + \epsilon \left[\frac{\partial k}{\partial t} + \left(U + \hat{\mathbf{s}} \cdot \frac{\partial \mathbf{R}}{\partial t} \right) \frac{\partial k}{\partial s} + \left(V - 2\kappa n \hat{\mathbf{n}} \cdot \frac{\partial \mathbf{R}}{\partial t} \right) \frac{\partial k}{\partial n} \right]$$

$$-\epsilon^2 n \left[2\kappa \frac{\partial k}{\partial t} + \left(\kappa U + \kappa \hat{\mathbf{s}} \cdot \frac{\partial \mathbf{R}}{\partial t} + \Omega \right) \frac{\partial k}{\partial s} + \kappa \left(2V - \kappa n \hat{\mathbf{n}} \cdot \frac{\partial \mathbf{R}}{\partial t} \right) \frac{\partial k}{\partial n} \right]$$

$$+\epsilon^3 \kappa n^2 \left[\kappa \frac{\partial k}{\partial t} + \Omega \frac{\partial k}{\partial s} + \kappa V \frac{\partial k}{\partial n} \right] = \mu \frac{\partial}{\partial n} \left(\nu_t \frac{\partial k}{\partial n} \right) - \langle uv \rangle \frac{\partial U}{\partial n} - \mu\varepsilon$$

$$-\epsilon \left[2\kappa n\mu \frac{\partial}{\partial n} \left(\nu_t \frac{\partial k}{\partial n} \right) - \left(\langle u^2 \rangle - \langle v^2 \rangle \right) \frac{\partial V}{\partial n} - 2\langle uv \rangle \kappa n \frac{\partial U}{\partial n} + \langle uv \rangle \kappa U - 2\kappa n\mu\varepsilon \right]$$

$$+\epsilon^2 \left[\mu \frac{\partial}{\partial s} \left(\nu_t \frac{\partial k}{\partial s} \right) + \kappa^2 n^2 \mu \frac{\partial}{\partial n} \left(\nu_t \frac{\partial k}{\partial n} \right) - 2\kappa n \left(\langle u^2 \rangle - \langle v^2 \rangle \right) \frac{\partial V}{\partial n} \right.$$

$$- \langle uv \rangle \left(\kappa^2 n^2 \frac{\partial U}{\partial n} + \frac{\partial V}{\partial s} - \kappa^2 n U \right) - \kappa^2 n^2 \mu \varepsilon \Bigg]$$

$$+ \epsilon^3 \kappa n \left[\kappa n \left(\langle u^2 \rangle - \langle v^2 \rangle \right) \frac{\partial V}{\partial n} + \langle uv \rangle \frac{\partial V}{\partial s} \right]. \tag{4.79}$$

Finally, the procedure is applied to the closure equations for the Reynolds' stresses, which gives

$$- \langle uv \rangle + \epsilon \kappa n \langle uv \rangle = \frac{\nu_t}{\mu} \frac{\partial U}{\partial n} + \epsilon \frac{\nu_t}{\mu} \kappa \left(U - n \frac{\partial U}{\partial n} \right) + \epsilon^2 \frac{\nu_t}{\mu} \frac{\partial V}{\partial s} , \tag{4.80}$$

$$\langle u^2 \rangle = 2 C_1 k + \epsilon \frac{2 \nu_t}{\mu} \frac{\partial V}{\partial n} , \qquad \langle v^2 \rangle = 2 C_3 k - \epsilon \frac{2 \nu_t}{\mu} \frac{\partial V}{\partial n}. \tag{4.81}$$

It is important to keep in mind that the model is formulated in terms of the kinematic parameter, μ, and the geometric parameter, ϵ, but ordered explicitly in terms of ϵ, with the assumption that $\epsilon \ll 1$, i.e., the turbulent layer is 'thin'. In the following, when referring to the leading order or $\mathcal{O}(1)$ model, the contributions of terms of $\mathcal{O}(\epsilon)$ and higher are neglected. Also, the particular flow regime analyzed is made explicit depending on the size of μ.

A first set of results can be obtained by retaining the leading $\mathcal{O}(1)$ terms in the momentum equations. At this order they read,

$$\hat{\mathbf{n}} \cdot \frac{\partial \mathbf{R}}{\partial t} \frac{\partial U}{\partial n} + \mu^2 \frac{\partial \langle uv \rangle}{\partial n} = 0 , \quad \text{and} \quad \frac{\partial P}{\partial n} = -\mu^2 \frac{\partial \langle v^2 \rangle}{\partial n}. \tag{4.82}$$

These can be regarded as an evolution equation for $\mathbf{R}$, describing its vertical motion, and an equation for the normal profile of the mean pressure. The hydrostatic assumption in MS83 and SM84 resulted in their neglecting the effects of normal turbulent stresses. It is evident that no coupling through the mean pressure occurs at the leading order. For the coupling to occur and in order to model the time evolution of the mean flow, it is necessary to retain also the $\mathcal{O}(\epsilon)$ terms in the streamwise momentum equation. If both $\mathcal{O}(1)$ and $\mathcal{O}(\epsilon)$ terms are retained, the streamwise component reads

$$\left[\mu^2 \frac{\partial \langle uv \rangle}{\partial n} + \hat{\mathbf{n}} \cdot \frac{\partial \mathbf{R}}{\partial t} \frac{\partial U}{\partial n} \right] + \epsilon \left[\frac{\partial U}{\partial t} + V \frac{\partial U}{\partial n} + \left(U + \hat{\mathbf{s}} \cdot \frac{\partial \mathbf{R}}{\partial t} \right) \frac{\partial U}{\partial s} - \kappa n \hat{\mathbf{n}} \cdot \frac{\partial \mathbf{R}}{\partial t} \frac{\partial U}{\partial n} \right.$$

$$-\mu^2 \left(\kappa n \frac{\partial \langle uv \rangle}{\partial n} - \frac{\partial \langle u^2 \rangle}{\partial s} + 2\kappa \langle uv \rangle \right) \Big] = \epsilon \left(\hat{\mathbf{s}} \cdot \mathbf{g}' - \frac{\partial P}{\partial s} \right), \qquad (4.83)$$

while the crossflow momentum equation is given by

$$\mu^2 \frac{\partial \langle v^2 \rangle}{\partial n} + \epsilon \left[\hat{\mathbf{n}} \cdot \frac{\partial \mathbf{R}}{\partial t} \frac{\partial V}{\partial n} - \mu^2 \kappa n \frac{\partial \langle v^2 \rangle}{\partial n} + \kappa U \hat{\mathbf{s}} \cdot \frac{\partial \mathbf{R}}{\partial t} + \kappa U^2 \right.$$

$$\left. + \mu^2 \left(\frac{\partial \langle uv \rangle}{\partial s} + \kappa \left(\langle u^2 \rangle - \langle v^2 \rangle \right) \right) \right] = -\frac{\partial P}{\partial n}$$

$$- \epsilon \left[U\Omega + \hat{\mathbf{n}} \cdot \mathbf{g}' - \kappa n \frac{\partial P}{\partial n} \right]. \qquad (4.84)$$

In order to substitute for the mean pressure into the streamwise component, it is necessary to integrate the crossflow component. It is clear that after integration and substitution, only the leading term in the normal turbulent stress is non-negligible. This suggests that a consistent set of equations is achieved if terms in the streamwise equation up to an order of magnitude $\mathcal{O}(\epsilon)$ smaller than the cross-flow equation are retained (Bradshaw, 1973). Contributions are considered up to $\mathcal{O}(\epsilon)$ in the streamwise momentum equation, which remains (4.83), and of $\mathcal{O}(1)$ in the crossflow momentum equation which is

$$\frac{\partial P}{\partial n} = -\mu^2 \frac{\partial \langle v^2 \rangle}{\partial n}. \qquad (4.85)$$

It is easy to show that choosing to scale contributions as for a mixing layer rather than for a 'breaker shear layer' or for a wake, the two momentum equations would reduce to those for curved mixing layers obtained by Bradshaw (1973) and Gibson and Rodi (1981) except for the extra terms representing the motion of the wave underlying the thin layer of turbulence and the rigid rotation, Ω, of the local frame of (s, n) coordinates.

The complete set of required equations is found by considering the equation for k up to $\mathcal{O}(\epsilon)$ in order to include the rate of change, $\partial k / \partial t$, among the retained contributions. To $\mathcal{O}(\epsilon)$,

$$\hat{\mathbf{n}} \cdot \frac{\partial \mathbf{R}}{\partial t} \frac{\partial k}{\partial n} + \epsilon \left[\frac{\partial k}{\partial t} + \left(U + \hat{\mathbf{s}} \cdot \frac{\partial \mathbf{R}}{\partial t} \right) \frac{\partial k}{\partial s} + \left(V - 2\kappa n \hat{\mathbf{n}} \cdot \frac{\partial \mathbf{R}}{\partial t} \right) \frac{\partial k}{\partial n} \right]$$

$$= \mu \frac{\partial}{\partial n} \left(\nu_t \frac{\partial k}{\partial n} \right) - \langle uv \rangle \frac{\partial U}{\partial n} - \mu \varepsilon$$

$$- \epsilon \left[2\kappa n \mu \frac{\partial}{\partial n} \left(\nu_t \frac{\partial k}{\partial n} \right) - \left(\langle u^2 \rangle - \langle v^2 \rangle \right) \frac{\partial V}{\partial n} - 2\langle uv \rangle \kappa n \frac{\partial U}{\partial n} + \langle uv \rangle \kappa U - 2\kappa n \mu \varepsilon \right].$$

$$(4.86)$$

The first term on the left hand side represents the transport of k due to the un-steadiness of the layer. Note that the leading order model is steady. The first term at the right hand side of the above equation is a diffusion term representing the redistribution of k due to eddy motion. This term usually vanishes when the equation is integrated over the layer thickness. In this model, the rate of dissipation of turbulent kinetic energy is a function of the curvature parameter. This is not unreasonable, and other models for curved shear layer have used a similar formulation (Launder *et al.*, 1977). The same equation for the transport of k is also valid for the other flow regimes (mixing layer and wake). The normal Reynolds' stresses are given by equation (4.81). From (4.80), the shear Reynold's stress up to $\mathcal{O}(\epsilon)$ is given by

$$-\langle uv \rangle + \epsilon \kappa n \langle uv \rangle = \frac{\nu_t}{\mu} \frac{\partial U}{\partial n} + \epsilon \frac{\nu_t}{\mu} \kappa \left(U - n \frac{\partial U}{\partial n} \right). \tag{4.87}$$

At leading order, the direct effects of curvature and rotation are absent in the governing equations (4.76-4.81). Curvature effects are first felt only at $\mathcal{O}(\epsilon)$. However, as Bradshaw (1973) points out, in fairly thin turbulent shear layers with streamline curvature or rotation, the magnitude of measured Reynolds' shear stress is an order of magnitude higher than that predicted by the exact transport equation. In a thin curved shear layer, such as one considered here, the extra strain rate is $e = \partial V/\partial x$ in Cartesian coordinates, or $e = -U/(n+R)$ in (s,n) coordinates, where R is the radius of curvature (See Section 3.1 of Bradshaw, 1973). The dimensional form of (4.87) is

$$\frac{-\langle uv \rangle}{\nu_t \frac{\partial U}{\partial n}} = 1 + \alpha_1 \frac{e_1}{\frac{\partial U}{\partial n}}, \tag{4.88}$$

where e_1 denotes the extra strain rate, and $\alpha_1 = 1$. Since the curvature, κ, here is equivalent to $-1/R$,

$$e_1 = \frac{\kappa U}{(1 - \kappa n)} = \frac{-U}{(n + R)}. \tag{4.89}$$

It has been seen in experimental data obtained from curved shear layers that $\alpha_1 \neq 1$, but $\alpha_1 \sim \mathcal{O}(10)$. At $\mathcal{O}(\epsilon^2)$, the extra strain rate is represented by

$$e_2 = \frac{\partial V}{\partial s} \frac{1}{(1 - \kappa n)}. \tag{4.90}$$

The influence of this particular term can be seen further by considering the production terms in the $\mathcal{O}(\epsilon)$ turbulent kinetic energy equation:

$$-\langle uv \rangle \kappa U - \langle uv \rangle (1 - 2\kappa n)\frac{\partial U}{\partial n} - \langle v^2 \rangle \frac{\partial V}{\partial n} + \langle u^2 \rangle \frac{\partial V}{\partial n}, \tag{4.91}$$

which, using (4.76) in the absence of rotation effects ($\Omega = 0$), can be written as

$$-\langle uv \rangle \kappa U - \langle uv \rangle (1 - 2\kappa n)\frac{\partial U}{\partial n} - \langle v^2 \rangle \frac{\partial V}{\partial n} + \langle u^2 \rangle \left(-\frac{\partial U}{\partial s} + \kappa V \right) + \underbrace{\langle u^2 \rangle \kappa n \frac{\partial V}{\partial n}}. \tag{4.92}$$

The production terms in equation (A 1.28) of Bradshaw (1973) are given by

$$-\langle uv \rangle \kappa U - \langle uv \rangle (1 - \kappa n)\frac{\partial U}{\partial n} - \langle v^2 \rangle \frac{\partial V}{\partial n} + \langle u^2 \rangle \left(-\frac{\partial U}{\partial s} + \kappa V \right) + \langle v^2 \rangle \kappa n \frac{\partial V}{\partial n} - \underline{\langle uv \rangle \frac{\partial V}{\partial s}}. \tag{4.93}$$

The under-braced term, which is the effect of longitudinal acceleration and geometric curvature on the normal stress, is absent in equation (4.93). Streamline curvature effects, such as the underlined term in (4.93) appear in the present case at $O(\epsilon^2)$ (see (4.79)). Note that there is also a difference of a factor, 2, in the simple shear strain rate term between the two equations. The reason for this apparent discrepancy is not immediately clear.

4.5 The $O(1)$ model

Previous analyses with both bores and hydraulic jumps suggest the use of a similarity profile for the velocity in the form of a cubic polynomial (MS83, SM84).

$$\langle u(1) \rangle (s, n, t) = \langle u(1) \rangle (s, 0, t) + f(s,t)g(\sigma) \text{ with } g(\sigma) = -A\sigma^3 + B\sigma^2 + C\sigma + D \text{ and } \sigma = n/b(s)$$

(4.94)

for the streamwise component of the mean, physical velocity, $\langle u(1) \rangle$, in the single phase turbulent layer. A cubic profile is chosen to model the inflection point of the velocity in the thin layer. Here, $b(s)$ is the local thickness of the single-phase, turbulent layer. In the assumption that the bulk of the wave can be modelled as irrotational, $\langle u(1) \rangle (s, 0, t) = \partial \phi / \partial s (s, 0, t)$, where ϕ is the velocity potential in the irrotational flow.

Equation (4.94) automatically sets a cubic profile for the relative flow velocity U. This is readily found by using (4.24) and (4.33), giving

$$\langle u(1) \rangle (s, n, t) = \hat{\mathbf{s}} \cdot \frac{\partial \mathbf{R}}{\partial t} + U(s, n, t) - n\Omega,$$

(4.95)

so that from the above two equations, the flow velocity can be expressed in terms of $f(s,t)$ and $g(\sigma)$ as

$$U(s, \sigma, t) = \langle u(1) \rangle (s, 0, t) + f(s,t)g(\sigma) - \hat{\mathbf{s}} \cdot \frac{\partial \mathbf{R}}{\partial t} + \sigma b(s)\Omega.$$

(4.96)

Both $f(s,t)$ and the coefficients of $g(\sigma)$ are to be found by means of matching conditions at $n = 0$ or $\sigma = 0$ [i.e. at the interface between the irrotational flow region $(n < 0)$ and the single-phase turbulent region $(0 \le n \le b)$], and at $n = b$ or $\sigma = 1$ (i.e., at the base of the surface layer).

Following MS83, the continuity of U at both boundaries of the layer, and vanishing turbulent shear stress at the interface with the irrotational flow region are imposed. Note that, as a major difference with the model of MS83, continuity of U at the upper boundary of the layer is achieved by forcing a boundary condition

132

at $n = b$ provided by the results of BP2, thus, taking the contribution of two-phase surface flow into account. As shown in the following, this fixes the coefficient, A, of the cubic profile, which was variable over the range $1/2 \leq A \leq 2$ in MS83. A represents the crossflow gradient of U at $n = b$.

The matching conditions are:

1. *Continuity of $\langle u(1) \rangle (s, n, t)$ at $n = 0$*

$$\lim_{n \to 0_-} \langle u(1) \rangle (s, n, t) = \lim_{n \to 0_+} \langle u(1) \rangle (s, n, t) \implies$$

$$\lim_{\sigma \to 0_-} \left[\frac{1}{(1 - \kappa \sigma b(s))} \frac{\partial \phi}{\partial s} \right] = \lim_{\sigma \to 0_+} \left[\frac{\partial \phi}{\partial s} + f(s, t) g(\sigma) \right]. \tag{4.97}$$

This gives the usual first condition:

$$g(0) = 0 \implies D = 0; \tag{4.98}$$

2. *Continuity of $\langle u(1) \rangle (s, n, t)$ at $n = b$*

The velocity at the bottom of the "surface layer" described in BP2 is set to $U(s, b, t) = U_b$, and continuity is enforced as

$$\lim_{n \to b_-} \langle u(1) \rangle (s, n, t) = \lim_{n \to b_+} \left[\hat{\mathbf{s}} \cdot \frac{\partial \mathbf{R}}{\partial t} + U(s, n, t) - n\Omega \right], \tag{4.99}$$

and from definition (4.95),

$$\langle u(1) \rangle (s, 0, t) + f(s, t) g(1) = \hat{\mathbf{s}} \cdot \frac{\partial \mathbf{R}}{\partial t} + U_b - b\Omega,$$

which guides the suitable choice for $f(s, t)$, i.e.,

$$\begin{aligned} f(s, t) &= \hat{\mathbf{s}} \cdot \frac{\partial \mathbf{R}}{\partial t} + U_b - b\Omega - \frac{\partial \phi}{\partial s}(s, 0, t) \\ &= -\hat{U} + U_b - b\Omega. \end{aligned} \tag{4.100}$$

So,

$$\hat{U} = \frac{\partial \phi}{\partial s}(s, 0, t) - \hat{\mathbf{s}} \cdot \frac{\partial \mathbf{R}}{\partial t}, \tag{4.101}$$

133

and the second standard condition is obtained:

$$g(1) = 1 \quad \Longrightarrow \quad C = A - B + 1. \tag{4.102}$$

3. *Vanishing turbulent shear stress at $n = 0$*

The leading-order contribution from equation (4.87) shows that the condition $[\langle uv \rangle]_{n=0}$ implies that

$$\left[\frac{\partial U}{\partial n} \right]_{n=0} = 0. \tag{4.103}$$

Using (4.102), the final condition linking A and B is found.

$$B = 1 + A + \frac{b(s)\Omega}{f(s,t)}. \tag{4.104}$$

This shows the second main difference between the present model and that of MS83: the coefficients of the cubic polynomial are not constants but functions of s. In either case, a strictly self-similar solution cannot be found (Madsen, 1981).

The above analysis gives the profiles for the physical and relative mean streamwise velocity. Plugging in for B, C and $D = 0$ in (4.94),

$$\langle u(1) \rangle (s, \sigma, t) = \frac{\partial \phi(s, 0, t)}{\partial s} f(s,t) A \sigma^3 + [f(s,t)(1 + A) + b(s)\Omega] \sigma^2 - b(s)\Omega\sigma, \tag{4.105}$$

which is identically satisfied at $\sigma = 0$. At $\sigma = 1$,

$$\langle u(1) \rangle (s, 1, t) = \langle u(1) \rangle (s, 0, t) + f(s), \tag{4.106}$$

which is satisfied by definition (4.94) since $g(1) = 1$. Using (4.95) and (4.105),

$$U(s, \sigma, t) = -\hat{\mathbf{s}} \cdot \frac{\partial \mathbf{R}}{\partial t} + \frac{\partial \phi(s, 0, t)}{\partial s} - f(s,t) A \sigma^3 + [f(s,t)(1 + A) + b(s)\Omega] \sigma^2. \tag{4.107}$$

Using (4.100), this can be written as

$$U(s, \sigma, t) = \hat{U} + (U_b - \hat{U})\sigma^2 + A \left[U_b - \hat{U} - b(s)\Omega \right] \sigma^2 (1 - \sigma). \tag{4.108}$$

134
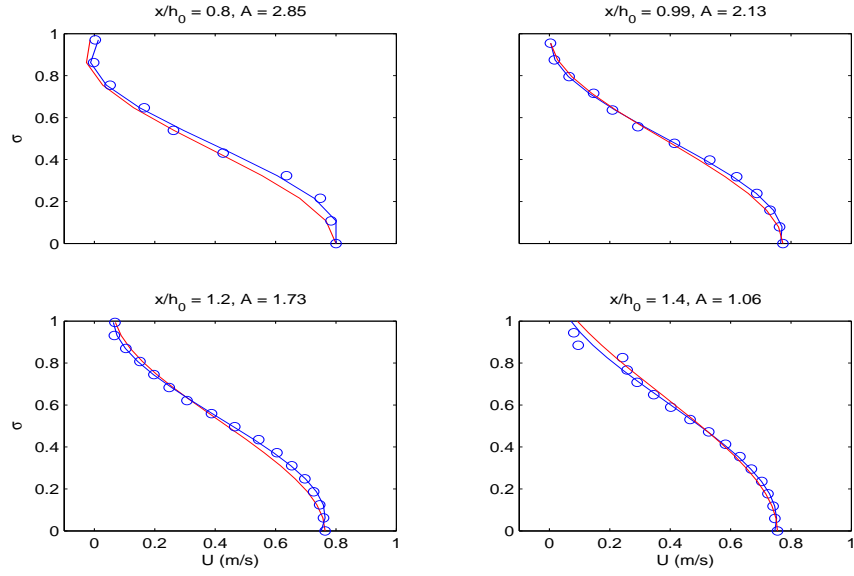
Figure 4.6: Cubic profile fit (blue solid line) for mean horizontal velocity data (circles). Red line is the estimated mean velocity from equation (4.109). σ is the non-dimensional vertical coordinate.

For $\Omega = 0$, this reduces to

$$U(s, \sigma, t) = \hat{U} + (U_b - \hat{U})\sigma^2[1 + A(1 - \sigma)]. \tag{4.109}$$

The analytical solution for the mean horizontal velocity can be checked using the present measurements. A cubic polynomial was fit to the measured values for U. This is shown as the blue solid line in Figure 4.6. The coefficient of the cubic term (A) was calculated from the fit and is shown at each horizontal location. Once A had been calculated, by approximating $\hat{U}$ and U_b with the mean horizontal velocity values at the bottom and top (at the 10 % contours of the Reynolds shear stress) of the mixing layer, the mean horizontal value at each vertical location was calculated from equation (4.109), and this is shown as the red line in the figure. Because of the small thickness of the shear layer near the toe, few data points were available for a robust fit to the profile. Therefore, the streamwise locations were chosen in

135

the middle part of the shear layer. Equation (4.109) is seen to provide a good approximation to the vertical variation of the velocity in the shear layer.

As a simple check for equation (4.108), $U(s, \sigma = 1, t)$ correctly gives U_b. The mean shear stress at $\sigma = 1$ is given by

$$\left[\frac{\partial U}{\partial n}\right]_{\sigma=1} = -f(s,t)\frac{\left[A - \left(2 + \frac{2b(s)\Omega}{f(s,t)}\right)\right]}{b(s)}. \tag{4.110}$$

This vanishes for $A = 2 + [2b(s)\Omega/f(s,t)]$, or in absence of rotation ($\Omega = 0$) for $A = 2$ as in MS83. To determine an analytic expression for A, the leading-order continuity equation is used to compute V, so that

$$
\begin{aligned}
V(s, n, t) &= -\int \frac{\partial U}{\partial s} dn + C_v(s, t) \\
\\
&= -\int \frac{\partial}{\partial s}\left[\frac{\partial \phi(s, 0, t)}{\partial s} + f(s, t)g\left(\frac{n}{b(s)}\right) - \hat{\mathbf{s}} \cdot \frac{\partial \mathbf{R}}{\partial t} + n\Omega\right] dn + C_v(s, t) \\
&= -n\frac{\partial \hat{U}}{\partial s} - b(s)\frac{\partial f(s, t)}{\partial s}G(\sigma) + f(s, t)\frac{\partial b(s)}{\partial s}\tilde{G}(\sigma) \tag{4.111} \\
&\quad - \frac{n^2}{2}\frac{\partial \Omega(s, t)}{\partial s} + C_v(s, t),
\end{aligned}
$$

where

$$G(\sigma) = \int g(\sigma)d\sigma = -\frac{A}{4}\sigma^4 + \frac{B}{3}\sigma^3 + \frac{(A - B + 1)}{2}\sigma^2, \tag{4.112}$$

$$\tilde{G}(\sigma) = \int \sigma \dot{g}(\sigma)d\sigma = -\frac{3A}{4}\sigma^4 + \frac{2B}{3}\sigma^3 + \frac{(A - B + 1)}{2}\sigma^2, \tag{4.113}$$

and $C_v(s, t)$ is an integration constant which, since $G(0) = 0$ and $\tilde{G}(0) = 0$, can be written in terms of the vertical velocity at the bottom of the layer: $V(s, 0, t) \equiv V_0$, as $C_v(s, t) = V_0$. As already mentioned, A is not a free parameter in the model. It is fixed by the boundary condition at $n = b$. The general expression for A is derived by means of the kinematic boundary condition found in BP2 to hold at the base of the 'surface layer' ($n = b$):

$$\frac{\partial b(s)}{\partial t} + U_b\frac{\partial b(s)}{\partial s} - V_b = -W, \tag{4.114}$$

in which W is the normal-to-surface velocity needed to model the inflow or outflow across the surface layer, $W = \frac{\partial}{\partial s}\int_b^h \gamma U_w dn + \frac{\partial d}{\partial t}$, γ is the intermittency factor, and U_w is the horizontal water velocity in the surface layer. Substituting for the mean velocities from (4.108) and (4.111),

$$
\begin{aligned}
A = \frac{1}{f(s,t)\frac{\partial}{\partial s}[b(U_b - \hat{U}) - b^2\Omega]} & \left[12(b\Omega + \hat{U} - U_b)\frac{\partial b}{\partial t} \right. \\
+\ & 2(-2U_b\hat{U} + U_b b\Omega + 5b\Omega\hat{U} - 2U_b^2 + 4\hat{U}^2)\frac{\partial b}{\partial s} + 2b(3b\Omega + 2\hat{U} - 2U_b)\frac{\partial U_b}{\partial s} \\
+\ & 2b(3b\Omega + 4\hat{U} - 4U_b)\frac{\partial \hat{U}}{\partial s} + 2b^2(\hat{U} - U_b)\frac{\partial \Omega}{\partial s} + 12(b\Omega + \hat{U} - U_b)(W - V_0) \left. \right].
\end{aligned}
\tag{4.115}
$$

Having determined the profiles for the mean flow, the profiles for turbulent velocity are readily found following the approach of MS83, i.e., by assuming that dissipation and production terms in the equation for k, the leading terms of equation (4.86), are expressed by the same crossflow profile. By expressing the turbulence dissipation ε through (4.45), the suitable choices are found to be

$$
k^{1/2} = \Lambda(s)f(s,t)\dot{g}(\sigma),
\tag{4.116}
$$

$$
\nu_t \propto k^{1/2}b = C_t\Lambda(s)f(s,t)b(s)\dot{g}(\sigma), \quad \text{and}
\tag{4.117}
$$

$$
\varepsilon \propto \frac{k^{3/2}}{b} = C_\varepsilon\frac{\Lambda(s)^3 f(s,t)^3}{b(s)}[\dot{g}(\sigma)]^3,
\tag{4.118}
$$

in which C_t and C_ε are empirical turbulent constants (Launder and Spalding, 1972), and $\Lambda(s)$ is a function measuring the local imbalance between turbulence production and dissipation (see MS83).

4.6   The $\mathcal{O}(\epsilon)$ model

As can be seen by considering equations (4.76)-(4.81), the $\mathcal{O}(\epsilon)$ model (retaining both $\mathcal{O}(1)$ and $\mathcal{O}(\epsilon)$ terms in the governing equations) is characterized by the direct effects of curvature. Therefore, it is necessary to begin by incorporating

137

these effects into the solution for the mean velocity. From equation (4.87), the third boundary condition (4.103) leads to

$$B = 1 + A + \frac{b}{f}(\Omega + \kappa\hat{U}). \tag{4.119}$$

Plugging in for B and C (which remains the same) in (4.96), the $O(\epsilon)$ solution for the mean horizontal velocity is found to be

$$U(s, \sigma, t) = \hat{U} - fA\sigma^3 + [f(1 + A) + b(\Omega + \kappa\hat{U})]\sigma^2 - b\kappa\hat{U}\sigma. \tag{4.120}$$

The mean flow shear at the top of the layer is given by

$$\left[\frac{\partial U}{\partial n}\right]_{n=b} = \frac{1}{b}[2(U_b - \hat{U}) - A(U_b - \hat{U} - b\Omega) + b\kappa\hat{U}], \tag{4.121}$$

which vanishes for

$$A = \frac{2(U_b - \hat{U}) + b\kappa\hat{U}}{(U_b - \hat{U} - b\Omega)}, \tag{4.122}$$

or for $\Omega = 0$ and $\kappa = 0$, for $A = 2$. Note that the $\mathcal{O}(1)$ expression for both A and B can be recovered by simply setting $\kappa = 0$. $V(s, n, t)$ is determined by using the $\mathcal{O}(\epsilon)$ continuity equation,

$$V(s, n, t) = \frac{1}{(1 - \kappa n)} \int \left(-\frac{\partial U}{\partial s} + n\frac{\partial \Omega}{\partial s}\right) dn + C_v(s, t), \tag{4.123}$$

where $C_v(s, t)$ is an integration constant, and equals $C_v(s, t) = V_0$, the vertical velocity at the boundary with irrotational flow. After some algebra, the expression for $V(s, n, t)$ is found to be

$$V(s, n, t) = \frac{1}{(1 - \kappa n)}\left[-n\frac{\partial \hat{U}}{\partial s} - b\frac{\partial f}{\partial s}G(\sigma) + f\frac{\partial b}{\partial s}\tilde{G}(\sigma) + V_0\right]. \tag{4.124}$$

Note that the direct effect of the rotation term cancels out in the final expression for $V(s, n, t)$. As before, using the kinematic boundary condition from BP2, the expression for A is found to be

$$A = \frac{1}{f(s,t)\frac{\partial}{\partial s}[b(U_b - \hat{U}) - b^2\Omega]}\left[12(1 - \kappa b)(b\Omega + \hat{U} - U_b)\frac{\partial b}{\partial t}\right. \qquad (4.125)$$

$$+ \quad 2(-2U_b\hat{U} + U_b b\Omega + 5b\Omega\hat{U} - 2U_b^2 + 4\hat{U}^2 - b\kappa\hat{U}^2 - 2b^2\Omega\kappa\hat{U} + 6U_b^2\kappa b - 5U_b b\kappa\hat{U}$$

$$- \quad 6U_b b^2\Omega\kappa)\frac{\partial b}{\partial s} + 2b(3b\Omega + 2\hat{U} - 2U_b + b\kappa\hat{U})\frac{\partial U_b}{\partial s} + 2b(3b\Omega + 4\hat{U} - 4U_b$$

$$- \quad b\kappa\hat{U})\frac{\partial \hat{U}}{\partial s} + 2b^2(2U_b - 2\hat{U} - 3b\Omega - b\kappa\hat{U})\frac{\partial \Omega}{\partial s} - 12(b\Omega + \hat{U} - U_b)\{V_0$$

$$- \quad \left. W(1 - \kappa b)\}\right].$$

Setting $\kappa = 0$ in the above expression does not recover the $\mathcal{O}(1)$ expression in (4.115). The difference lies in the coefficient for $\frac{\partial \Omega}{\partial s}$ and arises indirectly because of the presence of rotation effects in the continuity equation at this order.

4.7   The $O(1)$ integral equations

The model equations at the chosen order can be integrated in the cross-flow direction. The integration can be performed in two complementary ways. The first approach explicitly uses the profiles defined in the previous section. With this procedure, which follows the ideas of MS83, a quantitative description of the flow is found by forcing a solution which obeys one simple physical constraint, i.e., an inflection point for the velocity within the layer. Physical insights into the dynamics near the toe are obtained not only from the equations, but also from the solution. In addition, the boundary conditions at the interface between the single-phase turbulent layer and the irrotational flow are found. In the second approach, followed in section 4.8, the normally-integrated equations are recast in terms of layer-integrated variables to develop evolution equations for the thin-layer

dynamics. By definition, these equations are valid at the base of the layer, and are, therefore, boundary conditions for the irrotational flow.

The dynamics of the leading edge of the breaker region are analyzed first, where $\mu \sim \mathcal{O}(1)$. Since the continuity equation for the mean flow (the leading order terms of equation (4.76)) has already been used to determine $V(s, n, t)$, the integration of the equation is identically satisfied. The leading-order contributions from the normal component of the momentum equation (see equation (4.82)) are essentially a balance between the normal turbulent stress and the normal mean pressure gradient. Using the profiles for the normal stress and the turbulent kinetic energy, this can be integrated across the layer from $n = 0$ to $n = b$ to give

$$P_0 = P_b + 2\rho C_3 \Lambda^2 f^2 \left[(-A + 2) \left(-A + 2 + \frac{2b\Omega}{f} \right) \right]. \tag{4.126}$$

P_0 and P_b are respectively the pressure at the bottom and top of the layer, and P_b can be obtained from the dynamic boundary condition derived in BP2 (see their equation (5.19)) which includes the surface layer contributions. Note the presence of extra pressure with respect to P_b due to rotation and non-zero mean shear stress at the top of the layer. The effect of gravity is felt at a higher order $(O(\epsilon))$. The normal turbulent stresses make a dominant contribution to the non-hydrostatic component of the pressure. In the absence of rotation and mean shear at the top of the layer $(\Omega = 0$ and $A = 2)$, $P_0 = P_b$. In other words, there is uniform pressure across the layer. On integrating the $\mathcal{O}(1)$ contributions from the streamwise momentum equation and using the boundary condition (4.103),

$$\hat{\mathbf{n}} \cdot \frac{\partial \mathbf{R}}{\partial t} = \frac{C_t \Lambda f^2 (2 - A) \left[A - \left(2 + \frac{2b\Omega}{f} \right) \right]^2}{\left(U_b - \hat{U} \right)}, \tag{4.127}$$

which describes the unsteady vertical motion of the layer. Note that the steady state is recovered for $A = 2$.

Before integrating the turbulent kinetic energy balance, it is convenient to change from (s, n) coordinates to (s, σ) coordinates. The normal integration of the $\mathcal{O}(1)$ turbulent kinetic energy equation is thus given by

$$\underbrace{\hat{\mathbf{n}} \cdot \frac{\partial \mathbf{R}}{\partial t} \frac{\partial k}{\partial \sigma}}_{I} = \underbrace{\frac{\partial}{\partial \sigma} \left(\nu_t \frac{1}{b} \frac{\partial k}{\partial \sigma} \right)}_{II} + \underbrace{\nu_t \frac{1}{b} \left(\frac{\partial U}{\partial \sigma} \right)^2}_{III} - \underbrace{\varepsilon}_{IV}. \tag{4.128}$$

Using the expression derived in equation (4.127) for $\hat{\mathbf{n}} \cdot \frac{\partial \mathbf{R}}{\partial t}$, $-\langle uv \rangle = \nu_t \frac{\partial U}{\partial n}$, and using the profiles for ν_t, U, and k, each term is integrated across the layer.

$$I = \hat{\mathbf{n}} \cdot \frac{\partial \mathbf{R}}{\partial t} \Lambda^2 f^2 \left[\left(A - 2 - \frac{b\Omega}{f} \right)^2 - \left(\frac{b\Omega}{f} \right)^2 \right], \tag{4.129}$$

$$II = 2 C_t \Lambda^3 f^3 \left[\left(A - 2 - \frac{b\Omega}{f} \right)^2 \left(-4A + 2 + \frac{2b\Omega}{f} \right) \right. \tag{4.130}$$

$$\left. - \frac{b^2 \Omega^2 \left(2 + 2A + \frac{2b\Omega}{f} \right)}{f^2} \right],$$

$$III = -\tfrac{1}{105} C_t \Lambda (-490 f^2 b\Omega + 126 f^3 A - 70 b^3 \Omega^3 - 350 f b^2 \Omega^2 \tag{4.131}$$

$$- 49 b\Omega f^2 A^2 + 217 f^2 A b\Omega + 91 f A b^2 \Omega^2 + 6 A^3 f^3 - 63 A^2 f^3 - 210 f^3),$$

$$IV = C_\varepsilon \Lambda^3 f^3 \left[\left(-A + 2 + \frac{b\Omega}{f} \right)^3 + \left(\frac{b\Omega}{f} \right)^3 \right]. \tag{4.132}$$

Substituting for $\hat{\mathbf{n}} \cdot \partial \mathbf{R} / \partial t$ from equation (4.127), an expression for $\Lambda(s)$ describing the local imbalance between production and dissipation is found. In the absence of rotation,

$$\Lambda^2(s) = \frac{-6A^3 + 63A^2 - 126A + 210}{105(2 - A)^3 \left[(2 - A)^2 - 4 \frac{(1 - 2A)}{(2 - A)} + \frac{C_\varepsilon}{C_t} \right]}. \tag{4.133}$$

The first thing to note in the above expression is the singularity at $A = 2$. The variation of A with Λ^2 is shown in Figure 4.7. Since Λ^2 is the dissipation divided by the production, near the leading edge of the breaker, $\Lambda^2 < 1$. The singularity appears when the production vanishes, and this is expected to occur in the downstream direction. The increase in Λ^2 with decreasing A ($A > 2$) is consistent with the

141
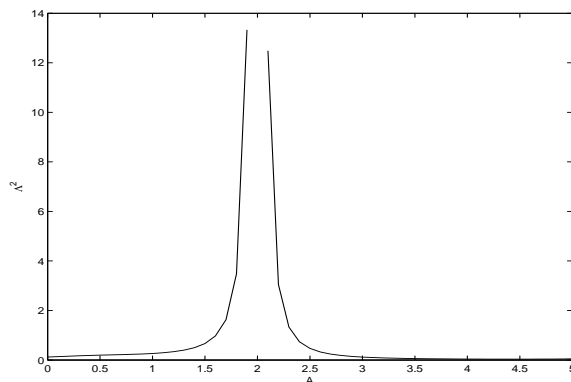
Figure 4.7: Variation of Λ^2 with A.

decreasing shear (quantified by A) in the downstream direction. In contrast to MS83, where A is a constant (chosen as a best-fit to data), $A(s)$ varies in the streamwise direction, and its variation can be modeled in terms of the dynamics of the turbulence near the foot of the breaker. As already noted, the streamwise dependence follows from the more complex flow situation analyzed here (e.g. non-hydrostatic pressure, vertical accelerations, etc.) with respect to those of MS83.

In the far wake regime ($\mu = \mathcal{O}(\epsilon) \ll 1$), the continuity equation, and hence the expression for $V(s, n, t)$, remains unchanged. From the leading-order term in the normal momentum equations, the pressure is uniform across the layer. The Reynolds shear stress equation shows that the mean horizontal velocity is also uniform across the layer, which when used in the turbulent kinetic energy balance, gives

$$\hat{\mathbf{n}} \cdot \frac{\partial \mathbf{R}}{\partial t} \frac{\partial k}{\partial n} = -\langle uv \rangle \frac{\partial U}{\partial n} \quad \Longrightarrow \quad \frac{\partial k}{\partial n} = 0, \tag{4.134}$$

i.e., the vertical distribution of the turbulent kinetic energy is uniform across the wake.

142

4.8 The $O(\epsilon)$ integral equations

In this section, the governing equations are integrated across the width of the thin layer (from $n = 0$ to $n = b$), and using the boundary conditions in BP2 and MB02 which are enforced at the top of the layer, the dynamics of the turbulent thin layer are described in terms of the layer-averaged variables. The aim is to develop a model which, apart from its governing variables, is determined entirely by the information provided from the underlying flow so that the integrated equations also serve as boundary conditions for the irrotational flow below. The variables for the model are the layer thickness, b, the layer-averaged mean horizontal velocity, $\overline{U} \equiv \frac{\int_0^b U\,dn}{b}$, and the layer-averaged turbulent kinetic energy, $\overline{k} \equiv \frac{\int_0^b k\,dn}{b}$. The following analysis assumes $\Omega = 0$. As opposed to plunging breakers, where the wave face overturns and falls onto the trough, in spilling breakers, the angular velocity in the turbulent layer can be assumed to be small. For steady breakers, the angular velocity is zero by definition. MS83 found that the streamwise variation of the calculated mean surface, when fit to available hydraulic jump data, was rather insensitive to the prescribed velocity profile, or in other words, the choice of A. In the present case, due to the additional effects of curvature, unsteadiness and non-hydrostatic pressure, this simplification cannot be made, as is obvious from the analytic expressions for $A(s)$ and the physical arguments discussed in the previous section which suggest a decrease in $A(s)$ in the downstream direction. For now, the streamwise variation of $A(s)$ is kept arbitrary. A physical model for $A(s)$ is described toward the end of the section.

4.8.1 The continuity equation

The normal integration of the $O(\epsilon)$ continuity equation is given by

$$\int_0^b \left[\frac{\partial U}{\partial s} + \frac{\partial[(1 - \kappa n)V]}{\partial n} = n\frac{\partial \Omega}{\partial s} \right] dn. \tag{4.135}$$
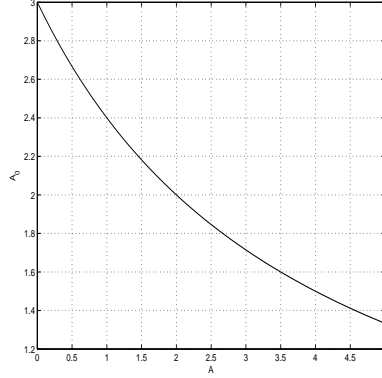
Figure 4.8: Variation of A_0 with A.

Applying Leibnitz rule,

$$b\frac{\partial \overline{U}}{\partial s} + \overline{U}\frac{\partial b}{\partial s} - U_b\frac{\partial b}{\partial s} + (1 - \kappa b)V_b = V_0. \tag{4.136}$$

U_b can be expressed in terms of $\overline{U}$ by integrating equation (4.109), giving

$$U_b = A_0(\overline{U} - \hat{U}) + \hat{U}, \tag{4.137}$$

where

$$A_0 = \frac{12}{(4 + A)}. \tag{4.138}$$

The streamwise dependence of the coefficient A_0, and other functions of $A(s)$ which follow, is shown indirectly through their dependence on $A(s)$. This is done to evaluate the order of magnitude contribution of the coefficients to the various terms.

V_b is eliminated from equation (4.136) by using the kinematic free surface boundary condition from BP2:

$$V_b = \frac{\partial b}{\partial t} + U_b\frac{\partial b}{\partial s} + W, \tag{4.139}$$

144
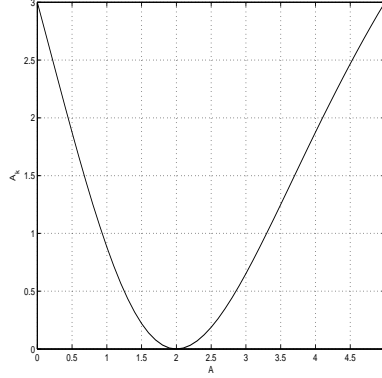
Figure 4.9: Variation of A_k with A.

where $W = \frac{\partial d}{\partial t} + \frac{\partial}{\partial s}\left[\int_b^h U_w \gamma dn\right]$ is a vertical velocity representing mass conservation within the surface layer. U_w is the zone-averaged velocity for the water phase in the surface layer, and d is the amount of water in the surface layer,

$$d \equiv \int_b^h \gamma dn. \tag{4.140}$$

$h(s,t)$ is the upper limit of the surface layer. From MB02 (see also Borue *et al.*, 1995), the zone averaged velocity for the water phase can be expressed in terms of the conventional averaged velocity for the single-phase flow as $U_w = \frac{U}{\gamma}$. Further, as in MB02, assuming an almost-uniform profile for the velocity in the surface layer,

$$\frac{\partial \left[\int_b^h U dn\right]}{\partial s} \approx \frac{\partial [U_b(h-b)]}{\partial s}. \tag{4.141}$$

In the case of weakly splashing regimes, both d and $(h-b)$ can be related to the turbulence intensity at the base of the layer as,

$$d \approx \frac{C_{1k}k_b}{g}, \quad (h-b) \approx C_{2k}\frac{k_b}{g}, \quad C_{2k} \approx 2C_{1k} = O(1). \tag{4.142}$$

This essentially states that the "weight" of the surface layer is given in terms of the turbulent kinetic energy at the base of the layer. Next, the $O(1)$ profile for the

145

turbulent kinetic energy is used to express k_b in terms of the layer-averaged kinetic energy $(\overline{k})$ as

$$k_b = A_k \overline{k}, \tag{4.143}$$

where A_k represents the coupling between the surface layer and the single phase turbulent layer.

$$A_k \equiv \frac{15(A-2)^2}{(2A^2 - 5A + 20)}. \tag{4.144}$$

After making the substitutions, V_b is given as

$$
\begin{aligned}
V_b \;=\; & \frac{\partial b}{\partial t} + [A_0(\overline{U} - \hat{U}) + \hat{U}]\frac{\partial b}{\partial s} \\
& + \frac{C_{2k}A_k}{g}[A_0(\overline{U} - \hat{U}) + \hat{U}]\frac{\partial \overline{k}}{\partial s} + \frac{C_{2k}A_k A_0 \overline{k}}{g}\frac{\partial \overline{U}}{\partial s} \\
& + \frac{C_{1k}A_k}{g}\frac{\partial \overline{k}}{\partial t} + \frac{C_{2k}A_k \overline{k}}{g}\left[(1 - A_0)\frac{\partial \hat{U}}{\partial s} + (\overline{U} - \hat{U})\frac{\partial A_0}{\partial s}\right].
\end{aligned} \tag{4.145}
$$

Using the integrated turbulent kinetic energy equation (derived later; see equation 4.218) to substitute for $\frac{\partial \overline{k}}{\partial t}$, the continuity equation can be written as

$$\frac{\partial b}{\partial t} + C_B \frac{\partial b}{\partial s} + C_U \frac{\partial \overline{U}}{\partial s} + C_K \frac{\partial \overline{k}}{\partial s} = C_R, \tag{4.146}$$

where

$$C_B \;=\; \frac{\overline{U}}{(1 - \kappa b)} - \frac{\kappa b}{(1 - \kappa b)}[A_0(\overline{U} - \hat{U}) + \hat{U}] - \frac{A_k}{g}C_{1k}K_B, \tag{4.147}$$

$$C_U \;=\; \frac{b}{(1 - \kappa b)} + \frac{A_k}{g}[C_{2k}A_0 \overline{k} - C_{1k}K_U], \tag{4.148}$$

$$C_K \;=\; \frac{A_k}{g}[C_{2k}\{A_0(\overline{U} - \hat{U}) + \hat{U}\} - C_{1k}K_K], \quad \text{and} \tag{4.149}$$

$$C_R \;=\; \frac{V_0}{(1 - \kappa b)} - \frac{A_k}{g}\left[C_{2k}(1 - A_0)\overline{k}\frac{\partial \hat{U}}{\partial s} + C_{2k}\overline{k}(\overline{U} - \hat{U})A_{0s} + C_{1k}K_R\right]. \tag{4.150}$$

Note that in the absence of curvature, and neglecting the surface-layer coupling, this reduces to

$$\frac{\partial b}{\partial t} + \overline{U}\frac{\partial b}{\partial s} = V_0, \tag{4.150}$$

146

which represents mass conservation in the thin layer. V_0 is a source term signifying the entrainment from the flow below. In a similar fashion, the normally integrated $O(1)$ continuity equation, which will be used later, can be written as

$$\frac{\partial b}{\partial s} + C'_B \frac{\partial b}{\partial s} + C'_U \frac{\partial \overline{U}}{\partial s} + C'_K = C'_R, \tag{4.151}$$

where

$$C'_B = \overline{U} - \frac{A_k}{g} C_{1k} K_B, \tag{4.152}$$

$$C'_U = b + \frac{A_k}{g} [C_{2k} A_0 \overline{k} - C_{1k} K_U], \tag{4.153}$$

$$C'_K = \frac{A_k}{g} [C_{2k}\{A_0(\overline{U} - \hat{U}) + \hat{U}\} - C_{1k} K_K], \quad \text{and} \tag{4.154}$$

$$C'_R = V_0 - \frac{A_k}{g} \left[C_{2k}(1 - A_0)\overline{k}\frac{\partial \hat{U}}{\partial s} + C_{2k}\overline{k}(\overline{U} - \hat{U})\frac{\partial A_0}{\partial s} + C_{1k} K_R \right].$$

This is derived for later use. Note that equation (4.146) can be reduced to the integrated $O(1)$ continuity equation by setting the geometric curvature to zero.

4.8.2 The streamwise momentum equation

The streamwise momentum equation can be written in conservative form as

$$\int_0^b \left[\underbrace{\frac{\partial U}{\partial t}}_{I} + \underbrace{\frac{\partial U^2}{\partial s}}_{II} + \underbrace{\frac{\partial (UV)}{\partial n}}_{III} + \underbrace{(1 - \kappa n)\left(\hat{\mathbf{n}} \cdot \frac{\partial \mathbf{R}}{\partial t}\right)\frac{\partial U}{\partial n}}_{IV} \right. \tag{4.155}$$

$$+ \underbrace{\left(\hat{\mathbf{s}} \cdot \frac{\partial \mathbf{R}}{\partial t}\frac{\partial U}{\partial s}\right)}_{V} = -\underbrace{\frac{\partial (P/\rho)}{\partial s}}_{VI} + \underbrace{\hat{\mathbf{s}} \cdot \mathbf{g}'}_{VII} - \underbrace{\frac{\partial[(1 - \kappa n)\langle uv \rangle]}{\partial n}}_{VIII}$$

$$\left. - \underbrace{\frac{\partial \langle u^2 \rangle}{\partial s}}_{IX} + \underbrace{2\kappa \langle uv \rangle}_{X} \right] dn.$$

Each under-braced term is integrated separately for clarity. Since some of the algebra becomes tedious when computed by hand, the symbolic mathematical software
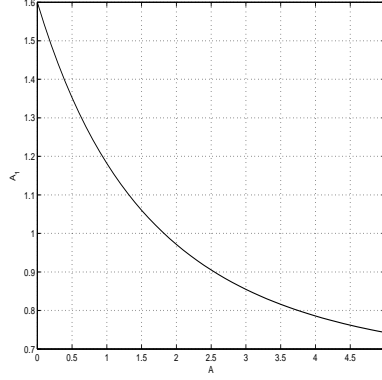
Figure 4.10: Variation of A_1 with A.

MAPLE is used. This also ensures greater accuracy. Applying Leibnitz rule on the first term,

$$I = \overline{U}\underbrace{\frac{\partial b}{\partial t}}_{Ia} + b\frac{\partial \overline{U}}{\partial t}\underbrace{-U_b\frac{\partial b}{\partial t}}_{Ic}, \qquad (4.156)$$

where Ia is replaced from the integrated $O(1)$ continuity equation, and Ic is to be combined later with other boundary terms. On substitution,

$$I = b\frac{\partial \overline{U}}{\partial t} - \overline{U}C'_B\frac{\partial b}{\partial s} - \overline{U}C'_U\frac{\partial \overline{U}}{\partial s} - \overline{U}C'_K\frac{\partial \overline{k}}{\partial s} + \overline{U}C'_R\underbrace{-U_b\frac{\partial b}{\partial t}}_{Ic}. \qquad (4.157)$$

Again, by applying the Leibnitz rule, the second term in equation (4.155) is given by

$$II = \underbrace{\frac{\partial \overline{\tau^D_{ss}}}{\partial s}}_{IIa} + \overline{U}^2\frac{\partial b}{\partial s} + b\overline{U}\frac{\partial \overline{U}}{\partial s}\underbrace{-U_b^2\frac{\partial b}{\partial s}}_{IIb}, \qquad (4.158)$$

where IIb is to be combined later with other boundary terms. $\overline{\tau^D_{ss}}$ is a kind of dispersive stress arising due to the vertical variation of the mean horizontal velocity, and is defined as

$$\overline{\tau^D_{ss}} \equiv \int_0^b (U - \overline{U})^2 dn. \qquad (4.159)$$

$$\frac{\partial \overline{\tau^D_{ss}}}{\partial s} = \frac{A_1}{2}(\overline{U} - \hat{U})^2\frac{\partial b}{\partial s} + A_1 b(\overline{U} - \hat{U})\frac{\partial \overline{U}}{\partial s} - A_1 b(\overline{U} - \hat{U})\frac{\partial \hat{U}}{\partial s} + A_2 b(\overline{U} - \hat{U})^2\frac{\partial A}{\partial s}, \quad (4.160)$$

148
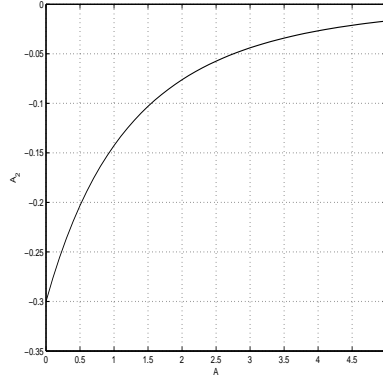
Figure 4.11: Variation of A_2 with A.

and

$$A_1 = \frac{2(13A^2 + 56A + 448)}{35(4 + A)^2} \tag{4.161}$$

$$A_2 = \frac{48(A - 14)}{35(4 + A)^3}.$$

Therefore, term II becomes

$$II = [\overline{U}^2 + \frac{A_1}{2}(\overline{U} - \hat{U})^2]\frac{\partial b}{\partial s} + [b\overline{U} + A_1 b(\overline{U} - \hat{U})]\frac{\partial \overline{U}}{\partial s} \tag{4.162}$$

$$- A_1 b(\overline{U} - \hat{U})\frac{\partial \hat{U}}{\partial s} + A_2 b(\overline{U} - \hat{U})^2\frac{\partial A}{\partial s} \underbrace{-U_b^2 \frac{\partial b}{\partial s}}_{IIb}.$$

The third term is given by

$$III = \underbrace{U_b V_b}_{IIIa} - \hat{U} V_0. \tag{4.163}$$

Ic, IIb and $IIIa$ are now combined. The kinematic boundary condition from BP2 is used again to get

$$Ic + IIb + IIIa = U_b W. \tag{4.164}$$

On replacing U_b and W as before,

$$III = [A_0(\overline{U} - \hat{U}) + \hat{U}]W - \hat{U}V_0 \tag{4.165}$$

$$= \frac{A_k}{g}[A_0(\overline{U} - \hat{U}) + \hat{U}]\left[(-C_{1k}K_B)\frac{\partial b}{\partial s}\right.$$

$$+ \; (-C_{1k}K_U + C_{2k}A_0\overline{k})\frac{\partial \overline{U}}{\partial s}$$

$$+ \; (-C_{1k}K_K + C_{2k}[A_0(\overline{U} - \hat{U}) + \hat{U}])\frac{\partial \overline{k}}{\partial s}$$

$$+ \; \left(C_{2k}\overline{k}(\overline{U} - \hat{U})A_{0s} + C_{1k}K_R + C_{2k}(1 - A_0)\overline{k}\frac{\partial \hat{U}}{\partial s}\right)\Bigg] - \hat{U}V_0.$$

Term IV is now integrated to yield

$$IV = \hat{\mathbf{n}} \cdot \frac{\partial \mathbf{R}}{\partial t}[(1 - \kappa b)U_b - \hat{U} + \kappa b\overline{U}]. \tag{4.166}$$

Replacing U_b, and after some algebra,

$$IV = \hat{\mathbf{n}} \cdot \frac{\partial \mathbf{R}}{\partial t}(\overline{U} - \hat{U})[A_0 + \kappa b(1 - A_0)], \tag{4.167}$$

which represents the vertical motion of the layer and vanishes in the absence of shear. Similarly, term V is integrated to give

$$V = \hat{\mathbf{s}} \cdot \frac{\partial \mathbf{R}}{\partial t}\left[\overline{U}\frac{\partial b}{\partial s} + b\frac{\partial \overline{U}}{\partial s} - U_b\frac{\partial b}{\partial s}\right] \tag{4.168}$$

$$= \hat{\mathbf{s}} \cdot \frac{\partial \mathbf{R}}{\partial t}\left[(1 - A_0)(\overline{U} - \hat{U})\frac{\partial b}{\partial s} + b\frac{\partial \overline{U}}{\partial s}\right].$$

Applying Leibnitz rule on the pressure term, the integration gives

$$VI = -\frac{1}{\rho}\left[\overline{P}\frac{\partial b}{\partial s} + b\frac{\partial \overline{P}}{\partial s} - P_b\frac{\partial b}{\partial s}\right]. \tag{4.169}$$

Since the $O(1)$ contribution from the normal momentum equation is given by $\overline{P} = -2\rho C_3\overline{k}$ (equation (4.81) and (4.82)), equation (7.9) can be written in terms of the layer-averaged kinetic energy as

$$VI = 2C_3\overline{k}\frac{\partial b}{\partial s} + 2C_3b\frac{\partial \overline{k}}{\partial s} + \underbrace{\frac{P_b}{\rho}\frac{\partial b}{\partial s}}_{VIc}. \tag{4.170}$$

150

The dynamic free surface condition is now used to evaluate the pressure at the top of the layer (P_b). From MB02,

$$\frac{P_b}{\rho} \approx -\langle v^2 \rangle_b - \frac{1}{\rho} \int_b^h \left[\frac{(1-\gamma)}{\gamma} P \right] \frac{\partial \gamma}{\partial n} dn + \mathbf{g} \cdot \hat{\mathbf{n}} d, \tag{4.171}$$

which shows the contributions from the normal turbulent stress, gravity, and the intermittency associated with the two-phase flow. The curvature effect in the surface layer pressure term has been neglected since it is an $O(\epsilon)$ term. Further, from equation (4.80), the $O(1)$ contribution to the normal stress is given by $\langle v^2 \rangle_b = 2C_3 k_b = 2C_3 A_k \overline{k}$. By a similar justification, the second term in (7.9), which is the contribution of the pressure due to the intermittency, can be related to the turbulent kinetic energy at the bottom of the surface layer, which can be given by the approximation

$$-\frac{1}{\rho} \int_b^h \left[\frac{(1-\gamma)}{\gamma} P \right] \frac{\partial \gamma}{\partial n} dn \approx C_{kp} \overline{k}, \tag{4.172}$$

so that

$$\frac{P_b}{\rho} \approx C_p \overline{k}. \tag{4.173}$$

$$C_p \equiv -2C_3 A_k + C_{kp} + \mathbf{g} \cdot \hat{\mathbf{n}} \frac{C_{1k} A_k}{g}. \tag{4.174}$$

Note again that neglecting the surface-layer turbulence leads to zero pressure at the top of the layer, which would be the case for an unbroken surface. Finally, the layer-averaged pressure term can be written as

$$VI = (2C_3 \overline{k} + C_p \overline{k}) \frac{\partial b}{\partial s} + 2C_3 b \frac{\partial \overline{k}}{\partial s}. \tag{4.175}$$

The gravity term is simply given by

$$VII = (\hat{\mathbf{s}} \cdot \mathbf{g}') b. \tag{4.176}$$

Since the Reynolds shear stress vanishes at the lower boundary ($[\langle uv \rangle]_{n=0} = 0$), applying Leibnitz on term VII gives

$$VIII = -(1 - \kappa b)\langle uv \rangle_b. \tag{4.177}$$

151
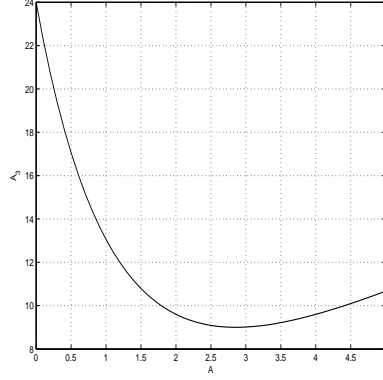
Figure 4.12: Variation of A_3 with A.

From MB02, the Reynolds shear stress at the bottom of the surface layer is approximated in terms of the turbulent kinetic energy at that boundary, and expressing that in terms of the layer-averaged kinetic energy,

$$\langle uv \rangle_b \approx \mathbf{g} \cdot \hat{\mathbf{s}} \frac{C_{1k} A_k \overline{k}}{g}, \tag{4.178}$$

so that

$$VIII \approx -(1 - \kappa b)\mathbf{g} \cdot \hat{\mathbf{s}} \frac{C_{1k} A_k \overline{k}}{g}. \tag{4.179}$$

Term IX is given by

$$IX = -\int_0^b \frac{\partial \langle u^2 \rangle}{\partial s} dn, \tag{4.180}$$

which, using the $O(1)$ equation for $\langle u^2 \rangle$ (equation (4.81)), can be written as

$$IX = -2C_1 \int_0^b \frac{\partial k}{\partial s} dn. \tag{4.181}$$

Applying Leibnitz rule,

$$\begin{aligned}
IX &= -2C_1 \left[b \frac{\partial \overline{k}}{\partial s} + \overline{k} \frac{\partial b}{\partial s} - b \frac{\partial k_b}{\partial s} \right] \\
&\approx -2C_1 b \frac{\partial \overline{k}}{\partial s} - 2C_1 \overline{k} \frac{\partial b}{\partial s} + 2C_1 b A_k \frac{\partial \overline{k}}{\partial s} + 2C_1 b \overline{k} \frac{\partial A_k}{\partial s}
\end{aligned} \tag{4.182}$$

152

The integration of the last term is

$$X = -\kappa b \Lambda C_t (\overline{U} - \hat{U})^2 A_3,$$ (4.183)

where

$$A_3 = \frac{96(2A^2 - 5A + 20)}{5(4 + A)^2}.$$ (4.184)

The layer-averaged streamwise momentum equation can be written as

$$\frac{\partial \overline{U}}{\partial t} + M_B \frac{\partial b}{\partial s} + M_U \frac{\partial \overline{U}}{\partial s} + M_K \frac{\partial \overline{k}}{\partial s} = M_R.$$ (4.185)

The coefficients are given as

$$
\begin{aligned}
M_B =\ & \frac{1}{b}\Bigg[(1 - A_0)(\overline{U} - \hat{U})\left(\frac{C_{1k} A_k K_B}{g} + \hat{\mathbf{s}} \cdot \frac{\partial \mathbf{R}}{\partial t} \right) + 2(C_1 - C_3)\overline{k} \\
& - C_p \overline{k} + \frac{A_0}{2}(\overline{U} - \hat{U})^2 \Bigg],
\end{aligned}
$$ (4.186)

$$
\begin{aligned}
M_U =\ & \frac{1}{b}\Bigg[\overline{U}(b - C_U') + A_1 b(\overline{U} - \hat{U}) + \frac{A_k}{g}(1 - A_0)(\overline{U} - \hat{U})(-C_{1k} K_U + A_0 C_{2k} \overline{k}) \\
& + \hat{\mathbf{s}} \cdot \frac{\partial \mathbf{R}}{\partial t} b \Bigg],
\end{aligned}
$$

$$
\begin{aligned}
M_K =\ & \frac{1}{b}\Bigg[-\overline{U} C_K' + \frac{A_k}{g}[A_0(\overline{U} - \hat{U}) + \hat{U}]\left\{ -C_{1k} K_K + C_{2k}[A_0(\overline{U} - \hat{U}) + \hat{U}] \right\} \\
& + 2b[C_1(1 - A_k) - C_3] \Bigg], \quad \text{and}
\end{aligned}
$$

$$
\begin{aligned}
M_R =\ & \frac{1}{b}\Bigg[-\overline{U} C_R' + A_1 b(\overline{U} - \hat{U})\frac{\partial \hat{U}}{\partial s} + \hat{U} V_0 - A_2 b(\overline{U} - \hat{U})^2 \frac{\partial A}{\partial s} \\
& - \frac{A_k}{g}[A_0(\overline{U} - \hat{U}) + \hat{U}]\left\{ C_{1k} K_R + C_{2k}(1 - A_0)\overline{k}\frac{\partial \hat{U}}{\partial s} + C_{2k}\overline{k}(\overline{U} - \hat{U})\frac{\partial A_0}{\partial s} \right\} \\
& - \hat{\mathbf{n}} \cdot \frac{\partial \mathbf{R}}{\partial t}(\overline{U} - \hat{U})[A_0 + \kappa b(1 - A_0)] + \hat{\mathbf{s}} \cdot \mathbf{g}' b - \frac{A_k}{g}(1 - \kappa b)\mathbf{g} \cdot \hat{\mathbf{s}} C_{1k} \overline{k} \\
& - \kappa b \Lambda C_t (\overline{U} - \hat{U})^2 A_3 + 2C_1 b \overline{k} \frac{\partial A_k}{\partial s} \Bigg].
\end{aligned}
$$

Even though the coefficients are mathematically complicated, the significance of each term can by interpreted through the coefficients, which provide a description of various physical mechanisms. For e.g., M_K provides the coupling between the momentum equation and the evolution of the turbulent kinetic energy and arises due to the surface-layer contribution represented by A_k. The equations get decoupled when $A_k = 0$ (since $C'_K = 0$), which, as can be seen from Figure 4.9, happens at $A = 2$, or for zero mean shear at the top of the layer. In such a case, $C'_U = b$, and M_U is given simply by $M_U = A_1(\overline{U} - \hat{U}) + \hat{\mathbf{s}} \cdot \frac{\partial \mathbf{R}}{\partial t}$. Also, in such a scenario, $M_K = 0$, since $C'_K = 0$. The anistropy of the turbulence is reflected in $C_1 \neq C_3$. This completes the layer integration of the streamwise momentum equation. Note that all the information required to model the evolution of $\overline{U}$ is provided by the dynamics of the layer itself, and the flow below. The information for the unsteady motion of the base of the layer (quantified by the terms $\hat{\mathbf{s}} \cdot \frac{\partial \mathbf{R}}{\partial t}$ and $\hat{\mathbf{n}} \cdot \frac{\partial \mathbf{R}}{\partial t}$) is specified by the boundary of the irrotational flow. In the next section, the turbulent kinetic energy equation is integrated across the layer.

4.8.3 The turbulent kinetic energy equation

Casting the convective terms in conservative form, equation (4.86) can be written in dimensional form as

$$
\int_0^b \left[\underbrace{\frac{\partial k}{\partial t}}_{I} + \underbrace{\frac{\partial (Uk)}{\partial s}}_{II} + \underbrace{\frac{\partial (Vk)}{\partial n}}_{III} + \underbrace{\hat{\mathbf{s}} \cdot \frac{\partial \mathbf{R}}{\partial t} \frac{\partial k}{\partial s}}_{IV} \right. \tag{4.187}
$$

$$
+ \underbrace{(1 - 2\kappa n)\hat{\mathbf{n}} \cdot \frac{\partial \mathbf{R}}{\partial t} \frac{\partial k}{\partial n}}_{V} = \underbrace{(1 - 2\kappa n)\frac{\partial \left(\nu_t \frac{\partial k}{\partial n} \right)}{\partial n}}_{VI}
$$

$$
- \underbrace{\langle uv \rangle \left\{ \kappa U + (1 - 2\kappa n)\frac{\partial U}{\partial n} \right\}}_{VII} + \underbrace{(\langle u^2 \rangle - \langle v^2 \rangle)\frac{\partial V}{\partial n}}_{VIII} - \underbrace{(1 - 2\kappa n)\varepsilon}_{IX} \left. \right] dn.
$$

154
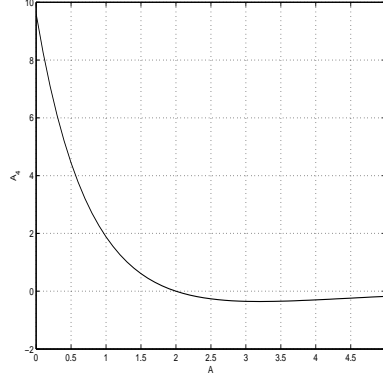
Figure 4.13: Variation of A_4 with A.

In the following, each underbraced term is integrated separately. Applying Leibnitz rule on the first term,

$$I = b\frac{\partial \overline{k}}{\partial t} + \overline{k}\frac{\partial b}{\partial t} - k_b\frac{\partial b}{\partial t}. \tag{4.188}$$

Using the integrated $O(1)$ continuity equation, this term can be written as

$$
\begin{aligned}
I &= b\frac{\partial \overline{k}}{\partial t} - \overline{k}\,\overline{U}\frac{\partial b}{\partial s} - \overline{k}b\frac{\partial \overline{U}}{\partial s} + \overline{k}(V_0 - W) - \underbrace{k_b\frac{\partial b}{\partial t}}_{Ia} \\[2mm]
&= \left[b - \frac{C_{1k}A_k\overline{k}}{g}\right]\frac{\partial \overline{k}}{\partial t} - \overline{k}\,\overline{U}\frac{\partial b}{\partial s} - \overline{k}\left[b + \frac{C_{2k}A_kA_0\overline{k}}{g}\right]\frac{\partial \overline{U}}{\partial s} \\[2mm]
&- \overline{k}[A_0(\overline{U} - \hat{U}) + \hat{U}]\frac{A_kC_{2k}}{g}\frac{\partial \overline{k}}{\partial s} + \overline{k}\left[V_0 - \frac{A_kC_{2k}}{g}\overline{k}\left\{(1 - A_0)\frac{\partial \hat{U}}{\partial s}\right.\right. \\[2mm]
&+ \left.\left.(\overline{U} - \hat{U})\frac{\partial A_0}{\partial s}\right\}\right] - \underbrace{k_b\frac{\partial b}{\partial t}}_{Ia}.
\end{aligned}
\tag{4.189}
$$

Ia is to be combined later with other terms.

$$II = b\overline{k}\frac{\partial \overline{U}}{\partial s} + b\overline{U}\frac{\partial \overline{k}}{\partial s} + \overline{k}\,\overline{U}\underbrace{\frac{\partial b}{\partial s} - U_b k_b\frac{\partial b}{\partial s}}_{IIa} + \underbrace{\frac{\partial \left[\int_0^b k(U - \overline{U})dn\right]}{\partial s}}_{IIb}, \tag{4.190}$$

155
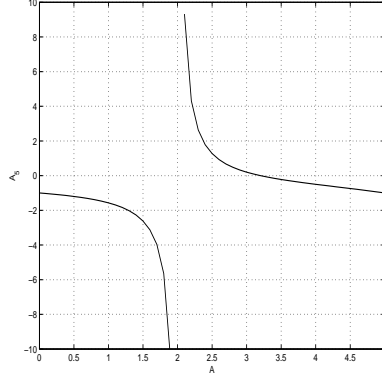
Figure 4.14: Variation of A_5 with A.

where IIa is to be combined with Ia and another term later.

$$IIb = A_4 \Lambda (\overline{U} - \hat{U})^2 \left[\Lambda (\overline{U} - \hat{U}) \frac{\partial b}{\partial s} + 3 b \Lambda \frac{\partial \overline{U}}{\partial s} \right. \tag{4.191}$$

$$+ \left. b \left\{ 2(\overline{U} - \hat{U}) \frac{\partial \Lambda}{\partial s} - 3 \Lambda \frac{\partial \hat{U}}{\partial s} + 6 A_5 \Lambda \frac{\partial A}{\partial s} \right\} \right],$$

where

$$A_4 = \frac{-24(A-2)(A-8)^2}{5(4+A)^3}, \quad \text{and} \tag{4.192}$$

$$A_5 = \frac{5A - 16}{(A-8)(A-2)}. \tag{4.193}$$

$$\tag{4.194}$$

Term IIb obviously vanishes for uniform flow. The term also vanishes when mean shear at the surface is neglected, which is evident from Figure 4.13, where $A_4 = 0$ for $A = 2$. Note the singularity of A_5 (which represents the streamwise variation of the dissipation) at $A = 2$.

So,

$$II = b\overline{U}\frac{\partial \overline{k}}{\partial s} + [\overline{k}\ \overline{U} + A_4\Lambda^2(\overline{U} - \hat{U})^3]\frac{\partial b}{\partial s} \tag{4.195}$$

$$+ [b\overline{k} + 3A_4b\Lambda^2(\overline{U} - \hat{U})^2]\frac{\partial \overline{U}}{\partial s}$$

$$+ A_4b\Lambda(\overline{U} - \hat{U})^2 \left[2(\overline{U} - \hat{U})\frac{\partial \Lambda}{\partial s} - 3\Lambda\frac{\partial \hat{U}}{\partial s} + 6A_5\Lambda\frac{\partial A}{\partial s}\right] + IIa.$$

The third term can be integrated easily and gives

$$III = \underbrace{k_bV_b}_{IIIa} - k_0V_0. \tag{4.196}$$

Ia, IIa and $IIIa$ are combined as

$$Ia + IIa + IIIa = -U_bk_b\frac{\partial b}{\partial s} - k_b\frac{\partial b}{\partial t} + k_bV_b \tag{4.197}$$

$$= k_bW$$

$$= \left[\frac{A_k^2C_{1k}}{g}\overline{k}\right]\frac{\partial \overline{k}}{\partial t} + \left[\frac{A_k^2C_{2k}}{g}\overline{k}[A_0(\overline{U} - \hat{U}) + \hat{U}]\right]\frac{\partial \overline{k}}{\partial s}$$

$$+ \left[\frac{A_k^2C_{2k}}{g}A_0\overline{k}^2\right]\frac{\partial \overline{U}}{\partial s} + \left[\frac{A_k^2C_{2k}}{g}\overline{k}^2(1 - A_0)\right]\frac{\partial \hat{U}}{\partial s}$$

$$+ \frac{A_k^2C_{2k}}{g}\overline{k}^2(\overline{U} - \hat{U})\frac{\partial A_0}{\partial s}.$$

Term IV can be easily integrated to give,

$$IV = \hat{\mathbf{s}} \cdot \frac{\partial \mathbf{R}}{\partial t}\left[b\frac{\partial \overline{k}}{\partial s} + \overline{k}\frac{\partial b}{\partial s} - k_b\frac{\partial b}{\partial s}\right] \tag{4.198}$$

$$\approx \hat{\mathbf{s}} \cdot \frac{\partial \mathbf{R}}{\partial t}\left[\overline{k}(1 - A_k)\frac{\partial b}{\partial s} + b\frac{\partial \overline{k}}{\partial s}\right].$$

Similarly, term V, describing the streamwise motion of the layer, can be integrated to give,

$$V = \hat{\mathbf{n}} \cdot \frac{\partial \mathbf{R}}{\partial t}\left[(1 - 2\kappa b)k_b - k_0 + 2\kappa\overline{k}b\right] \tag{4.199}$$

$$\approx \hat{\mathbf{n}} \cdot \frac{\partial \mathbf{R}}{\partial t}\left[\{(1 - 2\kappa b)A_k + 2\kappa b\}\overline{k} - k_0\right].$$

157
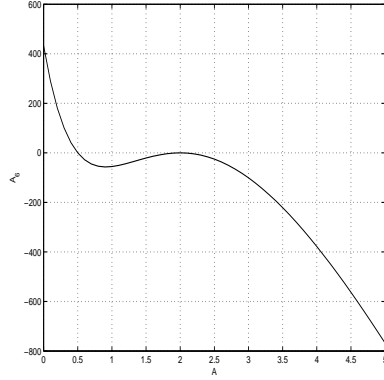
Figure 4.15: Variation of A_6 with A.
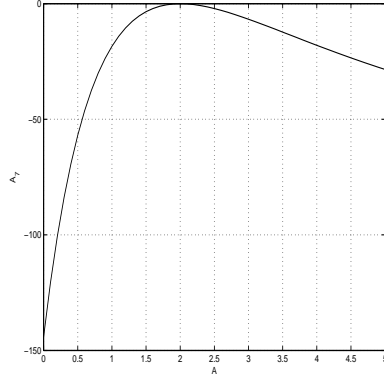
Figure 4.16: Variation of A_7 with A.

Term VI is the diffusion term in the turbulent kinetic energy equation and is given by

$$VI = \underbrace{(1 - 2\kappa b)\left[\nu_t \frac{\partial k}{\partial n}\right]_{n=b}}_{VIa} - \underbrace{\left[\nu_t \frac{\partial k}{\partial n}\right]_{n=0}}_{VIb} + \underbrace{2\kappa \int_0^b \nu_t \frac{\partial k}{\partial n} dn}_{VIc}. \qquad (4.200)$$

VIb is the $O(1)$ contribution at the lower boundary. From the profiles developed earlier for k and ν_t, $VIb = 0$. Therefore, there is no diffusive penetration of vorticity into the underlying irrotational flow. In other words, the thin layer of viscous laminar

158

flow between the turbulent and irrotational flow is disregarded.

$$VIa = A_6(\overline{U} - \hat{U})^3 C_t \Lambda^3 (1 - 2\kappa b), \tag{4.201}$$

where

$$A_6 = \frac{6912(2 - A)^2(1 - 2A)}{(4 + A)^3}. \tag{4.202}$$

$$VIc = A_7 b C_t \Lambda^3 \kappa (\overline{U} - \hat{U})^3, \tag{4.203}$$

where

$$A_7 = \frac{-2304(A - 2)^3}{(A + 4)^3}. \tag{4.204}$$

Therefore, term VI is finally given by

$$VI = C_t \Lambda^3 (\overline{U} - \hat{U})^3 [A_6 + (A_7 - 2A_6)\kappa b]. \tag{4.205}$$

Term VII signifies the production of turbulent energy from the work done by the Reynolds shear stresses on the mean shear. Note the explicit dependence on the geometric curvature.

$$
\begin{aligned}
VII &= \int_0^b -\langle uv \rangle \left[\kappa U + (1 - 2\kappa n)\frac{\partial U}{\partial n} \right] dn \tag{4.206} \\
&= VIIa + VIIb.
\end{aligned}
$$

$$
\begin{aligned}
VIIa &= -\kappa \int_0^b \langle uv \rangle U dn \tag{4.207} \\
&= \kappa \int_0^b \nu_t U \frac{\partial U}{\partial n} dn \\
&= b\kappa \Lambda C_t (\overline{U} - \hat{U})^2 K_1,
\end{aligned}
$$

where

$$
\begin{aligned}
K_1 &= \frac{24}{5(4 + A)^3} [A^3\hat{U} - 128\hat{U} + 96A\hat{U} - 18\hat{U}A^2 + 288\overline{U} + 3A^3\overline{U} \tag{4.208} \\
&\quad - 96A\overline{U} + 24\overline{U}A^2].
\end{aligned}
$$
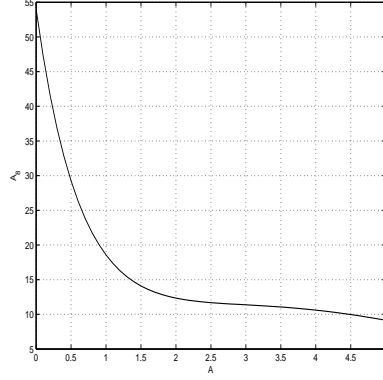
Figure 4.17: Variation of A_8 with A.

$$VIIb = -\int_0^b \langle uv \rangle (1 - 2\kappa n)\frac{\partial U}{\partial n}dn \tag{4.209}$$

$$= \int_0^b (1 - 2\kappa n)\nu_t \left[\frac{\partial(}{\partial n}U)\right]^2$$

$$= C_t\Lambda(\overline{U} - \hat{U})^3 K_2,$$

where

$$K_2 = A_8 + \kappa b A_9, \tag{4.210}$$

$$A_8 = \frac{432}{35(4 + A)^3}[-8A^3 + 84A^2 - 168A + 280], \quad \text{and} \tag{4.211}$$

$$A_9 = \frac{432}{35(4 + A)^3}[17A^3 - 144A^2 + 336A - 448]. \tag{4.212}$$

Term $VIII$, which is the work done by the normal stresses, is given by

$$VIII = 2(C_1 - C_3)\int_0^b k\frac{\partial V}{\partial n}dn \tag{4.213}$$

$$= 2(C_1 - C_3)\Lambda^2(\overline{U} - \hat{U})^2\left[-A_9(\overline{U} - \hat{U})\frac{\partial b}{\partial s} + A_{10}b\frac{\partial \overline{U}}{\partial s}\right.$$

$$\left. + A_{11}b\frac{\partial \hat{U}}{\partial s} - \frac{A_{12}}{(4 + A)}b\frac{\partial A}{\partial s}\right],$$

160
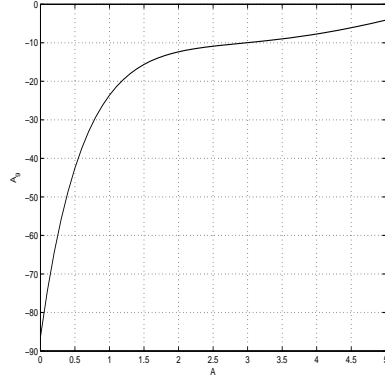
Figure 4.18: Variation of A_9 with A.
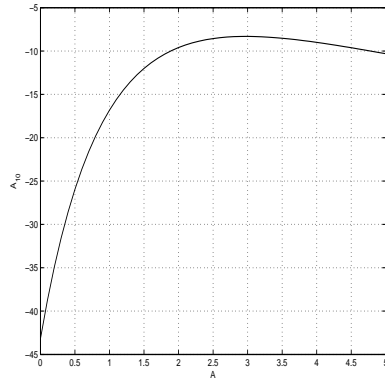
Figure 4.19: Variation of A_{10} with A.

where

$$A_{10} = -\frac{1008}{35(4+A)^3}[96 - 32A + A^3 + 8A^2], \tag{4.214}$$

$$A_{11} = -\frac{336}{35(A+4)^3}(A-2)(A-8)^2, \quad \text{and} \tag{4.215}$$

$$A_{12} = \frac{A_{10}}{(4+A)}. \tag{4.216}$$

Note that term $VIII$ vanishes for isotropic turbulence.

161
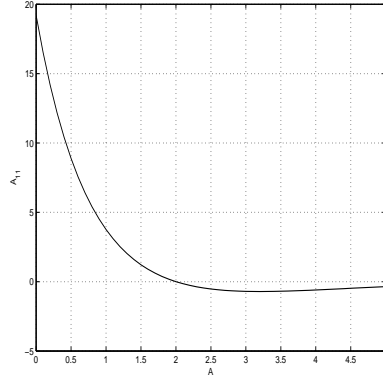
Figure 4.20: Variation of A_{11} with A.
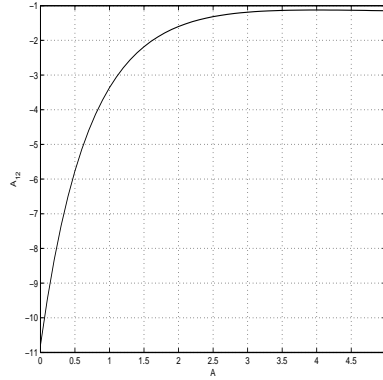
Figure 4.21: Variation of A_{12} with A.

The dissipation term can be integrated as

$$IX = -\Lambda^3 C_\varepsilon (\overline{U} - \hat{U})^3 K_2. \tag{4.217}$$

Finally, the integrated turbulent kinetic energy equation can be written as

$$\frac{\partial \overline{k}}{\partial t} + K_B \frac{\partial b}{\partial s} + K_U \frac{\partial \overline{U}}{\partial s} + K_K \frac{\partial \overline{k}}{\partial s} = K_R, \tag{4.218}$$

162

where

$$K_B = \frac{1}{D_k}\left[A_4\Lambda^2(\overline{U}-\hat{U})^3 + \hat{\mathbf{s}}\cdot\frac{\partial\mathbf{R}}{\partial t}\overline{k}(1-A_k) \right. \tag{4.219}$$

$$\left. - 2A_7(C_1-C_3)\Lambda^2(\overline{U}-\hat{U})^3 \right],$$

$$K_U = \frac{1}{D_k}\left[3A_4 b\Lambda^2(\overline{U}-\hat{U})^2 + \frac{A_0 A_k^2 C_{2k}}{g}\overline{k}^2 \right. \tag{4.220}$$

$$\left. - 2(C_1-C_3)\Lambda^2(\overline{U}-\hat{U})^2 A_{10}b \right],$$

$$K_K = \frac{1}{D_k}\left[\frac{A_k}{C_{2k}}g\overline{k}[A_0(\overline{U}-\hat{U})+\hat{U}](A_k-1) + b\left(\overline{U}+\hat{\mathbf{s}}\cdot\frac{\partial\mathbf{R}}{\partial t}\right) \right], \tag{4.221}$$

$$K_R = \frac{1}{D_k}\left[V_0(k_0-\overline{k}) - \frac{A_k C_{2k}}{g}(A_k-1)\overline{k}^2(1-A_0)\frac{\partial\hat{U}}{\partial s} \right. \tag{4.222}$$

$$- A_4 b\Lambda(\overline{U}-\hat{U})^2\left\{ 2(\overline{U}-\hat{U})\frac{\partial\Lambda}{\partial s} - 3\Lambda\frac{\partial\hat{U}}{\partial s} + 6A_5\Lambda\frac{\partial A}{\partial s} \right\}$$

$$- \hat{\mathbf{n}}\cdot\frac{\partial\mathbf{R}}{\partial t}\{[(1-2\kappa b)A_k + 2\kappa b]\overline{k} - k_0\} - \frac{A_k C_{2k}\overline{k}^2}{g}(\overline{U}-\hat{U})(1-A_k)\frac{\partial A_0}{\partial s}$$

$$+ C_t\Lambda^3(\overline{U}-\hat{U})^3[A_6 + (A_7-2A_6)\kappa b] + \Lambda C_t(\overline{U}-\hat{U})^2[\kappa bK_1 + (\overline{U}-\hat{U})K_2]$$

$$\left. + 2(C_1-C_3)\Lambda^2(\overline{U}-\hat{U})^2 b\left\{ A_{11}\frac{\partial\hat{U}}{\partial s} - \frac{A_{12}}{(4+A)}\frac{\partial A}{\partial s} \right\} - \Lambda^3 C_t(\overline{U}-\hat{U})^3 K_2 \right],$$

and

$$D_k = b + \frac{A_k C_{1k}}{g}\overline{k}(A_k-1). \tag{4.223}$$

The layer-averaged equations for conservation of mass, momentum and turbulent kinetic energy are given as

$$\frac{\partial b}{\partial t} + C_B\frac{\partial b}{\partial s} + C_U\frac{\partial\overline{U}}{\partial s} + C_K\frac{\partial\overline{k}}{\partial s} = C_R, \tag{4.224}$$

$$\frac{\partial\overline{U}}{\partial t} + M_B\frac{\partial b}{\partial s} + M_U\frac{\partial\overline{U}}{\partial s} + M_K\frac{\partial\overline{k}}{\partial s} = M_R, \quad\text{and} \tag{4.225}$$

$$\frac{\partial\overline{k}}{\partial t} + K_B\frac{\partial b}{\partial s} + K_U\frac{\partial\overline{U}}{\partial s} + K_K\frac{\partial\overline{k}}{\partial s} = K_R, \tag{4.226}$$

163

or in matrix form as

$$
\left\{ \begin{array}{c} b \\ \overline{U} \\ \overline{k} \end{array} \right\}_t + \left[\begin{array}{ccc} C_B & C_U & C_K \\ M_B & M_U & M_K \\ K_B & K_U & K_K \end{array} \right] \left\{ \begin{array}{c} b \\ \overline{U} \\ \overline{k} \end{array} \right\}_s = \left[\begin{array}{c} C_R \\ M_R \\ K_R \end{array} \right],
$$

where the subscripts denote partial differentiation with respect to the variables, and the coefficient are given in equations (4.147), (4.186), and (4.219). The above system of equations can either be regarded as a description for the turbulent dynamics in the thin layer, or as turbulent free surface boundary conditions for the irrotational flow below. The two flows are coupled through the mass exchange and pressure at the boundary. The mass exchange is represented by the mean velocities, V_0 and $\hat{U}$. The layer-averaged pressure $(\overline{P})$ and the pressure at the top of the layer (P_b) have been expressed in terms of $\overline{k}$. Since a consistent set of equations for the $O(\epsilon)$ model has contributions from the $O(1)$ normal momentum equation (equation (4.85)), using the $O(1)$ relationship between the normal turbulent stress and the turbulent kinetic energy (equation (4.81)), the pressure at the base of the layer is given by

$$
P_0 = P_b + 2\rho C_3(k_b - k_0). \tag{4.227}
$$

Since the diffusion of turbulent kinetic energy at the bottom has been neglected, in the absence of rotation, the profile for the turbulent kinetic energy (equation (4.116)) shows that $k_0 = 0$. Also, since k_b is related to $\overline{k}$ through $k_b = A_k \overline{k}$, and $P_b = \rho C_p \overline{k}$, the pressure at the base of the layer, and as a boundary condition for the irrotational flow is found to be

$$
P_0 = \overline{k}\rho(C_p + 2C_3 A_k). \tag{4.228}
$$

In the next section, a model for the streamwise variation of $A(s)$ is formulated. Once $A(s)$ is known, the coefficients related to $A(s)$, such as A_0, A_1, etc. are easily found.

4.9 A model for $A(s)$

In principle, the analytical expression for $A(s)$ (equation (4.125)) can be explicitly used in the above equations. However, the equations become rather intractable because of the dependence of $A(s)$ on $\overline{U}$ and b. To keep the mathematics simple, the streamwise dependence of $A(s)$ is determined based on physical reasoning and experimental measurements. As already seen in Figure 4.6, the cubic profile fits the measured data well. Further, the theoretical profile for the mean horizontal velocity (equation (4.109)), using the fitted values of A, agrees with the measured vertical variation of U. This is reassuring, since only an $O(1)$ solution for the mean velocity has been used. Some of the discrepancy between the theoretical profile and the measured data can, therefore, be due to the higher order effects which are neglected in the $O(1)$ model. From Figure 4.22, it can be seen that the values for $A(s)$ decrease in the downstream direction with increasing streamwise distances from the foot of the breaker. This is physically reasonable since $A(s)$ is a quantification of the mean shear at the top of the layer, and the shear decreases from the foot of the breaker toward the wake region.

From cubic profiles fit to the measured data, $A(s)$ can be calculated at various streamwise locations. These are shown as circles in Figure 4.22. The solid line is a linear fit to the estimated values, and is given by

$$A(\tilde{x}) = -3.28\tilde{x} + 5.38. \tag{4.229}$$

A more general expression can be easily obtained by using the foot of the breaker as the origin of the streamwise coordinate. However, since the theoretical model coordinate system is also arbitrary, and to allow an easier interpretation with the experimental results presented in Chapter 3, no such transformation is made. Further, the streamwise geometry of the lower boundary of the thin layer can be qualitatively assessed from Figure 3.8 and Figure 3.16. The base of the layer is seen to be nearly horizontal. This has also been observed for spilling breaking waves (Lin and
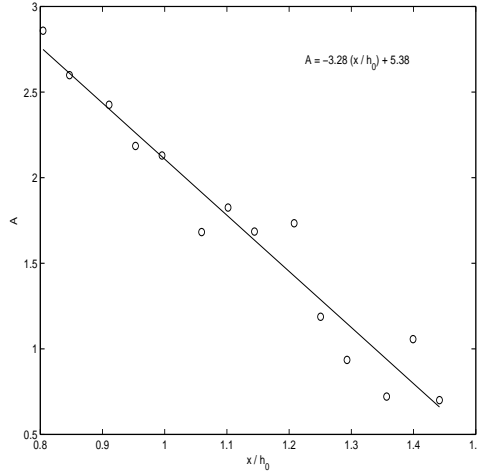
Figure 4.22: Measured (circles) and linear fit (solid line) to streamwise variation of $A(\tilde{x})$.

Rockwell, 1995; Stansby and Feng, 2005). Since the coordinate system is attached to the bottom boundary of the layer, the streamwise variation in $\tilde{x}$ can be assumed to be nearly the same as the streamwise dependence on the curvilinear coordinate, s, with the result that

$$A(s) \approx -3.28s + 5.38. \tag{4.230}$$

The linear variation is seen to be a reasonable fit to the estimated values. As mentioned before, because of the small thickness of the shear layer near the foot of the breaker, few measurement points were available to enable a robust fit. Therefore, the linear fit for A is extrapolated toward the foot of the breaker. As found in Chapter 3, the foot of the breaker is at $\tilde{x} \sim 0.47$, and the wake region further downstream of $\tilde{x} \sim 1.2$. The extrapolated values near the foot are admittedly uncertain since the dynamics near the toe of the breaker are highly complicated because of significant curvature and unsteady effects arising from the toe oscillation. In the following, the validity of the estimated streamwise variation of $A(s)$ is discussed with respect to the theoretical results and measurements.

166
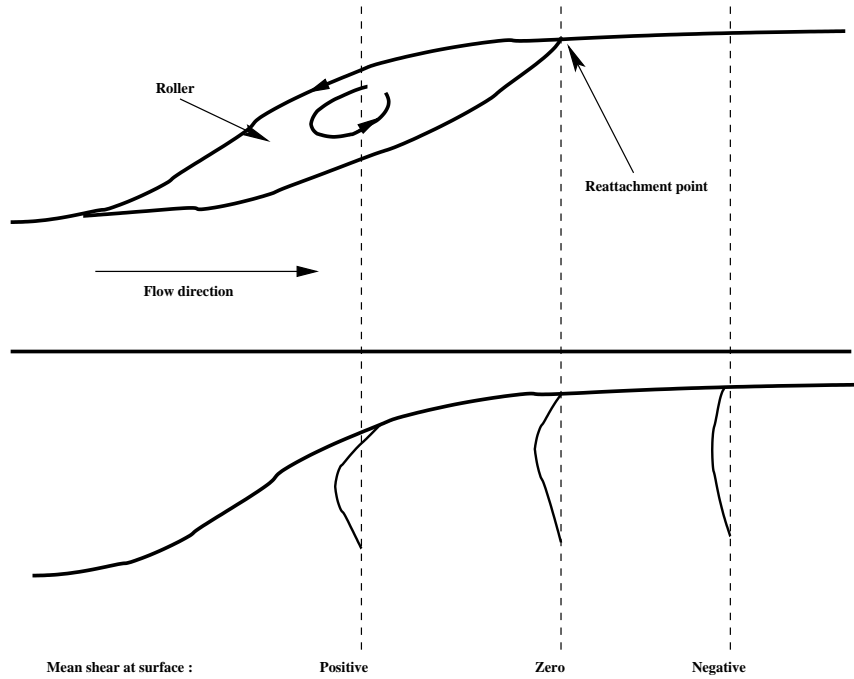
Figure 4.23: Schematic showing flow reversal in the roller region and the corresponding sign reversal in the mean surface shear at the reattachment point.

The $O(1)$ solution for the mean shear at the top of the layer is given by equation (4.110) with $\Omega = 0$. Since $f = (U_b - \hat{U})$ is negative in the thin layer, for $A > 2$, $\frac{\partial U}{\partial n} > 0$, and for $A < 2$, $\frac{\partial U}{\partial n} < 0$. Therefore, the streamwise location where the mean shear at the top of the layer is zero and undergoes a change of sign is given by the location where $A = 2$. From Figure 4.22, this is found to be at $\tilde{x} \sim 1.03$. This is approximately the location of the end of roller as shown in Figure 3.11, at $\tilde{x} \sim 1.05$. A possible reason for this is related to the reverse flow in the roller region which creates a positive shear near the mean surface. This is shown schematically in Figure 4.23. The singularity at $A = 2$ appears at the reattachment point where the mean surface shear vanishes. It is interesting to note that singularities for hydraulic jumps are known to occur at separation points (Bohr
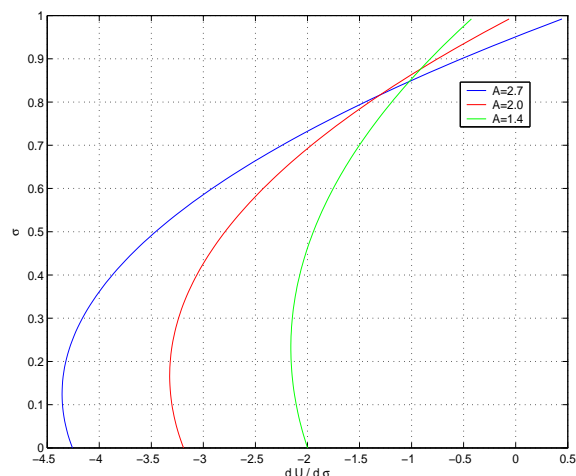
Figure 4.24: Mean surface shear for different values for A.

et al., 1997; Chang *et al.*, 2001). The author is unaware similar studies focussing on reattachment points. The present measurements do not afford a resolution high enough to accurately estimate the sign and magnitude of the mean shear at the surface, but the vertical profiles of IS00 certainly indicate such a scenario (see their Figure 15). The streamwise variation of A in the theoretical model predicts the correct sign of the mean shear at the top of the thin layer, and this is shown in Figure 4.24 for three different values of A.

Since dissipation increases and production decreases in the downstream direction, Λ^2 should increase in the downstream direction. Since $A(s)$ decreases in the downstream direction, Λ^2 should increase with decreasing values of $A(s)$. This is clearly seen in Figure 4.7 for $A(s) > 2$. Note that the theory predicts a singularity at $A = 2$. In reality, this essentially translates to very small values of production along with large values of dissipation. Whether this occurs at the location where $A(s) \sim 2$ cannot be confirmed from the present measurements because dissipation could not be estimated. A spatial resolution approximately equal to the Kolmogorov length scale is required to accurately estimate dissipation rates, and the present resolution
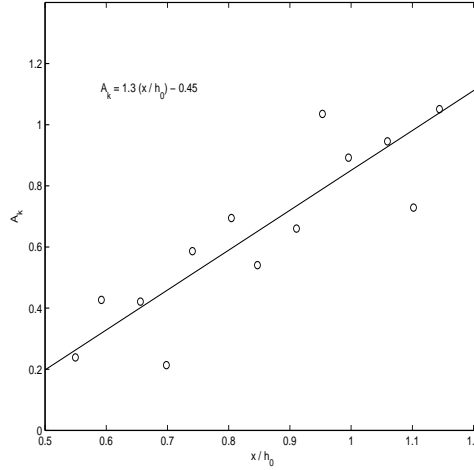
Figure 4.25: Measured (circles) and linear fit (solid line) to streamwise variation of A_k.

is much coarser.

Another qualitative check on the linear decay of $A(s)$ can be done by looking at the streamwise variation of A_k. A_k is defined as the ratio between the turbulent kinetic energy at the top of the layer and the layer-averaged value, i.e., $A_k = \frac{k_b}{\bar{k}}$. From the present measurements, the streamwise dependence of this coefficient can be calculated and is shown in Figure 4.25. Even though there is quite a bit of scatter, a linear fit to the measurements is shown to be reasonable in reproducing the basic trend of a linear increase with downstream distance. In Figure 4.9, the theoretically estimated values of A_k are seen to decrease linearly with $A(s)$ (for $A(s) > 2$). This is entirely consistent with the linear increase of A_k downstream, since $A(s)$ decreases downstream. Note that a comparison of the magnitudes for A_k from the theory and measurements also shows reasonable agreement.

Finally, the estimated values for A from the linear fit are found to be 3.84 near the foot of the breaker, decreasing to approximately 0.5 in the wake region ($\tilde{x} \sim 1.5$). The values in the downstream region are comparable to the values in

MS83, who used values of 0.5, 1.4, and 2 in fitting vertical profiles to measurements of mean horizontal velocity, turbulence intensity and Reynolds shear stress. They had suggested that a non-zero mean shear stress at the mean surface necessitated a value of $A < 2$, which, as is seen from the present analysis, is valid only in the region downstream of the roller. They had noted that measurements in the roller region were not available to substantiate the values chosen for A, and hence measurements downstream of the roller were used. Further, their conclusion that $A < 2$ was not based on any measurements, since values greater than two were not used to fit the profiles to the data. As the integrated equations were satisfied "at large", they found that the mean surface profile was insensitive to the chosen values of A. The linear decay model suggested here for $A(s)$ represents a more accurate description of the local details of the mean and turbulent flow dependence in various regimes of the flow.

4.10   Conclusions

A theoretical model for the description of the turbulent dynamics in quasi-steady spilling breaking waves has been developed. The model is part of a comprehensive three-layer system in which the top layer represents the two-phase flow near the surface, and the flow below is assumed to be irrotational. Therefore, the combined model is representative of the fully turbulent two-phase flow in the breaker region. The surface-layer model of MB2 is used to provide the boundary conditions at the top of the thin layer, whereas the irrotational flow is assumed to be known.

The governing equations for conservation of mass, momentum, and turbulent kinetic energy, derived by Brocchini (1996) are used as the framework for the present model. The main features of these equations, developed in orthogonal curvilinear coordinates, are a correct representation of unsteadiness, curvature, rotation, and non-hydrostatic effects. Reynolds-averaged equations for both the mean and turbulent flow are derived by splitting the velocities and pressure into mean and

turbulent parts. In addition, a one-equation $k - \epsilon$ turbulence model based on local equilibrium of Reynolds shear stress is used. An evolution equation is used to model the non-equilibrium in k. A Boussinesq eddy-viscosity closure was adopted through a length scale chosen as the width of the shear layer. In light of experimental observations of turbulence intensities in the roller region and crest of breaking waves, the turbulence is allowed to be anisotropic. This is particularly important for an accurate modeling of the turbulence near the foot of the breaker.

A scaling of the equations is performed through the introduction of two parameters. The geometric parameter ($\epsilon = \frac{b}{L}$) represents the shallowness of the flow in the layer, and is a ratio of the width of the layer to the streamwise length scale. Based on the measurements, and typical values found in jets and mixing layer, it is found that $\epsilon << 1$, or that the layer is thin. The governing equations are ordered in terms of ϵ, which gives clear insights into the relative contributions of various physical mechanisms represented in the governing equations. The kinematic parameter $\left(\mu = \frac{\tilde{u}}{\tilde{U}} \right)$ is a ratio of the turbulent fluctuations to the mean horizontal velocity, and is a direct indication of the intensity of turbulence. The flow is classified into three regimes dependent on the size of the kinematic parameter with $O(\epsilon) < \mu < O(1)$. Near the leading edge of the breaker, $\mu \sim O(1)$, and it decreases toward the wake region where $\mu << 1$. This classification is supported by the estimates of μ from the data. Estimates of curvature from the data substantiate the assumption of gentle curvature in the breaker region.

The leading order model describes the evolution of the lower boundary of the layer and shows that the normal profile of the mean pressure is determined by the turbulent normal stresses. Due to the "shallowness" assumption, the effects of gravity and mean vertical accelerations are felt by the pressure at $O(\epsilon)$ and $O(\epsilon^2)$ respectively in the normal momentum equation. Direct effects of rotation and curvature are absent in the $O(1)$ model. Explicit effects of curvature are found

to affect the $O(\epsilon)$ and higher order terms. In particular, the role of curvature in determining the Reynolds shear stress structure and production of turbulent kinetic energy is analyzed. It is found that extra strain rates due to streamline curvature appears only at $O(\epsilon^2)$. The simple shear strain rate is the leading order contributor to the generation of turbulent kinetic energy. However, as has previously been observed in experiments with curved shear layers, the measurements show that the anisotropy in the Reynolds shear stress is related to the streamline curvature strain rate, and not determined just by the dominant contribution of the simple shear.

A similarity profile in the form of a cubic polynomial is chosen to represent the vertical variation of the mean velocity and is found to be in good agreement with data in the shear layer. The coefficients for the polynomial, which vary in the streamwise direction, are obtained by matching conditions imposed at the top and bottom of the layer. Continuity of mean horizontal velocity at both boundaries and vanishing shear stress at the base of the layer are enforced. The general expression for the coefficient of the cubic term $(A(s))$ is found by enforcing the two-phase surface layer boundary condition at the top of the layer. $A(s)$ is evaluated from the measurements, and the theoretical profile for the mean horizontal velocity is seen to agree well with measured data. The profiles for the turbulent quantities are determined from the turbulence model.

The $O(1)$ model is integrated normally using the profiles to obtain physical insights into the streamwise variation of the turbulent kinetic energy budget and the vertical motion of the base of the layer. As expected, it is found that near the leading edge of the breaker, dissipation is smaller than production, whereas further downstream, the ratio of dissipation to production increases, and in fact attains a singularity, when, theoretically, the production vanishes. The pressure at the bottom of the layer is found to be in excess of the pressure at the top of the layer and is due to rotation and non-zero mean shear stress at the top of the layer. In the

172

far wake region, the pressure and the mean velocity are found to be uniform across the layer. The vertical variation of the turbulent kinetic energy is also uniform. As yet, this has not been verified with respect to data.

The governing equations at $O(\epsilon)$ are then integrated across the layer and formulated in terms of layer-averaged variables. These are chosen as the width of the layer (b), the layer-averaged mean horizontal velocity $(\overline{U})$, and the layer-averaged turbulent kinetic energy $(\overline{k})$. The turbulent surface-layer contributions are taken into account through boundary conditions applied at the top of the layer. This results in a coupled system of equations for the evolution of b, $\overline{U}$, and $\overline{k}$. The significance of the vertical shear in the layer and the non-zero mean shear stress at the top of the layer are pointed out at several stages of the derivation of the equations. The turbulent kinetic energy equation shows that there is no diffusive penetration of vorticity into the underlying flow, i.e., the thin layer of viscous laminar flow between the turbulent layer and the irrotational flow is disregarded in the present model. The final set of equations can either be considered as evolution equations for the variables or boundary conditions for the flow below. The coupling between the turbulent flow in the thin layer and the irrotational flow below is provided through mass entrainment and excess pressure at the boundary. The additional pressure at the base of the layer is found to be linked to the layer-averaged turbulent kinetic energy.

A model for the streamwise variation of $A(s)$ is developed based on physical reasoning and the present experimental measurements. A linear decay in the downstream direction is found to satisfy the requirements imposed by the theoretical model as well as the trends in the mean and turbulent quantities estimated from the measurements. Further comparison between the theoretical model and the measurements is in progress. It is noted that a higher resolution data-set would afford a more meaningful comparison, since turbulence production and dissipation rates

need to be available to confirm the theoretical trend observed in $\Lambda(s)$. A crucial issue in the model is the sign of the mean shear stress at the top of the layer, since a direct comparison of its streamwise variation can be made with the suggested model for $A(s)$. In addition, the analytical expression for $A(s)$ has to be compared to the values estimated from the data.

Chapter 5

COHERENT TURBULENT STRUCTURES

The true worth of an experimenter consists in his pursuing not only what he seeks in his experiment, but also what he did not seek

Claude Bernard

5.1 Introduction

In the "bulk" models described in Chapter 4 to represent spilling breakers, the turbulent structure of the flow, especially the details in the breaker shear layer and in the highly intermittent region near the surface, is either grossly simplified or completely disregarded. However, there are dominant and persisting energy containing scales in turbulent flows that exhibit evident and coherent structure. Although there are several definitions of coherent structures in literature, a generalized description provided by Robinson (1991) will suffice for the purpose of this chapter. A coherent structure or motion is defined as "a three-dimensional region of the flow over which at least one fundamental flow variable (velocity component, density, temperature, etc.) exhibits significant correlation with itself or with another variable over a range of space and/or time that is significantly larger than the smallest scales of the local flow". Laboratory experiments have clearly confirmed the existence of classes of eddies in breaking waves. Nadaoka (1986), using qualitative flow visualization techniques, was the first to examine the large scale eddy structure
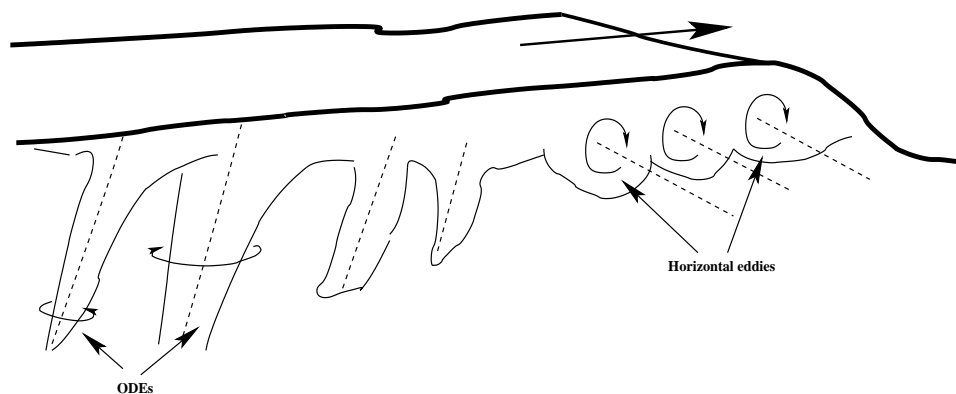
Figure 5.1: Horizontal and obliquely descending eddies in a breaking wave. Adapted from Nadaoka (1986).

under breaking waves. Around the wave crest, the "horizontal eddies" had a two-dimensional structure, with their axes parallel to the wave crest. Behind the crest, the ODEs stretched downward into the water column (see Figure 5.1). These were oriented along the mean strain rate and were mainly responsible for the generation of Reynolds stress in the upper layer of the water.

Yeh and Mok (1990) performed LIF experiments with hydraulic jumps and bores, and found sporadic three-dimensional turbulent patches created by mixing at the foot of the breaker. As the large-scale "eddies" were advected downstream (away from the crest), their shapes tended to become less elliptic and more circular in the vertical plane of measurement. Simultaneously, the major axis of the eddy rotated in the counter-clockwise direction because of stronger advection as the depth increased. This topological transformation was suggested as a mechanism for the spreading of turbulence in the mixing layer originating from the foot of the breaker. A schematic representation is shown in Figure 5.2. The mixing layer analogy with hydraulic jumps from flow visualization experiments (Hoyt and Sellin, 1989) has already been discussed. It is worth noting in the context of this chapter, that they found "a pattern of growing, whirling, and intersecting vortex structures" in the
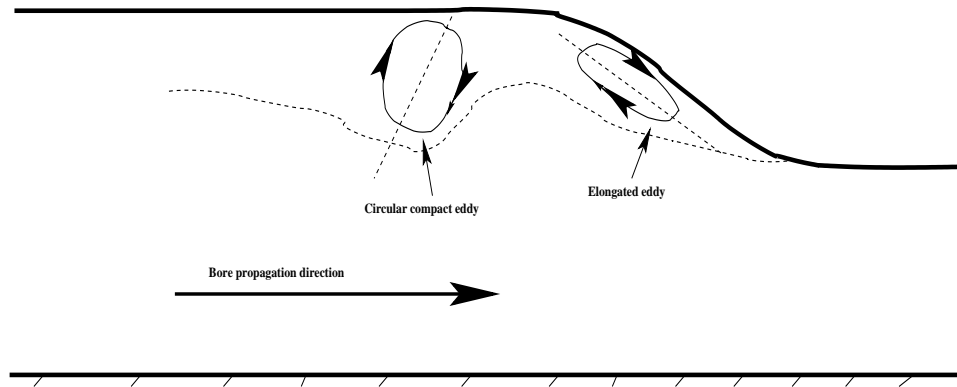
Figure 5.2: Mutation of eddy axis and change in topology of eddies in an unsteady bore. Adapted from Yeh and Mok (1990).

mixing layer.

Cox and Kobayashi (2000), using quadrant analysis and conditional sampling techniques, found intense, intermittent coherent motions under spilling breaking waves that accounted for 20 - 50 % of the turbulent motion. The large turbulent motions were found to be infrequent in time and were wave-phase dependent near trough level. This is in tune with Townsend's hypothesis that the dynamics of a turbulent shear flow are governed by a balance between the rate of energy extraction from the mean flow through the large-scale coherent structures and the rate of energy dissipation governed by the structures losing energy to the small-scale turbulence (Townsend, 1976). Therefore, the turbulence production at a fixed point is not a continuous process and is phase-related to the dynamics of the coherent structures. Since the LDV velocities were gathered at a fixed spatial location, the spatial structure of the coherent motions could not be studied. For spilling breakers, coherent toe oscillations have also been frequently observed in the laboratory (Duncan, 1981; Banner, 1988). Based on qualitative visualization studies, Mossa (1998) has suggested that vortex pairing mechanisms govern the oscillating characteristics of hydraulic jumps.

Non-intrusive, instantaneous whole-field measurement techniques such as PIV have aided the visualization and characterization of such organized motion in turbulent flows. Further, Melville *et al.* (2002) have shown that coherent structures in a deep water breaking wave can be studied using a mosaic of PIV images. In Lin and Rockwell (1995), the incipient and intermediate stages of evolution of a quasi-steady breaker were studied using high-image-density PIV. They found that with the onset of separation, which involves flow deceleration along a region of the free-surface having a large radius of curvature, a long mixing layer was formed with substantial levels of vorticity. In a frame moving with half the free stream velocity, they detected coherent vortical motions suggested by patterns of swirling velocity vectors along the mixing-layer originating from the toe of the breaker. In the same vein, during the incipient stages of breaking for a surface tension-dominated spilling breaker, Qiao and Duncan (2001) found coherent patches of vorticity along the wave crest. The measurements unfortunately ended before the formation of a fully-formed breaker. In studying the vertical vorticity generated by the jet of a plunging breaker, Chang and Liu (1998) observed that the number and locations of the vortices in the horizontal plane were random. Similarly, with a light sheet in the streamwise-spanwise plane, PIV laboratory experiments conducted by Cox and Anderson (2001) on the breaking of regular plunging breakers revealed the nominal diameter (l) of (instantaneous) eddies associated with wave breaking to be around 0.05 m. The breaking wave height (H_b) was 0.12 m, which gives $\frac{l}{H_b} = 0.42$. $\frac{l}{H_b}$ gives a dimensionless eddy size with respect to the integral length scale taken as the breaker height. The latter is a more suitable choice of length scale than the wavelength because it can be applied to steady breakers (such as a hydraulic jump) as well. They noted that they could not detect larger eddies because of the restriction imposed by their target area which was 10 cm $\times$ 10 cm. The detection of the smallest coherent motions was limited by the spatial resolution of 3.65 mm.

178

For many of their tests, they also found complex three-dimensional patterns with no well-defined eddies. Longo (2003), using orthogonal wavelets as a decomposition technique, found that more than 70 % of the total turbulent kinetic energy for spilling breakers was carried by micro (with a length scale in the range 2 mm $< l <$ 10 cm) and mid-size (10 cm $< l <$ 4.0 m) vortices, predominantly below the wave crest, and that most of the energy was transferred from the macro- and mid-size vortices to the micro-vortices after the passage of the breaker. The breaking wave height was 10 cm, giving a maximum and minimum $\frac{l}{H_b} = 1$ for the micro- and mid-size vortices respectively. For the mid-size vortices, the maximum $\frac{l}{H_b}$ is 40. This rather large value results due to the choice of the breaker wave height instead of the wavelength as a non-dimensionalizing length scale. Stansby and Feng (2005) used laser Doppler anemometry measurements of laboratory-generated bores and found multiple vortical structures at the initiation of breaking, which became elongated along the surface during bore propagation. With the increase in computing power, detailed numerical simulations of wave breaking have also been performed. These models are in the beginning stages of development, but the results indicate the presence of coherent eddies similar to ODEs (Rogers and Dalrymple, 2005) as well as a series of eddies in the shear layer below the surface roller (Christensen and Deigaard, 2001; Dimas and Fialkowski, 2000).

In none of the studies mentioned above has there been a detailed quantitative investigation of these coherent structures, especially for a quasi-steady fully-formed breaker. In particular, there has been no attempt to look into the role played by the strain rates in the generation and persistence of the structures, even though the tools for aiding such analyses (described further) have been demonstrated to be effective in turbulent shear layers. In this chapter, we focus our attention on characterizing the resolvable coherent turbulent motions in the breaker shear layer, which as we have already seen in Chapter 2, can be characterized as a mixing

layer. Even though Reynolds-averaging techniques do not explicitly reveal coherent motions in the turbulence, some sort of instantaneous organization is apparent even in the averaged terms, such as the Reynolds shear stress $- < \tilde{u}'\tilde{v}' >$. Note that $\tilde{u}'$ and $\tilde{v}'$ denote the instantaneous turbulent fluctuations and not the root mean square turbulent fluctuations analyzed in Chapter 3. This notation is followed throughout this chapter. The Reynolds stress would be zero if the motions in the shear layer were purely random without preferred correlations (in space and/or time) between the horizontal and vertical velocity fluctuations. As already seen in Chapter 2 (see Figure 3.16), the breaker mixing layer is characterized by regions of significant Reynolds shear stress, with visually detectable coherent patterns.

As an alternative to the classical theory of viewing turbulence as an essentially random process which can be described statistically, quasi-deterministic coherent structures provide a description of the main building blocks of turbulent mixing layers (Ho and Huerre, 1984). It is noted that there are two separate issues which need to be examined here: the presence and persistence of large-scale structures on the one hand, and their two-dimensional signature on the other. This is not to imply that the structures are two-dimensional in nature. One of the first indications of large-scale structures in a turbulent shear layer came from the discovery of a relatively sharp interface between turbulent and non-turbulent fluid by Corrsin (1943). It was the work of Kline *et al.* (1967) and Kim *et al.* (1971) through combined quantitative velocity measurements and visual observations that first demonstrated the temporal development of spatially coherent patterns. The presence of coherent structures in mixing layers is quite well documented, starting from the visualization studies of Brown and Roshko (1974) to two-dimensional (Bell and Keyser, 1993) and three-dimensional experimental investigations (Delville *et al.*, 1999). Several methods have been developed to identify these structures in a

wide variety of turbulent shear flows, including statistical means used for calculating double spatial correlations (Stanislas *et al.*, 1999; Liu *et al.*, 2001; Carlier and Stanislas, 2005) and linear stochastic estimates (Adrian, 1994), proper orthogonal decomposition (Berkooz *et al.*, 1993), wavelets (Farge, 1991), instantaneous flow patters decomposed by Galiliean transformations (Adrian *et al.*, 2000), flow-kinematics based critical point theory (Perry and Chong, 1994), topological methods using vortex identification algorithms (Soria and Cantwell, 1994; Agarwal and Prasad, 2002), and conditional sampling techniques such as quadrant analysis (Rajagopalan and Antonia, 1982). An extensive collection of papers dealing with these techniques can be found in Bonnet and Glauser (1993). Since each of these methods provides information about one or more particular aspect of the coherent structure (its shape, length scale, temporal evolution etc.), several of these methods need to be applied simultaneously for a robust detection and quantification (Kevlahan *et al.*, 1994).

In the following two sections, we implement methods based on the kinematics and ensemble statistics of the flow to provide insights into the coherent structures. In this chapter, for all analyses, we use dataset II because of its higher resolution ($\Delta\tilde{x} = \Delta\tilde{y} = 0.011$) compared to dataset I ($\Delta\tilde{x} = \Delta\tilde{y} = 0.021$). The velocity field in dataset II is seen to capture more details of the flow as shown by a plot of the instantaneous horizontal velocity in Figure 5.3. The reverse flow due to breaking downstream of the toe, indicated by the negative horizontal velocities below the instantaneous surface can be clearly seen. Note also the detailed resolution of the instantaneous surface. As compared to the GLCM-based interface algorithm used for dataset I, a more accurate algorithm based on factored sampling and active contours is used for dataset II (Thomas *et al.*, 2005b). The origin of the coordinate system is defined at the bottom left corner of the target area. Note that the coordinate system is independent of the one used for dataset I. It is not very meaningful to transform one to the other, since even though the flow is assumed to be steady, the instantaneous
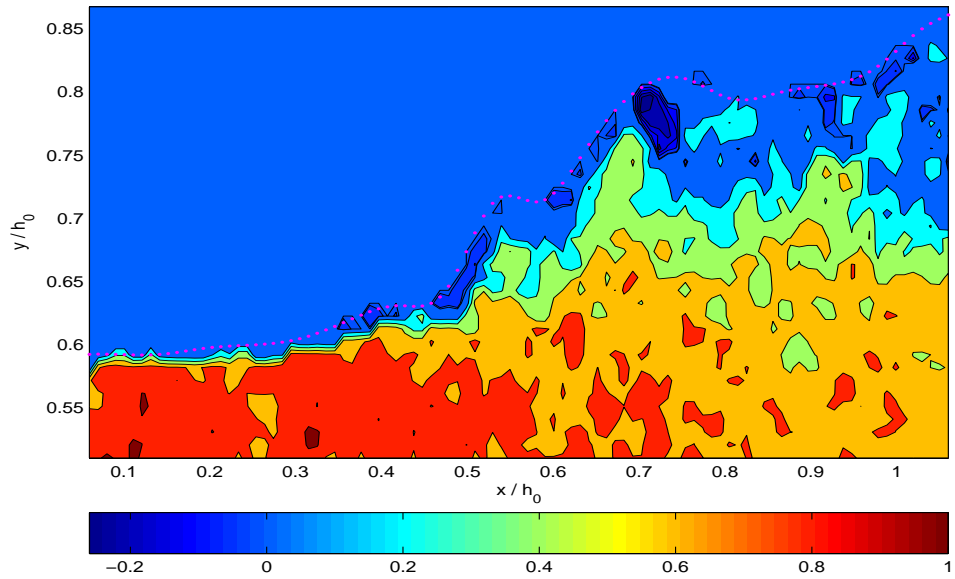
Figure 5.3: Typical realization of instantaneous horizontal velocity (m/s) showing reverse flow due to breaking at the surface (dotted magenta line).

realizations of the flow are different. In addition, the surface estimation algorithms used in the two data sets are different, and the geometric properties of the surface (such as the location of the toe and foot of the breaker) cannot be compared. This does not hamper the physical interpretation of the analysis in this chapter, since the main aim here is to take a detailed look at the flow structure in the mixing layer near the toe of the breaker.

5.2 Strain rate tensors

The evolution of a turbulent flow is essentially governed by vorticity dynamics. The growth of vorticity by stretching of vortex lines is the primary mechanism of energy dissipation. There is still considerable ambiguity in the definition of a vortex as evidenced by the numerous proposed characterizations one can find in literature (Chong *et al.*, 1990; Jeong and Hussain, 1995). A generally accepted definition is the one by Kline and Robinson (1989): "A vortex exists when instantaneous streamlines

mapped onto a plane normal to the core exhibit a roughly circular or spiral pattern when viewed in a reference frame moving with the center of the vortex core". As demonstrated by Jiménez *et al.* (1993), vortices are identified by isolating regions of concentrated vorticity. However, in complex flows (such as the breaker shear layer considered here) which are characterized by significant levels of shear in the velocity field, Adrian *et al.* (2000) point out that it is ambiguous to use vorticity maps to identify vortices since they are "masked" by the background shear. There are many ways of educting vortical structures from the flow, and these will be discussed further in this chapter. However, it is instructive to look at the strain rate tensors first, since the turbulence structure essentially evolves from interactions between vorticity and strain rate. The alignments (and topology of the vortex structures) are altered by interactions with mean strain and rotation rate depending on the structure of the mean gradients, the relative strengths of mean to fluctuating velocity gradients, and the Reynolds number.

The rate-of-displacement or velocity gradient tensor is given as

$$D_{ij} = \frac{\partial u_i}{\partial x_j},$$
(5.1)

where i and j (=1,2) are free indices and denote the Cartesian coordinate directions. D_{ij} can be decomposed into the symmetric rate-of-strain (deformation) tensor

$$S_{ij} = \frac{1}{2} \left(\frac{\partial u_i}{\partial x_j} + \frac{\partial u_j}{\partial x_i} \right),$$
(5.2)

and the skew-symmetric rate-of-rotation (spin) tensor (Tennekes and Lumley, 1972)

$$R_{ij} = \frac{1}{2} \left(\frac{\partial u_i}{\partial x_j} - \frac{\partial u_j}{\partial x_i} \right).$$
(5.3)

The diagonal terms of the rotation tensor are zero by definition. In the present case, where information is only available in the $x - y$ plane, the tensor components reduce

183
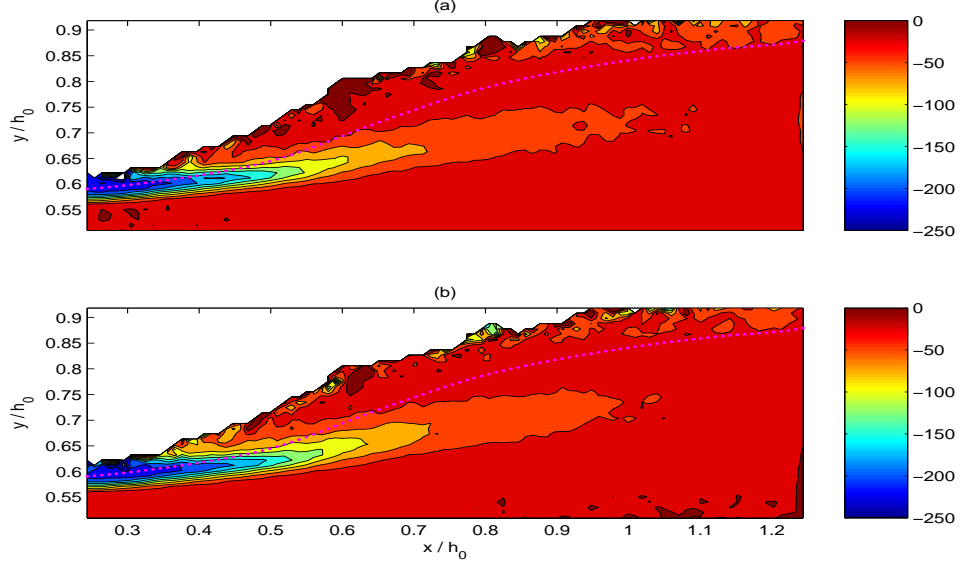
Figure 5.4: (a) $\langle S_{xy} \rangle$ (1/s), and (b) $\langle R_{xy} \rangle$ (1/s). The dotted magenta line is the ensemble-averaged free surface.

to

$$S_{xx} = \frac{\partial u}{\partial x}, \quad S_{yy} = \frac{\partial v}{\partial y}, \quad S_{xy} = S_{yx} = \frac{1}{2}\left(\frac{\partial v}{\partial x} + \frac{\partial u}{\partial y}\right), \tag{5.4}$$

$$R_{xy} = -R_{yx} = \frac{1}{2}\omega_z = \frac{1}{2}\left(\frac{\partial u}{\partial y} - \frac{\partial v}{\partial x}\right). \tag{5.5}$$

S_{xx} and S_{yy} are the normal/linear strain rates. ω_z is the vorticity in the span-wise direction. The ensemble-averaged values for the shear strain rate ($\langle S_{xy} \rangle$) and the rotation strain rate ($\langle R_{xy} \rangle$) are shown in Figure 5.4. The surface intermittency due to the interface fluctuations has been taken into account when estimating the ensemble-averaged strain rates, which results in non-zero values above the mean surface. $\langle S_{xy} \rangle$ and $\langle R_{xy} \rangle$ are remarkably similar, both in alignment, sign (they are both negative), and magnitude. This indicates that the ensemble-averaged contribution from the curvature term ($\langle S_{xy} \rangle - \langle R_{xy} \rangle = \langle \frac{\partial v}{\partial x} \rangle$) is small. From Figure 5.5, it is seen that the effect of positive curvature ($\langle \frac{\partial v}{\partial x} \rangle > 0$) is felt only near downstream of the

184
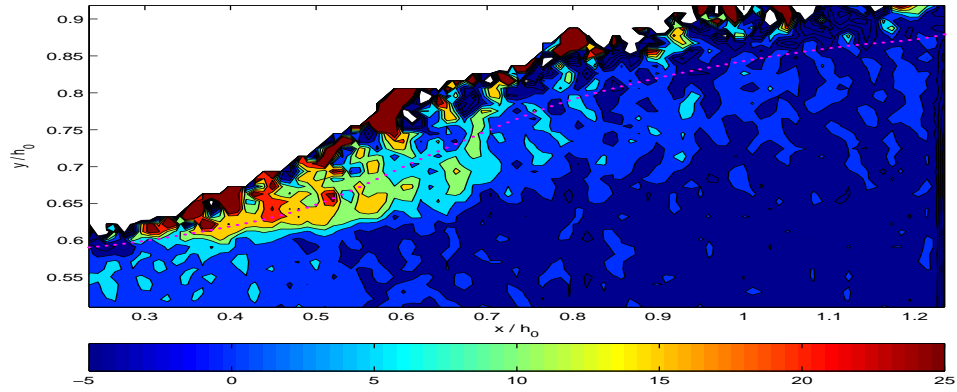
Figure 5.5: $\left\langle \frac{\partial v}{\partial x} \right\rangle$ (1/s).
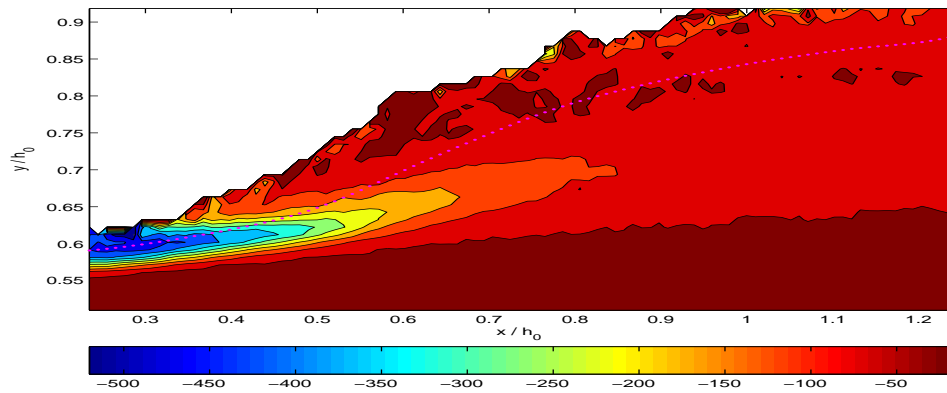
Figure 5.6: $\left\langle \frac{\partial u}{\partial y} \right\rangle$ (1/s).

foot of the breaker, and even here, the values are an order of magnitude smaller than the shear strain rate.

It is important to remember that relative vorticity, defined below, is a combination of shear vorticity (ω_z^s) and curvature vorticity (ω_z^c) (defined in equation (5.6)), and that they, and their rate of change, are not Galiliean invariant. For e.g., if a vortex with perfectly circular and symmetric streamlines is super-imposed on different irrotational streams, the relative vorticity of the combined flow does not change. However, the curvature vorticity in a fixed frame of reference decreases with increasing strength of the background irrotational flow. The shear vorticity

185

arises from a change in the horizontal velocity in the vertical direction, whereas ω_z^c arises due to the change in direction over some horizontal distance, which can be quantified by the local curvature of the streamlines. Both negative shear ($\frac{\partial u}{\partial y} < 0$) and positive curvature ($\frac{\partial v}{\partial x} > 0$) contribute to negative vorticity. This is the case near the toe of the breaker, where the effect of small positive curvature reinforces the contribution from the large negative shear, leading to large values of negative vorticity. Therefore, it is possible to have equal and opposite contributions from ω_z^c and ω_z^s so that the relative vorticity, $\omega_z = 0$. This can be seen more clearly in a natural coordinate system (s, n) where the velocity is always forward, following the streamlines of the flow. The relative vorticity can be written as (Holton, 2004)

$$\omega_z = \omega_z^s + \omega_z^c = \frac{\partial u_s}{\partial n} - \frac{u_s}{\kappa}, \tag{5.6}$$

where u_s is the speed (the normal component of the velocity is obviously zero on the streamline), and κ is the local curvature of the streamline. The first and second terms are the shear and curvature term respectively. It is obvious that a large contribution to ω_z^c arises in regions of large curvature, which happens in the present case only in a small region downstream of the foot. It can be seen in Figure 5.5 and Figure 5.6, that even in this region, the shear contribution is significantly larger.

From Figure 5.4, it can be concluded that about half of the ensemble averaged clockwise vorticity comes from the shear deformation of the flow. The other half, with the same clockwise sense of rotation, comes from the rotation strain of the flow. Also, the similar orientations of $\langle R_{xy} \rangle$ and $\langle S_{xy} \rangle$ indicate that the rotational component is oriented along the shear strain rate. In the following, the kinematic sources of ω_z^c are investigated. In particular, the contribution from coherent vortical structures in the flow is assessed. As an aside, the maximum non-dimensionalized magnitude of the ensemble-averaged vorticity (see IS00) near the toe is

$$\left(\frac{h_1 \xi}{U_0} \right) \overline{\omega}_z \sim 75. \tag{5.7}$$

186
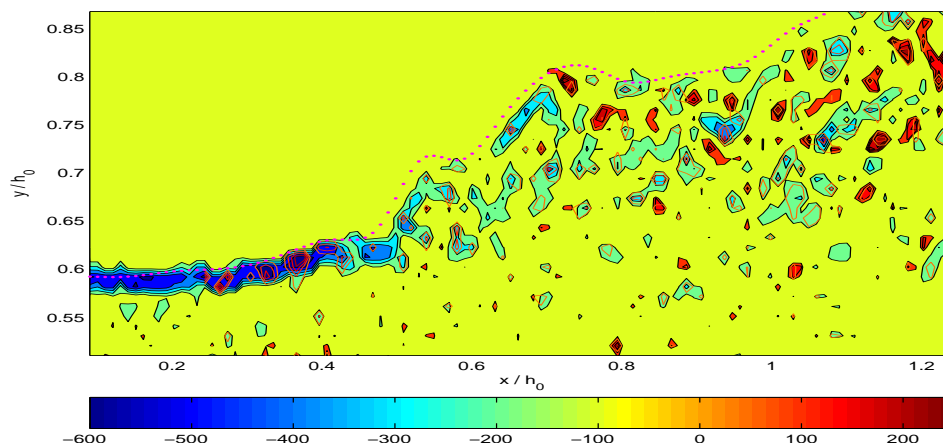
Figure 5.7: Instantaneous contours of ω_z (1/s) and λ_{ci} (1/s) at the 500th realization ($it = 500$). The dotted magenta line is the instantaneous free surface.

This is almost 4 times higher than the value reported by Veeramony and Svendsen (2000) of 17 at the bottom boundary of the roller, which was obtained by an extrapolation (because of lack of data near the toe) of the estimates in IS00. However, there was no physical justification for the formula used, and the extrapolation was performed to "ease numerical instabilities". The vorticity at the bottom boundary of the roller, especially near the toe, is an important boundary condition used in roller formulations for Boussinesq modeling of breaking waves. Values as high as 100 for the non-dimensional vorticity have been used successfully to model the dissipation of breaking waves in the surf-zone (Briganti *et al.*, 2004). Some of the discrepancy between the present result and the reported values of IS00 is also due to the different spatial resolutions (the present vertical resolution being 5 times higher than theirs). Further, they had neglected contributions from the streamwise gradient of the vertical velocity which attains its highest value near the toe.

The instantaneous total vorticity is shown in Figure 5.7. Note that, in the plot, vorticity values from -100 to 50 s^{-1} have been suppressed to clearly separate

187

the significant vorticity patches. A coherent stretch of negative (clockwise) vorticity can be seen near the toe of the breaker ($\tilde{x} \sim 0.3$, marked by the sudden rise in surface slope), whereas, further downstream, there are isolated and randomly distributed packets of weaker negative and positive (anti-clockwise) vorticity. The approximate magnitude of the vorticity near the toe is -500 s^{-1} and -230 s^{-1} to 200 s^{-1} in the far downstream region. For surface tension-dominated spilling breakers generated in the laboratory, Lin and Rockwell (1995) and Qiao and Duncan (2001) have reported maximum vorticity magnitudes of 456 s^{-1} and 320 s^{-1} respectively near the toe. The values here are higher in magnitude, and a direct comparison is difficult because the generation method of the breaker, the stage of breaker evolution, and the underlying background flow are different in each case. The sensitivity of the vorticity to the resolution of the free surface and the flow parameters was noted by Lin and Rockwell (1995). A slight change in Froude number (0.49 to 0.56) in their case led to an increase in the normalized maximum vorticity by a factor of 2.

To educt the instantaneous vortices in the flow, a critical point analysis of the local velocity gradient tensor and its corresponding eigenvalues based on Perry and Chong (1994) and Chong et $al.$ (1990) is used. In two-dimensions, the local velocity gradient tensor is given by

$$\mathbf{D} = \begin{bmatrix} \frac{\partial u}{\partial x} & \frac{\partial u}{\partial y} \\ \frac{\partial v}{\partial x} & \frac{\partial v}{\partial y} \end{bmatrix}.$$

$\mathbf{D}$ has either two real eigenvalues or a pair of complex conjugate eigenvalues ($\lambda_{cr} \pm i\lambda_{ci}$) (Adrian et $al.$, 2000). If the flow is pure shear flow, corresponding to $\lambda_{ci}=0$, the particle motion is essentially in the form of parallel streamlines, which can be thought of as infinitely-long ellipses. Since the period of "swirling" motion is given by λ_{ci}^{-1}, in pure shear flow, the orbit period is infinite. $\lambda_{ci} > 0$ corresponds to non-parallel flow conditions, or shorter, more circular motion, i.e., eddies. λ_{ci} is also defined as the "swirling strength" of the eddy (Zhou et $al.$, 1996, 1999). The
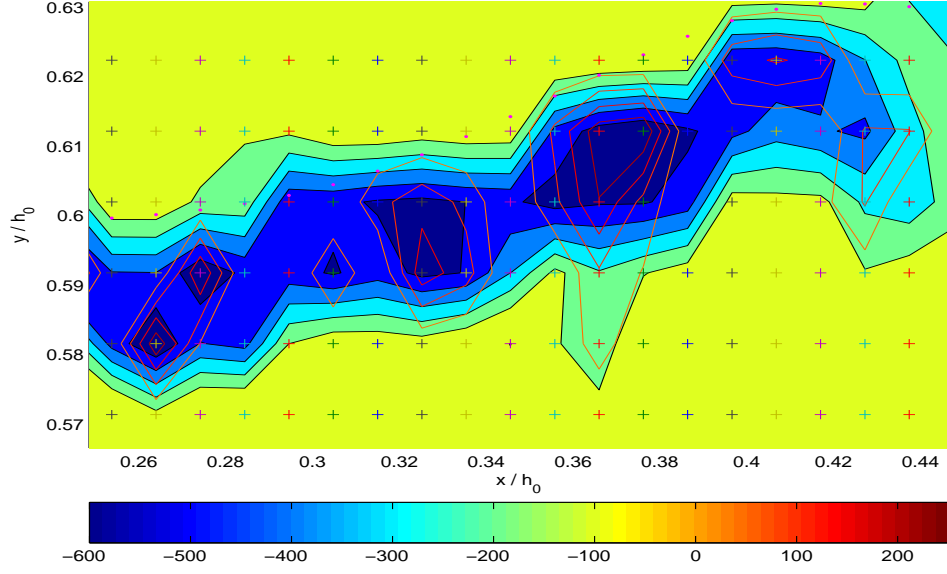
Figure 5.8: Measurement locations overlaid with instantaneous contours of ω_z and λ_{ci} at $it = 500$. The dotted magenta line is the instantaneous free surface.

enstrophy (for 2-D flow, it is given by $\frac{\omega_z^2}{2}$) is, therefore, measured by λ_{ci}^2. Note that λ_{ci} only gives a measure of the strength of swirling and not the sense of rotation.

Instantaneous iso-contours of λ_{ci} are shown overlaid with the vorticity in Figure 5.7. Near the toe, where the instantaneous vorticity has a clockwise orientation, the structures are arranged in an elongated (in the streamwise direction) packet just below the instantaneous surface. The streamwise length (L_s) of this "vortex packet", non-dimensionalized by the breaker height ($H_b = h_1 - h_0 = 2.22$ cm), is $\frac{L_s}{H_b} \sim 0.62$. The highest value of $\lambda_{ci} \sim 248$ s^{-1} is found in the core of the structure near the toe at $\tilde{x} \sim 0.37$ and $\tilde{y} \sim 0.61$, with smaller swirling strengths further downstream around the randomly distributed pockets of positive and negative vorticity. If a quantitative equivalence is assumed between the swirling strength and the vorticity magnitude, the "vortex packet" is seen to contribute approximately half of the instantaneous vorticity near the toe, the other half coming from the shear strain. Even though the
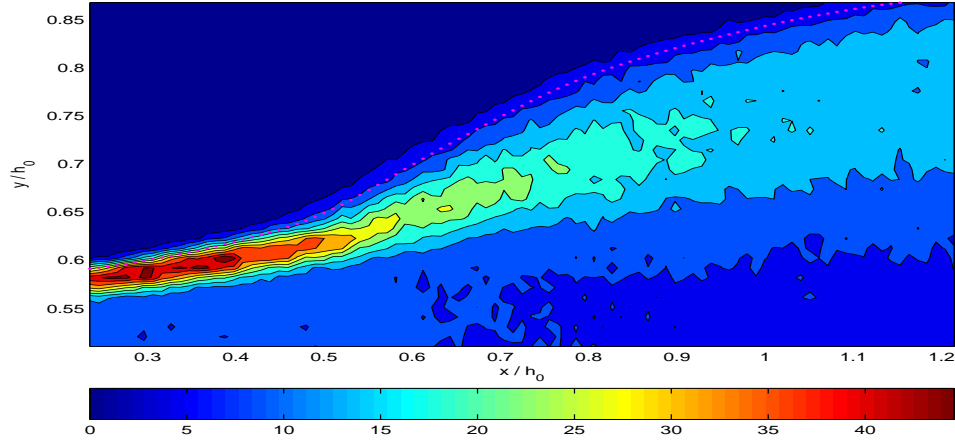
Figure 5.9: Ensemble-averaged λ_{ci} (1/s). The dotted magenta line is the ensemble-averaged free surface.

vorticity does identify some of the eddies, it also tends to identify local shear layers present in the flow, particularly upstream of the toe, and is generally much noisier than the swirling strength (Adrian *et al.*, 2000). A close-up view of the "vortex packet" is shown in Figure 5.8 with the measurement locations. It is seen that the size of the individual structures is reasonably resolved by the measurement grid. An average size of the eddies, non-dimensionalized by H_b, is calculated to be 0.16. It is noted that, with contours of swirling strength, a definition of size or diameter is subjective (Adrian *et al.*, 2000). A contour level of 25 s^{-1}($\sim 10\%$ of the maximum value) has been chosen here to calculate the average size.

The ensemble-averaged contribution given by the coherent structures can be assessed (and indeed their "persistence" tested and quantified) by constructing the ensemble-averaged field of λ_{ci}. This is shown in Figure 5.9. The streamwise localization of the coherent structures coincides with that of the maximum of the shear strain rate. The cross-flow spread increases in the downstream direction because of the random distribution, in space and time, of the individual structures. The "swirling strength" is higher near the toe region and decreases further downstream,
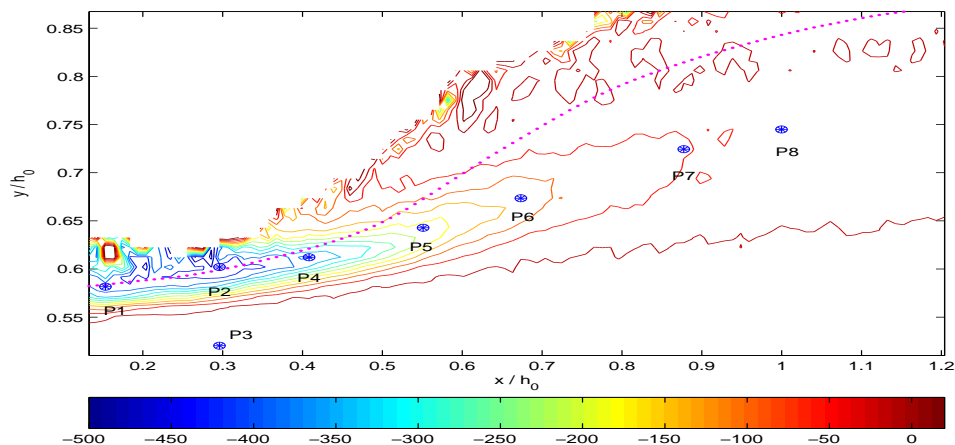
Figure 5.10: Locations of points chosen overlaid on ensemble-averaged ω_z (1/s). The dotted magenta line is the ensemble-averaged free surface.

indicative of the eddies' decreasing efficiency in extracting energy from the mean flow which results from increased misalignment with the mean shear strain rate. Approximately 20% of $\langle\omega_z^c\rangle$ (or $\sim 10\%$ of $\langle\omega_z\rangle$) is seen to come from the coherent structures. The rest, being the major part of the contribution, comes from the mean shear $\left(\left\langle\frac{\partial u}{\partial y}\right\rangle\right)$, which in this case is much larger than $\left\langle\frac{\partial v}{\partial x}\right\rangle$. This can be seen more clearly by realizing that a simple shearing motion can always be decomposed into a pure straining motion with zero rate of expansion and a rigid rotation (Batchelor, 1967),

$$\frac{\partial u}{\partial y} = \frac{1}{2}\left(\frac{\partial u}{\partial y} + \frac{\partial v}{\partial x}\right) + \frac{1}{2}\left(\frac{\partial u}{\partial y} - \frac{\partial v}{\partial x}\right). \tag{5.8}$$

In order to obtain a clearer insight into the contribution made by the coherent turbulent structures to the vorticity, it is necessary to look at the fluctuating component of the vorticity. This essentially removes the dominant contribution made by the shear of the background mean flow to the instantaneous vorticity. The fluctuating vorticity field can also provide information about the generation and advection mechanisms of the vortices (Higgins *et al.*, 2003; Fulgosi *et al.*, 2003). The

191

fluctuating vorticity is calculated as

$$\tilde{\omega}'_z = \omega_z - <\omega_z> . \tag{5.9}$$

It is essential to know the location of the free surface, since in the intermittent region, subtracting the ensemble-averaged values from the instantaneous values can lead to finite, yet artificial fluctuations. Therefore, all values of the fluctuating vorticity above the instantaneous surface are put to zero. To characterize the spatial dependence of the organized motions, the fluctuating vorticity at each realization of the ensemble was analyzed at eight different spatial locations. The locations are shown in Figure 5.10, and are given by P1(0.15, 0.58), P2(0.30, 0.60), P3(0.30, 0.52), P4(0.41, 0.61), P5(0.55, 0.64), P6(0.67, 0.67), P7(0.88, 0.72), and P8(1.00, 0.74). Except P3, which is below the lower boundary of the shear layer (defined at a contour level of approximately 10% of the maximum vorticity), the other seven locations are chosen along the visually-interpreted center line of the shear layer. Instead of computing the probability density function as in Lamballais *et al.* (1997), frequencies of occurrence of the vorticity fluctuations across the whole ensemble are calculated. These are shown in Figure 5.11 and Figure 5.12 as histograms. The red line is the normal distribution constructed with the mean and standard deviation at each location. This is shown for comparison, since a normal distribution of the fluctuations indicates a statistically random field without any coherence. Note that, because of the fluctuations of the interface, a point could either be in air or water in any given realization. If the point is above the interface, the vorticity fluctuation shows a value of zero. This can lead to ambiguities in interpretation of the histograms since a zero value is also physically possible. Therefore, the interface is tracked in time, and the fluctuation is included only when the point is in water. This leads to varying record lengths at each location. Therefore, instead of choosing a constant bin size, a constant number of bins is chosen equal to 20.
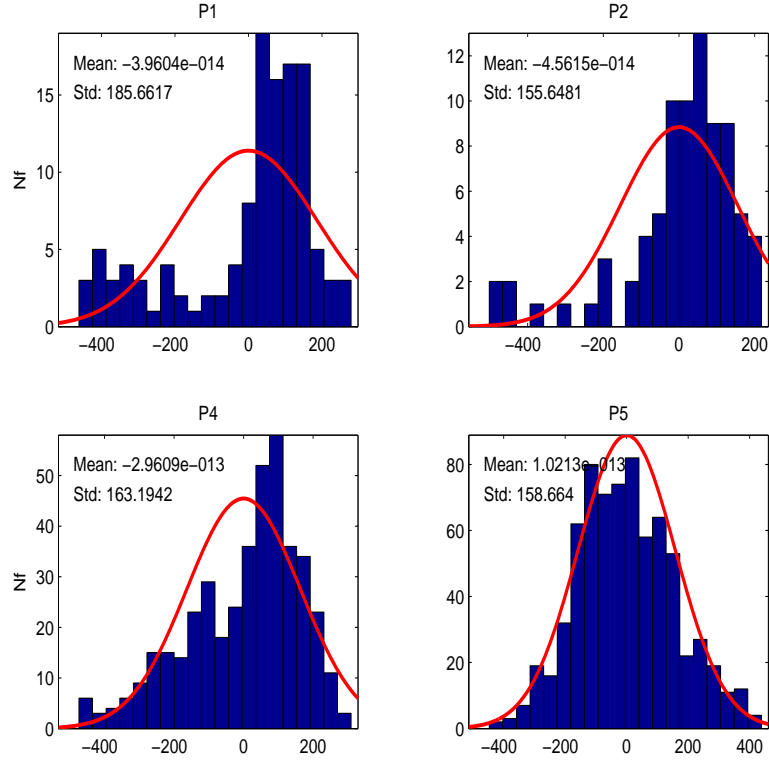
Figure 5.11: Frequencies of occurrence (Nf) of fluctuating vorticity at P1, P2, P4, and P5. Ensemble size = 1020.

The agreement with the normal distribution increases as we progress downstream, indicating a loss of coherence. The loss of coherence is implied only with respect to the present resolution, since coherent motions with sizes smaller than the grid resolution cannot be detected. The record length increases in the downstream direction, leading to more robust estimates of Nf. For example, at P1, the record length is 122, whereas at P8, it is 1017, almost equal to the ensemble size. In light of this, definite quantitative conclusions cannot be drawn with confidence. However, qualitatively, the distributions are skewed towards positive (anti-clockwise) vorticity values near the foot of the breaker. The positive values result from a positive shear ($\frac{\partial u}{\partial y} > 0$, which occurs near the surface from flow reversal due to breaking) in
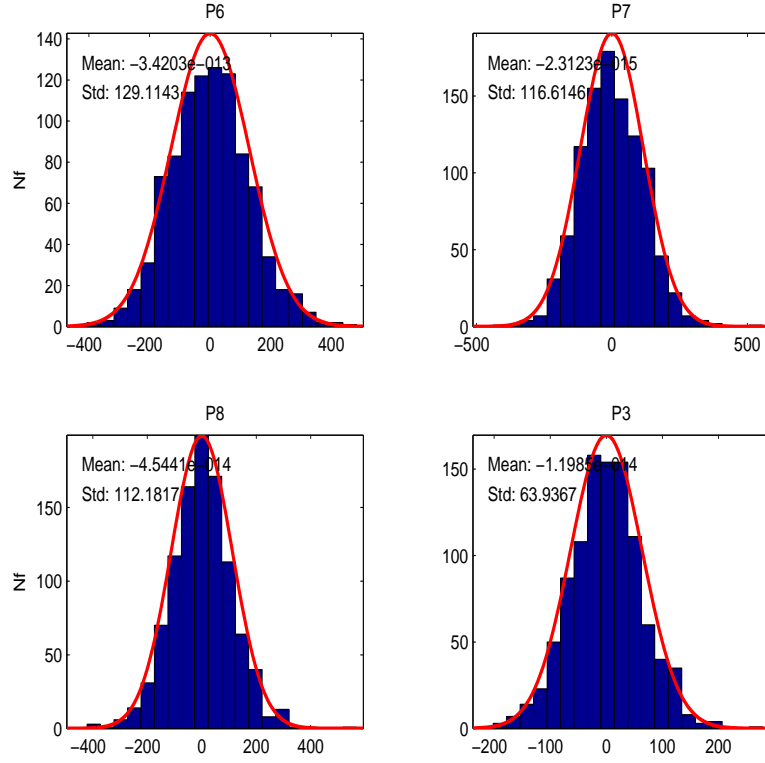
Figure 5.12: Frequencies of occurrence (Nf) of fluctuating vorticity at P6, P7, P8, and P3. Ensemble size = 1020.

conjunction with either a negative curvature $(\frac{\partial v}{\partial x} < 0)$ or small positive curvature $(\frac{\partial v}{\partial x} > 0$ and $\left|\frac{\partial v}{\partial x}\right| << \left|\frac{\partial u}{\partial y}\right|)$. Note that the standard deviation, indicative of the strength of the fluctuations, also decays in the downstream direction. These values are still approximately twice that found at P3. A higher spatial resolution and a bigger ensemble (with a higher sampling rate) would be required to quantitatively evaluate the spatial structure and temporal evolution of these coherent motions.

Since the coherent structures generally have a time history of development as they are generated and convected downstream by the mean flow while undergoing coalescence or "tearing" processes (both of which are known to occur in mixing layers at high Reynolds numbers), observations at one or more spatially fixed locations

194

should include realizations of a large number of these structures at various stages of their life history. As pointed out by Laufer (1975), simple time- and space-averaging techniques tend to "smear out" the essential features of the structures. Ensemble-averaged statistical methods such as two-point spatial correlations or double spatial correlations, which evaluate the simultaneous observations at two spatially separated locations, are particularly suited to the task of quantifying the persistence of the coherence over the ensemble, and are discussed in the next section.

5.3 Double spatial correlations

Some of the following material has appeared in a conference paper (Misra *et al.*, 2005). The correlation operator is frequently used in the statistical analysis of turbulent flows to investigate temporal or spatial coherence. A high degree of correlation indicates a deterministic link between otherwise random variables (such as the turbulent velocity fluctuations). The two-point spatial correlation was first used for planar PIV data of wall turbulence by Stanislas *et al.* (1999) and has since been used to look at large-scale coherence in turbulent boundary layers for stereoscopic PIV data as well (Ganapathisubramani *et al.*, 2005). For two variables A and B, the spatial double correlation operator is defined as

$$R_{AB}(x, y, \delta x, \delta y) \equiv \frac{< A(x, y) \ B(x + \delta x, y + \delta y) >}{\sqrt{< A(x, y)^2 >} \ \sqrt{< B(x + \delta x, y + \delta y)^2 >}}. \qquad (5.10)$$

δx and δy denote the horizontal and vertical distances between the "moving" point (B) and the "fixed" point (A). In the present case, A and B denote the instantaneous velocity fluctuations. Note that, since the correlation is done at the same instant in the whole space, the hypothesis of frozen turbulence is removed, and consequently, there is no restriction on the evolution of the coherent structures (Stanislas *et al.*, 1999). For quasi-steady flow fields, R_{AB} is a function only of locations A, B, and the direction. So, for given locations and a given direction, R_{AB} has a fixed

195

value. Therefore, the form of the two-point correlation is largely determined by the inhomogeneity of the flow field evident in the Reynolds stress structure.

Evidence suggests that the eddies that are the most effective in maintaining a correlation between $\tilde{u}'$ and $\tilde{v}'$ and in extracting energy from the mean flow through the Reynolds stresses are vortices whose main axis is roughly aligned with that of the mean strain rate. The correlation coefficient (C_{uv}) defined by Tennekes and Lumley (1972) as

$$C_{uv} \equiv \frac{< \tilde{u}'\tilde{v}' >}{\sqrt{< \tilde{u}'^2 >< \tilde{v}'^2 >}}, \tag{5.11}$$

is believed to be $O(1)$ in shear-driven turbulent flows, with $|C_{uv}| \sim 0.4$. The values of C_{uv} obtained in the present case are indeed close to 0.4, with the correlation being consistently higher toward the foot of the breaker (discussed below).

Before analyzing the results of the double spatial correlation, it is noted that the auto-correlation coefficient at zero lag is identically unity, as can be easily verified from equation (5.10). Also, note that $R_{uv}(x, y, 0, 0) = C_{uv}$, and therefore, at zero lag, the double cross-correlation coefficient should have values around 0.4. Due to computational restrictions, only a truncated section of the whole domain has been analyzed here. The same eight distinct locations (shown in Figure 5.10) are treated as the fixed points, and all four correlations (R_{uu}, R_{vv}, R_{uv}, and R_{vu}) are calculated for each possible two-dimensional lag within the truncated domain. In Figures 5.13-5.20, the horizontal and vertical axes denote the horizontal and vertical lags with respect to the fixed point, with positive and negative horizontal lags signifying downstream and upstream distances respectively. For the vertical lags, positive and negative values signify distances toward the mean surface and bottom respectively. The lags are given in physical units (mm) for easier physical interpretation of the length scales. Positive contour levels are shown at 0.08 increments for R_{uu} and R_{vv} (minimum and maximum contour levels are 0.25 and 1.0 respectively) and 0.06 increments for R_{uv} and R_{vu} (minimum and maximum contour levels are 0.2 and 0.6

196
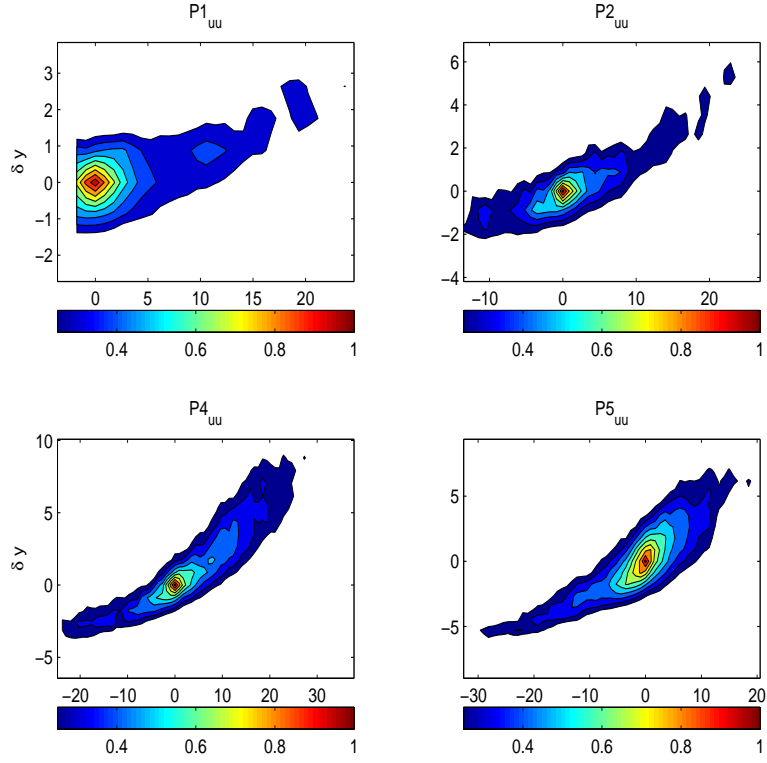
Figure 5.13: R_{uu} at P1, P2, P4, and P5.

respectively).

The structure of the turbulence can be determined by analyzing the shape of the correlation coefficients. At P3, below the shear layer, the turbulence is (predictably) nearly isotropic, with no preferred orientation for either of the correlation coefficients. Note that, in the downstream locations, the values for $R_{uv}(0,0)(= C_{uv})$ are closer to the typical value (0.4) for shear layers, but higher (~ 0.6) values are found close to the foot of the breaker. This is due to the enhanced turbulence generated near the foot from the breaking as well as the presence of an adverse pressure gradient, which distinguish the breaker shear from typical zero-pressure gradient shear layers for which the values of $C_{uv} \sim 0.4$. A noticeable feature of the correlation maps is the absence of significantly large negative values indicating
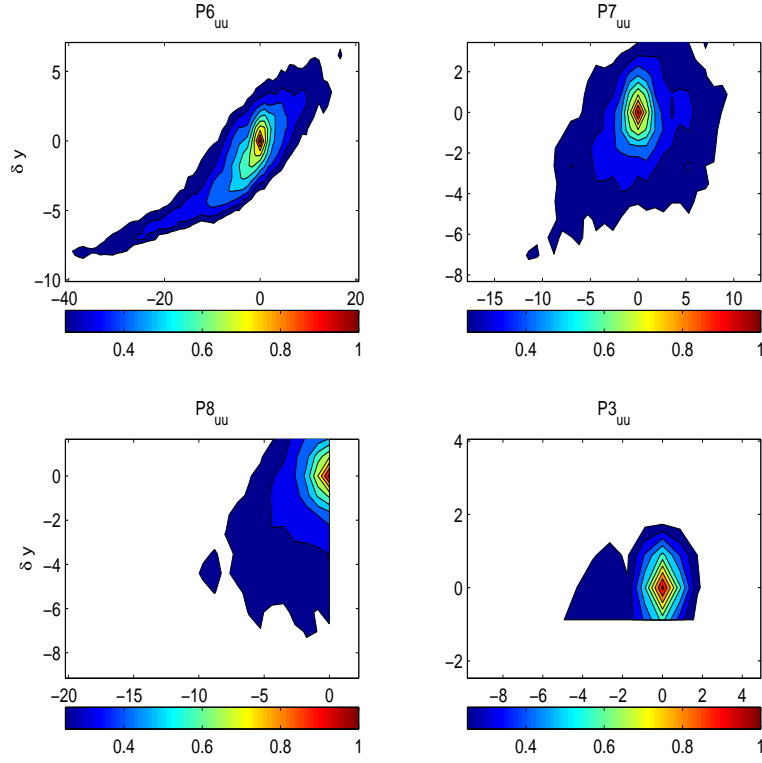
Figure 5.14: R_{uu} at P6, P7, P8, and P3.

the absence of stationary (across the ensemble) two-dimensional eddies or vortices in the streamwise-cross-stream plane. This is in agreement with the more detailed measurements obtained by Lin and Rockwell (1995) for the incipient and intermediate stages of a breaker, who found no indication of a "recirculation vortex with closed streamlines" even in an instantaneous sense. This is also justified in light of the results of the previous section, where the vorticity patches were seen to be generated near the toe and advected downstream. P2 and P4-P6 show significant packets of coherence throughout the shear layer, with the structures elongated and parallel to the surface near the foot in accordance with the "vortex packet" observed in the previous section, and increasingly compact (especially for R_{vv}) and oriented normal to the surface further downstream, around $\tilde{x} \sim 0.7$. This scenario is similar
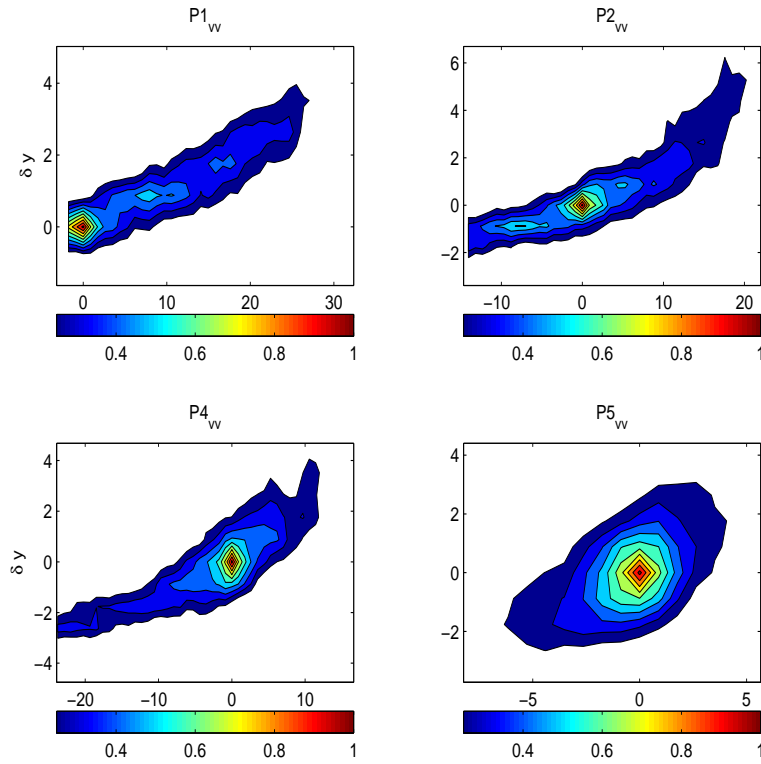
Figure 5.15: R_{vv} at P1, P2, P4, and P5.

to the qualitative observations of Yeh and Mok (1990) and Stansby and Feng (2005).

It is fairly well established that vortex stretching is associated with the energy transfer from the mean flow to the turbulent stresses. It is important to note that the interaction between the mean flow and the turbulent eddies is three-dimensional. Further, this interaction is modified appreciably in the presence of a free surface which induces topological changes of the coherent eddies resulting in strong turbulence anisotropy near the surface (Hunt, 1987). The shape of the structures near the foot of the breaker is elliptical, with the major axis aligned along the mean strain rate. Therefore, these structures are most efficient in extracting energy from the mean flow. Further downstream, they become more compact and circular in form, losing this efficiency. This is reflected in the decreasing intensity of the
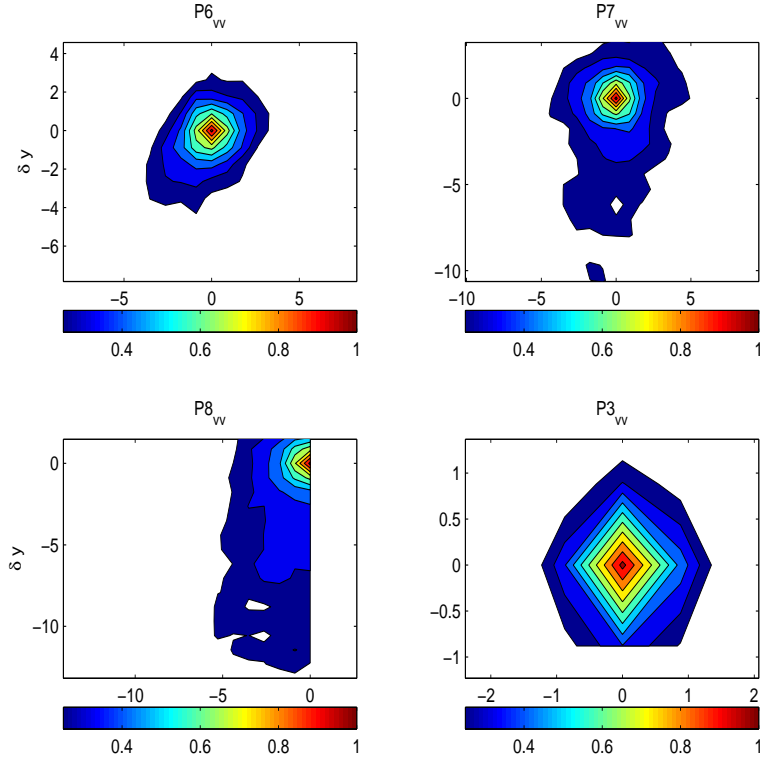
Figure 5.16: R_{vv} at P6, P7, P8, and P3.

Reynolds shear stress in the downstream region. In P4-P6, the coherence is skewed in the streamwise direction parallel to the mean surface, extending further in the upstream direction than in the downstream direction. To quantitatively comment on the length scales, a cut-off value for each correlation coefficient has to be chosen. The contour at this value is used to demarcate the extent of the coherence of the structure. Even though this is subjective and depends on the specific flow under investigation, reasonable values can be chosen based on the "background" values found close to zero lag at P3, since it is seen that the turbulence there is nearly isotropic. For R_{uu} and R_{vv}, a value of 0.4, and for the cross-correlation coefficients, a value of 0.25 is chosen. The average length scale (l_s in the surface parallel direction) for R_{uu} and both cross-correlations, from P4-P6, is found to be approximately
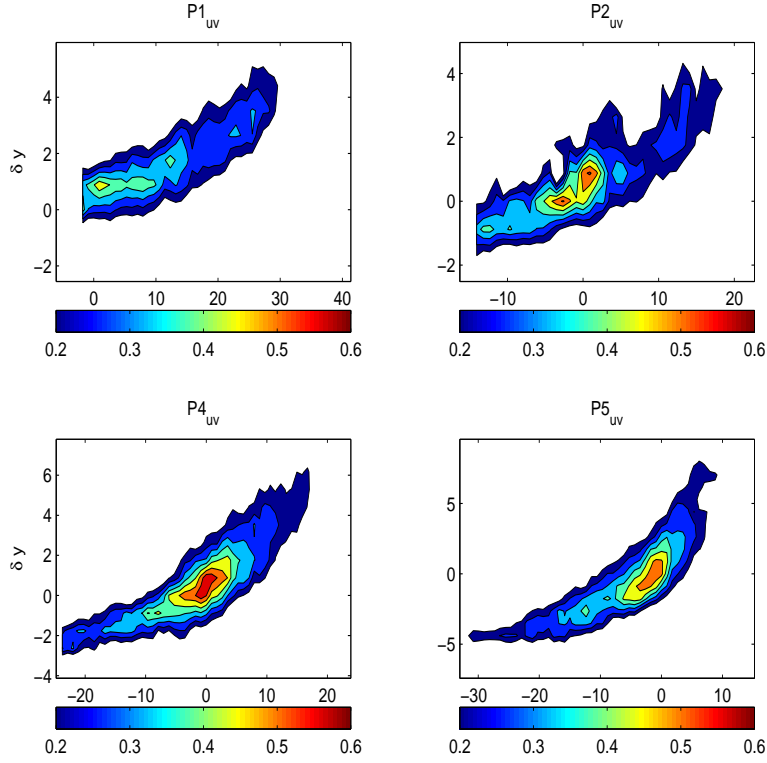
Figure 5.17: R_{uv} at P1, P2, P4, and P5.

2.5 cm, with the surface-normal length scale (l_n) being about a quarter of this value. For the vertical correlation, near the foot of the breaker, $l_s \sim 2.0$, Therefore, near the foot of the breaker, $\frac{l_s}{H_b} \sim 1$, whereas further downstream, the ratio for both streamwise and normal length scales gets smaller, with $\frac{l}{H_b} \sim 0.1 - 0.3$. The non-dimensional length scales are in the range of values reported by Longo (2003) and Cox and Anderson (2001). Instead of the breaker height, if the upstream water depth is chosen as a relevant scale for non-dimensionalizing the integral turbulent scales, near the foot of the breaker, $\frac{l_s}{h_0} \sim 0.26$. This is in agreement with Stansby and Feng (2005), who found that the length scales of structures near the surface varied from greater than, to a fraction of the water depth. For laboratory generated spilling breaking waves, throughout the transition region from the breaking point
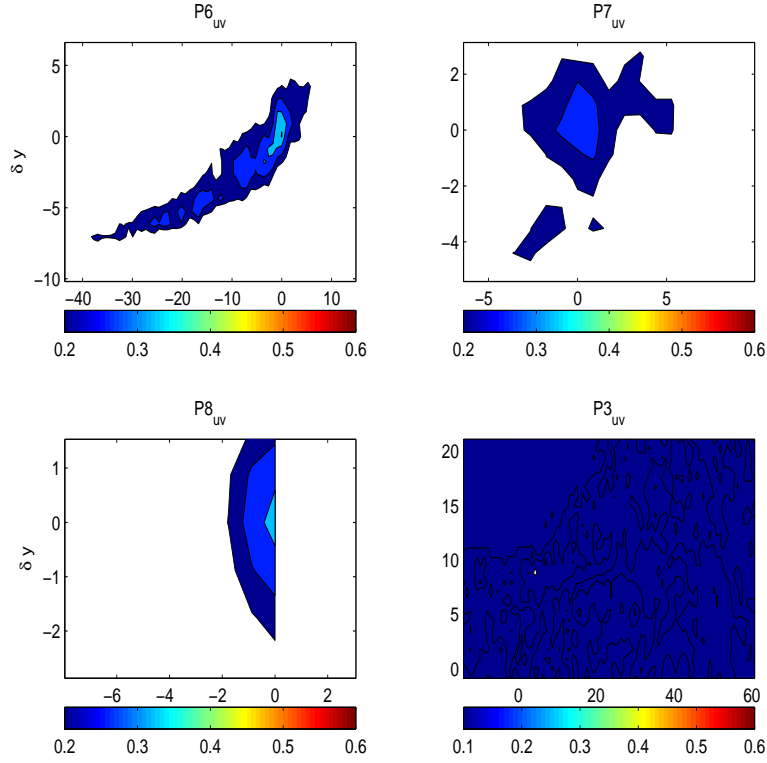
Figure 5.18: R_{uv} at P6, P7, P8, and P3.

to the inner surf-zone, Govender *et al.* (2002b) had also found integral length scales on the order of $\frac{l}{h_0} \sim 0.1 - 0.3$.

5.4   Conclusions

The instantaneous and fluctuating velocity and vorticity fields have been investigated using kinematics based and statistical techniques to analyze coherent motions in the breaker shear layer. In an ensemble-averaged sense, there is an equipartition between the shear deformation and the rotation strain contributions to the vorticity in the breaker shear layer. The effect of streamline curvature is found to be small and reinforces the negative vorticity due to the shear strain. A critical
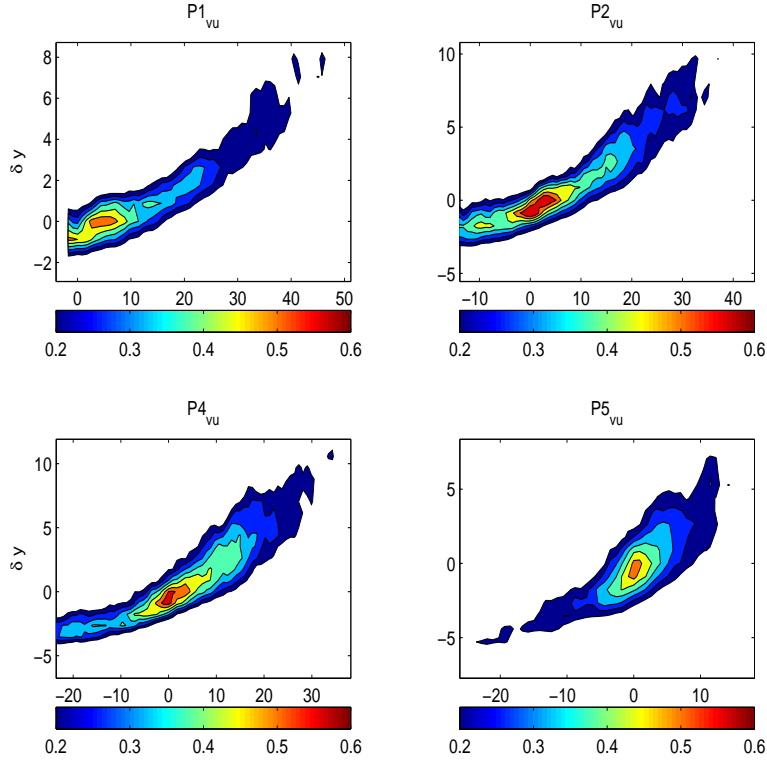
Figure 5.19: R_{vu} at P1, P2, P4, and P5.

point analysis of the velocity gradient tensor is used to localize the coherent vorti-
cal motions. Near the foot of the breaker, the eddies are arranged in a streamwise
elongated "vortex packet" just below the instantaneous surface, contributing nearly
half of the instantaneous vorticity in this region. Further downstream, the eddies
are randomly distributed in space and time. The ensemble-averaged localization of
the structures are coincident with the maximum shear strain rate. The fluctuating
vorticity is positive near the toe of the breaker for most of the ensemble, indicating
the generation of coherent anti-clockwise vortices. The mean fluctuating vorticity
reaches its peak near the foot of the breaker, with the coherence decreasing in the
downstream direction. The two-point spatial correlations also confirm the presence
of elliptical streamwise elongated structures near the foot of the breaker, with their
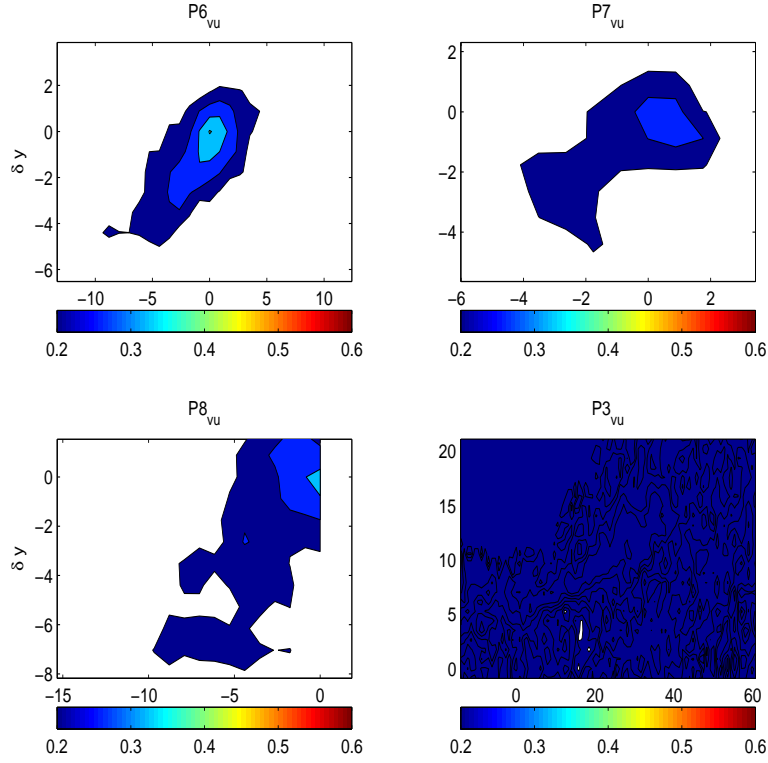
Figure 5.20: R_{vu} at P6, P7, P8, and P3.

major axes oriented along the mean strain rate. The reduction in efficiency of the more compact and normally oriented structures further downstream is reflected in the decreasing Reynolds shear stress. The calculated average length scales are found to be in reasonable agreement with previously reported values for laboratory generated breakers. Near the foot of the breaker, $\frac{l_s}{H_b} \sim 1$ whereas, with increasing downstream distance, the normal and streamwise length scales reduce to 10 to 30 % of H_b. There are indications of coherence in the intermittent region resulting from the breaking process. Intuitively, the inflection point in the velocity profile near the surface would probably generate counter-rotating vortices, with positive vorticity near the surface which would be modified by the local curvature of the instantaneous surface. A higher spatial and temporal resolution of both the free

surface and the velocity field would be necessary in investigating the detailed structure of the coherent motions near the instantaneous surface as well as in the shear layer downstream of the toe. A more robust characterization of the integral scales and the relative contribution of the underlying modes can be achieved by applying other techniques such as POD to the dataset. In light of recent presumed analogies between near-wall and interfacial turbulence (Fulgosi *et al.*, 2003), it is essential to implement stochastic sampling techniques (such as quadrant analysis) to investigate possible "sweep" and "ejection" processes in the shear layer below the surface.

Chapter 6

CONCLUSIONS

If you follow reason far enough, it always leads to conclusions that are contrary to reason

Samuel Butler

The goal of the research presented in this dissertation was to provide a detailed description of the turbulence structure and its effects on the mean flow of fully-formed, quasi-steady spilling breakers. This was achieved through a combination of two complementary approaches: an experimental investigation of a laboratory generated quasi-steady breaker, and a theoretical model for the evolution of turbulent dynamics in a spilling breaking wave. PIV measurements were used to provide a detailed picture of the mean and turbulent structure of an air-entraining hydraulic jump set up in Froude similitude with surf-zone breakers. The theoretical model focussed on a meticulous and accurate mathematical incorporation of the effects of the two-phase surface layer, unsteadiness, curvature, rotation, and non-hydrostatic pressure into evolution equations for the mean flow and turbulent kinetic energy in the turbulent layer. Since each chapter of the dissertation has provided its own comprehensive summary and conclusions, only the key points of each are presented here.

Two unique algorithms were developed to estimate the instantaneous air-water interface and velocities from the raw PIV images. Their generality, accuracy,

and robustness makes them ideal candidates for applications in other PIV experimental studies of interfacial flows. Conditional averaging techniques were implemented to calculate the mean and turbulent quantities. The turbulent interface fluctuations were seen to fit theoretical profiles of the intermittency function well. The traditional concept of a roller in the form of a recirculating region is seen to be only a partial description of the mean flow near the interface, since along with a weak downslope flow above the mean surface, there is mass exchange with the underlying flow across the lower boundary of the roller. Consequently, the lower boundary cannot be a dividing mean streamline. All evidence suggests that continued breaking in a fully-formed spilling breaker is driven by the combined effects of an adverse surface-parallel pressure gradient and streamwise flow deceleration occuring upstream of the foot of the breaker. Both effects force the shear layer to thicken rapidly, inducing a sharp free surface curvature at the foot.

The turbulence structure of the breaker shear layer is seen to resemble that of a mixing layer originating at the foot of the breaker followed by a wake further downstream. The average growth rate is in good agreement with observed values in typical mixing layers. The marked anisotropy in the Reynolds shear stress structure in the mixing layer is influenced by the effects of streamline curvature and not just by the simple shear strain rate. Several analytical and statistical techniques were implemented to investigate the coherent structures in the shear layer. Near the foot of the breaker, the eddies are arranged in elongated streamwise structures skewed toward the mean surface. As they are oriented along the mean strain rate, they are the most efficient in extracting energy from the mean flow through the action of the Reynolds shear stresses. Further downstream, the structures become more compact and are oriented normal to the surface. The streamwise integral length scales estimated near the foot of the breaker are approximately equal to the height of the breaker, and both the normal and streamwise scales decrease downstream.

Governing equations for the mean flow and turbulence structure in the shear layer are developed through suitable Reynolds averaging techniques. By introducing kinematic and geometric scaling assumptions suggested by the measurements, the relative importance of distinct physical mechanisms is analyzed in different regimes of the turbulent layer, namely the leading edge of the breaker, the mixing layer, and the wake. By fitting a similarity profile to the measured mean horizontal velocities in the form of a cubic polynomial, the vertical variations of the mean and turbulent quantities are obtained. The normal integration of the leading order governing equations across the layer is used to obtain analytic expressions for the motion of the layer and the streamwise dependence of the relative strengths of turbulence production and dissipation. Near the leading edge of the breaker, production dominates over dissipation, whereas further downstream, the reverse is true. The turbulent kinetic energy is seen to be vertically uniform in the wake, and at the base of the layer there is no diffusive penetration of turbulence.

A layer-averaged system of equations is developed by integrating the higher-order model in the cross-stream direction. The mean and turbulent surface-layer contributions are taken into account through boundary conditions at the top of the layer and are found to play an integral role in determining the dynamics of the single-phase shear layer. The mean shear at the top of the layer significantly affects the mean and turbulent flow in the layer. The layer-averaged equations are coupled to the underlying flow through mass entrainment and excess pressure at the interface, and they serve as boundary conditions for the flow below. Based on the experimental data, a physical model for the streamwise variation of the mean velocity is developed, which is not only consistent with the theoretical results, but also provides for an accurate modeling of the measurements of the mean and turbulent flow structure in the quasi-steady breaker.

In conclusion, this dissertation has provided several new and interesting insights into the turbulent dynamics of quasi-steady spilling breakers through a combined theoretical and experimental study which will lead to a more complete understanding of the complicated phenomena in breaking waves.

Chapter 7

ONGOING AND FUTURE WORK

Prediction is very difficult, especially about the future

Niels Bohr

In this chapter, ongoing and future research on several aspects of both the experimental and theoretical results obtained in this dissertation are discussed. The theoretical model is being used to analyze the dynamics at the leading edge of the breaker analytically. The role played by extra strain rates and coherent structures in a more complete description of the turbulence structure is emphasized, and the limitations imposed by the resolution of the current measurements is underlined. An outline for the implementation of the theoretical model results into practical numerical models of breaking waves is provided. Conceptual, and at times, notional proposals are described to simulate further experimental work in the study of both steady breakers and unsteady breaking waves.

7.1   The layer-averaged model - a hyperbolic system?

The layer-averaged system of equations (equation (4.224)) describing the evolution of b, $\overline{U}$ and $\overline{k}$ in Chapter 4 were developed by assuming the turbulent shear layer to be thin, or shallow, with the width of the layer being much smaller than the streamwise length scale, i.e., $b << L$. Therefore, in the normal momentum equations, the effects of gravity and mean vertical accelerations were seen to be felt by

the pressure at $O(\epsilon)$ and $O(\epsilon^2)$ respectively. The layer-averaged equations are in a sense equivalent to the shallow water equations along with the effects of turbulence. The equations are quasi-linear first order partial differential equations, since they are linear in the first derivatives of the dependent variables, but their coefficients are functions of the dependent variables. These partial differential equations can be reduced to ordinary differential equations along the characteristics of the system. Three independent equations in characteristic form are needed for the system to be hyperbolic. The Riemann invariants can be determined by calculating the eigenvalues of the matrix

$$\begin{bmatrix} C_B & C_U & C_K \\ M_B & M_U & M_K \\ K_B & K_U & K_K \end{bmatrix},$$

or analytically, by casting the system into characteristic form (Whitham, 1974). Due to the complicated nature of the coefficients, it is rather difficult to use the first method directly in the present case. Therefore, the second approach is followed after simplifying the equations based on the measurements. If a "thin-layer phase-speed" is defined as $C^2 \equiv bg$, and a turbulent velocity ,$q^2 \equiv \overline{k}$, so that $b_s = \frac{2CC_s}{g}$, $b_t = \frac{2CC_t}{g}$, $\overline{k}_s = 2qq_s$, and $\overline{k}_t = 2qq_t$, the system of equations can be written as

$$2C_t + 2C_B C_s + \frac{C_U g}{C}\overline{U}_s + \frac{2C_k g}{C}qq_s = \frac{C_R g}{C}, \tag{7.1}$$

$$\overline{U}_t + \frac{M_B 2CC_s}{g} + M_U \overline{U}_s + M_K 2qq_s = M_R, \quad \text{and} \tag{7.2}$$

$$2q_t + \frac{K_B 2CC_s}{qg} + \frac{K_U \overline{U}_s}{q} + K_K 2q_s = \frac{K_R}{q}. \tag{7.3}$$

The coefficients need to be simplified to facilitate an easier interpretation of the nature of the system of equations. For example, based on the measurements, terms of $O(\kappa b)$ and higher can be neglected in a leading order analysis. The streamwise variation of (κb) is shown in Figure 7.1. The highest values result from the high negative curvature at the end of the breaker region, combined with large values for b.
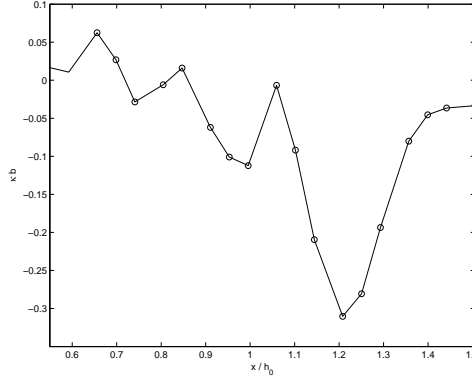
Figure 7.1: Streamwise variation of (κb).

However, the far downstream region is not of immediate interest. The characteristics are desired near the leading edge of the breaker, and in this part of the flow, $(\kappa b) <<$ 1. Therefore, C_B can be written as

$$C_B = \overline{U} - \frac{A_k}{g} C_{1k} K_B + O(\kappa b) \quad \text{and higher.} \tag{7.4}$$

Note that, if there was no coupling with the turbulent kinetic energy equation, $C_B = \overline{U}$, which is the coefficient found in a typical shallow water system. In the turbulent kinetic energy equation,

$$
\begin{aligned}
D_k &= b + \frac{A_k C_{1k} \overline{k}}{g}(A_k - 1) \\
&\approx b\left[1 + \frac{(h-b)}{2b}(A_k - 1)\frac{2C_{1k}}{C_{2k}}\right] \\
&\approx b,
\end{aligned}
\tag{7.5}
$$

since the surface-layer thickness $(h-b)$ is much smaller than b (except near the toe), $\frac{2C_{1k}}{C_{2k}} \sim 1$, and $(A_k - 1) \sim 1$. Similarly, the magnitude of other coefficients are being evaluated from the present data. The form of the characteristics are suggested from the time derivatives in the equations, and the three equations can be collapsed in the form

$$\frac{\partial R_+}{\partial t} + (\overline{U} + C + q)\frac{\partial R_+}{\partial s} = \text{Forcing terms}, \tag{7.6}$$

212
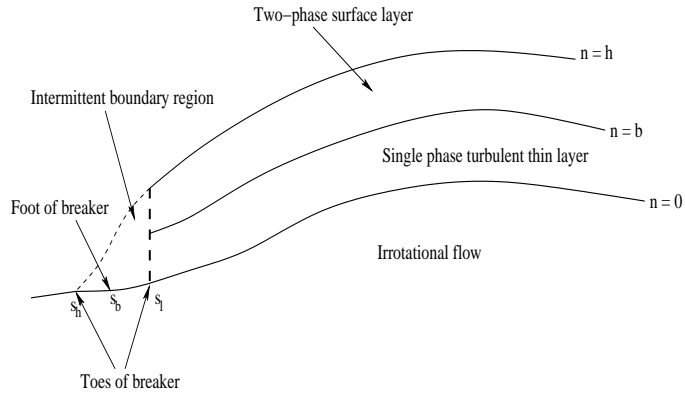
Figure 7.2: Schematic view of the geometry used near the foot of the breaker.

where the Riemann invariant is given by $R_+ = \overline{U} + 2C + 2q$. Such an analysis is in progress.

7.2 The dynamics at the leading edge of the breaker

Utilizing the analogy with the swash zone, in which the turbulence and the mean flow in the breaker can be thought of as the short-wave and long-wave contributions to the motion of the shoreline (Brocchini and Peregrine, 1996; Brocchini and Bellotti, 2002), the layer-integrated equations are to be integrated in the streamwise direction to provide a description of the dynamics of the foot of the breaker. A theoretical framework within the two-phase surface layer boundary conditions has already been provided by Brocchini and Peregrine (1999). A similar procedure is being followed for the layer-integrated equations derived in Chapter 4.

A schematic figure of the adopted geometry is shown in Figure 7.2. The whole region at the breaker front which the turbulence only meets intermittently is taken as a 'boundary region', such that there is non-zero depth at the front edge of the thin layer. The lower and upper limits of the toe excursion are represented as mathematical boundaries denoted by s_l and s_h respectively. As per the terminology proposed in Part 1, the mean position of the base of the breaker, called the 'foot'

213

of the breaker, is therefore located at s_b, in between s_l and s_h. Note that averaging over the turbulence is inadequate in this region where the turbulent water reaches rarely, and there is little dynamical significance in such a thin intermittent layer of turbulent water. Therefore, the toe positions are assumed to be obtained after an averaging over the turbulent time scale, and their motion is described at the intermediate time scale (see Chapter 4).

7.3 Turbulent free-surface boundary conditions

The layer-integrated equations derived in Chapter 4 describe the evolution of the dynamics of the free surface turbulence due to breaking. They can be used as surface boundary conditions for numerical modeling of spilling breakers, since they are valid at the boundary between the turbulent thin layer and the flow below. They can be implemented into RANS models, which are discussed further, as well as irrotational flow solvers for the flow below (Grilli and Subramanya, 1996). There are three essential requirements to model free surfaces: the shape and location of the surface, the evolution of the surface in time, and free-surface boundary conditions. For a given initial spatial location of the surface, it is the boundary conditions that determine the first two requirements. Various methods are available for predicting the surface, and they can be broadly classified into interface tracking and volume tracking methods. An extensive review is provided in Scardovelli and Zaleski (1999). One of the several volume tracking methods, the volume of fluid (VOF) method, is discussed below. The method was introduced by Hirt and Nichols (1981) for Eulerian grids, and can handle complex physical situations such as breaking surfaces, splash-ups, and fluid detachment. The main idea of the VOF method is to introduce a function F whose value is one at any point occupied by fluid and zero otherwise. The average value of F in a cell represents the fractional volume of the cell occupied by the fluid. Therefore, $0 < F < 1$ represents a cell containing the free surface. The

evolution of the $F-$function is governed by an advection equation,

$$\frac{\partial F}{\partial t} + \nabla \cdot (\mathbf{V}F) = 0. \tag{7.7}$$

Integral formulations of this equation,

$$\frac{\partial \int_{\mathfrak{D}} Fd\mathfrak{D}}{\partial t} + \int_S F\mathbf{V} \cdot \mathbf{n}dS = 0, \tag{7.8}$$

have also been used (Muzaferija and Perić, 1999). The problem associated with the $F-$function is that a free surface is represented by a discontinuity in the volume fraction leading to unphysical oscillations and numerical diffusion in the case of high and low resolution schemes respectively (Chen *et al.*, 1997). In addition, in the second step of the VOF algorithm, the evolution is governed by a simple advection by the mean flow. When the free surface is turbulent, and the turbulent fluctuation velocities are on the order of the mean velocity, it becomes important to account for the effect of the turbulence into the advection velocity. The second step is inherently linked to the imposition of boundary conditions on the free surface. For numerical simulations of breaking waves, RANS models using VOF agorithms have typically imposed the vanishing normal gradient of the turbulent kinetic energy and dissipation on the surface, i.e., $\frac{\partial k}{\partial n} = 0$, and $\frac{\partial \varepsilon}{\partial n} = 0$ (Lin and Liu, 1998; Zhao *et al.*, 2004a). As already seen in Chapter 4, the former is only an $O(1)$ boundary condition true in the wake region. This is possibly one of the reasons that, near the breaking point, the numerical model of Lin and Liu (1998) "significantly overestimates the turbulence intensity, which results in excessive energy dissipation". The experimental and theoretical profiles for the intermittency factor, along with the turbulent thin layer equations that include the effect of the two-phase surface layer, can be used to improve both the spatial specification of the $F-$function and its temporal evolution. Quite simply, the layer-averaged horizontal velocity ($\overline{U}$), which includes the surface-layer and turbulent dynamics, can be used as an advection velocity for the $F-$function.

To facilitate a more accurate modeling of the two-phase surface turbulence, heterogenous domain decomposition techniques have been used to separately model the viscous breaker region and the irrotational flow underneath (Rhee and Stern, 2002; Iafrati and Campana, 2005). A critical component of the coupling is the mean pressure at the interface, which is used in the dynamic boundary condition (the Bernoulli equation) to solve for the potential flow (Iafrati *et al.*, 2001; Iafrati and Campana, 2003). In the theoretical model developed in Chapter 4, the coupling between the dynamics of the turbulent shear layer and the irrotational flow is provided through mass entrainment and excess pressure at the interface. The additional pressure is found to be linked with the layer-averaged turbulent kinetic energy as shown in equation (7.9).

$$P_0 = \overline{k}\rho(C_p + 2C_3 A_k), \tag{7.9}$$

where P_0 is the pressure at the irrotational flow interface, C_p and C_3 are coefficients in the model, and A_k represents the contribution of the surface layer turbulence. Several aspects of the theoretical model, including the dynamic interfacial boundary condition, are being incorporated into a two-dimensional Reynolds-averaged Navier-Stokes model (Shi *et al.*, 2004) in order to accurately model the turbulent dynamics of spilling breaking waves (Misra *et al.*, 2006).

7.4 Extra strain rates

Nearly all complex turbulent flows have simple shear layers perturbed by other shear layers, body forces, or extra rates of strain (e) in the plane of the mean shear. The extra rates of strain can be typically classified as those arising from longitudinal acceleration ($\frac{-\partial U}{\partial \xi}, \frac{\partial V}{\partial \zeta}$), bulk compression or dilation ($\nabla \cdot \mathbf{v}$), rotation of the flow system (Ω), and streamline curvature ($\frac{\partial V}{\partial \xi}$) (Bradshaw, 1973). $\mathbf{v}$ is the mean velocity in the (ξ, ζ) coordinate system and ∇ is the two-dimensional gradient operator. Bradshaw (1973) shows that in fairly thin shear layers, where the

216

simple mean shear is an order of magnitude larger than the extra strain rate ($\frac{\partial U}{\partial \zeta} > 10e$), streamline curvature caused by surface curvature or helical streamlines is the most common and probably the most important in determining the magnitude and distribution of the turbulence structure. Even though, from a theoretical point of view, extra strain rates seem negligible compared to the effect of the simple shear (see equations (4.92) and (4.88)), experiments (Castro and Bradshaw, 1976; Holloway and Tavoularis, 1992; Chebbi *et al.*, 1998) and modeling investigations (Holloway and Tavoularis, 1998) on sheared turbulence have underlined the importance of streamline curvature on the integral scales, anisotropy, and spectra of turbulence. From the simplest local equilibrium formula using an eddy viscosity (such as the one used here; see equation (4.87)) to the most advanced transport models, it becomes imperative to consider and account for extra strain rates in the modeling of the turbulence structure (Gibson and Rodi, 1981; Rumsey *et al.*, 1999).

The existence of curved shear layers originating from the toe of a breaking wave is well established. The ensemble-averaged Reynolds shear stress, the simple shear ($\frac{\partial U}{\partial y}$), and the streamline curvature strain rate ($\frac{\partial V}{\partial x}$) are shown for the present measurements in Figure 7.3. Since the Reynolds stresses are generated by an interaction of existing turbulence with mean strain rates (the simple shear being dominant in the present case), it is puzzling that the streamwise localization of the peak in the shear stress is displaced further downstream compared to the peak value in the simple shear. The anisotropy seen in the Reynolds shear stress seems to be influenced not just by the simple shear, but also by the strain due to streamline curvature. The reason for the reversal in sign of the Reynolds shear stress in the far upstream region is not clear. A comparison of the average magnitudes of the two strain rates shows that $\left| \frac{\partial U}{\partial y} \right| \sim 200 \left| \frac{\partial V}{\partial x} \right|$. Therefore, in the classification suggested by Bradshaw (1973), the extra strain rate is "small" and the shear layer can be termed as "fairly thin". It is also in fairly thin shear layers that the Reynolds stress

217
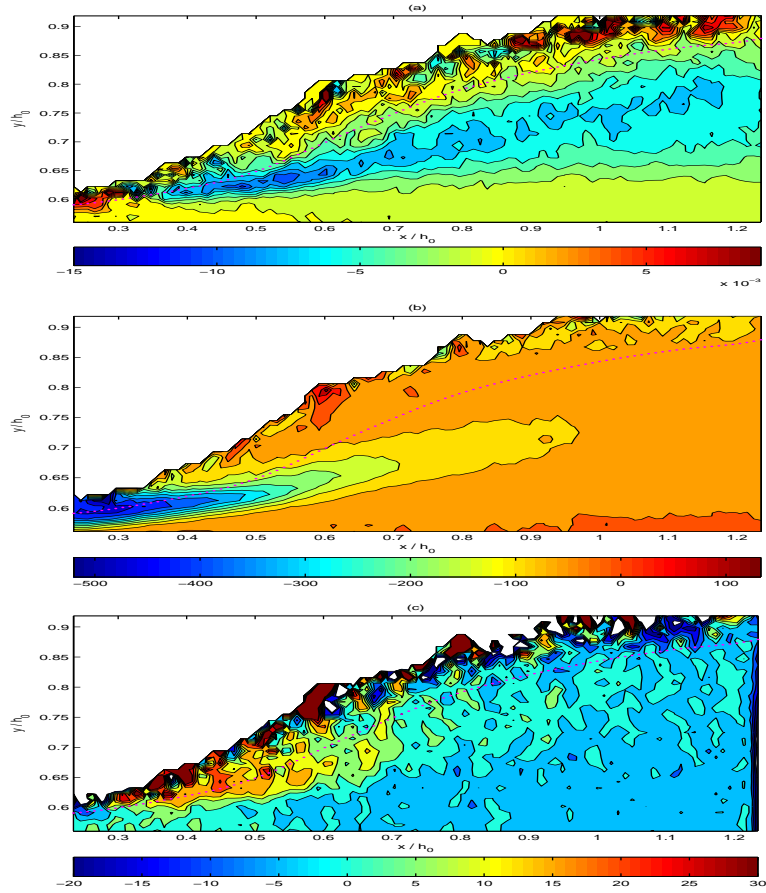
Figure 7.3: (a) Ensemble-averaged Reynolds shear stress strain rate (m²/s²), and (b) $\frac{\partial U}{\partial y}$ (1/s), (c) $\frac{\partial V}{\partial x}$ (1/s).

gradients significantly affect the mean motion as suggested by Bradshaw (1973) based on limiting arguments and subsequently observed in experiments (Plesniak and Johnston, 1991). This is because extra strain rates have a direct effect (they cause changes in the higher-order structural parameters, which in turn cause the Reynolds stresses to change) on terms of the Reynolds stress transport equation which do not explicitly contain the mean rate of strain.

The dimensionless factor, $S = \frac{\kappa U}{\left(\frac{\partial U}{\partial n}\right)}$, is considered to be a measure of the orientation and strength of curvature relative to the mean shear (Bradshaw, 1973;

Holloway and Tavoularis, 1998). The sign and magnitude of this parameter have been well correlated with dramatic, and at times unexpected, effects of the strain rate on the turbulence structure, particularly on the Reynolds shear stress anisotropy (Hunt and Joubert, 1979). In general, for curved mixing layers, it has been observed that a convex (concave) curvature has a de-stabilizing (stabilizing) effect on the turbulence (Wyngaard *et al.*, 1968). Here, the notion of instability (stability) only indicates an increased (decreased) turbulence production compared to what would have been present in the absence of curvature. Note that these conclusions are drawn from uniform shear flows. In the present case, as would be true for any other breaker, the shear is strongly inhomogenous in the streamwise direction and is related to the curvature of the flow. In addition, the sign of the curvature changes in the streamwise direction. Isolating the effect of streamline curvature in this particular flow is not trivial because of the presence of an adverse pressure gradient, entrainment effects, and streamwise vortices in the shear layer, all of which are known to influence the response of the turbulent stresses to the mean strain rates (Holloway *et al.*, 2005). However, the interaction between the pressure gradient and streamline curvature effects are known to be weak even when they are comparable in magnitude to the mean strain due to shear. This is due to the fact that the effects of pressure gradient are typically limited to the production of normal stresses, while curvature has a stronger effect on the shear stresses (Baskaran *et al.*, 1991). A detailed look at the effects of extra strain rates on breaking wave turbulence seems to be warranted. This is relevant from a modeling perspective as well and is discussed below.

The discrepancy between results from Reynolds averaged Navier-Stokes (RANS) models, with the standard $k - \epsilon$ turbulence model, and data, for steady breakers such as hydraulic jumps, has often been ascribed to neglecting streamline curvature effects (Long *et al.*, 1991; Ma *et al.*, 2001). In general, two equation models of

the eddy viscosity type cannot properly account for extra strain rates and neglect non-local and historical effects of the Reynolds stress anisotropies (Speziale, 1991). In Lin and Liu (1998), even a higher order, more complicated, non-linear algebraic closure model developed by Shih *et al.* (1996) was not able to accurately predict wave breaking turbulence near the breaking region in the surf-zone. They point out the failure of the model in the "rapidly distorted shear flow region" at the initial stage of breaking, specifically, where the effects of curvature are dominant. However, for small rates of strain ($e < 0.05$), as in the present case, linear corrections can be made to the eddy viscosity or length-scale formulations of the turbulence model to parametrically account for curvature effects. The following analysis closely follows Bradshaw (1973). From the turbulent kinetic energy equation (equation 4.79), the production terms due to the Reynolds shear stress are given by

$$\text{Prod} = -\langle uv \rangle \frac{\partial U}{\partial n} \left[1 + \underbrace{2\kappa n + \frac{\kappa U}{\left(\frac{\partial U}{\partial n}\right)} + \frac{\frac{\partial V}{\partial s}}{\left(\frac{\partial U}{\partial n}\right)}}_{O(\epsilon)} + \underbrace{\kappa^2 n^2 - \frac{\kappa^2 n U}{\left(\frac{\partial U}{\partial n}\right)}}_{O(\epsilon^2)} + \underbrace{\kappa n \frac{\frac{\partial V}{\partial s}}{\left(\frac{\partial U}{\partial n}\right)}}_{O(\epsilon^3)} \right], \quad (7.10)$$

which, with the assumptions of gentle curvature and the thin-layer approximation, can be written as

$$\text{Prod} \approx -\langle uv \rangle \frac{\partial U}{\partial n} \left[1 + a_1 \frac{e_1}{\left(\frac{\partial U}{\partial n}\right)} + a_2 \frac{e_2}{\left(\frac{\partial U}{\partial n}\right)} \right]. \quad (7.11)$$

a_1 and a_2 are coefficients signifying the $O(\epsilon)$ and $O(\epsilon^2)$ contributions of the extra strain rates due to geometric curvature ($e_1 = \kappa U$) and streamline curvature ($e_2 = \frac{\partial V}{\partial s}$) respectively. The dissipation rate can be represented as the cube of a turbulent velocity scale such as $-\langle uv \rangle^{3/2}$ divided by a turbulence length scale L, $\varepsilon \approx \frac{-\langle uv \rangle^{3/2}}{L}$. For the moment, assuming local equilibrium for the turbulent kinetic energy (Production $\approx$ Dissipation),

$$-\langle uv \rangle \frac{\partial U}{\partial n} f \approx \frac{-\langle uv \rangle^{3/2}}{L_0}, \quad (7.12)$$

where $f = \left[1 + a\frac{e}{\left(\frac{\partial U}{\partial n}\right)}\right]$, $ae = (a_1 e_1 + a_2 e_2)$, and L_0 would be the length scale given by a theoretical formulation, which at most contains the factor f. As pointed out before, experimental observations suggest that

$$-\langle uv \rangle \frac{\partial U}{\partial n} F \approx \frac{-\langle uv \rangle^{3/2}}{L}. \tag{7.13}$$

Therefore,

$$\frac{L}{L_0} \approx F = 1 + \alpha \frac{e}{\left(\frac{\partial U}{\partial n}\right)}. \tag{7.14}$$

The coefficient α, which is of $O(10)$, has to be adjusted through empirical agreements between predictions and experimental results. The assumption of local equilibrium can be removed once the length scale has been calculated. See Bradshaw (1973) for a detailed explanation. The length scale in a local equilibrium approximation for the Reynolds stresses (b in the present case) can be treated similarly. For rapidly changing extra strain rates, which would be the likely scenario in unsteady breaking waves, α can no longer be assumed to be a constant, and an ordinary differential equation in space has to be solved to account for the memory of the stress-containing eddies (Bradshaw, 1973). The solution is straightforward for a given distribution of the strain rates, which can be deduced from the measurements. It remains to be seen whether the present theoretical results and the measurements of extra strain rates and length scale variations can successfully guide such a parametrization of the eddy viscosity or the length scale towards more accurate modeling of breakers. An implementation into a Reynolds averaged Navier-Stokes model with a standard $k - \epsilon$ closure is currently in progress (Zhao *et al.*, 2004b).

7.5 Proper orthogonal decomposition

The proper orthogonal decomposition (POD), also known as the Karhunen-Loeve expansion (Kosambi, 1943; Karhunen, 1946; Loeve, 1955), and closely related to principal component analysis, singular value decomposition, and empirical eigenfunction decomposition, is a well-known technique for determining an optimal basis

set for the reconstruction of a signal. It is optimal in the sense of maximizing the energy content of the signal in the basis. It was introduced to fluid mechanics in the context of turbulence by Lumley (1967). Berkooz *et al.* (1993) provide a comprehensive literature survey of its theoretical background and applications in turbulent flows. A brief summary is given below. From a given instantaneous velocity field ($\mathbf{v}$), a candidate structure, ϕ, can be selected so that it is the structure with the largest mean-square projection on the velocity field. This projection maximizes the energy content of the candidate structure:

$$\max_\phi \frac{\langle |\mathbf{v}, \phi|^2 \rangle}{(\phi, \phi)}, \tag{7.15}$$

where (f, g) defines the standard inner product of f and g. Note that, since the degree of projection is of primary interest, the amplitude is removed by normalization. Using the calculus of variations, the maximization leads to the following integral eigenvalue problem:

$$\int_{\mathfrak{D}} \mathbf{R}_{ij}(\mathbf{x}, \mathbf{x}', t, t) \psi_j(\mathbf{x}', t') d\mathbf{x}' dt' = \lambda \psi_i(\mathbf{x}, t), \tag{7.16}$$

where the kernel is the velocity cross-correlation tensor,

$$R_{ij}(\mathbf{x}, \mathbf{x}', t, t') = \langle \mathbf{v}_i(\mathbf{x}, t) \mathbf{v}_j(\mathbf{x}', t') \rangle .$$

$\mathfrak{D}$ is the space-time domain, and $\mathbf{v}_i$ are the instantaneous realizations of the velocity field. The eigenvalue, λ, is representative of the turbulent kinetic energy, and ψ_i are the eigenfunctions or the modes of the velocity field. Since R_{ij} is symmetric and positive definite, the solutions of equation (7.16) can be used to expand each realization as an infinite sum of the eigenfunctions:

$$\mathbf{v}_i(\mathbf{x}, t) = \sum_{n=1}^{\infty} a^{(n)} \psi_i^{(n)}(\mathbf{x}, t), \tag{7.17}$$

and because of the orthogonality of the basis,

$$a^{(n)} = \int_{\mathfrak{D}} \mathbf{v}_i(\mathbf{x}, t) \psi_i^{(n)}(\mathbf{x}, t) d\mathbf{x} dt, \tag{7.18}$$

are the coefficients governing the time evolution of each mode. This is called the direct method for evaluating the POD basis functions and eigenvalues and is computationally demanding for typical vector fields output from PIV datasets. The solution to equation (7.16) involves the inversion of a matrix of size equal to the total number of instantaneous vectors. Therefore, as an alternative, the snapshot method by Sirovich (1987) is typically used. In this case, the dimension of the matrix is equal to the size of the ensemble. A first step is the extraction of the ensemble-average from each realization. This is performed so that the individual realizations are linearly uncorrelated. With N snapshots, the fluctuating components are given as

$$\mathbf{v}'_i = \mathbf{v}_i - \frac{1}{N}\sum_{j=1}^{N}\mathbf{v}_j, \quad i = 1, ..., N. \tag{7.19}$$

From these vectors, the kernel R_{ij}, which is the autocovariance matrix, is formed with elements $R_{ij} = \mathbf{v}'_i \cdot \mathbf{v}'_j$, where the inner dot product is implied between the components. The algebraic eigenvalue solution for this matrix yields an orthonormal basis given by

$$\psi^k = \frac{\sum_{i=1}^{N}\varrho_i^k\mathbf{v}'_i}{\left|\left|\sum_{i=1}^{N}\varrho_i^k\mathbf{v}'_i\right|\right|}, \tag{7.20}$$

where ϱ_i^k is the i-th component of the normalized eigenvector corresponding to the k-th eigenvalue (λ_k), and the double vertical bars denote the L_2 norm. Since the eigenvalues represent the energy contained in the corresponding modes, ordering the eigenvalues in decreasing order as $\lambda_1 > \lambda_2 > .... > \lambda_N - 1 > 0$ yields the modes in the decreasing order of energy content. Once the orthonormal basis is found, the flow field is given by

$$\mathbf{V}' = \varrho\mathbf{A}, \tag{7.21}$$

where $\mathbf{V}$, ϱ, and $\mathbf{A}$ are matrices containing the $\mathbf{v}'_k$, ϱ^k, and a_k matrices respectively. a_k are the coefficients associated with each vector $\mathbf{v}'_k$, and represent the amplitudes

of each mode. Since the POD modes form an orthonormal basis,

$$\mathbf{A} = \varrho\mathbf{V}'. \tag{7.22}$$

The evolution of the amplitudes in time give important information about the time history of each corresponding eigenfunction and, therefore, the associated time scales in different regions of the flow. Finally, once the coefficients are known, each snapshot can be reconstructed as

$$\mathbf{v}_k \approx \sum_{i=1}^{M} \psi^i a_i^k + \frac{1}{N}\sum_{j=1}^{N}\mathbf{v}_j. \tag{7.23}$$

M is the total number of basis functions included in the reconstruction and, to give a satisfactory representation of the flow, increases with the complexity of the flow.

7.5.1   A simple test case

To test the algorithms for both the direct and the snapshot methods, a simple test example was designed. The realizations consisted of surface elevation maps for a two-dimensional (x, y) Gaussian hump decaying linearly with time and superimposed on a two-dimensional standing wave. The standing wave is given by

$$\eta_s(x, y, t) = A_s\cos\left(\frac{N_x\pi x}{L_x}\right)\cos\left(\frac{N_y\pi y}{L_y}\right)\cos\left(\frac{2\pi t}{T}\right). \tag{7.24}$$

A_s is the amplitude, L_x and L_y are the wavelengths in the x and y directions respectively. N_x and N_y are the corresponding mode numbers of the standing wave. T is the time period and t is time. The gaussian is given by

$$\eta_g = \left(\frac{A_g}{\sqrt{2\pi}\sigma}\exp\left[-\frac{(x - x_c)^2 + (y - y_c)^2}{2\sigma^2}\right]\right)t, \tag{7.25}$$

where A_g is the amplitude of the Gaussian, σ is the standard deviation and x_c and y_c denote the location of the peak of the Gaussian. A random noise field chosen from a normal distribution with a mean of zero and standard deviation of one was
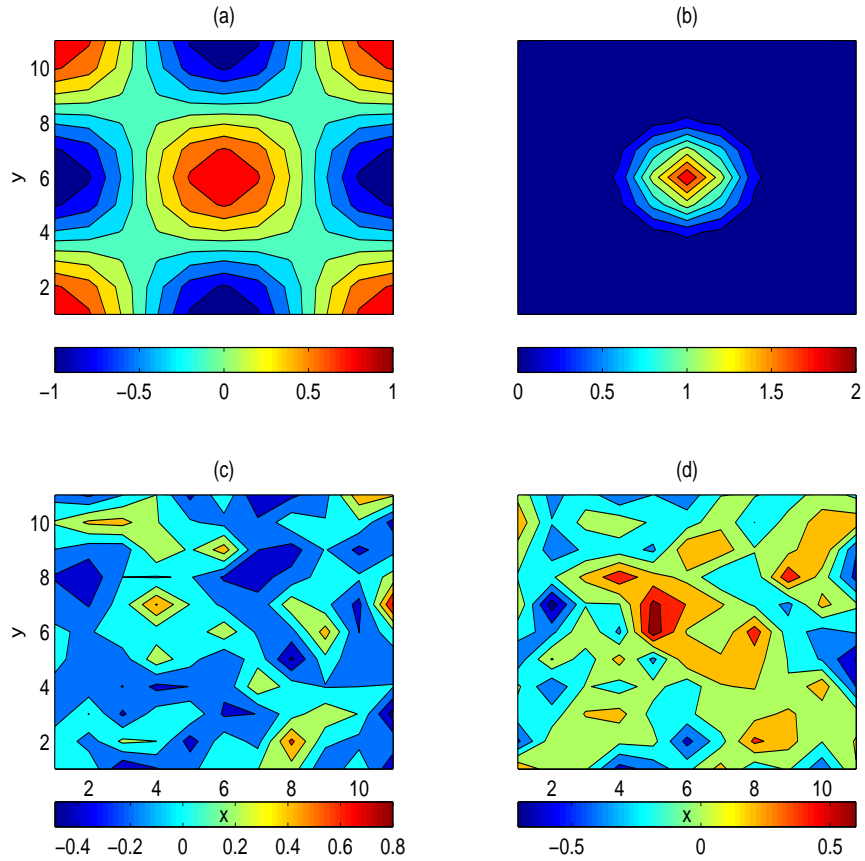
Figure 7.4: (a) Two-dimensional standing wave at $t = 0$, $N_x = N_y = 2$, (b) Gaussian at $t = 0$, (c) random noise field at $t = 0$, and (d) superimposed surface field at $t = \frac{T}{4}$.

added to each instantaneous superposition of the two elevation maps. The final displacement field is given by

$$\eta = \eta_s + \eta_g + \text{Random noise}. \tag{7.26}$$

The parameters for the test case shown here are : $A_s = 1$, $L_x = L_y = 10$, $N_x = N_y = 2$, $T = 1$, $A_g = 2$, and $x_c = y_c = 5$. x and y varied from 0 to 1 at 0.1 increments, i.e., there were a total of 121 spatial sampling points for each instantaneous surface field. The total time was one period, and the ensemble size
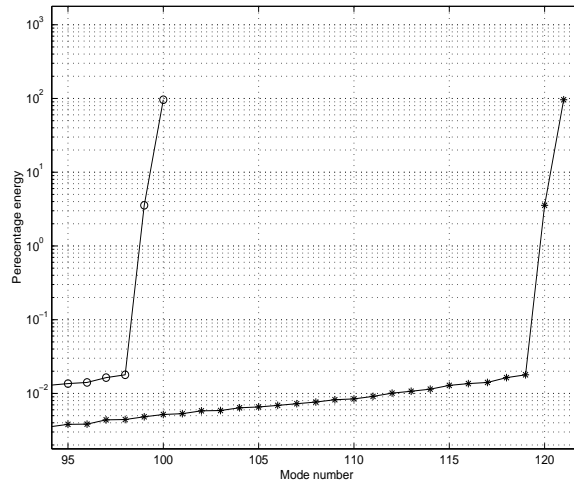
Figure 7.5: Non-dimensionalized squared eigenvalues from direct (*) and snapshot (○) methods.

was 100. The individual surface maps and the superimposed field are shown in Figure 7.4. The squared eigenvalues are non-dimensionalized by the total energy, which is the sum of squares of the eigenvalues. The percentage energy for each mode for both direct and snapshot methods is shown in Figure 7.5. Note that both methods give the same answer. Approximately 96.5 % of the total energy is in the first mode, 3.35 % in the second mode, and the rest is contributed by noise. The normalized mode shapes are shown in Figure 7.6 and Figure 7.7, and are nearly identical for both methods. The standing wave and Gaussian are recovered as the first and second modes. The time evolution of the normalized coefficients is shown in Figure 7.8. The first coefficient recovers the oscillation of the first mode at a period equal to T. The coefficient of the second mode shows the linear decay of the Gaussian till realization number 75. Beyond that, the surface field due to the decaying Gaussian cannot be distinguished from the background noise.
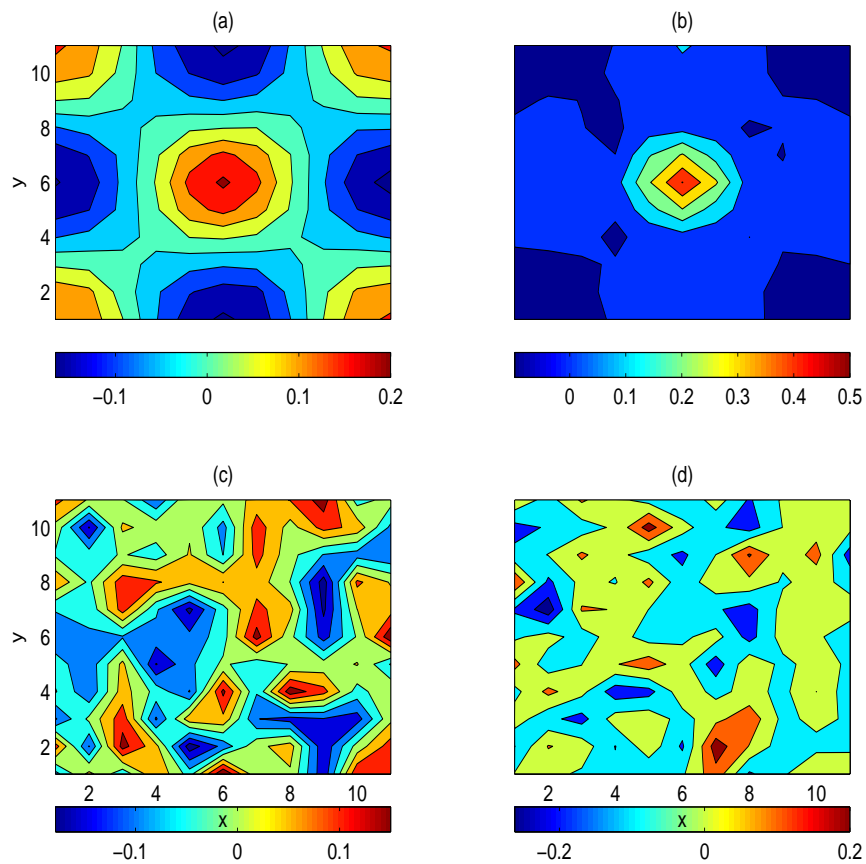
Figure 7.6: POD modes (ψ^i) from direct method. (a) Mode 121, (b) Mode 120, (c) Mode 119, and (d) Mode 118.

7.5.2 Coherent structures

The specific application of the POD technique, such as for construction of low-order dynamical systems for the flow, investigation of turbulent quantities, or identification of coherent structures, determines the choice of variable. As has already been discussed, a Galilean invariant quantity such as the vorticity is a better descriptor than the velocity for the identification of coherent structures in turbulent flow. Recently, Kostas *et al.* (2005) have demonstrated through planar PIV data
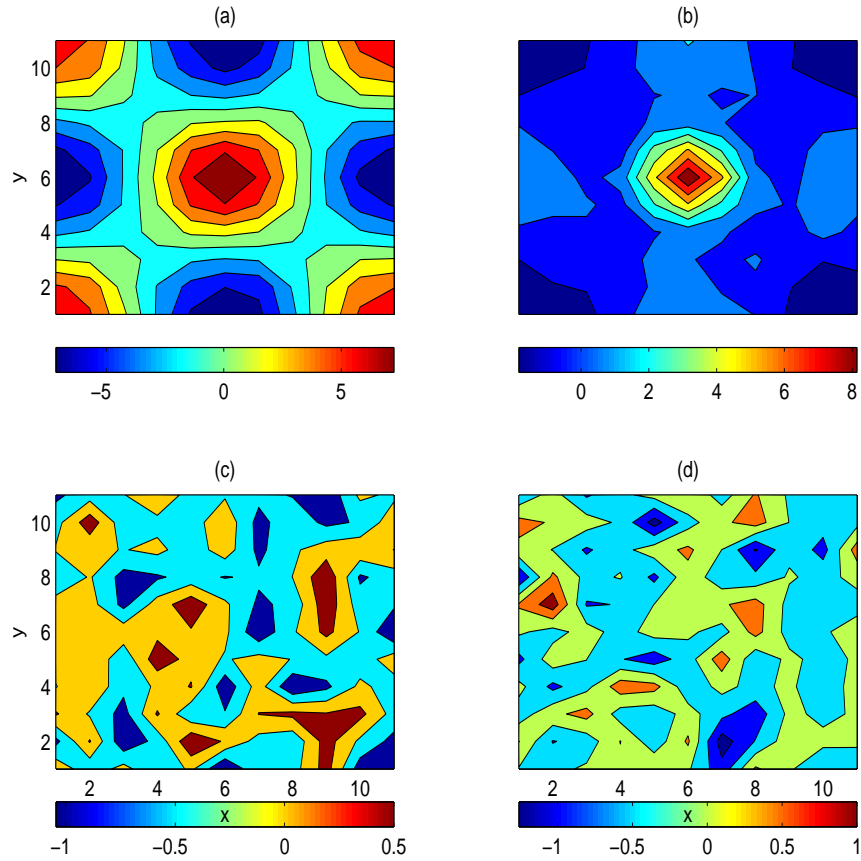
Figure 7.7: POD modes (ψ^i) from snapshot method. (a) Mode 100, (b) Mode 99, (c) Mode 98, and (d) Mode 97.

of a backward-facing step flow that the unambiguous indentification and description of the dominant vortical structures was more effective using a POD analysis of the out-of-plane vorticity field than the two-dimensional velocity field. This was suggested to be particularly true for high Reynolds number flows. Since one of the primary objectives of this study was to investigate the presence of coherent structures, the snapshot method POD is performed on the fluctuating vorticity fields as calculated in Chapter 5. The presence of two inhomogeneous directions (streamwise and crosswise) in the flow means that shot-noise decomposition was not required
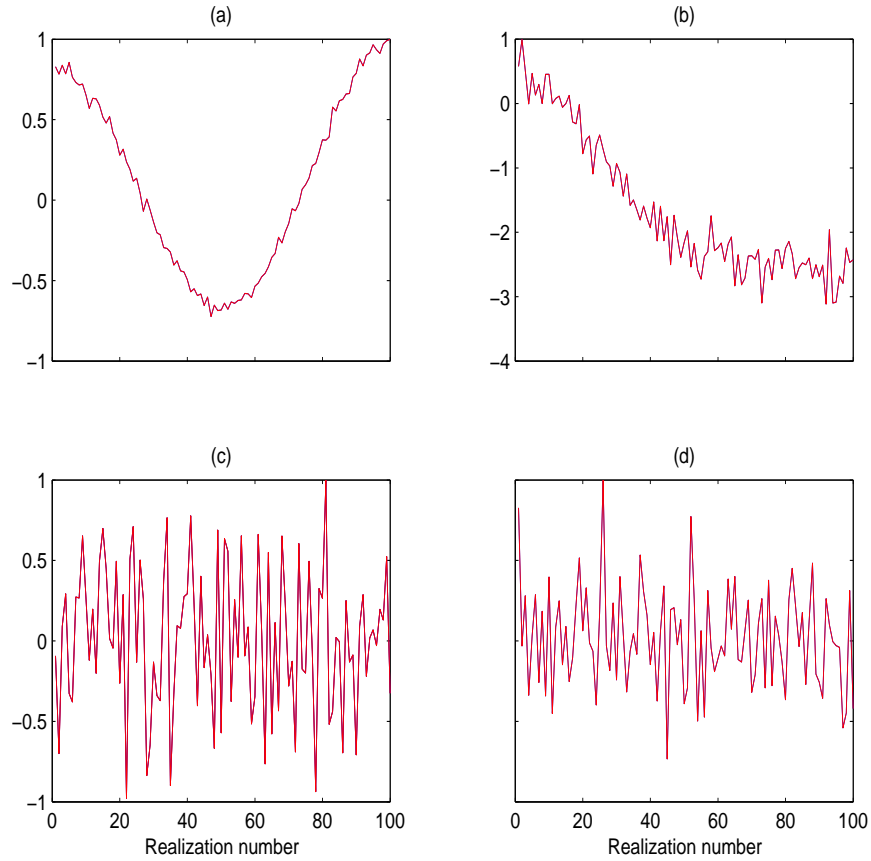
Figure 7.8: Coefficients (a_k) from direct (blue) and snapshot (red) methods. The two are indistinguishable.

(Lumley, 1981).

The non-dimensionalized square of eigenvalues $(\frac{\lambda_k^2}{\Sigma_{k=1}^{1020}\lambda_k^2})$, or percentage energy for each mode, is shown in Figure 7.9. The first four modes are seen to capture approximately 28 %, 7 %, 4.7 %, and 1.7% of the total energy respectively, i.e., the first four modes cummulatively account for approximately 41 % of the total energy. The energy in this case is equivalent to the quasi-enstrophy, since only one component of the enstrophy is estimated. Approximately 110 modes are required to capture 50 % of the energy. The convergence rate depends on several reasons.
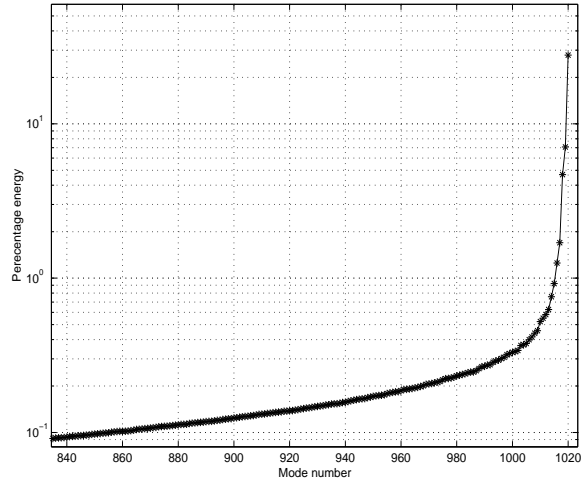
Figure 7.9: Non-dimensionalized squares of eigenvalues showing convergence as a function of number of modes.

First, in a fully turbulent high Reynolds number complex flow such as the present, the turbulence structure is composed of an infinite number of spatial and temporal scales, only a limited number of which can be resolved by the measurement resolution. Note that some of the contribution to the resolvable scales can also arise due to the aliasing from smaller scales. In addition, the number of accurately resolved POD modes and their associated eigenvalues are dependent on the ensemble size. Even though convergence for the turbulence statistics was satisfactory in the single phase region of the flow, the robustness of the estimated fluctuating quantities in the intermittent region is still in doubt. The numerical calculation of vorticity from the velocity components also introduces some noise into the field. There are also bias and random errors introduced into the velocity from the PIV algorithm. However, the results of Breuer and Sirovich (1991) indicate that for random noise levels of the order of 10^{-2} on a sample size of 400, the computed eigenvalues remain accurate for mode numbers at least up to 50, while the eigenfunctions begin to deviate from the true solution for mode numbers less than this.
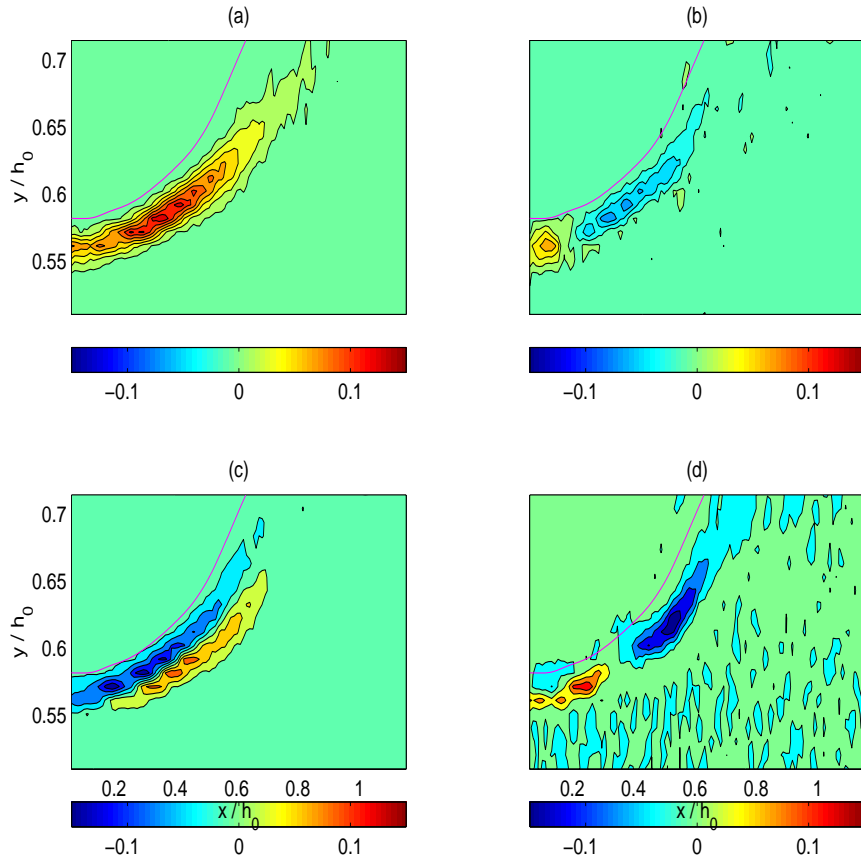
Figure 7.10: The first four eigenfuctions computed from the snapshot method. (a) Mode 1020, (b) Mode 1019, (c) Mode 1018, and (d) Mode 1017.

The four most energetic modes are shown in Figure 7.10, and the associated coefficients are shown in Figure 7.11. The eigenmodes have been normalized with respect to their L_2 norm. In view of the uncertainty in the resolvable scales, only a qualitative discussion is provided. The most energetic mode is dominated by positive vorticity fluctuations, which, as suggested before, arise due to the combined effects of reverse flow due to breaking and curvature. In all of the four modes, the elongated bands of coherent fluctuations are skewed parallel to the surface. Note that the sign has no bearing on the flow feature represented by the mode, since the sign of
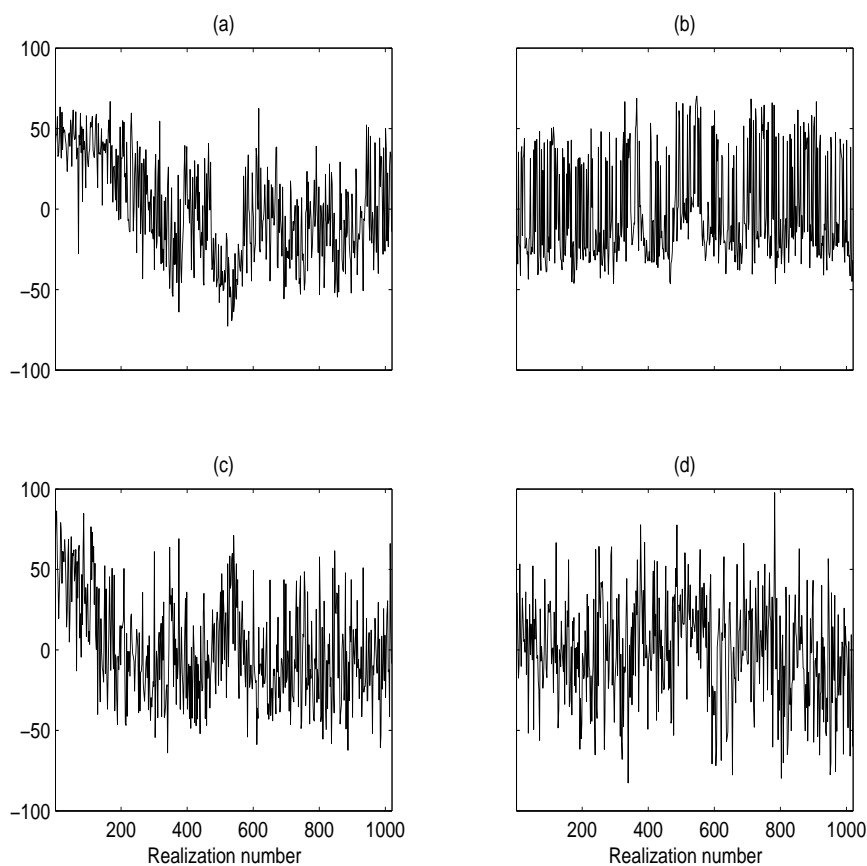
Figure 7.11: Time evolution of the first four coefficients computed from the snap-shot method. (a) Mode 1020, (b) Mode 1019, (c) Mode 1018, and (d) Mode 1017.

the reconstruction coefficient determines the positive/negative vorticity bands. The elongated structures are in close proximity to the lower boundary of the recirculating region which is located below the mean interface (see Chapter 3). Particularly, the 3rd mode is in striking similarity with the fluctuating vorticity bands observed in the case of a backward facing step flow by Kostas *et al.* (2005)(see their Figure 10 a-d). There are obvious qualitative similarities between the two flow configurations: the formation of a curved shear layer from the toe (step), the reattachment near the surface (wall) and the recirculation zone (separation bubble) formed between the two

locations. The similarity between the global mean flow solutions has been discussed theoretically by Soldini *et al.* (2004). An investigation into this analogy, especially with regard to the smaller scales of the flow, would be an interesting experiment in itself. More confident conclusions can only be drawn with larger ensembles of data in the intermittent region and increased spatio-temporal resolution. Lastly, other techniques, including the ones mentioned in Chapter 4 for the extraction of coherent motions and quantification of their spatio-temporal scales need to be implemented.

7.6 Spilling breaker experiments

7.6.1 Temporal evolution

The twenty second oscillation in the flume has precluded a meaningful investigation into the temporal behaviour of the breaker dynamics, including toe oscillations and their possible correlation with coherent structures in the mixing layer. This correlation has qualitatively been studied by Mossa (1998) and Mossa and Tolve (1998), who suggested that a vortex roll-up process was linked to the fluctuations of the longitudinal oscillation of the toe. On the other hand, Dabiri and Gharib (1997) had found that the frequency of the persistent streamwise oscillation of the shear layer below the surface was much smaller than the vortex shedding frequency. The evolution of the coherent structures in time, including their advection, has only been paid a cursory qualitative examination in this dissertation. Further, the dynamical processes such as merging and tearing have not been investigated. It is obvious that a more carefully controlled experiment with a higher spatio-temporal resolution than the present is necessary to investigate these phenomena. The accurate resolution of the air-water interface is vital in correlating the velocity field with the geometric and dynamic properties of the surface. This can be done either by developing more accurate image processing techniques, which is currently being pursued, or a simultaneous LIF experiment to independently locate the interface. With respect to checking the validity of the theoretical model results, an accurate estimate of the

spatial distributions of production and dissipation is essential. Further, it would be interesting to investigate the similarities/differences in the turbulence structure between quasi-steady breakers and unsteady breaking waves.

7.6.2 Spanwise turbulence structure

The measurements from the experiments have been limited to the streamwise-crossstream plane, precluding any investigation into the three-dimensionality of the turbulence. To the best of the author's knowledge, the spanwise structure of turbulence for steady breakers has received no attention in current literature. As an extension of the present study, it is of interest to determine the possible three-dimensional structure of the coherent motions discussed in Chapter 5. Two-dimensional signatures of streamwise vortices in the longitudinal plane of turbulent boundary layers have been shown to be actually due to three-dimensional coherent structures such as hairpin packets (Meinhart and Adrian, 1995; Zhou *et al.*, 1999). It would indeed be interesting to see if the coherent motions detected in the present study have spanwise structures with similar/alternate topologies. With respect to breaking waves, barring Cox and Anderson (2001) and the visualization studies of Nadaoka (1986) on obliquely descending eddies, little attention has been paid to the spanwise structure of coherent motions. Preliminary results from stereoscopic PIV of solitary waves breaking as spilling breakers have shown randomly distributed spiral eddies (Ting, 2004). Detailed investigations such as these are also of relevance with respect to recent numerical simulations of breaking waves, such as those by Christensen (2004) and Rogers and Dalrymple (2005), whose simulations have indicated coherent three-dimensional motions but await experimental observations for validation.

Finally, the author believes that the current state of knowledge about the turbulent flow under breaking waves is still nascent, and there are numerous other aspects beyond the few treated in this dissertation which need attention, both theoretically and experimentally. As Winston Churchill famously said, "*This is not*

the end. It is not even the beginning of the end. But it is, perhaps, the end of the beginning."

BIBLIOGRAPHY

Adrian, R. J. (1991). Particle-imaging techniques for experimental fluid mechanics. *Ann. Rev. Fluid Mech.*, **23**, 261–304.

Adrian, R. J. (1994). Stochastic estimation of conditional structure: A review. *Appl. Sci. Res.*, **53**, 291–303.

Adrian, R. J., Christensen, K. T., and Liu, Z. C. (2000). Analysis and interpretation of instantaneous turbulent velocity fields. *Exp. Fluids*, **29**, 275–290.

Agarwal, A. and Prasad, A. K. (2002). Properties of vortices in the self-similar turbulent jet. *Exp. Fluids*, **33**, 565–577.

Akgul, Y. S. and Kambhamettu, C. (2003). A coarse-to-fine deformable contour optimization framework. *IEEE Trans. Patt. Ana. Mach. Intel.*, **25**(2), 177–86.

Al-Janobi, A. (2001). Performance evaluation of cross-diagonal texture matrix method of texture analysis. *Patt. Recog.*, **34**, 171–80.

Antonia, R. A. (1981). Conditional sampling in turbulent measurement. *Ann. Rev. Fluid Mech.*, **13**, 131–156.

Aris, R. (1962). *Vectors, tensors, and the basic equations of fluid mechanics*. Prentice-Hall, Englewood Cliffs, N.J.

Bakunin, J. (1995). *Experimental Study of Hydraulic Jumps In Low Froude Number Range*. Master's thesis, Dept. of Civil and Env. Engrng, University of Delaware.

Banner, M. L. (1988). Surging characteristics of spilling zones of quasi-steady breaking water waves. In K. Horikawa and H. Maruo, editors, *Nonlinear Water Waves*, IUTAM Symposium, pages 151–158. Natl. Academic.

Banner, M. L. and Peregrine, D. H. (1993). Wave breaking in deep water. *Ann. Rev. Fluid Mech.*, **25**, 373–97.

Banner, M. L. and Phillips, O. M. (1974). On the incipient breaking of small scale waves. *J. Fluid Mech.*, **65**, 647–656.

Barber, D. G. and LeDrew, E. F. (1991). Sar sea ice discrimination using texture statistics: A multivariate approach. *Photo. Engrng. Rem. Sens.*, **57**(4), 383–95.

Barron, J. L., Fleet, D. J., Beauchemin, S. S., and Burkitt, T. A. (1994). Performance of optic flow techniques. *Int. J. Com. Vis.*, **12**, 43–77.

Baskaran, V., Smits, A. J., and Joubert, P. N. (1991). A turbulent flow over a curved hill. Part 2. effects of streamline curvature and streamwise pressure gradient. *J. Fluid Mech.*, **232**, 377–402.

Batchelor, G. K. (1967). *An introduction to fluid dynamics*. Cambridge university press.

Battjes, J. A. (1988). Surf-zone dynamics. *Ann. Rev. Fluid Mech.*, **20**, 257–293.

Battjes, J. A. and Sakai, T. (1981). Velocity field in a steady breaker. *J. Fluid Mech.*, **111**, 421–437.

Bell, G. D. and Keyser, D. (1993). Shear and curvature vorticity and potential-vorticity interchanges : Interpretation and application to a cutoff cyclone event. *Mon. Wea. Rev.*, **121**, 76–102.

Berkooz, G., Holmes, P., and Lumley, J. L. (1993). The proper orthogonal decomposition in the analysis of turbulent flows. *Ann. Rev. Fluid Mech.*, **25**, 539–575.

Black, M. J. (1992). *Robust incremental optic flow*. Ph.D. thesis, Yale University.

Bohr, T., Putkaradze, V., and Watanabe, S. (1997). Averaging theory for the structure of hydraulic jumps and separation in laminar free-surface flows. *Phys. Rev. Lett.*, **79**(6), 1038–1041.

Bolinger, J. (1999). On the accuracy of a digital particle image velocimetry system. Technical Report ISSN 0282-1990, Lund Institute of Technology, Sweden.

Bonnet, J. P. and Glauser, M. N., editors (1993). *Eddy structure identification in free turbulent shear flows*. Kluwer Academic.

Borue, V., Orszag, S. A., and Staroselsky, I. (1995). Interaction of surface waves with turbulence: Direct numerical simulations of turbulent open-channel flow. *J. Fluid Mech.*, **286**, 1–23.

Bracewell, R. N. (1993). Affine theorum for two-dimensional fourier transform. *Elec. Letters*, **29**, 304.

Bradshaw, P. (1973). Effects of streamline curvature on turbulent flow. *AGARDo-graph*, (169).

Breuer, K. and Sirovich, L. (1991). The use of Karhunen-Loève procedure for the calculation of linear eigenfunctions. *J. Comp. Phys.*, **96**(2), 277–296.

Briganti, R., Musumeci, R. E., Bellotti, G., Brocchini, M., and Foti, E. (2004). Boussinesq modeling of breaking waves: Description of turbulence. *J. Geophys. Res.*, **109**(C07015), 1–17.

Brocchini, M. (1996). *Flows with freely moving boundaries: the swash zone and turbulence at a free surface*. Ph.D. thesis, Univ. of Bristol.

Brocchini, M. (2002). Free surface boundary conditions at a bubbly/weakly-splashing air-water interface. *Phys. Fluids*, **14**(6), 1834–1840.

Brocchini, M. and Bellotti, G. (2002). Integral flow properties of the swash zone and averaging. part2. shoreline boundary conditions for wave-averaged models. *J. Fluid Mech.*, **458**, 269–281.

Brocchini, M. and Peregrine, D. H. (1996). Integral flow properties of the swash zone and averaging. *J. Fluid Mech.*, **317**, 241–273.

Brocchini, M. and Peregrine, D. H. (1999). The modelling of a spilling breaker: strong turbulence at a free surface. In B. L. Edge, editor, *Coastal Engineering 1998 (Proceedings of the International Conference held in Copenhagen, Denmark, June 22-26, 1998)*, volume 1, pages 72–85, Reston, VA. ASCE.

Brocchini, M. and Peregrine, D. H. (2001a). The dynamics of turbulent free surfaces. part 1. Description. *J. Fluid Mech.*, **449**, 225–254.

Brocchini, M. and Peregrine, D. H. (2001b). The dynamics of strong turbulence at free surfaces. part 2. Free-surface boundary conditions. *J. Fluid Mech.*, **449**, 255–290.

Brown, G. L. and Roshko, A. (1974). On density effects and large structures in turbulent mixing layers. *J. Fluid Mech.*, **64**, 775–816.

Burt, P. J. and Adelson, E. H. (1983). The laplacian pyramid as a compact image code. *IEEE Trans. Comm.*, **31**, 532–40.

Canny, J. F. (1986). A computational approach to edge detection. *IEEE Trans. Patt. Anal. Machine Intel.*, **8**, 679–698.

Carlier, J. and Stanislas, M. (2005). Experimental study of eddy structures in a turbulent boundary layer using particle image velocimetry. *J. Fluid Mech.*, **535**, 143–188.

Castro, I. P. and Bradshaw, P. (1976). The turbulent structure of a highly curved mixing layer. *J. Fluid Mech.*, **73**, 265–304.

Chang, H. C., Demekhin, E. A., and Takhistov, P. V. (2001). Circular hydraulic jumps triggered by boundary layer separation. *J. Colloidal Interface Sc.*, **233**, 329–338.

Chang, K. and Liu, P. L. (1998). Velocity, acceleration and vorticity under a breaking wave. *Phys. Fluids*, **10**(1), 327–329.

Chang, K. A. and Liu, P. L. F. (1999). Experimental investigation of turbulence generated by breaking waves in water of intermediate depth. *Phys. Fluids*, **11**(11), 3390–3400.

Chang, K. A. and Liu, P. L. F. (2000). Pseudo turbulence in piv breaking-wave measurements. *Exp. Fluids*, **29**, 331–338.

Chang, T. and Kuo, C. (1993). Texture analysis and classification with tree-structured wavelet transform. *IEEE Trans. Image Proc.*, **2**(4), 429–441.

Chanson, H. (1996). *Air bubble entrainment in free-surface turbulent shear flows*. Academic Press.

Chanson, H. and Brattberg, T. (2000). Experimental study of the air-water shear flow in a hydraulic jump. *Intl. J. Multiphase Flow*, **26**, 583–607.

Chanson, H. and Toombes, L. (2003). Strong interactions between free-surface aeration and turbulence in an open channel flow. *Exp. Thermal and Fluid Sci.*, **27**, 525–535.

Chebbi, B., Holloway, A. G. L., and Tavoularis, S. (1998). The response of sheared turbulence to changes in curvature. *J. Fluid Mech.*, **358**, 223–244.

Chen, S., Johnson, D. B., Raad, P. E., and Fadda, D. (1997). The surface marker and micro cell method. *Intl. J. Num. Meth. Fluids*, **25**(7), 749–778.

Chippada, S., Ramaswamy, B., and Wheeler, M. F. (1994). Numerical simulation of hydraulic jump. *Intl. J. Num. Meth. Fluids*, **37**, 1381–97.

Chong, M. S., Perry, A. E., and Cantwell, B. J. (1990). A general classification of three-dimensional flow fields. *Phys. Fluids A*, **2**(5), 765–777.

Christensen, E. D. and Deigaard, R. (2001). Large eddy simulation of breaking waves. *Coastal Engrng.*, **42**, 53–86.

Christensen, K. T. (2004). The influence of peak-locking errors on turbulence statistics computed from PIV ensembles. *Exp. Fluids*, **36**(3), 484–497.

Clausi, D. A. (2002). An analysis of co-occurrence texture statistics as a function of grey-level quantization. *Can. J. Rem. Sens.*, **28**(1).

Coakley, D. B. and Duncan, J. H. (1997). The flow field in steady breaking waves. In *21st Symp. on Naval Hydrodynamics, Trondheim, Norway, 24-28 June 1996*, pages 534–549, Washington, D.C. Natl. Acad. Press.

Cointe, R. (1987). *A theory of breakers and breaking waves*. Ph.D. thesis, University of California at Santa Barbara.

Cointe, R. and Tulin, M. P. (1994). A theory of steady breakers. *J. Fluid Mech.*, **276**, 1–20.

Collicott, S. H. (1993). *Applications of laser techniques to fluid mechanics*, chapter Transition from particle image velocimetry to laser speckle velocimetry with increasing seeding density, pages 181–94. Springer, Berlin.

Conners, R. W. and Harlow, C. A. (1980). A theoretical comparison of texture algorithms. *IEEE Trans. Patt. Ana. Machine. Intel.*, **PAMI-2**(3), 204–22.

241

Corrsin, S. (1943). Investigation of flow in an axially symmetrical heated jet of air. Technical Report TR 1244, NACA, Washington, D. C.

Corrsin, S. and Kistler, A. L. (1955). Free-stream boundaries of turbulent flows. Technical Report 1244, Nat. Adv. Ctee. Aero., Washington.

Cox, D. T. and Anderson, S. L. (2001). Statistics of intermittent surf zone turbulence and observations of large eddies using PIV. *Coast. Engrng. J.*, **43**(2), 121–131.

Cox, D. T. and Kobayashi, N. (2000). Identification of intense, intermittent coherent motions under shoaling and breaking waves. *J. Geophys. Res.*, **105**(C6), 14223–36.

Cox, D. T. and Shin, S. (2003). Laboratory measurements of void fraction and turbulence in the bore region of surf zone waves. *J. Engrng. Mech.*, **129**(10), 1197–1205.

Dabiri, D. and Gharib, M. (1997). Experimental investigation of the vorticity generation within a spilling water wave. *J. Fluid Mech.*, **330**, 113–139.

Delville, J., Ukeiley, L., Cordier, L., Bonnet, J. P., and Glauser, M. (1999). Examination of large-scale structures in a turbulent plane mixing layer. Part 1. Proper orthogonal decomposition. *J. Fluid Mech.*, **391**, 91–122.

Dewey, C. F. (1976). Qualitative and quantitative flow field visualization using laser- induced flourescence. *AGARD conference on application of non-intrusive instrumentation in fluid flow research*, **AGARD-CP-193**(17), 1–7.

Dimas, A. and Fialkowski, L. (2000). Large-wave simulation (LWS) of free-surface flows developing weak spilling breaking waves. *J. Comp. Phys.*, **159**, 172–96.

Donelan, M. A., Haus, B. K., Reul, N., Plant, W. J., Stassnie, M., Graber, H. C., Brown, O. B., and Saltzman, E. S. (2004). On the limiting aerodynamic roughness of the ocean in very strong winds. *J. Geophys. Letters*, **31**(L18306).

Duda, R. O., Hart, P. E., and Stork, D. G. (2000). *Pattern Classification*. Wiley-Interscience, New York, second edition.

Duncan, J. H. (1981). An experimental investigation of breaking waves produced by a towed hydrofoil. *Proc. R. Soc. Lond. Series A*, **377**, 331–348.

Duncan, J. H. (2001). Spilling breakers. *Ann. Rev. Fluid Mech.*, **33**, 519–547.

Duncan, J. H., Philomin, V., Behres, M., and Kimmel, J. (1994). The formation of spilling breaking water waves. *Phys. Fluids*, **6**(8), 2558–2560.

Duncan, J. H., Qiao, H., Philomin, V., and Wenz, A. (1999). Gentle spilling breakers: crest profile evolution. *J. Fluid Mech.*, **379**, 191–222.

Farge, M. (1991). Wavelet analysis of coherent structures in two-dimensional turbulent flows. *Phys. Fluids*, **3**(9), 2029.

Forliti, D. J., Strykowski, P. J., and Debatin, K. (2000). Bias and precision errors of digital particle image velocimetry. *Exp. Fluids*, **28**(5), 436–447.

Foroosh, H., Zerubia, J. B., and Berthod, M. (2002). Extension of phase correlation to subpixel registration. *IEEE Trans. Image Proc.*, **11**, 188–200.

Fulgosi, M., Lakehal, D., Banerjee, S., and Angelis, V. D. (2003). Direct numerical simulation of turbulence in a sheared air-water flow with a deformable interface. *J. Fluid Mech.*, **482**, 319–345.

Galvin, C. J. (1968). Breaker type classification on three laboratory beaches. *J. Geophys. Res.*, **73**(12), 3651–59.

Ganapathisubramani, B., Hutchins, N., Hambleton, W. T., Longmire, E. K., and Marusic, I. (2005). Investigation of large-scale coherence in a turbulent boundary layer using two-point correlations. *J. Fluid Mech.*, **524**, 57–80.

Gibson, M. M. and Rodi, W. (1981). A reynolds-stress closure model of turbulence applied to the calculation of a highly curved mixing layer. *J. Fluid Mech.*, **103**, 161–182.

Goldstein, S. (1938). *Modern developments in fluid mechanics I.*. Dover, New York.

Gonzales, R. C. and Woods, R. E. (2002). *Digital Image Processing*. Prentice Hall, second edition.

Govender, K., Alport, M. J., Mocke, G., and Michallet, H. (2002a). Video measurements of fluid velocities and water levels in breaking waves. *Physica Scripta*, **T97**, 152–159.

Govender, K., Mocke, G., and Alport, M. (2002b). Video imaged surf zone wave and roller structures and flow fields. *J. Geophys. Res.*, **107**(C10), 3177.

Green, R. B., Doolan, C. J., and Cannon, R. M. (2000). Measurements of the orthogonal blade-vortex interaction using a particle image velocimetry technique. *Exp. Fluids*, **29**, 369–79.

Grigorescu, S. E., Petkov, N., and Kruizinga, P. (2002). Comparison of texture features based on gabor filters. *IEEE Trans. Image Proc.*, **11**(10), 1160–67.

Grilli, S. T. and Subramanya, R. (1996). Numerical modeling of wave breaking induced by fixed or moving boundaries. *Comp. Mech.*, **17**(6), 374–391.

Haralick, R. M., Shanmugam, K., and Dinstein, I. (1973). Textural features for image classification. *IEEE trans. on systems, man and cybernetics*, **SMC-3**, 610–621.

Hassan, Y. A., Okamoto, K., and Philip, O. G. (1996). Investigation of the interaction between a fluid flow and the fluid's free surface using particle image

velocimetry. In *9th Int. symp. on transport phenomena in thermal-fluids engg.*, pages 566–574.

He, D. and Wang, L. (1991). Texture features based on texture spectrum. *Pattern Recognition*, **24**(5), 391–399.

Henderson, F. M. (1970). *Open Channel Flow*. The MacMillan Company.

Hibberd, S. and Peregrine, D. H. (1976). Surf and run-up on a beach : a uniform bore. *J. Fluid Mech.*, **95**, 323–345.

Higgins, C. W., Parlange, M. B., and Meneveau, C. (2003). Alignment trends of velocity gradients and subgrid-scale fluxes in the turbulent atmospheric boundary layer. *Boundary-Layer Meteorology*, **109**, 59–83.

Hirt, C. W. and Nichols, B. D. (1981). Volume of fluid (VOF) method for the dynamics of free boundaries. *J. Comp. Physics*, **39**, 201–225.

Ho, C.-M. and Huerre, P. (1984). Perturbed free shear layers. *Ann. Rev. Fluid Mech.*, **16**, 365–424.

Holloway, A. G. L. and Tavoularis, S. (1992). The effects of curvature on sheared turbulence. *J. Fluid Mech.*, **237**, 569–603.

Holloway, A. G. L. and Tavoularis, S. (1998). A geometric explanation of the effects of mild streamline curvature on the integral length scales of sheared turbulence. *Phys. Fluids*, **10**(7), 1733–41.

Holloway, A. G. L., Roach, D. C., and Akbary, H. (2005). Combined effects of favorable pressure gradient and streamline curvature on uniformly sheared turbulence. *J. Fluid Mech.*, **526**, 303–336.

Holton, J. R. (2004). *An introduction to dynamic meteorology*, volume 88 of *The international geophysics series*. Academic Press, fourth edition.

Hong, W. and Walker, D. T. (2000). Reynolds-averaged equations for free-surface flows with application to high-froude-number jet spreading. *J. Fluid Mechanics*, **417**, 183–209.

Horebeek, J. V. and Tapia-Rodriguez, E. T. (2001). The approximation of a morphological opening and closing in the presence of noise. *Signal Processing*, **81**, 1991–1995.

Horn, B. K. P. and Schunck, B. G. (1981). Determining optical flow. *Art. Intel.*, **17**, 185–203.

Hornung, H. G., Willert, C., and Turner, S. (1995). The flow field of a hydraulic jump. *J. Fluid Mech.*, **287**, 299–316.

Hoyt, J. W. and Sellin, R. H. J. (1989). Hydraulic jump as "Mixing layer". *J. Hyd. Engrng.*, **115**(12), 1607–1614.

Huang, H., Dabiri, D., and Gharib, M. (1997). On errors of digital particle image velocimetry. *Meas. Sci. and Tech.*, **8**, 1427–1440.

Hunt, I. A. and Joubert, P. N. (1979). Effects of small streamline curvature on turbulent duct flow. *J. Fluid Mech.*, **91**, 633.

Hunt, J. C. R. (1987). Turbulent structure and turbulent diffusion near gas-liquid interfaces. In W. Brutsaert and G. H. Girka, editors, *Gas transfer at water surfaces*, pages 67–82. Reidel, Dordrecht.

Iafrati, A. and Campana, E. F. (2003). A domain decomposition approach to compute wave breaking (wave-breaking flows). *Int. J. Numer. Meth. Fluids*, **41**, 419–445.

Iafrati, A. and Campana, E. F. (2005). Free-surface fluctuations behind micro-breakers: space-time behaviour and subsurface flow field. *J. Fluid Mech.*, **529**, 311–347.

Iafrati, A., diMascio, A., and Campana, E. (2001). A level set technique applied to unsteady free surface flows. *Int. J. Num. Meth. Fluids*, **35**, 281297.

Iverson, H. W. (1952). Laboratory study of breakers. In *Gravity waves*, volume Circ. 521, pages 9–32. Natl. Bur. Stand.

Jansen, P. C. M. (1986). Laboratory observations of the kinematics in the aerated region of breaking waves. *Coastal Engrng.*, **9**, 463–477.

Jeong, J. and Hussain, F. (1995). On the identification of a vortex. *J. Fluid Mech.*, **285**, 69–94.

Jiménez, J., Wray, A. A., Saffman, P. G., and Rogallo, R. S. (1993). The structure of intense vorticity in isotropic turbulence. *J. Fluid Mech.*, **255**, 65–90.

Kambhamettu, C., Goldgof, D. B., Terzopoulos, D., and Huang, T. S. (1994). *Handbook of Pattern Recognition and Image Processing: Computer Vision*, chapter Nonrigid motion analysis. Academic Press, San Diego.

Karhunen, K. (1946). Zur spektraltheorie stochasticher. *Annales Academiae Scientiarum Fennicae Series A*, **1**, 34.

Kass, M., Witkin, A., and Terzopoulos, D. (1987). Snakes: Active contour models. *Int. J. Comp. Vis.*, **1**, 321–31.

Keane, R. D. and Adrian, R. J. (1990). Optimization of particle image velocimeters. part I: Double pulsed systems. *Meas. Sci. Technol.*, pages 1202–1215.

Kevlahan, N. K. R., Hunt, J. C. R., and Vassilicos, J. C. (1994). A comparison of diffferent analytical techniques for identifying structures in turbulence. *Appl. Sci. Res.*, **53**, 339–355.

Kim, H. T., Kline, S. J., and Reynolds, W. C. (1971). The production of turbulence near a smooth wall in a turbulent boundary layer. *J. Fluid Mech.*, **50**(1), 133–160.

Kline, S. J. and Robinson, S. K. (1989). *Near wall turbulence. Proceedings of Zaric Memorial Conference*, chapter Quasi-coherent structures in the turbulent boundary layer. Part I: status report on a community-wide summary of the data, pages 200–217. Hemisphere, New York.

Kline, S. J., Reynolds, W. C., Schraub, F. A., and Runstadler, P. W. (1967). The structure of turbulent boundary layers. *J. Fluid Mech.*, **30**, 741–73.

Kobus, H. (1991). Introduction to air water flows. In I. R. Wood, editor, *Air entrainment in free-surface flows*, chapter 1. A. A. Balkema, Netherlands.

Kosambi, D. (1943). Statistics in function space. *J. Indian Math. Soc.*, **7**, 76–88.

Kostas, J., Soria, J., and Chong, M. S. (2005). A comparison between snapshot POD analysis of PIV velocity and vorticity data. *Exp. Fluids*, **38**, 146–160.

Kruger, S. A. and Calway, A. D. (1996). A multiresolution frequency domain method for estimating affine motion parameters. In *Intl. Conf. Image Proc.*, pages 113–116.

Lamballais, E., Lesieur, M., and Métais, O. (1997). Probability distribution functions and coherent structures in a turbulent channel. *Phys. Rev. E*, **56**(6), 6761–6766.

Laufer, J. (1975). New trends in experimental turbulence research. *Ann. Rev. Fluid Mech.*, **7**, 307–326.

Launder, B. E. and Spalding, D. B. (1972). *Mathematical models of turbulence*. Academic Press, London and New York.

Launder, B. E., Priddin, C. H., and Sharma, B. R. (1977). The calculation of turbulent boundary layers on spining and curved surfaces. *ASME J. Fluids Engrng.*, **99**, 321.

Law, C. N. S., Khoo, B. C., and Chen, T. C. (1999). Turbulence structure in the immediate vicinity of the shear-free air-water interface induced by a deeply submerged jet. *Exp. Fluids*, **27**, 321–31.

Lennon, J. and Hill, D. H. (2004). Particle image velocimetry measurements of undular and hydraulic jumps. Submitted.

Leutheusser, H. J. and Kartha, V. C. (1972). Effects of inflow condition on hydraulic jump. *J. Hyd. Div.*, **98**(HY8), 1367–1385.

Leymarie, F. and Levine, M. D. (1993). Tracking deformable objects in the plane using an active contour model. *IEEE-PAMI*, **15**(6), 617–34.

Liiv, T. (2001). Investigation of turbulence in a plunging breaking wave. *Proc. Estonian Acad. Sci. Engrng.*, **7**(1), 58–78.

Lin, H. J. and Perlin, M. (1998). Improved methods for thin, surface boundary layer investigations. *Exp. Fluids*, **25**, 431–444.

Lin, J. C. and Rockwell, D. (1994). Instantaneous structure of a breaking wave. *Phys. Fluids*, **6**(9), 2877–2879.

Lin, J. C. and Rockwell, D. (1995). Evolution of a quasi-steady breaking wave. *J. Fluid Mech.*, **302**, 29–44.

Lin, P. and Liu, P. L. F. (1998). A numerical study of breaking waves in the surf zone. *J. Fluid Mech.*, **359**, 239–264.

249

Liu, M., Rajaratnam, N., and Zhu, D. Z. (2004). Turbulence structure of hydraulic jumps of low Froude numbers. *J. Hyd. Engrng.*, **130**, 511–520.

Liu, X. and Duncan, J. H. (2003). The effects of surfactants on spilling breaking waves. *Nature*, **421**, 520–524.

Liu, Z., Adrian, R. J., and Hanratty, T. J. (2001). Large-scale modes of turbulent channel flow: transport and structure. *J. Fluid Mech.*, **448**, 53–80.

Loeve, M. (1955). *Probability theory*. Van Nostrand, New York.

Long, D., Steffler, P. M., and Rajaratnam, N. (1990). LDA structure of flow structure in submerged hydraulic jumps. *J. Hyd. Res.*, **4**, 437–460.

Long, D., Steffler, P., and Rajaratnam, N. (1991). A numerical study of submerged hydraulic jumps. *J. Hyd. Res.*, **29**(3), 293–308.

Longo, S. (2003). Turbulence under spilling breakers using discrete wavelets. *Exp. Fluids*, **34**, 181–191.

Longuet-Higgins, M. S. (1973). A model of flow separation at a free surface. *J. Fluid Mech.*, **57**(1), 129–148.

Longuet-Higgins, M. S. (1994). Shear instability in spilling breakers. *Proc. R. Soc. Lond. A*, **446**, 399–409.

Longuet-Higgins, M. S. (1995). On the disintegration of the jet in a plunging breaker. *J. Phys. Ocean.*, **25**, 2458–62.

Longuet-Higgins, M. S. (1998a). Vorticity and curvature at a free surface. *J. Fluid Mech.*, **356**, 149–153.

Longuet-Higgins, M. S. (1998b). Instabilities of a horizontal shear flow with a free surface. *J. Fluid Mech.*, **364**, 147–162.

Longuet-Higgins, M. S. and Cleaver, R. P. (1994). Crest instabilities of gravity waves. I. The inner solution. *J. Fluid Mech.*, **258**, 115–129.

Longuet-Higgins, M. S. and Dommermuth, D. G. (1997). Crest instabilities of gravity waves. Part 3. Nonlinear development and breaking. *J. Fluid Mech.*, **336**, 33–50.

Longuet-Higgins, M. S. and Turner, J. S. (1974). An entraining plume model of a spilling breaker. *J. Fluid Mech.*, **63**, 1–20.

Longuet-Higgins, M. S., Cleaver, R. P., and Fox, M. J. H. (1994). Crest instabilities of gravity waves. II. matching and asymptotic expansion. *J. Fluid Mech.*, **259**, 333–344.

Lumley, J. (1967). The structure of inhomogeneous turbulent flows. In A. M. Yaglam and V. I. Tatarsky, editors, *Proceedings of the international colloquium on the fine scale structure of the atmosphere and its influence on radio wave propagation*, pages 166–178, Moscow.

Lumley, J. L. (1981). *Transition and turbulence*, chapter Coherent structures in turbulence, pages 215–242. Academic, New York.

Ma, F., Hou, Y., and Prinos, P. (2001). Numerical calculation of submerged hydraulic jumps. *J. Hyd. Res.*, **39**(5), 1–11.

Madsen, P. A. (1981). A model for a turbulent bore. Technical Report 28, Inst. Hydrodyn. and Hydraul. Engrng., Tech. Univ. Denmark.

Madsen, P. A. and Svendsen, I. A. (1983). Turbulent bores and hydraulic jumps. *J. Fluid Mech.*, **129**, 1–25.

Manduchi, R. and Mian, G. A. (1993). Accuracy analysis for correlation-based image registration algorithms. In *Proc. ISCAS*, pages 834–37.

Marceau, D. J., Howarth, P. J., Dubois, J.-M. M., and Gratton, D. J. (1990). Evaluation of the grey-level co-occurrence matrix method for land cover classification using spot imagery. *IEEE Trans. Geosci. Rem. Sens.*, **28**(4), 513–19.

Marr, D. and Hildreth, E. (1980). Theory of edge detection. *Proc. R. Soc. London B*, **207**, 187–217.

Mason, M. A. (1952). Some observations of breaking waves. In *Gravity waves*, volume Circ. 521, pages 215–220. Natl. Bur. Stand.

Maxey, M. R. (1987). The gravitational settling of aerosol particles in homogenous turbulence and random flow fields. *J. Fluid Mech.*, **174**, 441.

Meinhart, C. D. and Adrian, R. J. (1995). On the existence of uniform momentum zones in a turbulent boundary layer. *Phys. Fluids*, **7**, 694–696.

Melville, W. K., Veron, F., and White, C. J. (2002). The velocity field under breaking waves: coherent structures and turbulence. *J. Fluid Mech.*, **454**, 203–233.

Misra, S. K., Kirby, J. T., Brocchini, M., Thomas, M., Veron, F., and Kambhamettu, C. (2004). Extra strain rates in spilling breaking waves. In J. M. Smith, editor, *Proc. 29th Intl. Conf. Coastal Engrng*, volume 1, pages 370–378. ASCE.

Misra, S. K., Kirby, J. T., Brocchini, M., Veron, F., Thomas, M., and Kambhamettu, C. (2005). Coherent turbulent structures in a quasi-steady spilling breaker. In *Proc. WAVES 2005 - 5th Intl. Symp. Ocean Wave Meas. Anal.*, Madrid, Spain.

Misra, S. K., Shi, F., Brocchini, M., and Kirby, J. T. (2006). Turbulent interfacial boundary conditions for numerical modeling of spilling breaking waves. In *30th Intl. Conf. Coastal Engrng*. Submitted.

Mobbs, F. (1968). Spreading and contraction at the boundaries of free turbulent flows. *J. Fluid Mech.*, **33**, 227–240.

Moore, D. W. (1978). The equation of motion of a vortex layer of small thickness. *Stud. Appl. Math.*, **58**, 119–140.

Moré, J. J. (1977). *Lecture notes in mathematics 630*, chapter The Levenberg-Marquardt algorithm: Implementation and theory, pages 105–116. Springer-Verlag.

Mori, K. H. (1986). Sub-breaking waves and critical condition for their appearance. *J. Soc. Naval Arch. Japan*, **159**(23), 1–8.

Mossa, M. (1998). On the oscillating characteristics of hydraulic jumps. *J. Hyd. Res.*, **37**, 541–558.

Mossa, M. and Tolve, U. (1998). Flow visualization in bubbly two-phase hydraulic jumps. *J. Fluids Engrng.*, **120**, 160–165.

Muzaferija, S. and Perić, M. (1999). *Nonlinear wave interaction*, chapter Computation of free surface flows using interface-tracking and interface-capturing methods., pages 59–100. WIT Press.

Nadaoka, K. (1986). A fundamental study on shoaling and velocity field structure of water waves in the nearshore zone. Technical Report 36, Dept. of Civil Engrng, Tokyo Inst. of Tech.

Narayanan, R. (1975). Wall jet analogy to hydaulic jump. *J. Hydr. Div., ASCE*, **101**(3), 347.

Nepf, H. M., Wu, C. H., and Chan, E. S. (1998). A comparison of two- and three-dimensional wave breaking. *J. Phys. Oceanogr.*, **28**, 1496–1510.

Nogueira, J., Lecuona, A., and Rodriguéz, P. A. (1997). Data validation, false vectors correction and derived magnitudes calculation on PIV. *Meas. Sc. Technol.*, **8**, 1493–1501.

Nogueira, J., Lecuona, A., and Rodriguez, P. A. (2001). Identification of a new source of peak locking, analysis and its removal in conventional and super-resolution PIV techniques. *Exp. Fluids*, **30**, 309–316.

Okamoto, K., Nishio, S., Saga, T., and Kobayashi, T. (2000). Standard images for particle-image velocimetry (www.vs.or.jp/piv/). *Meas. Sci. Technol.*, **11**, 685–91.

Peirson, W. L. (1997). Measurement of surface velocities and shear at a wavy air-water interface using particle image velocimetry. *Exp. Fluids*, **23**, 427–437.

Peregrine, D. H. (1983). Breaking waves on beaches. *Ann. Rev. Fluid Mech.*, **15**, 149–178.

Peregrine, D. H. (1992). Mechanism of wave breaking. In M. L. Banner and R. H. J. Grimshaw, editors, *Proceedings of the IUTAM symp. on breaking waves*, volume 41. Springer-Verlag.

Peregrine, D. H. and Svendsen, I. A. (1978). Spilling breakers, bores and hydraulic jumps. In *Proceedings of the 16th ICCE, Hamburg*, pages 540–555. ASCE.

Perlin, M., He, J., and Bernal, L. P. (1996). An experimental study of deep water plunging breakers. *Phys. Fluids*, **8**(9), 2365–2374.

Perry, A. E. and Chong, M. S. (1994). Topology of flow patterns in vortex motions and turbulence. *Appl. Sci. Res.*, **53**, 357–374.

Plesniak, M. W. and Johnston, J. P. (1991). Reynolds stress evolution in curved two-stream turbulent mixing layers. In F. Durst, B. E. Launder, W. C. Reynolds, F. W. Schmidt, and J. H. Whitelaw, editors, *Turbulent shear flows*, volume 7, pages 239–252. Springer-Verlag.

Prasad, A. K. (2000). Particle image velocimetry. *Current Science*, **79**(1), 51–60.

Prasad, A. K., Adrian, R. J., Landreth, C. C., and Offutt, P. W. (1992). Effect of resolution on the speed and accuracy of particle image velocimetry interrogation. *Exp. Fluids*, **13**, 105–116.

Prasad, R. R. and Sreenivasan, K. R. (1989). Scalar interfaces in digital images of turbulent flow. *Exp. Fluids*, **7**(4), 259–64.

Proakis, J. G. and Manolakis, D. G. (1995). *Digital signal processing: Principles, algorithms and applications*. Prentice Hall, Englewood Cliffs, NJ.

Qiao, H. and Duncan, J. H. (2001). Gentle spilling breakers: crest flow-field evolution. *J. Fluid Mech.*, **439**, 57–85.

Quenot, G. M., Pakleza, J., and Kowalewski, T. A. (1998). Particle image velocimetry with optical flow. *Exp. Fluids*, **25**, 177–89.

Raffel, M., Willert, C., and Kompenhans, J. (1998). *Particle image velocimetry - a practical guide*. Springer-Verlag.

Rajagopalan, S. and Antonia, R. A. (1982). Use of a quadrant analysis technique to identify coherent structures in a turbulent boundary layer. *Phys. Fluids*, **25**(6), 949–956.

Rajaratnam, N. (1965). The hydraulic jump as a wall jet. *J. Hydr. Div., ASCE*, **91**(5), 107–132.

Rapp, R. J. and Melville, W. K. (1990). Laboratory measurements of deep-water breaking waves. *Phi. Trans. Roy. Soc. Lond. A*, **331**, 735–800.

Reddy, B. and Chatterji, B. (1996). An fft based technique for translation, rotation and scale-invariant image registration. *IEEE Trans. Image Proc.*, **5**, 1266–71.

Resch, F. J. and Leutheusser, H. J. (1972). Reynolds stress measurements in hydraulic jumps. *J. Hyd. Res.*, **10**, 409–430.

Rhee, S. H. and Stern, F. (2002). RANS model for spilling breaking waves. *J. Fluids Engrng.*, **124**, 424–432.

Richmond, M. C., Chen, H. C., and Patel, V. C. (1986). Equations of laminar and turbulent flows in general curvilinear coordinates. Technical Report IIHR, 300, University of Iowa.

Robinson, S. K. (1991). Coherent motions in the turbulent boundary layer. *Ann. Rev. Fluid Mech.*, **23**, 601–639.

Roesgen, T. (2003). Optimal subpixel interpolation in particle image velocimetry. *Exp. Fluids*, **35**, 252–256.

Rogers, B. D. and Dalrymple, R. A. (2005). Three-dimensional SPH-SPS modeling of wave breaking. To be presented at WAVES 2005.

Roth, G. I., Mascenik, D. T., and Katz, J. (1999). Measurements of the flow structure and turbulence within a ship bow wave. *Phys. Fluids*, **11**(11), 3512–23.

Rouse, H., Siao, T. T., and Nagarathnam, S. (1959). Turbulence characteristics of the hydraulic jumps. *Trans. ASCE*, **124**, 926–966.

Rumsey, C. L., Gatski, T. B., and Morrison, J. H. (1999). Turbulence model predictions of extra strain rate effects in strongly-curved flows. *AIAA*, **99-0157**.

Scarano, F. and Riethmuller, M. L. (1999). Iterative multigrid approach in PIV image processing with discrete window offset. *Exp. Fluids*, **26**, 513–23.

Scardovelli, R. and Zaleski, S. (1999). Direct numerical simulation of free-surface flow and interfacial flow. *Ann. Rev. Fluid Mech.*, **31**, 567–603.

Schaffer, H. A., Madsen, P. A., and Deigaard, R. (1993). A Boussinesq model for waves breaking in shallow water. *Coastal Engrng.*, **20**, 185–202.

She, K., Greated, C., and Easson, W. (1994). Experimental study of three-dimensional wave breaking. *J. Waterway, Port, Coastal, Ocean Engrng.*, **120**, 20–36.

Shi, F., Zhao, Q., and Kirby, J. T. (2004). Modeling of wave interaction with complex coastal structures using an enhanced VOF model. In J. M. Smith, editor, *Coastal Engineering 2004, Proc. 29th Intl. Conf. Coastal Engrng.*, volume 1, pages 581–593.

Shih, T. H., Zhu, J., and Lumley, J. L. (1996). Calculation of wall-bounded complex flows and free shear flows. *Intl. J. Num. Meth. Fluids*, **23**, 1133–44.

Simpson, R. L. (1989). Turbulent boundary layer separation. *Ann. Rev. Fluid Mech.*, **21**, 205–34.

Sirovich, L. (1987). Turbulence and dynamics of coherent structures, part I, II and III. *Quart. Appl. Math.*, **XLV**, 561–590.

Soldini, L., Piattella, A., Mancinelli, A., Bernetti, R., and Brocchini, M. (2004). Macro-vortices induced horizontal mixing in compound channels. *Ocean Dyn.*, **54**(3-4), 333–339.

Song, C. and Sirviente, A. I. (2004). A numerical study of breaking waves. *Phys. Fluids*, **16**(7), 2649–2667.

Soria, J. and Cantwell, B. J. (1994). Topological visualization of focal structures in free shear flows. *Appl. Sci. Res.*, **53**, 375–386.

Speziale, C. G. (1991). Analytical methods for the development of Reynolds-stress closures in turbulence. *Ann. Rev. Fluid Mech.*, **23**, 107–157.

Stanislas, M., Carlier, J., Foucaut, J.-M., and Dupont, P. (1999). Double spatial correlation, a new experimental insight into wall turbulence. *C. R. Acad. Sci. Paris*, **327**(II b), 55–61.

Stanislas, M., Okamoto, K., and Kähler, C. (2003). Main results of the first international PIV challenge (www.pivchallenge.org). *Meas. Sci. Technol.*, **14**, R63–89.

Stansby, P. and Feng, T. (2005). Kinematics and depth-integrated terms in the surf zone waves from laboratory measurement. *J. Fluid Mech.*, **529**, 279–310.

Svendsen, I. A. (1987). Analysis of surf zone turbulence. *J. Geophys. Res.*, **92**(C5), 5115–5124.

Svendsen, I. A. and Madsen, P. A. (1984). A turbulent bore on a beach. *J. Fluid Mech.*, **148**, 73–96.

Svendsen, I. A., Veeramony, J., Bakunin, J., and Kirby, J. T. (2000). The flow in weak turbulent hydraulic jumps. *J. Fluid Mech.*, **418**, 25–57.

Tennekes, H. and Lumley, J. L. (1972). *A first course in turbulence*. MIT Press.

Thandaveswara, B. S. (1974). *Self aerated flow characteristics in developoing zones and inhydraulic jumps*. Ph.D. thesis, Dept. of Civil Engineering, Indian Institute of Science, Bangalore, India.

Thomas, G. A. (1987). Television motion measurement for datv and other applications. Technical report, BBC Research Department.

Thomas, M., Misra, S. K., Kambhamettu, C., and Kirby, J. T. (2005a). A robust motion estimation algorithm for PIV. *Meas. Sci. and Tech.*, **16**(3), 865–77.

Thomas, M., Misra, S. K., Kambhamettu, C., and Kirby, J. T. (2005b). Contour estimation using factored sampling for fluid interface estimation. Submitted

to *Energy Minimization Methods in Computer Vision and Pattern Recognition* (EMMCVPR).

Thornton, E. B. and Guza, R. T. (1983). Transformation of wave height distribution. *J. Geophys. Res.*, **88**(C10), 5925–5938.

Ting, F. C. (2004). Turbulence dynamics in irregular breaking waves. Technical Report N00014-00-1-0461, Office of Naval Research.

Ting, F. C. K. (2002). Wave and turbulence characteristics in narrow-banded irregular breaking waves. *Coastal Engineering*, **46**, 291–313.

Ting, F. C. K. and Kirby, J. T. (1995). Dynamics of surf-zone turbulence in a strong plunging breaker. *Coastal Engrng.*, **24**, 177–204.

Ting, F. C. K. and Kirby, J. T. (1996). Dynamics of surf-zone turbulence in a spilling breaker. *Coastal Engrng.*, **27**, 131–160.

Torrence, C. and Compo, G. P. (1998). A practical guide to wavelet analysis. *Bull. Amer. Meteor. Soc.*, **79**, 61–78.

Townsend, A. A. (1976). *The structure of turbulent shear flow*. Cambridge University Press, second edition.

Truco, E. and Verri, A. (1998). *Introductory techniques for 3-D computer vision*. Prentice Hall, Englewood Cliffs.

Tsuei, L. and Savaş, O. (2000). Treatment of interfaces in particle image velocimetry. *Exp. Fluids*, **29**, 203–14.

Tuceryan, M. and Jain, A. K. (1998). *The handbook of pattern recognition and computer vision*, chapter Texture analysis, pages 207–248. World Scientific, second edition.

Tulin, M. P. and Cointe, R. (1988). Steady and unsteady spiling breakers : Theory. In K. Horikawa and H. Maruo, editors, *Nonlinear Water Waves*, IUTAM Symposium, pages 159–167. Springer-Verlag.

Turk, M. and Pentland, A. (1991). Eigenfaces for recognition. *J. Cognitive Neuroscience*, **3**, 72–86.

Turner, J. S. (1962). The starting plume in neutral surroundings. *J. Fluid Mech.*, **13**, 356–368.

Veeramony, J. and Svendsen, I. A. (2000). The flow in surf-zone waves. *Coastal Engrng.*, **39**, 93–122.

Vernon, D. (2001). *Fourier Vision - Segmentation and velocity measurement using Fourier transform*. Kluwer, Dodrecht.

Walker, D. T. (1997). On the origin of the 'surface current' in turbulent free-surface flows. *J. Fluid Mech.*, **339**, 275–285.

Wang, Q., Squires, K. D., and Wang, L. (1998). On the effect of nonuniform seeding on particle dispersion in two-dimensional mixing layers. *Phys. Fluids*, **10**(7), 1700–1714.

Westerweel, J. (1994). Efficient detection of spurious vectors in particle image velocimetry data. *Exp. Fluids*, **16**, 236–247.

Westerweel, J. (2000). Effect of sensor geometry on the performance of PIV interrogation. In R. J. A. *et al*, editor, *Laser techniques applied to fluid mechanics*, pages 37–55. Springer.

Westerweel, J., Dabiri, D., and Gharib, M. (1997). The effect of a discrete window offset on the accuracy of cross-correlation analysis of digital PIV recordings. *Exp. Fluids*, **23**, 20–28.

Westerweel, J., Hofmann, T., Fukushima, C., and Hunt, J. C. R. (2002). Experimental investigation of the turbulent/non-turbulent interface at the outer boundary of a self-similar turbulent jet. *Exp. Fluids*, **33**, 873–878.

Weszka, J. S., Dyer, C. R., and Rosenfeld, A. (1976). A comparative study of texture measures for terrain classification. *IEEE Trans. Sys. Man Cybernetics*, **SMC-6**(4), 269–85.

Whitham, G. B. (1974). *Linear and nonlinear waves*. Wiley-Interscience, New York.

Willert, C. E. and Gharib, M. (1991). Digital particle image velocimetry. *Exp. Fluids*, **10**, 181–93.

Williams, D. J. and Shah, M. (1992). A fast algorithm for active contours and curvature estimation. *CVGIP: Image Understanding*, **55**(1), 14–26.

Wyngaard, J. C., Tennekes, H., Lumley, J. L., and Margolis, D. P. (1968). Structure of turbulence in a curved mixing layer. *Phys. Fluids*, **11**(6), 1251–1253.

Xu, C. and Prince, J. L. (1998). Snakes, shapes and gradient vector flow. *IEEE Trans. Image Proc.*, **7**(3), 359–69.

Yeh, H. H. and Mok, K.-M. (1990). On turbulence in bores. *Phys. Fluids*, **2**(5), 821–828.

Yip, K. (1995). Reasoning about fluid motion I: Finding structures. In *QR'95, Ninth International Workshop on Qualitative Reasoning*, pages 201–207, Amsterdam, Netherlands.

Zhao, Q., Armfield, S., and Tanimoto, K. (2004a). Numerical simulation of breaking waves by a multi-scale turbulence model. *Coastal Engrng.*, **51**, 53–80.

Zhao, Q., Misra, S. K., Svendsen, I. A., and Kirby, J. T. (2004b). Numerical study of a turbulent hydraulic jump. In *Proc. 17th Engrng. Mech. Div. Conf.*, Newark. ASCE.

Zhou, J., Adrian, R. J., and Balachander, S. (1996). Autogeneration of near-wall vortical structures in channel flow. *Phys. Fluids*, **8**, 288–290.

Zhou, J., Adrian, R. J., Balachander, S., and Kendall, T. M. (1999). Mechanisms for generating coherent packets of hairpin vortices in channel flow. *J. Fluid Mech.*, **387**, 353–359.